# Direct Measurements of Colloidal Interactions in the Presence of Different Analytes

*By*

**V. MAHENDRAN**

**Enrolment No: PHYS0220104010**

**Indira Gandhi Centre for Atomic Research, Kalpakkam,**
**Tamil Nadu, India 603 102**

***A Thesis submitted to the***
***Board of Studies in Physical Sciences***
***In partial fulfillment of requirements***
***For the degree of***

**DOCTOR OF PHILOSOPHY**

*of*

**HOMI BHABHA NATIONAL INSTITUTE**

**May, 2015**

# Homi Bhabha National Institute

## Recommendations of the Viva Voce Board

As members of the Viva Voce Board, we certify that we have read the dissertation prepared by **V.Mahendran** entitled "**Direct Measurements of Colloidal Interactions in the Presence of Different Analytes**" and recommend that it may be accepted as fulfilling the dissertation requirement for the Degree of Doctor of Philosophy.

________________________________________________ **Date:**

Chairman-**Dr. T. Jayakumar**

________________________________________________ **Date:**

Convener-**Dr. John Philip**

________________________________________________ **Date:**

Member 1-Examiner

________________________________________________ **Date:**

Member 2-**Dr. B. V. R. Tata**

________________________________________________ **Date:**

Member 3- **Dr. T. R. Ravindran**

Final approval and acceptance of this dissertation is contingent upon the candidate's submission of the final copies of the dissertation to HBNI.

I hereby certify that I have read this thesis prepared under my direction and recommend that it may be accepted as fulfilling the thesis requirement.

**Date:** **Dr. John Philip**

**Place:** (Guide)

# STATEMENT BY AUTHOR

This dissertation has been submitted in partial fulfillment of requirements for an advanced degree at Homi Bhabha National Institute (HBNI) and is deposited in the Library to be made available to borrowers under rules of the HBNI.

Brief quotations from this dissertation are allowable without special permission, provided that accurate acknowledgement of source is made. Requests for permission for extended quotation from or reproduction of this manuscript in whole or in part may be granted by the Competent Authority of HBNI when in his or her judgment the proposed use of the material is in the interests of scholarship. In all other instances, however, permission must be obtained from the author.

**Kalpakkam** **(V. MAHENDRAN)**

**May, 2015**

# DECLARATION

I, hereby declare that the investigation presented in the thesis has been carried out by me. The work is original and has not been submitted earlier as a whole or in part for a degree/diploma at this or any other Institution/University.

**Kalpakkam** **(V. MAHENDRAN)**

**May, 2015**

# List of Publications arising from the thesis

1. "Probing of Competitive Displacement Adsorption of Casein Molecules at Oil-in-Water Interface using Equilibrium Force Distance Measurements", **V. Mahendran**, J. Sangeetha and John Philip *J. Phys. Chem. B* **2015** *(In press).*
2. "Non-enzymatic glucose detection using magnetic nanoemulsions", **V. Mahendran** and John Philip, *Appl. Phys. Lett.*, **2014,**105, 12311.
3. "Influence of $Ag^+$ interaction on 1D droplet array spacing and the repulsive force between stimuli-responsive nanoemulsion droplets", **V. Mahendran** and John Philip *Langmuir,* **2014**, 30, 10213−10220.
4. "Magnetic nanofluid based approach for imaging defects" **V. Mahendran,** R. Ancy Beautlin and John Philip, *J. Nanofluids,* **2013**, *2*, 165-174.
5. "A Simple, In-Expensive and Ultrasensitive Magnetic Nanofluid Based Sensor for Detection of Cations, Ethanol and Ammonia", J. Philip, **V. Mahendran**, and Leona J. Felicia, *J. Nanofluids*, **2013**, *2*,112-119.
6. "A methanol sensor based on stimulus-responsive magnetic nanoemulsions", **V. Mahendran** and John Philip, *Sens. Actuators B Chem.*, **2013,** *185*, 488–495.
7. "Sensing of Biologically Important Cations like $Na^+$, $K^+$, $Ca^{2+}$, $Cu^{2+}$and $Fe^{3+}$ using Magnetic Nanoemulsions", **V. Mahendran** and John Philip, *Langmuir,* **2013,** *29*, 4252−4258.
8. "Spectral response of magnetic nanofluid to toxic cations", **V. Mahendran** and John Philip, *Appl. Phys. Lett.***, 2013***,102*,163109.
9. "Naked eye visualization of defects in ferromagnetic materials and components", **V. Mahendran** and John Philip, *NDT & E Int.* **2013**, *60***,**100 - 109.
10. "An optical technique for fast and ultrasensitive detection of ammonia using magnetic nanofluids", **V. Mahendran** and John Philip, *Appl. Phys. Lett***., 2013,***102*, 063107.
11. "Nanofluid based optical sensor for rapid visual inspection of defects in ferromagnetic materials", **V. Mahendran** and John Philip, *Appl. Phys. Lett***., 2012,** *100*, 073104.

**Communicated/ in preparation**

12. "Forces between Neutral Polymer Stabilized Emulsion Droplets in Aqueous Salt Solutions", **V. Mahendran** and John Philip (***under Preparation)***

13. “Stimuli responsive colloidal photonic crystals and their novel applications”, **V. Mahendran** and John Philip (***under Preparation)***

## Conferences

1. **V. Mahendran** and John Philip **“**Detection of Salinity of Water Using Magnetic Nanoemulsion” at the ***International symposium on Under Water Technology 2015(UT15)***, Organized by National Institute of Ocean Technology, Chennai, India, during 23-26 February, 2015. P-30.
2. **V. Mahendran** and John Philip “Detection of Cations Using Smart Magnetic Nanofluids” at the ***7th ISSS International Conference on Smart structures & Systems (ISSS-2014)*** Organized by Institute Science, Bangalore, India during 8-11 July, 2014. P-25.
3. **V. Mahendran** and John Philip “A new method for Detection of Methanol using Magnetic Nanoemulsions” at the ***International Conference on Nanoscience and Technology (ICONSAT)-2014*** Organized by Institute of Nano Science and Technology, Chandigarh, India during 3-5March, 2014.
4. **V. Mahendran** and John Philip “Probing of Intermolecular Forces at Interfaces in Presence of Triblock Polymers” at the ***13th International Conference on Magnetic Fluids- ICMF-13*** held at National Physical Laboratory, New Delhi, India during 7-11 January, 2013. P-365.
5. **V. Mahendran** and John Philip “Nanofluid based optical sensor for detection of defects” at ***International Conference on Material Science and Technology (ICMST) -2012***, Kottayam, Kerala, India, during 10-14 June 2012. P-175.

**Other publications (not included in thesis)**

1. “Temperature dependent light transmission in ferrofluids” Surajit Brojabasi, **V. Mahendran**, B.B. Lahiri, John Philip, *Optics Commun.* **2015,** *342*,224-229.
2. “Microwave Assisted Synthesis of Ferrite Nanoparticles and Nanofluids with Tunable Curie Temperature”, S.S. Pati, S. Kalyani, **V. Mahendran**, John Philip, *J. Nanofluids,* **2014,** *03*,210-216.
3. “Microwave Assisted Synthesis of Magnetite Nanoparticles”, S. S. Pati, S. Kalyani, **V. Mahendran**, John Philip, *J. Nanoscience Nanotechnol.* **2014,** *14*, 5790-5797.

4. "Near infrared light absorption in magnetic nanoemulsion under external magnetic field", Surajit Brojabasi, **V. Mahendran**, B.B. Lahiri, John Philip, *Optics Commun.* **2014,** *323*, 54-60.
5. "Infrared thermography based defect detection in ferromagnetic specimens using low frequency alternating magnetic field induced heating", B.B. Lahiri, S. Bagavathiappan, C. Soumya, **V. Mahendran**, V.P.M. Pillai, John Philip, T. Jayakumar, *Infrared Phys. Technol.*, **2014,** *64*:125-133.

## Awards and Recognition of Thesis Work

- "**ISSS award 2014**" for the **FIRST best PhD student** by Institute of Smart Structures and Systems (ISSS), Indian Institute of Science Bangalore, India. July, 2014.

- "Magnetic fluid sense blood glucose" Editors choice news story in the Technology Update section of **Nanotech Web, Institute of Physics, UK**, October 27, 2014 (Based on publication, ***Appl. Phys. Lett***., 105, 12311(2014)).

- **Nature India research highlights**, September 26, 2014 "Magnetic nanoemulsion sense glucose" (Based on publication, ***Appl. Phys. Lett***., 105, 12311(2014)).

- "Colour changing nanofluid senses Ammonia". Editors choice news story in the Technology Update section of **Nanotech Web, Institute of Physics, UK**, March 7, 2013, (Based on publication, ***Appl. Phys. Lett.*** 102, 063107(2013)).

- **Nature India Research highlights,** March 12, 2013 **"**Optical toxic-gas detector" (Based on publication, ***Appl. Phys. Lett.*** 102, 063107(2013)).

- **"Cheaper way to detect ammonia"** Sci. Tech. News story, **Hindu Daily**, March 21, 2013, (Based on publication, ***Appl. Phys. Lett.*** 102, 063107(2013)).

- **American Institute of Physics (AIP, USA) as top 50 breakthrough research**. "Nanofluid based optical sensor for rapid visual inspection of defects in ferromagnetic materials" ***Appl. Phys. Lett.*** 100, 073104, 2012.

- "Nanofluid sensor images defects", Editors choice news story in the Technology Update section of **Nanotech Web, Institute of Physics, UK**, 27 February, 2012, (Based on publication, ***Appl. Phys. Lett.*** 100, 073104, 2012).

- **Nature India Research highlights,** February 15, 2012, "Sensor detects cracks in magnetic matter" (Based on publication, ***Appl. Phys. Lett.*** 100, 073104, 2012).

- "IGCAR develops sensors to inspect defects in materials" Sci. Tech. News story, **Hindu Daily**, March 21, 2012. (Based on publication, ***Appl. Phys. Lett.*** 100, 073104, 2012).

**Kalpakkam** **(V. MAHENDRAN)**

**May, 2015**

# DEDICATIONS

To my parents,

L. Vellaichamy and V. Perumayee

# ACKNOWLEDGEMENTS

I thank Almighty for the bestowed blessings. A Doctor of Philosophy tenure is an enlightening experience. There are certain individuals to whom I am indebted for making this experience richer.

With great privilege I would like to thank former centre directors, **Dr. Baldev Raj** and **Shri. C. Chetal** and the present Director, **Dr. P. R. Vasudeva Rao** for allowing me carry out research work in Indira Gandhi Centre for Atomic Research.

With deepest sense of gratitude I thank my guide, **Dr. John Philip**, Head SMARTS & RTS, MMG for his guidance, love and motivation. I always admire his passion towards research and the way he approaches the research problems. His advice and suggestions have put me where I am now. I have been taking heed of his advice perpetually.

I am thankful to my doctoral committee chairman **Dr. T. Jayakumar** and members **Dr. B. V. R. Tata**, **Dr. T. R. Ravindran** and **Dr. V. P. Venugopalan** for their valuable comments and support.

I am grateful for the financial assistance from **DAE-BRNS** through a perspective research grant **(2009/38/01/BRNS)**. I am grateful to **Dr. Sai Baba** for the wonderful hospitality during my stay in the JRF enclave. I owe a big thanks to **SMARTS** and **RTS members** for the encouragements and for providing me a family ambience. I am thankful to **Ms. Sithara Vinod** and **Ms. M. Suganya** for proof reading. A special thanks to all **IGCAR research scholars** for making my daily routine more pleasant.

Finally but most importantly, I am indebted to my parents **Vellaichamy, Perumayee** and family members for their everlasting love and support. I am delightful to remember the contributions from **L. Saranya** and **Vishalini Sivarajan** in all my hard times.

# CONTENTS

**Page No.**

## Chapter I

## Introduction

# Chapter II

## Materials and Experimental Techniques

# Chapter III

## Interaction of mono, di and tri valent Cations with Surfactant and Polymer Stabilized Emulsions and its Influence on Interaction Forces

## Chapter IV

### Interaction of Alcohol with Surfactant Stabilized Emulsion and its Consequence on Interaction Forces

## Chapter V

### Interaction of Glucose with Electrostatically Stabilized Emulsions and a Novel Application of Magnetic Nanoemulsion

# Chapter VI

## Probing of Competitive Displacement Adsorption of Casein at Oil-Water Interface by using Equilibrium Force Distance Measurements

# Chapter VII

## Role of Ionic Structure on the Adsorbed Macromolecular Conformation at Oil-Water Interface

# Chapter VIII

## Conclusions and Recommendations for Future Work

# SYNOPSIS

Emulsions are a class of metastable colloidal dispersion of two immiscible liquids, where a surface active species is used to make them kinetically stable. Magnetic nanoemulsions are dispersions of ferrofluid oil in water, stabilized by a suitable surfactant, comes under the category of oil-in water emulsion. Magnetic nanoemulsions form different structures under the influence of an applied magnetic field due to the dipolar interactions within the particles. When the dipolar interactions are sufficiently strong, the colloidal droplets can undergo a phase transition from a liquid to a columnar chain like structures. The phase behavior of magnetic fluids is of considerable research interest from fundamental understanding and application point of view. Besides, magnetic colloidal dispersions are wonderful model systems to probe fundamental issues in condensed matter physics.

Understanding of forces between emulsion droplets is essential, in industrial process, materials engineering and biology, to extend the shelf life of formulations. Among various available direct force measurement tools, magnetic chaining technique (MCT) is a unique in-situ force measurement approach that allows measurement of force between magnetic colloidal particles in liquids. The important feature of the MCT is that, it can measure very weak forces as a function of distance with a force resolution of $10^{-13}$ N. This technique has been successfully used to study the intermolecular interactions such as, electrostatic, steric, electro-steric, depletion, irreversible polymer bridging, and bio-molecule growth kinetics. The prime objective of this thesis is to get better insights into the effect of cations of various valencies, biomolecules and alcohol molecules on electrostatic and steric forces and the stability of emulsions, such an understanding can aid in the development of ionic and molecular recognition sensors for practical applications. Another objective of this work was to probe the competitive displacement adsorption of protein at emulsion stabilized with di-block copolymer by using equilibrium force-distance measurements, light scattering and zeta potential measurements. Final goal is to explore the sensing abilities of magnetic nanoemulsion for cations, organic molecules and magnetic flux leakage (defects).

Thesis contains eight chapters, which are organized as follows: Chapter 1 gives a brief introduction on soft materials and magnetic colloidal dispersions. Chapter 2 describes the materials preparation and the working principles of different characterization techniques used. Chapter 3 concerns the study of the interaction of cations with anionic surfactant and di-block copolymer stabilized emulsions. Chapter 4 deals with interaction of alcohols with anionic surfactant stabilized emulsion. Chapter 5 concerns the interaction of glucose at surfactant stabilized emulsion interface. An interesting application of magnetic nanoemulsion for magnetic flux leakage (MFL) detection is also discussed. Chapter 6 describes the competitive adsorption and replacement of polymer by casein. Chapter 7 concerns the role of cation hydration on colloidal forces. Chapter 8 presents the conclusion and future perspective. The key findings of this thesis are: cation interactions on O/W emulsions lead to a large blue shift in the diffracted wavelength, due to changes in the interdroplet spacing and the electrical double layer around them. The order of increasing of Bragg peak shift for different cations followed a sequence $Pb^{2+} < Ni^{2+} < K^{+} < Cu^{2+} < Mn^{2+} < Na^{+} < Cd^{2+} < Ca^{2+} < Ag^{+}$. In the presence of interfering cations, excellent selectivity is observed for $Ag^{+}$ due to strong interaction of hydrated $Ag^{+}$ with surfactant/polymer, which offers a possibility of selective detection of $Ag^{+}$ using magnetic nanoemulsions. It is observed that a very small concentration of alcohol in nanoemulsion alters the inter-droplet spacing of droplet significantly. The measurement of intermolecular forces in the presence of alcohol molecules shows that the diffusion of organic molecules into the electric double layer reduces the dielectric constant, resulting in an extended electric double layer and a red shift in the diffracted Bragg peak. The Bragg reflected light intensity from the emulsions shows that the equilibrium interdroplet distance between the emulsion droplets is increased by several nanometers in the presence of glucose because of the intermolecular hydrogen bonding of glucose molecules with SDS molecules, giving rise to a stretched lamellae like structure that increases the onset of repulsion and the decay length**.** The large red shift in the diffracted Bragg peak for glucose concentration range of 0-30 mM and the fast response of nanoemulsions offer possibilities of detection of glucose by looking at the color change in the emulsion. Using the interesting response stimulus properties of nanoemulsion, a new methodology to detect MFL signals to image morphologies of defects buried inside ferromagnetic components is developed. Studies on forces between polymer covered emulsion in the presence of casein shows that extended polymer coils are replaced by smaller size casein molecules. The hydrodynamic size and zeta potential results corroborate the casein mediated polymer displacement and adsorption of casein at oil-water interface. It appears that the greater adsorption energy of protein molecules than the PVA-Vac adsorption energy favors the competitive displacement adsorption of casein. On increasing cation concentrations, the adsorbed polymer chains undergo a collapsed conformation. The order of collapse of polymers follows as $Fe^{3+} > Ca^{2+} > Na^{+}$ for both *EPVA40* and *EPV155* emulsions. The results suggest that the hydrated cations and their interaction with polymer can greatly alter the polymer conformation at oil-water interfaces.

# LIST OF FIGURES

## LIST OF TABLES

## LIST OF ABBREVIATIONS

| | |
|---|---|
| CMC | Critical micellar concentration |
| SDS | Sodium Dodecyl Sulfate |
| SFA | Surface force apparatus |
| AFM | Atom Force Microscope |
| TIRM | Total internal reflection microscopy |
| MCT | Magnetic chaining technique |

| | |
|---|---|
| PVA-Vac | Poly(vinyl alcohol-Vinyl acetate) |
| TGA | Thermo gravimetric analysis |
| FTIR | Fourier transformed infrared spectroscopy |
| VSM | Vibrating sample magnetometer |
| PCS | Photo correlation spectroscopy |
| DLS | Dynamic Light Scattering |
| TCF | Time auto correlation function |
| NIBS | Non-invasive back scattering |
| PALS | Phase analysis light scattering |
| TEM | Transmission Electron Microscope |
| XRD | X-ray diffraction |
| JCPDS | Joint committee on powder diffraction standards |
| MFL | Magnetic flux leakage |
| SQUID | Superconducting quantum interference device |
| GMR | Giant magneto resistance |
| GMI | Giant magneto impedance |
| AMR | Anisotropic magneto resistance |

## LIST OF SYMBOLS

| | |
|---|---|
| $U_d$ | Contact potential |
| $\phi_m$ | Micelle volume fraction |
| $a_m$ | Micelle radius |
| $d_{hkl}$ | Crystal lattice spacing |
| $F_{rep}$ | Repulsive force between droplets |
| $F_{chain}$ | Magnetic force acting between droplets |
| $F_{VdW}$ | Vann der Waals force |
| $H_I$ | Induced dipole field on droplets |
| $H_a$ | Applied magnetic field |

|  |  |
|---|---|
| $A$ | Hamaker constant |
| $\nu_e$ | plasma frequency of electron gas |
| $\varepsilon_p$ | Dielectric constant of particle/ droplet |
| $\varepsilon_w$ | Dielectric constant of water/base fluid |
| $n_p$ | Refractive index of particle/droplet |
| $n_w$ | Refractive index of water/ Base fluid |
| $g^{(2)}(t)$ | Normalized intensity correlation function |
| $g^{(1)}(t)$ | Normalized electric filed correlation |
| $\tau$ | Relaxation time |
| $\Gamma$ | Relaxation rate |
| $D_t$ | Translational diffusion coefficient |
| $q$ | Wave vector |
| $H_d$ | Hydrodynamic diameter |
| $U_E$ | Electrophoretic mobility |
| $\zeta$ | Zeta potential |
| $f(ka)$ | Hendry function |
| $d, 2a$ | Emulsion droplet diameter |
| $a$ | Emulsion droplet radius |
| $\eta$ | Viscosity of the medium |
| $r$ | Distance between droplets |
| $F_{chain}$ | Magnetic force acting between droplets |
| $t_c$ | Time required to form a 1D droplet arrays |
| $\Lambda$ | Coupling constant |
| $H_a$ | Applied external field |
| $k_B T$ | Thermal energy |
| $\chi$ | Magnetic susceptibility |
| $m$ | Induced magnetic moment |

| | |
|---|---|
| $\mu_0$ | Magnetic permeability |
| $H_T$ | Total magnetic field acting on each droplet |
| $\zeta$ | Riemann  function |
| $n$ | Refractive index of suspending medium |
| $\lambda_{peak}$ | Wavelength of Bragg diffracted light/ Diffraction peak wavelength |
| $h$ | Interfacial separation / Interdroplet spacing |
| $F_r(r)$ | Electrostatic repulsive force |
| $\psi_0$ | Electrical surface potential |
| $\kappa$ | Inverse Debye length |
| $\varepsilon$ | Dielectric permittivity |
| $C_s$ | Salt concentration |
| $L_B$ | Bjerrum length |
| C* | Overlap concentration |
| $\lambda$ | Adsorbed layer thickness |
| $\lambda_d$ | Decay length |
| $z^*$ | Adsorption strength |
| $b$ | Macroscopic length |
| $R_g$ | Radius of gyration of free polymer |
| $\phi_0$ | bulk polymer volume fraction |
| $\nu$ | Flory excluded volume parameter |
| $\varepsilon_b$ | Effective binding energy per monomer |
| $\xi$ | Bulk correlation length |
| $K$ | Force magnitude / preexponential factor |
| $2L_0$ | First interaction length / Onset repulsion distance |
| $\lambda_d$ | Decay length |
| $\Delta S_{hydr}$ | Hydration entropy |
| $\Delta H_{hydr}$ | Hydration enthalpy |

|  |  |
|---|---|
| $\Delta G_{hydr}$ | Hydration free energy |
| $N$ | Number of monomer units |
| $N_A$ | Avogadro’s number |
| $z$ | Ion valency |
| $e$ | Electron charge |
| $r_{ion}$ | Radius of the central ion plus the diameter of the water molecule |
| $\Delta\chi^{do}$ | Combined solvency parameter |
| $\phi_{cr}$ | Critical displacer concentration |
| $\Delta\chi^{pd}$ | Displacer adsorption energy |
| $\chi^{po}$ | Contact free energies between polymer and solvent |
| $\chi^{do}$ | Contact free energies between displacer and solvent |
| $\chi^{pd}$ | Contact free energies between polymer and displacer |
| $H_x$ | Tangential component of leakage filed |
| $H_Y$ | Normal component of leakage filed |
| $H_g$ | Filed inside defect |
| $H_a$ | Applied magnetic field |
| $x, y$ | Tangential and Normal Positions |
| $l_g$ | Defect width |
| $Y_0$ | Defect depth |
| $l_g$ | Gap between the adjacent defects |

# Chapter- I

## Introduction

# 1 Introduction

## 1.1 Soft Condensed Matter

Soft matter has very rich and complicated morphology, and its components can be arranged in complex ways involving features at length scales intermediate between the atomic and the macroscopic. Soft matter lacks long range three dimensional ordering but, possesses local ordering due to intermolecular forces. The molecular kinetic energy of soft matter is close to $k_B T$, whereas it is much less than $k_B T$ for hard materials. Therefore soft materials such as colloids, surfactants, liquid crystals, certain biomaterials and polymer in melt or in the solution can flow under certain conditions.

### Colloidal Dispersions

In a normal solution, solute is dispersed uniformly in solvent as the solute and solvent molecule sizes are akin. Colloidal dispersion is a class of soft matter, in which kinetic units are distributed uniformly in another medium, the former is called as the dispersed phase and the latter is called dispersion medium.[1] Both these phases can be solid or liquid or gas. **Table 1.1** lists the different classes of colloidal dispersions with examples. The dispersed phase size ranges from 1 nm to several microns. Colloidal dispersions could be classified into two categories called lyophilic or solvent loving and lyophobic or solvent hating.

| Dispersed phase | Dispersion medium | Terminology | Examples |
|---|---|---|---|
| Gas | Liquid | Foam | Fire-Extinguisher Foam |
| Liquid | Liquid | Emulsion | Milk, Butter |
| Solid | Liquid | Sol, Suspension | Paint, Blood, Syrup |

| | | | |
|---|---|---|---|
| Gas | Solid | Rigid Foams | Insulating Foam |
| Liquid | Solid | Solid Emulsion | Ice Cream |
| Solid | Solid | Rigid Sols | Doped Crystals |
| Liquid | Gas | Aerosols | Hairspray, Mist, Fog |
| Solid | Gas | Aerosols | Smoke |

**Table 1.1** Classifications of colloidal dispersions and their examples.[1]

## 1.2 Emulsions

Emulsions are metastable colloids[2] of liquid- liquid dispersion of two immiscible liquids. In general, emulsions are metastable and they require specific entities at the interface to remain stable. Emulsions are formed by shearing of two immiscible liquids, one dispersed phase and the other the dispersion phase or continuous phase. Surface active species such as surfactants, polymers, nanoparticles etc., are used to stabilize freshly formed fragments as they provide sufficient colloidal repulsive force between fragments.

Emulsion exhibits colloidal behaviors such as, Brownian motion, reversible and irreversible phase transitions and behaves as a viscous Newtonian fluid at low concentrations. Concentrated emulsion dynamics is restricted and it behaves like a viscoelastic fluid. Direct emulsions are those composed of oil droplets dispersed in water and the inverse emulsions are composed of water droplets dispersed in oil. Emulsion may also contain smaller droplets of the continuous phase within each dispersed phase and is called double emulsion or multiple emulsion. Irrespective of the classification by the dispersion or dispersive phase, each of the aforementioned emulsions is classified further based on their droplet size as macro emulsion, where the droplet size is > 400 nm, miniemulsion or nanoemulsion whose size ranges from 100-400 nm and microemulsion whose size is less than 100 nm. Emulsions are used in wide range of applications such as, paint, paper coating, road surfacing, lubrication, food, cosmetics and pesticide products etc., owing to its ability to transport or solubilize hydrophobic substances in a continuous phase.

### 1.2.1 Emulsion Preparation

Emulsification process involves dispersing one fluid into another immiscible fluid. High pressure homogenization, membrane, microchannel, spontaneous emulsification and application of controlled shear are some of the emulsion preparation techniques.[2] Several parameters such as temperature, composition, droplet size distribution etc., affects the final properties of emulsion.

***High Pressure Homogenization:*** High pressure homogenization or microfluidization is a two step technique widely used for producing dairy and food emulsions[3] where the first step involves preparation of coarse premix of two fluids and the second step involves forcing it to a flow through an inlet valve and a mixing chamber under very high pressure. The fluids undergoing a combination of elongation and shear flows, produces cavitations.[4] This technique is quite reproducible and ideal to produce droplet size ranging from 50 nm to 5 μm. The concentration of stabilizing agents, applied pressure and number of cycles determine the final emulsion size and stability.[5-6] In high-pressure homogenization, with the surfactant concentration < CMC/10 (critical micellar concentration), the average droplet size is weakly dependent on the applied pressure.[7] In the surfactant concentration range > 10 CMC, the average droplet size ranges from 50-350 nm and is almost independent of surfactant concentration.[8] The size of the emulsion droplets (d) scales with the applied pressures $P_h$ as,

$$d \propto P_h^{-\alpha} \tag{1.1}$$

where the power $\alpha$ typically varies from 0.6 to 0.9.[9-10] The dispersed phase volume fraction and number of passes are the two other parameters that determine the droplet size distribution.

***Membrane Emulsification :*** In membrane emulsification process, the dispersed phase is forced to permeate into continuous phase through a membrane with a uniform pore size distribution.[11] The dispersed phase is pressed perpendicular to the membrane while the continuous phase flows tangentially. Monodisperse emulsion can be produced by using a membrane with a narrow pore size distribution.[12]

***Microchannel Emulsification:*** Microchannel emulsification can produce monodisperse emulsions with an average droplet diameter ranging from 10 to100 μm.[13] The principle is similar to membrane emulsification, where the dispersed phase is forced into the continuous phase through microchannels.[14] The phase to be dispersed is pushed through a hole in the center of a plate in such a way that it passes through the microchannels and inflates on the terrace in a disk like shape. When it reaches the end of the terrace, the drop detaches. The spontaneous detachment and relaxation into a spherical drop are driven by interfacial tension. This emulsification process is more suitable for polymeric microsphere synthesis, microencapsulation, sol-gel chemistry and electro-optical materials.[15] Direct, inverse and multiple emulsions can be prepared by this method.

***Spontaneous Emulsification:*** Spontaneous emulsification is a process that occurs without external energy supply when two immiscible fluids with very low interfacial tension are brought in contact.[16] Different mechanisms proposed for such spontaneous emulsifications are interfacial turbulence,[17] negative interfacial tension and diffusion stranding.[18]

***Phase Inversion:*** Emulsification through phase inversion requires low energy input and hence called spontaneous emulsification process. Its advantage resides in the possibility of producing concentrated emulsions and is widely used in cosmetics industry. Phase inversion occur when the structure of the emulsion inverts (when the continuous phase becomes the dispersed phase and vice versa). The variables such as temperature, pressure, salinity, co-surfactant content or the proportion of oil and water affects phase inversion. Due to the low energy input requirement, the emulsion obtained is usually fine and monodisperse. The mechanism behind this interesting phenomenon is still not understood.

***Emulsification by Application of Controlled Shear:*** In this process, emulsions are obtained by exerting crude stirring by a combination of extensional and shearing flows in a mixture of two immiscible liquids in the presence of surfactants. Shearing leads to elongation and rupturing of the liquid droplets into smaller ones. The controlled high shear applied to crude polydisperse emulsions can lead to monodisperse systems.[19] The initial crude viscoelastic emulsion is subjected to a controlled transverse shear over a thin gap of height around 200 μm. To prepare an emulsion, the layering of the two liquid phases should be minimized by applying external energy to the system. The mechanical device which is used to break the layers into droplets by applying constant shear is called as homogenizer. Two steps are involved in the homogenization process. In the first step, oil and water are converted to a coarse emulsion of larger size droplets and in the second step, the coarse emulsion droplet size is reduced by further shearing. The emulsifiers reduce the interfacial tension by adsorbing at the interface and form a protective layer at the interface to prevent aggregation of droplets. The schematic of various emulsion preparation techniques are shown in **Fig. 1.1**.

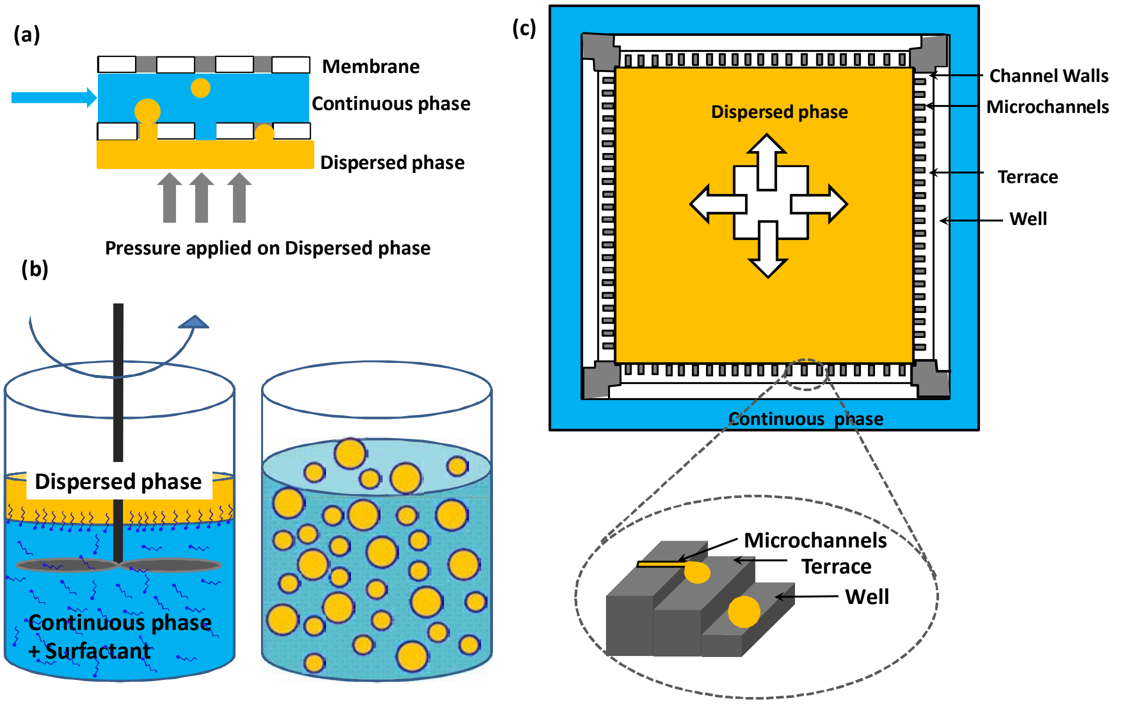

**Figure 1.1** Schematic of various emulsion preparation techniques (a) membrane emulsification (b) emulsification by constant applied shear and (c) microchannel emulsification (top view and enlarged side view).$^{2}$

### 1.3 Emulsion Stability

Stability is one of the key parameters important for practical applications. The change in the emulsion properties affects its stability. Therefore it is important to understand the causes of instabilities in the emulsions in order to prepare stable emulsions.

#### 1.3.1 Factors Affecting Emulsion Stability

Emulsions are thermodynamically unstable but can be made kinetically stable by using suitable surfactants. During the emulsification, if the overall free energy is positive, then the emulsion formation is thermodynamically unfavorable. In general, the thermodynamic instability takes over only after a long period of time. **Fig. 1.2** schematically shows different factors affecting stability of emulsions.

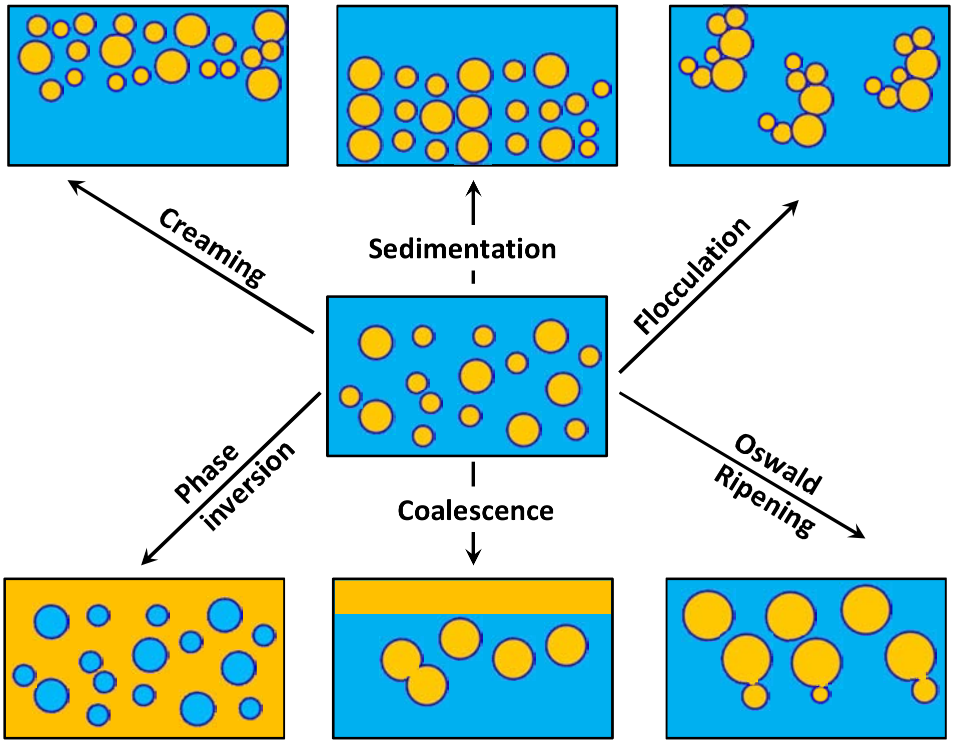

**Figure 1.2** Schematic representation of various mechanisms affecting the stability of emulsion.[20]

**Phase Separation:** The density mismatch between dispersed phase and the dispersion phase results in an upward or downward movement of droplets in a dispersion. The formation of dispersed phase at the top is called as creaming and, the formation of dispersed phase layer at the bottom is called sedimentation. In general, oil in water emulsions tend to cream and water in oil emulsions tend to sediment, owing to the higher density of water than that of oil. Sedimentation can be overcome by minimizing the density gradient or by reducing the droplet size or by increasing the viscosity of the dispersion phase.

**Droplet Aggregation:** Droplets under random Brownian motion due to thermal agitation or by mechanical agitation can collide with each other and stick together to form aggregates. Aggregation of droplets while keeping their physical properties intact is called as flocculation. If the droplets aggregate or fuse together to form bigger droplets, then it is called as coalescence. Coalescence is an irreversible phenomenon while flocculation can either be reversible or irreversible.

**Ostwald Ripening:** Ostwald ripening is another instability that results from the finite solubility of the liquid phases. The gradual growth of the larger droplets at the expense of smaller droplets due to transport of soluble dispersed phase through the continuous phase is called as Ostwald ripening. After the formation of emulsion drops, the smaller droplets will have a greater solubility when compared to larger droplets due to curvature effects. With time, the smaller droplets disappear and their molecules diffuse into the bulk and deposit on the larger droplets.

## 1.4 Magnetic Nanoemulsion

Magnetic nanoemulsions are dispersions of ferrofluid oil in water, stabilized by suitable surfactants.[21-22] Ferrofluid oil contains ferrimagnetic nanoparticles ($Fe_3O_4$ or $\gamma$-$Fe_2O_4$) of typical size ~10 nm coated with a layer of surfactant. A concentrated magnetic nanoemulsion is produced by vigorously mixing ferrofluid oil and water in the presence of surfactant. At this stage the emulsion is highly polydisperse with droplet size ranging from 0.01 to a few μm. Highly monodisperse emulsions with narrow size distribution can be obtained from the concentrated coarse emulsion by fractionation crystallization technique.[23]

## 1.5 Applications

### Emulsions

One of the reasons for the tremendous interest on emulsions is because of its wide range of industrial applications in food, cosmetics, pharmaceutical and paint products. **Table 1.2** gives some applications of emulsions in different fields.

| Field | Applications |
|---|---|
| Environment and meteorology | Water/sewage treatment emulsions, oil spill mousse emulsions |
| Foods | Milk, butter, creams, mayonnaise, cheese, sauce, cream liqueurs |
| Geology, agriculture and soil science | Insecticides and herbicides, sulfidic melt in magma |
| Manufacturing and materials science | Polishes, asphalt(paving) emulsion, latex paint |
| Biology and medicine | Soluble vitamin and hormone products, biological cells, blood, vesicles |
| Petroleum production and mineral processing | Emulsion drilling and stimulation fluids, in situ reservoir emulsions, transportation emulsions |
| Home and personal care products | Hair and skin creams and lotions, Dry cleaning formulations. |

**Table 1.2** Applications of emulsions in different fields.[24]

### Magnetic Nanoemulsion

In the absence of an external magnetic field, the magnetic nanoemulsion behaves as a nonmagnetic colloid, where droplets are in Brownian motion. Magnetic nanoemulsion forms different structures under the influence of an applied magnetic field. When an external magnetic field is applied to an emulsion comprised of particles with permeability different from that of the dispersion medium, dipolar interactions are induced within the particles. When the dipolar interactions are sufficiently strong, the colloidal particles can undergo a phase transition from liquid to solid by forming columnar structures.[25] The nature of this phase transition is of considerable research interest from fundamental and applications point of view. This field induced self assembly of nanoemulsions dramatically modify their physical properties leading to many applications such as, developing tunable photonic structures,[26] optical limiters,[27-28] optical filter,[29] artificial swimmers,[30] colloidal gels[31], biomolecular recognization probe,[32-33] defect sensor,[34-35] cation sensors[36-38] etc. In addition, they have also been used as model systems to study the microstructural transition,[39-41] polymer bridging,[42] adhesion between surfaces,[43-44] gelation kinetics,[45-46] growth kinetics of biomolecules,[47] probing the intermolecular interaction,[48-49] rupturing of droplets under external fields[50-51] etc.

## 1.6 Colloidal Interactions

### 1.6.1 Van der Waals Forces

The simplest force operating at very short distances between colloids and microbodies is the Van der Waals attraction, which can be described by two ways: (i) microscopic and (ii) macroscopic approach. The former [52] is based on the assumption that interactions between a pair of molecules can be added together to obtain the total interaction, i.e., the interaction between a molecule in one colloidal particle and a molecule in another particle is unaffected by the presence of all the other molecules.[1] Dispersion or London-Van der Waals forces act between all atoms and molecules and the intermolecular attractive forces arise from cooperative oscillations of electron clouds when molecules are at the close range. When the colloidal particles in a background medium are in close proximity, the interaction between all atoms contribute to an effective colloidal attraction, which is sum of all atomic Van der Waals interactions, where the dielectric property of background medium determines the strength of interactions. For two spheres with radius R, the Van der Waals attraction is given by,[53]

$$W_{VdW}(h) = -\frac{A}{6} f\left(\frac{h}{R}\right), \qquad (1.2)$$

where,

$$f\left(\frac{h}{R}\right) = \frac{2R^2}{h^2 + 4Rh} + \frac{2R^2}{h^2 + 4Rh + R^2} + \ln\left(\frac{h^2 + 4Rh}{h^2 + 4Rh + R^2}\right) \qquad (1.3)$$

Here '*A*' is the Hamaker constant and 'h' is the closest distance between the surfaces of two spheres.

The Hamaker constant for the interaction between two colloidal particles without the intervening medium is given by,

$$A = C\pi^2 n^2 \qquad (1.4)$$

where, 'C' is the coefficient of dispersion interaction between the atoms of the colloidal particles, n is the number density of atoms which scales as $n \approx 1/\sigma_a^3$, where $\sigma_a$ is the diameter of the charged spherical cloud surrounding a point nucleus. According to London theory,[52] for the dispersion interaction, the coefficient 'C' can, to a good degree of approximation, be written as,

$$C = \frac{3}{4}\bar{E}\left(\frac{\alpha_p}{4\pi\varepsilon_0}\right)^2 \qquad (1.5)$$

Here, $\overline{E}$ is the average electronic excitation energy, $\alpha_p$ is the static polarizability, and $\varepsilon_0$ is the vacuum permittivity. In the presence of external electric field the nucleus will be shifted while the electron cloud (*-e* charge with diameter $\sigma_a$) moves in the opposite direction.[54] By assuming that the electron cloud retains its spherical shape, this leads to a dipole moment $\overline{\mu} = ed_n = \frac{\pi\varepsilon_0\sigma_a^3}{2}E_e$, where '$d_n$' is the displacement of the nucleus from the center of negative charge and it is determined by the balance forces acting on the nucleus due to the external field '$E_e$' and the internal field '$E_i$' caused by displacement of the nucleus.

The static polarizability,

$$\alpha_p = 4\pi\varepsilon_0\frac{\sigma_a^3}{8}, \tag{1.6}$$

By incorporating **Eqn. 1.5** and **1.6**, in **Eqn. 1.4** we get,

$$A = \frac{3\pi^2}{256}\overline{E} \tag{1.7}$$

The typical value of Hamaker constant at room temperature is of the order of $10^{-20}$ J. Van der Waals attraction is very strong at short interparticle separations, where, $W_{VdW} \approx -{}^{AR}\!/_{h}$, due to the 1/h dependence. In order to stabilize a colloidal dispersion against Van der Waals attractions, a significant repulsion is needed to prevent the particles from getting too close and flocculating irreversibly.

### 1.6.2 Double Layer Interaction

Double layer forces can be described by the Poisson-Boltzmann (PB) theory, or by its linearized version, the Debye-Huckel (DH) theory.[55] A charged colloid is surrounded by the solution having an inhomogeneous distribution of ions, where the co-ions with the same charge as the colloidal particles are depleted from the surface while counter ions with opposite charge adsorb at the surface. Far from the colloidal surface, the concentrations of the co- and counter ions attain a constant averaged value, and this inhomogeneous layer is termed as a double layer and its spatial extension depends on the ion concentration in the bulk solution. When two double layers of charged colloids overlap, a repulsive pair potential develops which leads to a repulsive pressure due to screened –coulomb or double layer repulsion.

**Charge Regulations or Charging Mechanisms**

The charging of the surface of particles or a liquid interface can be done by the ionization or dissociation of surface groups. For e. g., the dissociation of $Na^+$ from SDS, which leaves behind ($RSO_4^-$) a negatively charged surface, or by the adsorption or binding of ions from solution onto a previously uncharged surface. For e.g., the adsorption of $OH^-$ groups to the water-air or water-hydrocarbon interfaces that charge them negatively, or by the adsorption of ions from solution onto oppositely charged surface sites and such surfaces are called as ion exchangeable surfaces.

Charge exchange occurs between two dissimilar surfaces which are very close together because protons or electrons hop across from one dissimilar surface to the other, which gives rise to an electrostatic attraction between the oppositely charged surfaces (acid-base type interaction).

Whatever be the charging mechanism, the final surface charge of co-ions is balanced by counterions. Some of the counter ions are bound transiently to the surface and the layer thus formed is called the Stern layer or Helmholtz layer. Other counter ions form an atmosphere of ions, which are in rapid thermal motion, close to the surface, known as diffuse electric double layer.

Taking into account the counterion distribution and the force between two similarly charged planar surfaces in pure water (without added electrolytes), the Poisson- Boltzmann theory gives the chemical potential of any ion as,

$$\mu = ze\psi + kT\log\rho, \tag{1.8}$$

where, $\psi$ is the electrostatic potential and $\rho$ is the number density of ions of valency z at any point x between the two surfaces and is given by the Nernst equation,[56]

$$\rho = \rho_0 e^{-ze\psi/kT} \tag{1.9}$$

The net excess charge density at '*x*' is given by the Poisson equation,

$$ze\rho = -\varepsilon_0\varepsilon\left(\frac{d^2\psi}{dx^2}\right) \tag{1.10}$$

By incorporating **Eqn. 1.9** into **Eqn. 1.10**, we get,

$$\left(\frac{d^2\psi}{dx^2}\right) = -(ze\rho_0 / \varepsilon_0\varepsilon)e^{-ze\psi/kT} \tag{1.11}$$

This equation is known as Poisson-Boltzmann (PB) equation. By solving PB equation, the surface potential, $\psi$, electric field, $E = -\partial\psi/\partial x$ and the counterion density, $\rho$ at any point x in the gap between the two surfaces can be obtained. These quantities are often called as contact values. Since PB equation is a nonlinear second-order differential equation, to solve for $\psi$ two boundary conditions are needed. The first one is that the field at the midplane must be zero, i.e., $E_0$=0 and the second condition is that the total charge of the counter ion in the gap must be equal (and opposite) to the charges on the surface to meet electroneutrality condition. If $\sigma$ is the surface charge density on each surface and *D* is the distance between the surfaces then,

$$\sigma = -\int_0^{D/2} ze\rho \mathrm{dx} = \varepsilon\varepsilon_0 \int_0^{D/2} \left[ {d^2\psi}/{dx^2} \right] dx = -\varepsilon\varepsilon_0 \left( {d^2\psi}/{dx^2} \right)_{D/2} = -\varepsilon\varepsilon_0 E_S \tag{1.12}$$

The general relationship between the concentration of counterions at the surface and at the midplane is obtained by differentiating **Eqn. 1.9**,

$$\frac{d\rho}{dx} = -\frac{ze\rho_0}{kT} e^{-ze\psi/kT} \left( \frac{d\psi}{dx} \right) = \frac{\varepsilon\varepsilon_0}{2kT} \frac{d}{dx} \left( \frac{d\psi}{dx} \right)^2 \tag{1.13}$$

$$\rho_x - \rho_0 = \int_0^x d\rho = \frac{\varepsilon\varepsilon_0}{2kT} \frac{d}{dx} \left( \frac{d\psi}{dx} \right)_x^2, \ \rho_x = \rho_0 + \frac{\varepsilon\varepsilon_0}{2kT} \frac{d}{dx} \left( \frac{d\psi}{dx} \right)_x^2 \tag{1.14}$$

This gives $\rho$ at any point x in terms of $\rho_0$ at the midplane and $\left( \frac{d\psi}{dx} \right)^2$ at *x*. At the surface x=D/2, the contact value of $\rho$ is, $\rho_s = \rho_0 + {\sigma^2}/{2\varepsilon\varepsilon_0 kT}$. Therefore, the concentration of counterions at the surface depends only on the surface charge density, $\sigma$ and the counter ion concentration at the midplane, $\rho_0$.

The repulsive pressure '*P*' of the counterions at any position x from the center is given by,

$$(\partial P / \partial x')_{x,T} = \rho(\partial\mu / \partial x')_{x,T} \tag{1.15}$$

The change in the pressure at x on bringing two plates together from infinity to a finite separation at a constant temperature is,

$$\begin{aligned} P_x(D) - P_x(\infty) = P_x(D) &= -\int_{x'=D}^{x'=\infty} [ze\rho(d\psi/dx')_x dx' + kTd\rho_x] \\ &= \left[ -\frac{1}{2}\varepsilon\varepsilon_0 \left( \frac{d\psi}{dx} \right)_{x(D)}^2 + kT\rho_{x(D)} \right] - \left[ -\frac{1}{2}\varepsilon\varepsilon_0 \left( \frac{d\psi}{dx} \right)_{x(\infty)}^2 + kT\rho_{x(\infty)} \right] \end{aligned} \tag{1.16}$$

The first term is always negative and the force is attractive except at the midplane, x=0, where it is zero and it is of electrostatic origin. The second term is positive and hence repulsive and has an entropic (osmotic) origin.

The interaction between two solid surfaces immersed in an aqueous electrolyte solution can also be explained by PB equations. The non linear PB equation for the electrostatic potential at a distance '*x*' between two infinite plates is,

$$\varepsilon\varepsilon_0 \frac{d^2\psi}{dx^2} = -e\sum_i Z_i n_{i,\infty} \exp(-Z_i \beta e \psi), \tag{1.17}$$

where, $Z_i$ is the valency of the $i^{th}$ electrolyte, $n_{i,\infty}$ is the bulk concentration of the $i^{th}$ electrolyte and $\beta = (k_B T)^{-1}$. For 1:1 electrolytes PB equation assumes,

$$\frac{d^2\psi}{dx^2} = \frac{\kappa^2}{\beta e}\sinh(\beta e \psi) \tag{1.18}$$

and for 2:1 electrolytes PB equation is given by

$$\frac{d^2\psi}{dx^2} = \frac{\kappa^2}{3\beta e}\left[\exp(\beta e \psi) - \exp(-2\beta e \psi)\right] \tag{1.19}$$

where, $\kappa$ is the inverse Debye length, which denotes the spatial extension of electric double layer and is defined as,

$$\kappa^2 = \frac{(2N_A \beta e^2 I)}{(\varepsilon_0 \varepsilon)} \tag{1.20}$$

here, '$N_A$' is the Avogadro number and the ionic strength, 'I' is given by $I = \frac{1}{2}\sum_{i=1}^{n} c_i Z_i^2$ .

The magnitude of Debye length solely depends on the properties of the solution and not on any property of the surface such as surface charge or surface potential. For monovalent (1:1) electrolytes at 298 K, the Debye length of aqueous solution is,[24, 56]

$$\kappa^{-1} = \frac{0.304 \times 10^{-9}}{\sqrt{M}} \mathrm{m}, \tag{1.21}$$

For 2:1 and 1:2 electrolytes [24, 56]

$$\kappa^{-1} = \frac{0.178 \times 10^{-9}}{\sqrt{M}} \mathrm{m} \tag{1.22}$$

For 2:2, 3:1 and 1:3 electrolytes[25]

$$\kappa^{-1} = \frac{0.152 \times 10^{-9}}{\sqrt{M}} \mathrm{m} \tag{1.23}$$

For 2:3 and 3:2 electrolytes[25]

$$\kappa^{-1} = \frac{0.136 \times 10^{-9}}{\sqrt{M}} \mathrm{m} \tag{1.24}$$

where, 'M' is the electrolyte concentration in the bulk solution (in mole). PB equations are solved as a function of '$x$' for different distances '$D$' between the surfaces either by using constant potential (CP) or a constant charge (CC) at the two surfaces as a boundary condition. In CP the surface potential is kept constant, i.e., $\psi(0) = \psi(D) = \psi_0$ and in the case of CC the surface charge density is fixed, i.e., $\sigma(0) = \sigma(D) = \sigma_0$. The relationship between the surface potential and the surface charge for large distances can be calculated by the Grahame equations as follows.[57]

For 1:1 electrolytes, $\sigma_0^2 = \frac{4\varepsilon\varepsilon_0 n_\infty^+}{\beta}[\cosh(\beta e \psi_0) - 1]$ (1.25)

For 2:1 electrolytes, $\sigma_0^2 = \frac{2\varepsilon\varepsilon_0 n_\infty^+}{\beta}[\exp(-2\beta e \psi_0) + 2\exp(\beta e \psi_0) - 3]$ (1.26)

Here the number concentration $n_\infty^+$ corresponds to the bulk concentration of positively charged ions. The pressure between the gap is calculated as shown below,[57] For 1:1 electrolytes, $P(D) = \frac{2n_\infty^+}{\beta}[\cosh(\beta e\psi_0) - 1] - \frac{\varepsilon\varepsilon_0}{2}\left(\frac{d\psi}{dx}\right)^2$ (1.27)

For 2:1 electrolytes,

$$P(D) = \frac{2n_\infty^+}{\beta}[\exp(-2\beta e\psi_0) + 2\exp(\beta e\psi_0) - 3] - \frac{\varepsilon\varepsilon_0}{2}\left(\frac{d\psi}{dx}\right)^2 \quad (1.28)$$

The interaction force between two spherical particles of radius '*a*' separated by a distance '*r*' with small charge densities (extended electric double layer, $\kappa a < 5$) is given by,[58]

$$F_r(r) = 4\pi\varepsilon\psi_0^2 a^2\left[\frac{\kappa}{r} + \frac{1}{r^2}\right]\exp[-\kappa(r-2a)] \quad (1.29)$$

For a spherical particle with high charge density (a thin electric double layer, $\kappa a > 5$) the alternative Derjaguin approximation[59] provides the appropriate interaction force with the assumption that the surface potential ($\psi_0$) remains constant and independent of *r-2a.* It is represented by,

$$F_r(r) = 2\pi\varepsilon\psi_0^2 a\kappa\frac{\exp[-\kappa(r-2a)]}{1+\exp[-\kappa(r-2a)]} \quad (1.30)$$

### 1.6.3 DLVO Interactions

Derjaguin, Landau, Verwey and Overbeek (DLVO)[58-60] pointed out that in a dispersion of charged colloids in an electrolyte solution, the Van der Waals attraction between two colloidal particles is opposed by the repulsive force originating from the electrical double layers. This concept is used to explain stability of colloids and is known as DLVO theory. By assuming additivity of the interactions, the total DLVO potential is given by,

$W_{DLVO} = W_{VdW} + W_{DR}$, which is schematically shown in **Fig. 1.3**.

Polymers either adsorbed or anchored to the colloidal surface or depleted from surface or polymer – charged surfactant complex (electrosteric) can also strongly influence colloidal interactions and these are known as non-DLVO interactions.[54] Colloidal stability is governed by the balance of various interactions such as Van der Waals attraction, double layer repulsion, steric and depletion forces.[61]

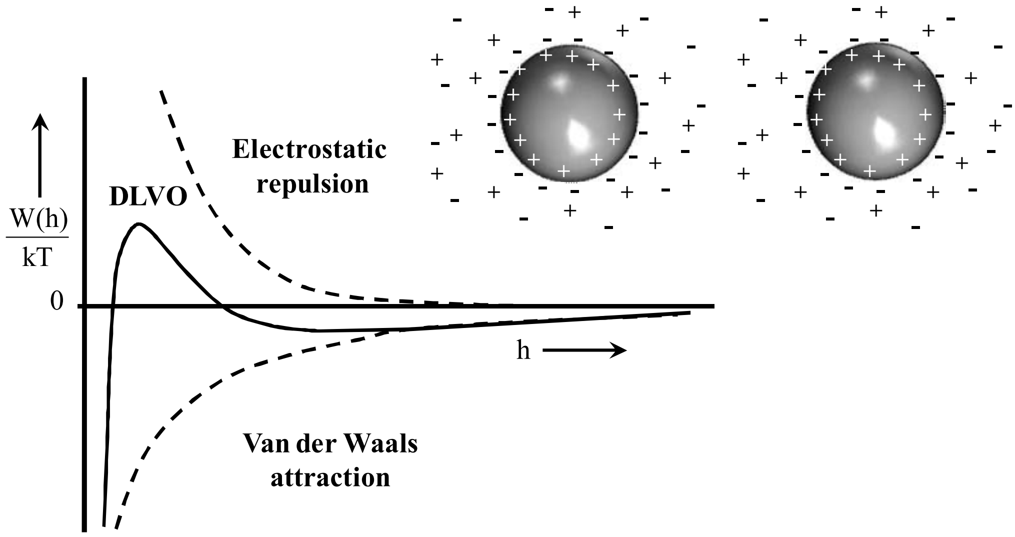

**Figure 1.3** Schematic plot of typical double layer repulsion between charged colloidal spheres (top dotted line), the Van der Waals attraction (bottom dotted line) and the net DLVO interaction potential (solid line).[54] Charged colloidal spheres with counter and co-ions are also shown in the figure.

### 1.6.4 Non-DLVO Interactions in Colloidal Systems

When two surfaces or particles approach closer than few nanometers, continuum theories of both Van der Waals and double layer forces fail to describe the interactions. Additional non-DLVO interaction mechanisms that are responsible for colloidal forces are ion-ion correlation forces,[55, 62] specific interactions induced by polymers[63] and polyelectrolytes.[64] The special interactions of water at the surface or interface contribute to the intermolecular forces in the form of hydrophilic and the hydrophobic interactions.[65-66]

### Polymeric or Steric Stabilization

The spatial extensions of polymer molecules of even modest molecular weights are usually comparable to or greater than the range of London attraction between the colloidal particles. When long chain molecules such as polymers are attached to a surface at some point, they protrude into the solution where they are thermally mobile. When two such surfaces approach each other, there is a reduction in the entropy which results in a repulsive entropic force called steric repulsion. Schematic plot of interaction potential between two colloidal spheres covered with polymer in a good solvent with Van der Waals attraction is shown in **Fig. 1.4**.

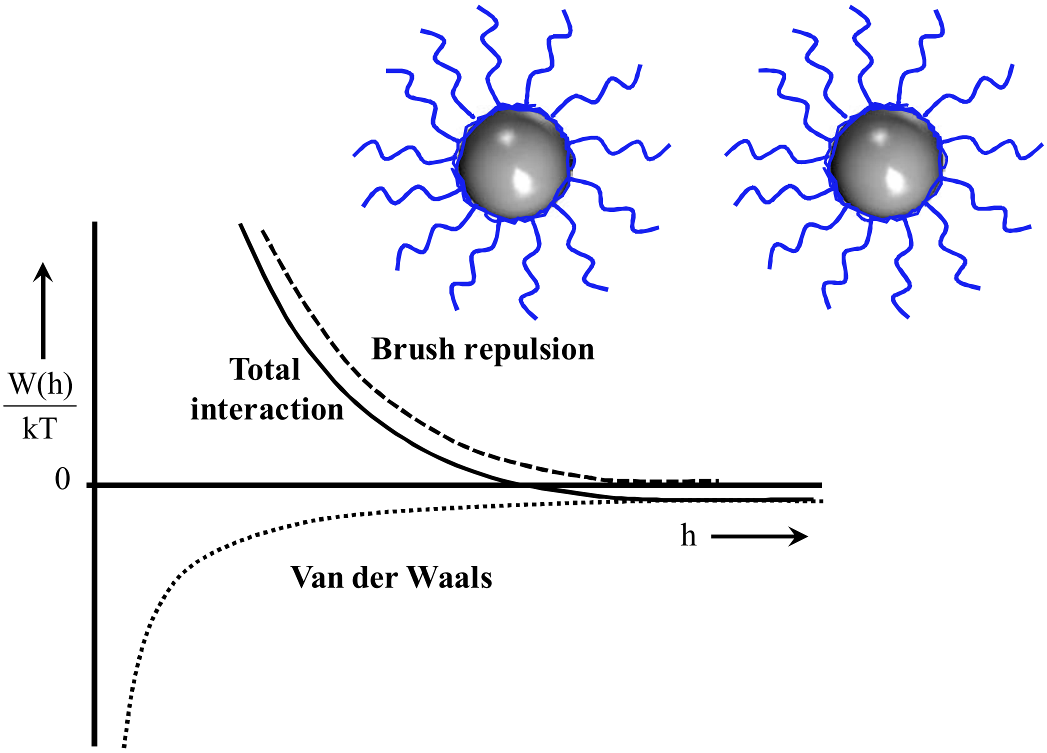

**Figure 1.4** Schematic plot of interaction potential between two colloidal spheres covered with polymer in a good solvent with Van der Waals attraction.[54]

A polymer in good solvent condition that is not perturbed by any segment-segment interactions undergoes random coil conformations and the typical length scale of the coil radius is given by the radius of gyration $R_g$. In contrast, in a poor solvent or bad solvent the polymer segments attract each other and the coil shrinks due to intra ionic, Van der Waal, hydrophobic or hydrogen bond interactions and collapse into a compact structure.[54]

The interactions between colloidal particles can be strongly modified by addition of linear polymers to the solution. The polymer mediated interaction between colloidal particles strongly depends on the solvent quality for the polymer, the reversibility of adsorption and the amount adsorbed on colloidal particles. When the polymer is adsorbing from a good solvent onto colloidal particles, the force between the particles is repulsive if the particles are saturated with polymer due to the excluded volume interaction between adsorbed layers. If surface is not saturated, the bridging of the polymer chains between different particles results in an attractive force.

A colloidal suspension may be stabilized by the adsorption of polymer molecules onto the particles in the suspensions. When two such particles approach each other, the reduction in the number of available configurations of the polymer chains gives rise to ‘entropic’ repulsive force.[67] The polymer molecules may be adsorbed at many points along the chain or adsorption may be selective. For example, the molecules may be adsorbed by one or both ends solely due to the presence of a different functional group. Hence steric stabilization of colloidal particles is brought about by macromolecules that are attached by grafting or by physical adsorption onto the surface of particles.

From the theoretical point of view, the interaction between colloidal particles mediated by a polymer solution results from a balance between osmotic pressure, excluded volume fraction and the entropy of the chain conformations. Meanfield theory with ground state dominance approximation accounts for the interaction between two polymers on adsorbed surfaces.[68-70] According to the general rules of statistical physics, the force ($F_s$) between the polymer adsorbed plates is obtained by taking the derivative of the thermodynamic potential (Ω) with respect to the distance between the plates,

$$F_s = -\frac{\partial \Omega}{\partial h} \tag{1.31}$$

The equilibrium value of the grand canonical potential $\Omega = \Omega\ (\mu_0,\ h)$ results from the minimization of the functional Ω [ψ, η] for a given distance 'h'. If there is a slight increase in the distance from h to h + δh, a convenient way to change the order parameter is to keep these functions identical in the region $0 < z \leq h$ and to define them as constant in the region $h \leq z < h + \delta h$. Then the force related to the monomer concentration, $\phi$ and the end-concentration, $\rho_c$ at the midplane between the plates[71] is,

$$F_s = -\frac{v}{2}[\phi(h) - \phi_0]^2 + \rho_c(h) - \varepsilon_b \phi(h) - N\psi_0^2(h) - \frac{\phi_0}{N} \tag{1.32}$$

This force also includes the osmotic pressure acting on the plates from the bulk solution. The term $-N\psi_0^2(h)$ is not important in the regime of strong adsorption ($\varepsilon_b N \rangle\rangle 1$).

### Interaction between two Plates in Equilibrium with a Bulk Solution Containing Polymers

The adsorption of polymer chains at an interface and the determination of the concentration profiles over the whole range of bulk concentration were studied using two order parameter mean-field theories.[71] In addition to the extrapolation length, '*b*' which measures the strength of the adsorption, two more characteristic length scales of the bulk solution such as, the

Gaussian coil size $R = N^{1/2}$ and bulk correlation length $\xi = 1/(2\mathrm{v}\phi_0)^{1/2}$ were included in the calculations. The other two length scales which were found to play an important role are the crossover length $Z^*$ between the inner region, where the concentration is dominated by monomers belonging to loops, and the outer region, where the concentration is dominated by monomers belonging to tails,[71]

$$Z^* = \begin{cases} \left[Nb\ln\dfrac{N}{b^2}\right]^{1/3}, & 0 < \phi_0 < \phi_1 = \dfrac{1}{\mathrm{v}(bN)^{2/3}} \\ Nb\mathrm{v}\phi_0, & 0 < \phi_0 < \phi_2 = \dfrac{1}{\mathrm{v}bN^{1/2}} \\ R, & \phi_0 > \phi_2 \end{cases} \tag{1.33}$$

where, $\mathrm{v}$ is the monomer excluded volume, $N$ is the number of monomers, $\phi_0$ is bulk solution polymer concentration, and the size of the adsorbed layer or cut-off length, $\lambda = 1/\varepsilon_b^{1/2}$, where the effective binding energy per monomer is, $\varepsilon_b = \phi_0\mathrm{v} - E_0$ and it is determined by total absorbance,

$$\Gamma = \phi_0 K_0^2 e^{\varepsilon_b N} \tag{1.34}$$

where, $E_0$ is the eigen value of the partition function for a single polymer chain.

For $\phi_0 > \phi_2$, the cut off length has only formal meaning and for the other cases,

$$\lambda = \begin{cases} \dfrac{R}{\left(\ln\dfrac{1}{\phi_0 \mathrm{v}b^2}\right)^{1/2}}, & 0 < \phi_0 < \phi_1 \\ \dfrac{R}{\left(4\ln\dfrac{\phi_2}{\phi_1}\right)^{1/2}}, & 0 < \phi_0 < \phi_2 \\ \mathrm{v}b\phi_0 N/4, & \phi_2 < \phi_0 < \dfrac{1}{\mathrm{v}b^2} \end{cases} \tag{1.35}$$

The force as a function of the distance between the adsorbing surfaces at different ‘h’ is given by,

$$f = \begin{cases} -\dfrac{1}{2vb^2h^2}, & h << b \\ -\dfrac{5.9}{vh^4}, & b << h << z^* \\ \dfrac{420}{vh^4}, & z^* << h << \lambda \\ \dfrac{const}{v}\dfrac{1}{\lambda^4}\dfrac{h}{\lambda}e^{-2h/\lambda} - \dfrac{\phi_0}{N'}, & \lambda << h << R \end{cases} \tag{1.36}$$

If the distance between the two surfaces is smaller than $\lambda$, then the polymer mediated interaction decays as a power law of $h^{-4}$. The sign of the force depends on the reversibility of adsorption and the force is repulsive at short distances only if the adsorption is irreversible. At distances larger than $\lambda$, the interaction is dominated by the tails and the force is always repulsive and decays exponentially with distance. Matching this exponential decay to the power law decay at smaller distances and using Derjaguin approximation, the force between the spherical droplets of radius $a$, is obtained from the scaling theory, which is more appropriate to describe polymers in good solvents, [72]

$$F(h) = \left(\frac{k_B T \pi a}{\lambda^2}\right)\exp(-h/\lambda) \tag{1.37}$$

where, $k_B$ is the Boltzmann constant and ‘$T$’ is the temperature. This expression is valid for a polymer adsorbed in amounts close to the saturation value. For smaller adsorbed amounts, the force may become attractive even in the case of irreversible adsorption.

### 1.6.5 Other Special Interactions

It is possible to have combinations of electrostatic and steric stabilization which has been termed electrosteric stabilization. The electrostatic component may originate from a net charge on the particles surface and charges associated with polymers attached to the surface, e.g., attached polyelectrolyte. Electrosteric stabilization is common in biological systems.[56] The overlap interaction between two polyelectrolyte layers is repulsive due to both steric and double-layer repulsions between the loops and tails.

Two types of special interactions particularly relevant to the interactions of water are the hydrogen bond and the hydrophobic effect.[56] Hydrogen bonds can occur intermolecularly as well as intramolecularly and can exist in a nonpolar environment, and play a key role in macromolecular and biological assemblies. The immiscibility of inert substances and the entropic nature of this incompatibility are known as the hydrophobic effect and such substances are known as hydrophobic substances. The interaction between a hydrocarbon molecule and water is attractive due to the dispersion force.

For small or multivalent ions in highly polar solvents like water, the strong orientation dependence of their ion-dipole interaction will tend to orient the solvent molecules around them.[56] These bound water molecules are not completely immobilized and they do move and exchange with bulk water, albeit more slowly. The first shell of water molecules around a strongly solvated ion is called as the primary hydration shell, where the water molecules are structured most but the effect propagates beyond the first hydration shell, but much weakly. The water molecules in the first hydration shell interacts directly with the charged ion, while the second hydration shell and the subsequent shells interact with other water molecules and the ion indirectly.

## 1.7 Direct Measurements of Interaction Forces

There are many techniques for measuring the interaction forces. Among them, the most widely used techniques (**Fig. 1.5**) are Surface force apparatus (SFA), Atomic force microscopy (AFM), total internal reflection microscopy (TIRM), optical tweezers, and Magnetic chaining technique (MCT). SFA measures the force between two atomically smoothed mica surfaces, which is well known for its distance resolution which is ~ 0.1nm. However, the mica surfaces limit its broad applicability.[73] AFM measures the force between the sharp tip and the surface. Colloidal force probe technique replaces the sharp cantilever tip with the so called colloidal-probe which consists of μm sized colloidal particle that attach to a tipless AFM cantilever.[74] TIRM is an alternative technique for force measurements between the particle and planar substrates.[75] Optical tweezers measure the forces between pairs of micron sized particles in aqueous solutions.[76] MCT is used to measure interparticle forces in magnetic colloids.[48] It allows the measurement of very small interaction energies per unit area and interparticle forces as small as $10^{-13}$ N. Moreover, in contrast with other force measurement techniques, the forces measured by MCT are based on averaging over an extremely large number of particles.[77] A schematic of various force measurement techniques are shown in **Fig. 1.5**.

### Magnetic Chaining Technique (MCT)

MCT, developed in 1994, is used to probe short range interactions such as screened electrostatic interactions,[48] steric forces,[63, 72, 78-79] electrosteric force under polymer surfactant interactions[49, 80-82] and polyelectrolyte interaction.[64] It has also been applied for the characterization of small biomolecules such as DNA,[32, 83-85] proteins,[47, 86] and to probe elastic parameters such as, magnetoelastic number of flexible magnetic filaments, swing speed of micro swimmers and persistence length of DNA.[30, 32, 87] MCT can also measure attractive forces such as depletion forces[88] or the spring constant extended of DNA.[32]

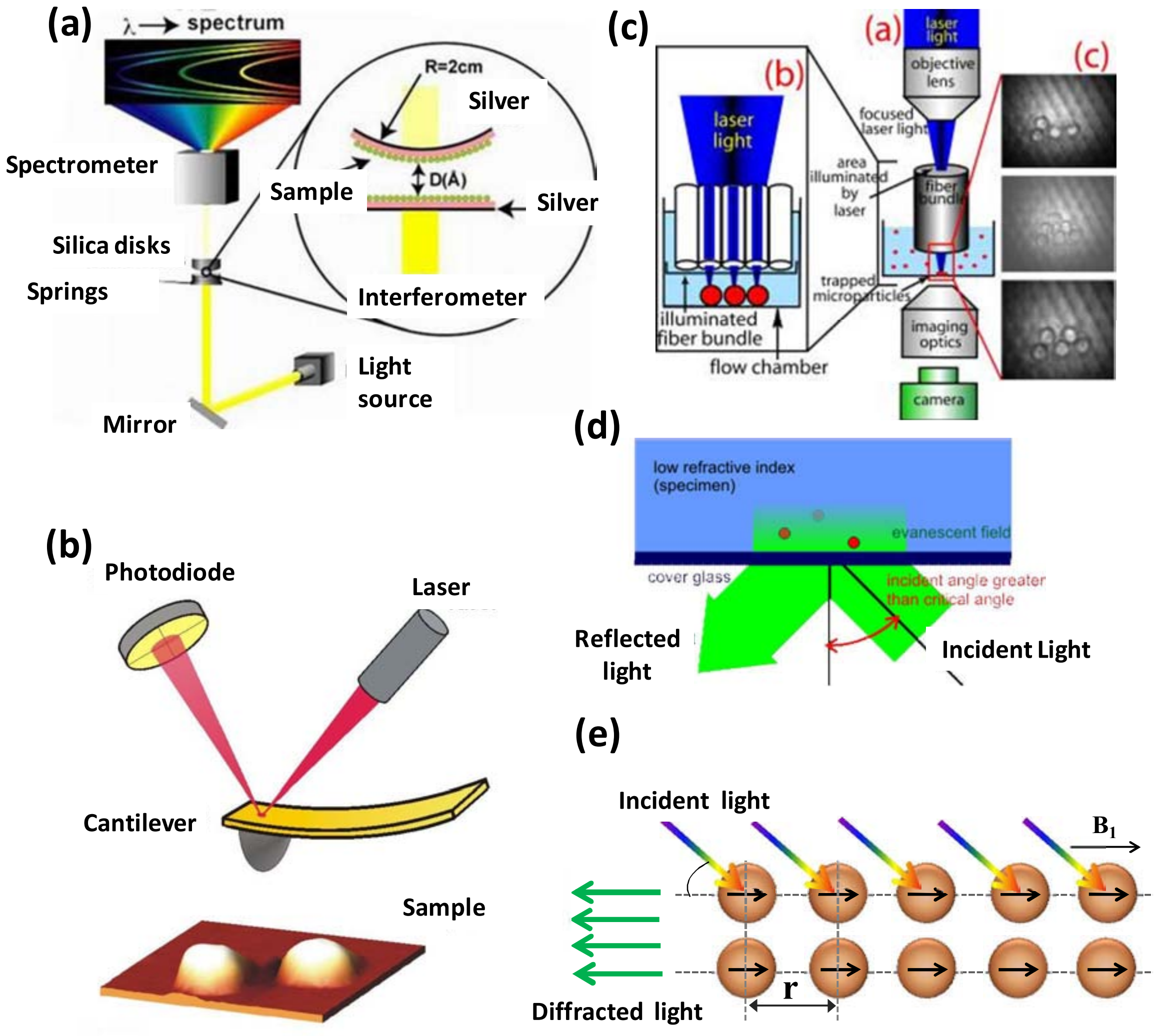

**Figure 1.5** Schematic representations of different force measurement techniques. (a) Surface force apparatus (b) AFM (c) Optical tweezers (d) Total internal reflection microscopy and (e) Magnetic chaining technique.

## 1.8 Motivations

Interaction of natural or synthetic polymers and surfactants in aqueous solutions are intensely studied because of their widespread applications and also for understanding their complex interactions. Although the behavior of ionic surfactants and polymers at emulsion interfaces and their role on stability of emulsions are well studied and extensive literature is available on the subject, the effects of interaction of cations, alcohols, glucose and casein on the intermolecular forces between the emulsion droplets are not attempted.[86, 89] The interactions between protein covered colloids are of particular importance as they are employed as emulsifiers in nutrition and cosmetic products.[90-92] In casein based food and cosmetic products, surfactants are often added to attain better performance and stability.[91] The interactions between proteins and surfactants have attracted much interest because of their widespread applications and their relatively complex behaviors. The modification in the physico-chemical properties of proteins upon the addition of surfactant often enhances the overall capabilities and applications. It is therefore important to understand the interaction between proteins and surfactants at the molecular level.[92] However, the interaction between protein and surfactant are different in bulk and at interfaces.[93] The interfacial properties of such mixed layers strongly influence the formation and stabilization of respective foams and emulsions. The properties of water-air or oil-water interface also strongly influence the adsorption behavior of protein molecules due to their different degrees of polarity and hydrophobicity. Therefore, studies concerning protein adsorption at the oil-water interface in the presence of surface active molecules, that are able to modify its interfacial structure, are very important.[94]

## 1.9 Objectives

- ➢ To study the effect of cation on 1D droplet spacing and the intermolecular forces between electrostatically and sterically stabilized emulsions.
- ➢ To study the effect of alcohol on the interaction forces between the electrostatically stabilized emulsions.

- Probe the role of glucose molecules on 1D droplet array spacing and the electrostatic interaction between anionic surfactant stabilized emulsions.
- To probe the competitive displacement adsorption of casein at diblock copolymer stabilized emulsion interface by intermolecular force measurements.
- Probing the role of cations on the polymer conformation by intermolecular force measurements.
- To explore novel optical sensing methods for analytes detection using magnetic nanoemulsions.

### 1.10 Thesis Overview

Thesis consists of eight chapters. **Chapter 1** is an introduction to soft matter and the different interactions involved. **Chapter 2** describes the preparation of materials and the working principles of different characterization techniques used. Preparation of ferrofluid and ferrofluid emulsion and its characterization are discussed. Details of the intermolecular force-distance and diffraction peak measurement techniques are also discussed. **Chapter 3** concerns the study of the interaction of cations with anionic surfactant and di-block copolymer stabilized emulsions. The effect of interaction of cations on 1D droplet array spacing and the repulsive forces between stimuli-responsive nanoemulsion droplets are discussed. The force-distance results are compared with the predictions of electrical double-layer and repulsive steric forces. The dramatic decrease in the 1D array spacing in the presence of cations is employed for cation detection with ultrahigh sensitivity. **Chapter 4** deals with interaction of alcohols with anionic surfactant stabilized emulsions. The effect of interaction of alcohol on 1D droplet array spacing and the repulsive forces between nanoemulsion droplets, stabilized with an anionic surfactant (sodium dodecyl sulphate), is studied. The shift in the Bragg peak wavelength in the presence of methanol is employed for the sensitive detection of methanol in aqueous solution. **Chapter 5** concerns the interaction of glucose at surfactant stabilized emulsion interface. The optical properties and intermolecular interactions in nanoemulsions in the presence of D-glucose are studied. The equilibrium interdroplet distance between the emulsion droplets in a 1-dimensional array is increased by several nanometers in the presence of glucose because of intermolecular hydrogen bonding of glucose with sodium dodecyl sulphate molecules at the oil-water interface which gives rise to a stretched lamellae-like structure. The observed large red shift in the diffracted Bragg peak and the linear response in the glucose concentration range of 0.25-25 mM offer a simple, fast and cost effective non-enzymatic approach for glucose detection. An interesting application of magnetic nanoemulsion for magnetic flux leakage (MFL) detection is also discussed. Here, the response of the nanoemulsions to the leaked magnetic flux from the defective region is exploited to locate the defect region. **Chapter 6** describes the competitive adsorption and replacement of polymer by casein. The nature of forces involved in the surfactant-casein and polymer-casein interactions is probed by equilibrium force distance measurement, dynamic light scattering and zeta potential measurements. The competitive displacement adsorption of casein at oil-water (O/W) emulsion interface that was initially adsorbed with either di-block polymers of different molecular weight or an anionic surfactant are also probed. A significant change in the force distance profiles was observed under the competitive displacement adsorption of casein, which is further confirmed from the hydrodynamic size and zeta potential measurements. **Chapter 7** concerns the role of cation hydration on colloidal forces. Forces between neutral diblock copolymer stabilized magnetic nanoemulsion in aqueous solution at varying concentration of monovalent, divalent and trivalent cations are studied by equilibrium force measurements. The change in the onset repulsion is in good agreement with the hydration parameters. The possible mechanisms of interaction of cations with polymer at the emulsion interface are also discussed. **Chapter 8** presents the conclusions and recommendations for future work.

# Chapter- II

## Materials and Experimental Techniques

# 2 Materials and Experimental Techniques

## 2.1 Materials

***Salts***

Ferric chloride ($FeCl_3.6H_2O$), ferrous sulphate ($FeSO_4.7H_2O$), potassium chloride (KCl), sodium chloride (NaCl), cadmium chloride ($CdCl_2$), nickel chloride ($NiCl_2$), manganese chloride ($MnCl_2$), lead nitrate ($Pb(NO_3)_2$), silver nitrate ($AgNO_3$) and copper sulphate ($CuSO_4$). All the salts used in our experiments were GR grade with 99 % purity and were used without any further purification.

***Surfactants***

Oleic Acid, 30 % $NH_4OH$ used in our experiments were GR grade with 99 % purity and were used without any further purification. The anionic surfactant used in our experiments is sodium dodecyl sulphate ($C_{12}H_{25}$-$SO_4$ Na), hereafter referred as SDS. The purity of SDS was 99.9 % and was obtained from Sigma.

***Polymers***

The polymer used in the experiments was statistical copolymer of vinyl alcohol-vinyl acetate ($CH_2CHOH$ [88 %] - $CH_2CH$ ($OCOCH_3$) [12 %]), with an average molecular weight of 40000,115000 and 155000 (referred as PVA-Vac 40K, PVA-Vac 115K and PVA-Vac 155K, respectively) purchased from Aldrich, USA and used as received. PVA-Vac is a water soluble polymer at room temperature and its theta temperature in water is around 97 ˚C.

***Alcohol***

Methanol G.R grade with 99.9 % purity was purchased from E-Merck and used as received.

***Glucose***

D-Glucose anhydrous, G.R. grade with 99.9 % purity was purchased from E-Merck and used as received. Ultrapure MilliQ water with a resistivity value of 18 MΩ cm was used in the preparation of emulsions and polymeric solutions.

### 2.2 Ferrofluid Preparation

Ferrimagnetic $Fe_3O_4$ nanoparticles were synthesized by co-precipitation method.[95-96] The synthesis of magnetite nanoparticles is carried out by precipitating iron salts in alkaline medium. The iron salts used were freshly prepared 0.2 M $FeSO_4.7H_2O$ and 0.4 M $FeCl_3.6H_2O$. The salt solutions are prepared in acidic medium in order to avoid formation of iron hydroxides before initiation of the reaction. The above solutions with 1:1 ratio are mixed with constant stirring. This mixture is heated in a water bath until the required temperature of 60 ˚C is reached. On vigorous stirring, the above solution pH is increased rapidly to ~ 10 by adding 25 % aqueous ammonia. The solution turned to black at this stage indicating the formation of $Fe_3O_4$ nanoparticles. The rapid addition of ammonia allows the formation of excess number of nuclei and vigorous stirring prevents the coagulation of particles.

The precipitated particles are left for finite digestion time until the nucleated particles attain a thermodynamic equilibrium state. The overall chemical reaction can be written as,

$$2Fe^{3+} + Fe^{2+} + 8OH^- \rightarrow Fe_3O_4 + 4H_2O \tag{2.1}$$

After the preparation of magnetite nanoparticles, the solution is digested for 30 minutes and 20 ml of oleic acid is added to the dispersion. Then, the dispersion pH is adjusted to 9.5 with dilute hydrochloric acid and the temperature is increased to 70 ˚C. At the same pH, temperature and stirring speed, the solution is kept for 30 minutes to finish the coating process. An alkaline medium and higher temperature favor the oleic acid adsorption on magnetite. In the presence of ammonia, oleic acid forms water soluble ammonium oleate salt. The higher temperature helps to increase the solubility and decreases the viscosity of the surfactant. In alkaline medium, the surface of nanoparticles will have surface bound $OH^-$ ions and hence they are charge stabilized. At this stage, ionized ammonium oleate surfactant forms ammonium cation and oleate anion. The oleate anions replace the magnetite surface bound $OH^-$ ions by ion-exchange adsorption phenomena. After ammonium oleate adsorption, particles become hydrophilic in nature and cannot be dispersed in non-polar solvents. The neutralization of dispersion has been achieved by eliminating excess ammonia by heating. After this step, the temperature is increased to 80 ˚C in order to eliminate the excess ammonia and the protonation of adsorbed and un-adsorbed ammonium oleate. After ammonia is excluded, particles are separated from the dispersion. The top water layer with excess salts was discarded. The surfactant coated particles have been washed with water at 60 ˚C, until the pH became 7 to remove the ionic impurities trapped or adhered to the coagulum. Later, the water washed particles are dispersed in hexane. The hexane dispersion is treated with acetone to induce aggregation of particles. The aggregated particles are then separated from dispersion by centrifugation at 2500 rpm for 30 minutes. The hexane-acetone mixture washing procedure was repeated to remove excess surfactant in the dispersion. Schematic representation of oleic acid coated $Fe_3O_4$ nanoparticles is shown in **Fig. 2.1**. The surfactant coated magnetite nanoparticles were dried at room temperature in an inert atmosphere. The prepared nanoparticles were characterized by X-ray diffraction (XRD), Vibrating sample magnetometer (VSM), Thermo gravimetric analysis (TGA) and Fourier transformed infrared spectroscopy (FTIR) for crystal structures, magnetic properties, magnetic phase stability and coating thickness, nature of oleic acid binding to the nanoparticle surface respectively.

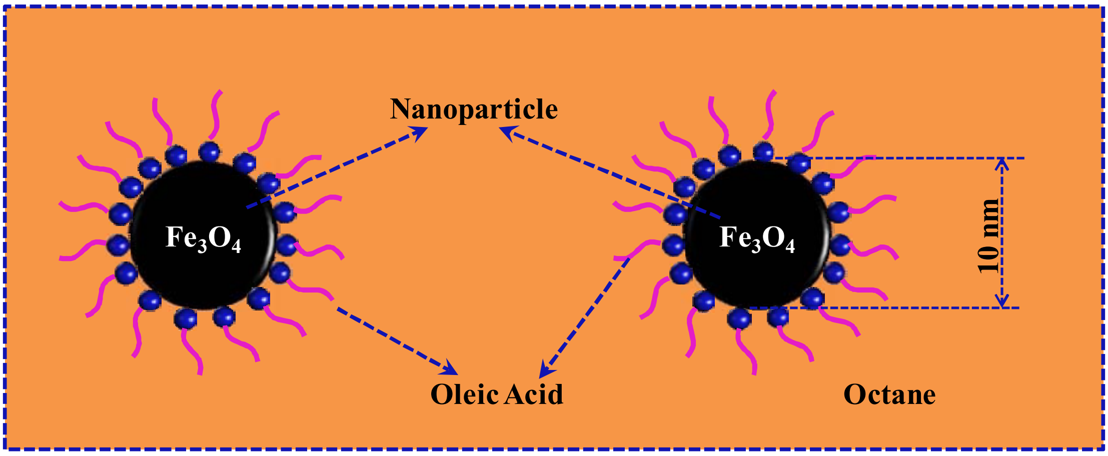

**Figure 2.1** Schematic representation of oleic acid coated $Fe_3O_4$ nanoparticles in octane.

### 2.3 Ferrofluid Emulsion Preparation

The ferrofluid nanoemulsion was prepared by shearing ferrofluid oil, water and surfactant in the ratio of 5 : 10 : 5, respectively using a homogenizer (IKA werke, T25 Germany).[64] Monodispersed emulsion from coarse emulsion with wider size distribution is achieved by fractionation technique,[23] where excess surfactant solution is added into the continuous medium to induce an attractive interaction between droplets and to phase separate between a dilute phase with smaller droplets and a dense phase with larger droplet size. The dilute phase is removed and the dense phase is diluted with surfactant solution further. By repeating this process, a highly monodisperse ferrofluid emulsion was obtained. The interaction generated by the excess surfactant leads to depletion of micelles from the interdroplet spacing when the distances between the droplets is less than the surfactant micelle diameter.

The depleted micelles exert a non-compensated osmotic pressure on the droplets which results in the attraction as shown in the **Fig. 2.2**.

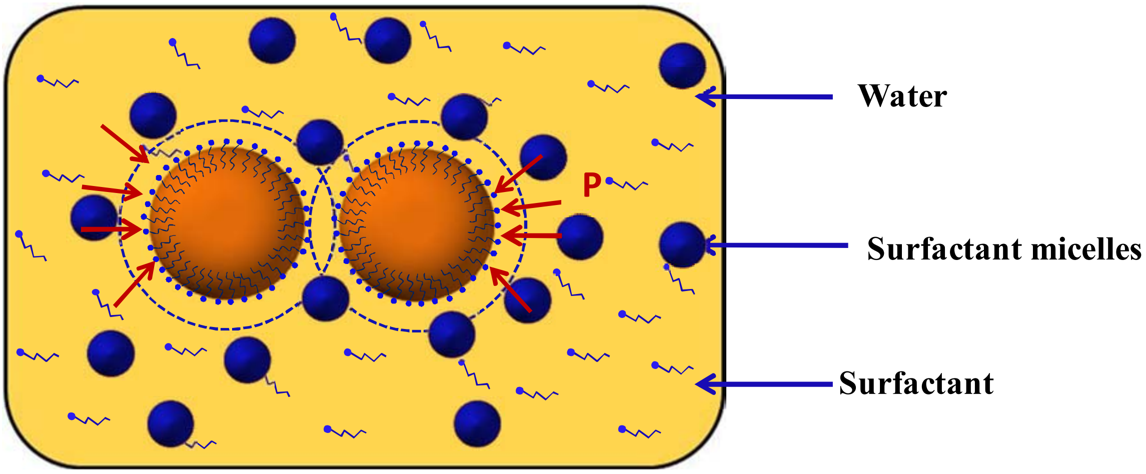

**Figure 2.2** Schematic of two emulsion droplets in the presence of surfactant micelles as depletants. The surfactant micelles impose an unbalanced pressure ‘P’ between the emulsion droplets resulting in an attractive force between them.

The contact potential between droplets is well described by,

$$U_d = \frac{3}{2} kT\phi_m \frac{2a}{2a_m} \tag{2.2}$$

where, $\phi_m$ is the micelle volume fraction, $2a$, $2a_m$ is the diameter of the emulsion droplet and micelle, respectively, and $k_B T$ is the thermal energy. The prepared emulsions were characterized with, dynamic light scattering, electrophoretic mobility measurements and phase contrast optical microscopy. A schematic of ferrofluid emulsion is shown in **Fig. 2.3**.

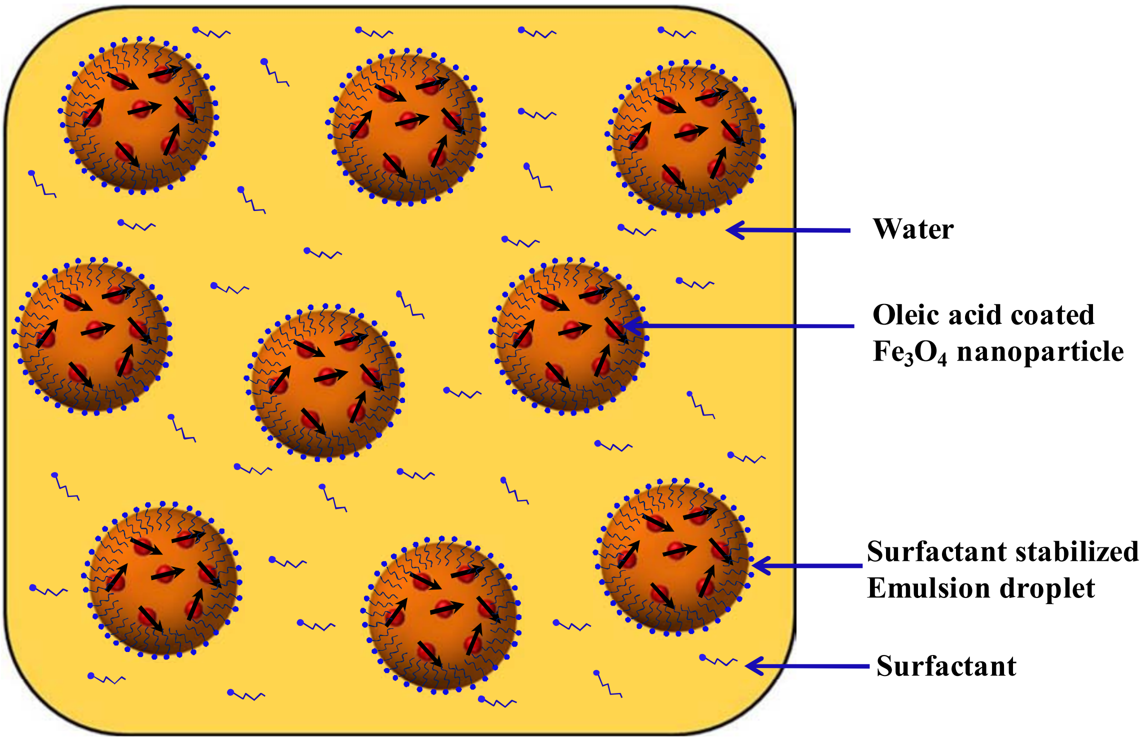

**Figure 2.3** Schematic representation of surfactant stabilized emulsion droplets containing ferrimagnetic $Fe_3O_4$ nanoparticles.

### 2.3.1 Emulsion Stabilization with Surfactant and Polymers

To provide electrostatic stabilization, an anionic surfactant - sodium dodecyl sulphate (SDS) is used. The molecular structure of SDS is shown in **Fig. 2.4a**. In aqueous solutions, SDS $Na^+$ dissociates and form counter ion cloud around the negatively charged $DS^-$ head group which is hydrophilic in nature. At the emulsion interface, the hydrophobic alkyl chain adsorbs on to the interface in a disordered state and partially in contact with water, and the $DS^-$ is exposed to water. The dissociated $Na^+$ and $DS^-$ at the interface forms an electrical double layer and provides electrostatic stabilization.

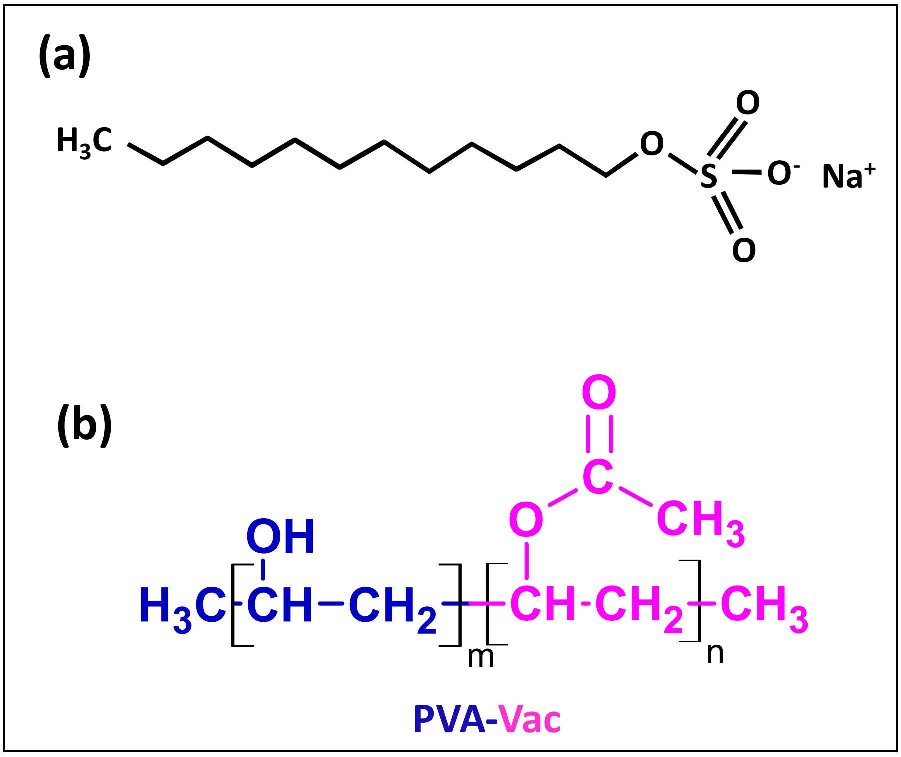

**Figure 2.4** Molecular structure of (a) sodium dodecyl sulphate (SDS) and (b) PVA-Vac.

The molecular structure of diblock copolymer PVA-Vac is shown in **Fig. 2.4b**. PVA-Vac is an amphiphilic polymer with a hydrophilic poly vinyl alcohol group (88 %) and the hydrophobic vinyl acetate group (12 %). These polymers are water soluble at room temperature and the theta temperature of PVA–Vac in water is around 97 °C.[81] At the emulsion interface, hydrophobic Vac part adsorb into the oil phase and hydrophilic PVA protrudes into water. The configurational entropy of the adsorbed polymer results in the repulsion between adjacent polymer chains that mediate a steric repulsion.

***Preparation of SDS Stabilized Emulsions***

Ferrofluid emulsion with desired surfactant stabilization is achieved by incubation followed by a washing procedure.[80] The initial emulsion is diluted with desired concentration of SDS solutions and then the emulsion droplets are separated by applying a magnetic field gradient. The same procedure was repeated at least three times to remove excess surfactant present at the interface. Finally, the emulsion is diluted with SDS of desired concentration and used in experiments. Emulsions stabilized with 0.8 and 0.08 mM SDS are labeled as ***ESD0.8*** and ***ESD0.08,*** respectively.

***Preparation of PVA-Vac Stabilized Emulsions***

Initial emulsion is washed with 0.08 mM SDS to remove excess surfactant present. Then the emulsion is washed three times with polymer solutions of desired concentration and incubated for 72 hrs for uniform polymer adsorption. In all the experiments polymer concentration is well below the critical aggregation concentration ($c^*$) of PVA. The $c^*$ values for 40K and 155K are 3.1 and 1.1 wt%, respectively.[78, 80] Here after emulsion stabilized with PVA-Vac 40K, PVA-Vac 115K and PVA-Vac 155K are labeled as ***EPVA40, EPVA115*** and ***EPVA155,*** respectively. The $R_g$ of 40K, 115K and 155K polymers obtained from viscomettry are found to be 8, 12 and 16 nm, respectively.

## 2.4 Experimental Techniques

### 2.4.1 Magnetic Chaining Technique based Force Measurement

MCT was introduced in 1994 and was adapted for the measurement of interparticle forces of magnetic colloids under various conditions.[23, 32, 42, 47-49, 64, 78] The technique is based on the diffraction of light by magnetic colloidal particle chains formed under the influence of an external magnetic field. It allows measuring the interparticle force as small as $10^{-13}$ N and the force measurement is based on averaging over a large number particles.

## Experimental Setup

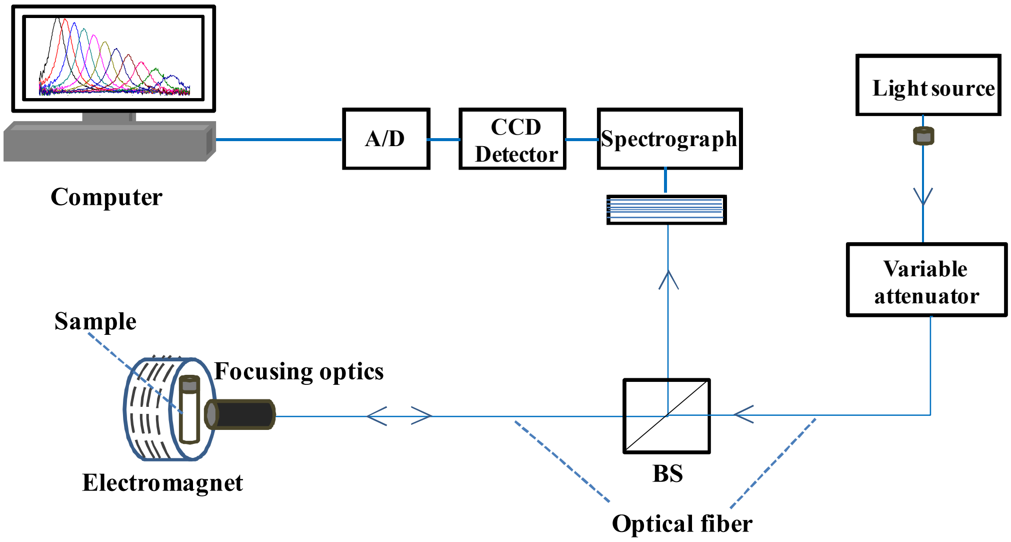

**Figure 2.5** Schematic representation of the force measurement set up. Electromagnet is powered by a programmable DC power supply.

The in-house developed experimental setup is schematically represented in **Fig. 2.5**.[49] It consist of a white light source (AvaLight-HAL Tungsten Halogen light source, Avantes, Netherlands), a custom made solenoid type electromagnet, a programmable DC power supply (Agilent technologies, USA) and a fiber optic spectrometer with CCD linear array with 2048 pixels (AvaSpec 2048-USB2, Avantes, Netherlands). The light is guided through the bundle of optical fibers (200 µm diameter, numerical aperture of 0.22) to illuminate the sample. The diffracted light is collected into a read optical fiber which guides the diffracted light to a spectrometer. A DC power supply powers the solenoid type electromagnet where the applied current is varied to change the magnetic field.

As the droplets are superparamagnetic in nature, without external field, they have no permanent magnetic moments because of the random orientation of the magnetic grains within the droplets due to thermal motion. When an external magnetic field is applied, ferrimagnetic particles in the droplets are magnetized and interact with neighboring droplets. When the repulsion between the droplets is equal to the attractive force, they form one dimensional chain like structures. The attractive force includes induced magnetic dipolar forces ($F_{chain}$) and the short range Van der Waals forces ($F_{VdW}$). The repulsive force ($F_{rep}$) can be electrostatic or steric or electro-steric depending upon the nature of stabilization. At equilibrium,

$$F_{rep}(d) = F_{chain}(d, B_{applied}) + F_{VdW}(d) \tag{2.3}$$

As the magnetic field increases, the sample color shows a blue shift, which can be well explained by Bragg's condition for white light,

$$r = \frac{N\lambda_{peak}}{n(1+\cos\theta)} \tag{2.4}$$

where, $r$ is the distance between the droplets in a chain, $n$ is the refractive index of carrier medium and $\lambda_{peak}$ is the wavelength of diffracted light.

For $180^{\circ}$ scattering geometry,

$$r = \frac{N\lambda_{peak}}{2n} \tag{2.5}$$

Because of the larger droplet size, the lattice of droplets diffracts light in the visible region. The distance between droplets '$r$'decreases with increasing magnetic field and hence the light is blue shifted. **Fig. 2.6 (a-c)** shows the schematic representation of emulsion droplets without and with two different applied magnetic fields along with phase contrast microscopic images under similar conditions on the right (d-f). The interdroplet distance $r$ is directly deduced from the measurement of $\lambda_{peak}$ by using a spectrometer. By varying the magnetic field strength, the distance between the colloidal particles is controlled. Because the droplets are monodisperse and negligibly deformable owing to their large capillary pressure, the corresponding droplet separation is $h = r - 2a$. The sensitivity in the distance measurement is 0.1 nm. The range of force that can be probed using this technique is a $10^{-11}$ to $10^{-13}$ N.

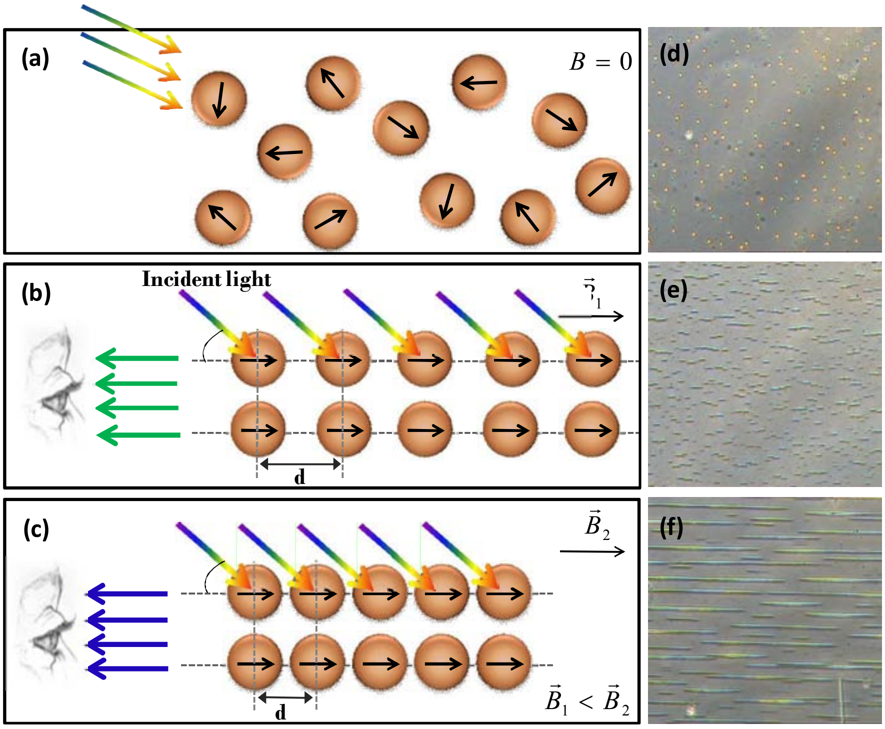

**Figure 2.6** Schematic representations of ferrofluid emulsion droplets (a) without and (b & c) with magnetic field $B_1 < B_2$ (d-f) Phase contrast optical microscopic images of emulsions at B=0, $B_1$ and $B_2$, respectively.

### Magnetic Dipolar Attractive Force-Theory

To form a stable chain of droplets, the repulsive force between the droplets must exactly balance the attractive force between the dipoles induced by the applied magnetic field. The dominant force in a field induced droplet chain is the dipole-dipole attraction. For two dipoles $m_1 = m_2 = m$, at separation $r$, their attractive force is,

$$F_{pair} = -\frac{6m_1m_2}{r^4} = -\frac{6m^2}{r^4} \tag{2.6}$$

In calculating the induced dipole moment of each droplet, the dipole fields from other droplets in addition to the applied field is also included. For a weak field, magnetization $M$ depends on the external field $H_{ext}$ and the shape dependent magnetic susceptibility, $\chi_{shape}$,

$$M = \chi_{shape} H_T \frac{\chi}{1+4\pi N\chi} H_{ext}, \tag{2.7}$$

where, $N$ is the shape dependent demagnetization factor (for sphere $N = \frac{1}{3}$) and $\chi$ is the magnetic field independent susceptibility. For an emulsion droplet of radius $a$, the dipole moment is given by,

$$m = MV = \frac{4\pi}{3} a^3 \chi_{sphere} H_{ext} \tag{2.8}$$

The mutual induction between the adjacent droplets under applied magnetic field generates an induced field. When two dipole moments align with separation $r$ in the field direction, each droplet generates a field at the centre of each other as,

$$H_I = \frac{2m}{r^3} \tag{2.9}$$

The external field acting on each droplet is the sum of applied field and field induced dipole field. Therefore

$$H_T = H_0 + H_I \tag{2.10}$$

and the attractive dipole force within an infinitely long chain is,

$$F_{chain} = -\sum_{n=1}^{\infty} n \frac{6m^2}{(nr)^4} = -\zeta(3)\frac{6m^2}{r^4} - \frac{1.202}{2\pi\mu_o}\frac{3m^2}{r^4} \tag{2.11}$$

where, $m$ is the induced magnetic moment of each drop, which can be determined self consistently from the intrinsic susceptibility of the ferrofluid and spherical shape of the droplet.[97]

**Van der Waals Attractive Force**

The other contribution to the attractive interactions between the droplets is the Van der Waals force. The integrated Van der Waals force between two spheres of radius 'a' separated at a distance 'r' is obtained by assuming Derjaguin approximation $\frac{r}{a} << 1$:[56]

$$F_{VdW}(d) = \frac{Aa}{12(r-2a)^2} \tag{2.12}$$

and $$A = \frac{3}{4}k_b T\left(\frac{\varepsilon_p - \varepsilon_w}{\varepsilon_p - \varepsilon_w}\right)^2 + \frac{3h\nu_e}{16\sqrt{2}}\frac{(n_p^2 - n_w^2)^2}{(n_p^2 + n_w^2)^{3/2}} \tag{2.13}$$

where, 'A' is Hamaker constant, $\varepsilon_p, \varepsilon_w$ are real part of the dielectric constant of particle and water, respectively, $n_p, n_w$ are refractive indices of particle and water, respectively. $h$ and $\nu_e$ are the Planck's constant and the plasma frequency of electron gas, respectively. Van der Waals force is short range, and become negligible for h >15 nm. Since the magnetic chaining technique is able to measure 'h' as small as few nm, the Van der Waals force is taken into account at h > 15 nm. For example, for a droplet of 200 nm size, with $A = 0.7\times10^{-20}$ J at h < 15 nm, $F_{VdW}(d)$ contributes to ~ 10 % of total force. The absolute error on 'd' measurement is about 1 nm and the force resolution is ~ 0.2 pN.[77]

### 2.4.2 Light Scattering Measurements

### Hydrodynamic Size Measurements

Dynamic light scattering, also known as photon correlation spectroscopy (PCS), is widely used for measuring hydrodynamic size in the sub-micron range in dilute solution. This technique measures the time-dependent fluctuations in the intensity of scattered light that occurs because of the Brownian motion of particles. Analysis of this intensity fluctuation allows the determination of the translational diffusion coefficient of particles. The intensities are measured at a short time intervals $\delta t$ (micro to milliseconds) for long periods of time 't' (milliseconds to seconds).[98] The intensity normalized time correlation function is given by,

$$g^{(2)}(t) = \frac{I(t)I(t+\delta t)}{I(t)^2} \tag{2.14}$$

where, $I(t)$ is the scattered intensity at time $t$ and $I(t+\delta t)$ is the scattered intensity recorded after a small time interval $\delta t$. This function has a value of 2 at small $\delta t$ and a value of zero at large $\delta t$. The measured time-auto-correlation function (TCF) is related to the normalized correlation function of the scattered electric field, $g^{(1)}(t)$ by the Siegert's relation,

$$g^{(2)}(t) = 1 + \beta \left| g^{(1)}(t) \right|^2 \tag{2.15}$$

where, $\beta$ is (a constant) characteristic of the instrument and is approximately close to one. For monodisperse particles, $g^{(1)}(t)$ is a single exponential function given by,

$$g^{(1)}(t) = \exp(-\Gamma \tau) = \exp(-D_t q^2 \tau) \tag{2.16}$$

where, $'\Gamma'$ is the relaxation rate, $'q'$ is the wave vector of the laser light and $'D_t'$ is the translational diffusion coefficient. The relaxation time $\tau$ at which $g^{(1)}(t)$ decays to $1/e$ of its initial amplitude, is related to the translational diffusion coefficient ($D_t$) of the solute particles as,

$$\Gamma = D_t q^2 \tag{2.17}$$

For small, non-interacting, dilute spheres the Stokes–Einstein relationship can be used to calculate the hydrodynamic diameter of the sample,

$$H_d = \frac{k_B T}{3\pi\eta D_t} \tag{2.18}$$

where, $k_B$ the Boltzmann constant, 'η' is the solvent viscosity and $H_d$ is the hydrodynamic diameter of the particle.

A typical DLS system (**Fig. 2.7**) comprises of five major components. A laser, attenuator, detector, auto correlator and computer interface. A monochromatic, polarized and continuous laser is used to illuminate the sample. Most of the laser beam passes straight through the sample, but some are scattered by the particles in the sample. Sample is usually taken in a square cuvette or in folded capillary cell. A detector is used to measure the intensity of the scattered light. As particles scatter light in all directions, it is possible to place the detector in any position and it will still detect the scattering. The intensity of the scattered light must be within a specific range for the detector to measure successfully. If too much light is detected, the detector will become saturated. To overcome this, an attenuator is used to reduce the intensity of the laser and hence the intensity of scattering. For samples that do not scatter much light, such as very small particles or samples of low concentration, the amount of scattered light must be increased. In this situation, the attenuator will allow more light to pass through the sample. For samples that scatter more light, such as large particles or sample of higher concentration, the amount of scattered light must be decreased. The scattering light signal from the detector is then passed to a digital signal processing board called correlator. The correlator collects and integrates the scattering intensity at different time intervals to derive the rate at which the intensity is varying. This correlator information is then passed to a computer, where algorithms are used to extract the decay rates for a number of size classes.

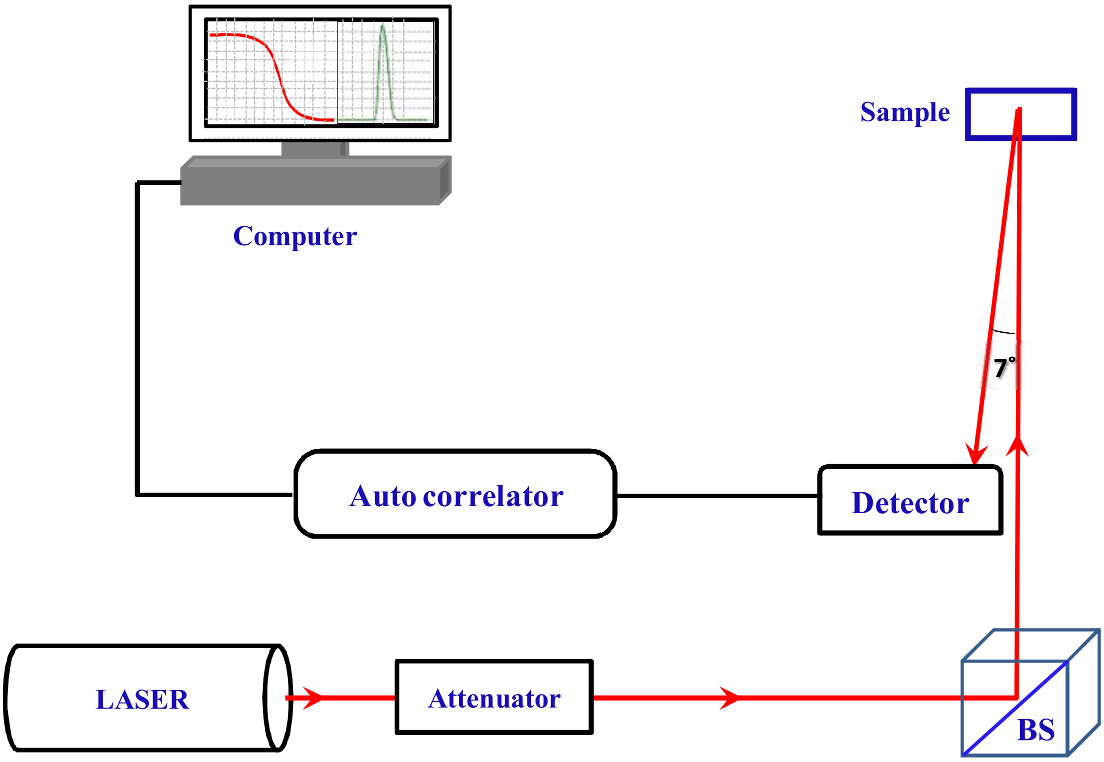

**Figure 2.7** Block diagram of dynamic light scattering set up.

The size distribution of nanoemulsion is determined by using Zetasizer-Nano (Malvern Instrument, UK) at 25 ˚C. It uses a 4 mW He–Ne laser operating at a wavelength of 633 nm, avalanche photodiode detector and incorporates non-invasive back scatter (NIBS) optics. The scattered light is detected at an angle of 173 ° and this optics arrangement maximizes the detection of scattered light while maintaining signal quality as shown in **Fig. 2.7**. The major advantages of this technique are as follows: (i) As the backscatter is being measured, the incident beam does not have to travel through the entire sample. As light passes through a shorter path length of the sample, concentrated sample can be measured; (ii) It reduces multiple scattering, where the scattered light from one particle is itself scattered by other particles. (iii) Contaminants such as dust particles within the dispersant are typically large compared to the sample size and mainly scatter light in the forward direction. By measuring the backscatter, the effect of dust and other foreign materials can be greatly reduced.

### Electrophoretic Mobility Measurement

When a charged particle is introduced into a polar medium, the depletion of co-ions (ions with same charge as the particle surface) from the surface and adsorption of counter ions (ions with opposite charge as the particle surface) occurs. The development of a net charge at the particle surface through ionization or by dissociation of surface groups affects the distribution of ions in the surrounding interfacial region, resulting in an increased concentration of counter ions (ions of opposite charge to that of the particle) close to the surface. Whatever be the charging mechanism, the final surface charges of co-ions is balanced by an equal but oppositely charged region of counterions. Some of the counterions are bound, usually transiently to the surface within the so called *Stern layer* or *Helmholtz layer*, while other ions form an atmosphere of ions in rapid thermal motion close to the surface, known as the diffuse electrical double layer (**Fig. 2.8a**). The difference between the bound and free ions in the diffuse layer is analogous to the difference between a water molecule in a sea and in the atmosphere.[56] Within the diffuse layer there is a notional boundary inside which the ions and particles form a stable entity. When a particle moves (e.g. due to gravity), ions within the boundary move with it, but any ions beyond the boundary do not travel with the particle. This boundary is called the surface of hydrodynamic shear or slipping plane. The potential that exists at this boundary is known as zeta potential as shown in **Fig. 2.8b**.

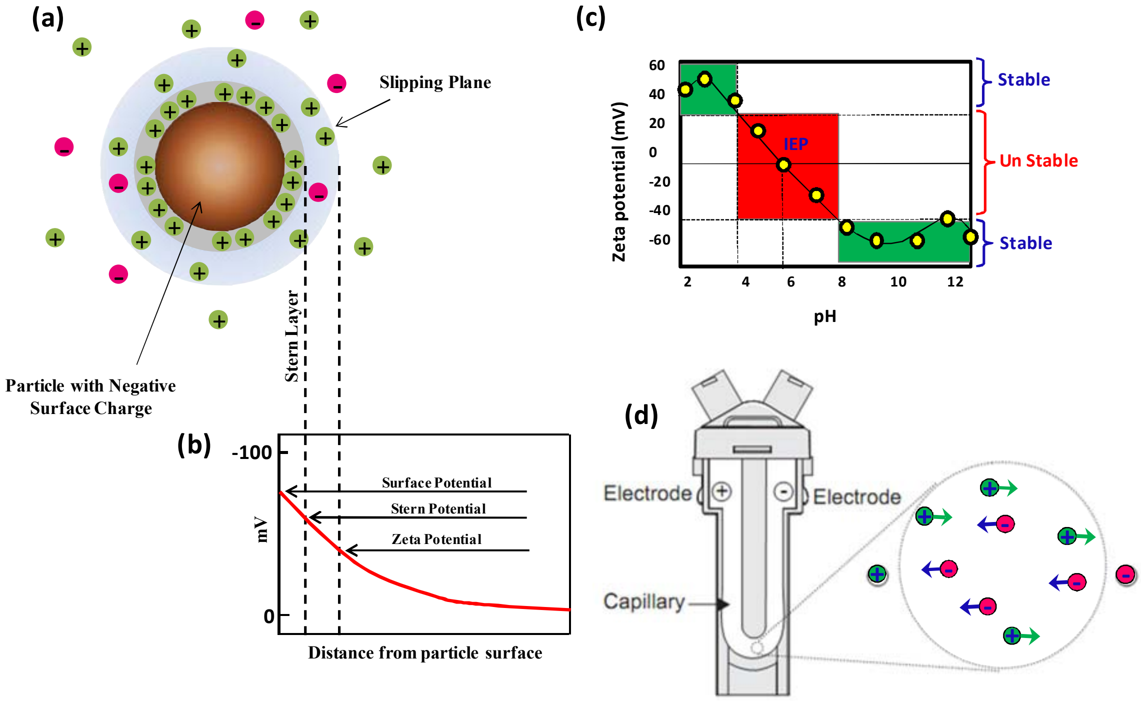

**Figure 2.8** Schematic representation of (a) charged particle with electric double layer , (b) distance from the particle surface and the corresponding potentials (c) Typical plot of zeta potential versus pH showing the position of the isoelectric point and the pH values where the dispersion is stable and unstable, (d) electrophoretic mobility in a folded capillary cell.

The magnitude of the zeta potential gives an indication of the potential stability of the colloidal system. If all the particles in a suspension have a large negative or positive zeta potential then they will tend to repel each other and there will be no tendency to flocculate. However, if the particles have low zeta potential values then there is no force to prevent the particles coming together and flocculating. The general dividing line between stable and unstable suspensions is +30 mV or -30 mV. Particles with zeta potentials above ±30 mV are normally considered stable (**Fig. 2.8c**). However, if the particles have a large density different from the dispersant, they will eventually sediment. The important factors affecting the zeta potential are pH, conductivity and concentration of formulations.

In our present study, zeta potential measurement is done based electrophoresis approach. When an electric field is applied across an electrolyte, charged particles suspended in the electrolyte are attracted towards the electrode of opposite charge as shown in **Fig. 2.8d**, where the viscous forces acting on the particles tend to oppose this movement. When equilibrium is reached between these two opposing forces, the particles move with a constant velocity. The velocity of the particle is dependent on the strength of electric field or voltage gradient, the dielectric constant of the medium, the viscosity of the medium and the zeta potential. The velocity of a particle in an electric field is referred to as its electrophoretic mobility, which is related to the Zeta potential by the Henry equation,

$$U_E = \frac{2\varepsilon\zeta f(ka)}{3\eta} \tag{2.19}$$

where, $U_E$ is the electrophoretic mobility, $\zeta$ is the zeta potential, $\varepsilon$ is the dielectric constant, $\eta$ is the viscosity and $f(ka)$ is the Henry's function (≈1.5 by *Smoluchowski* approximation for the particle larger than 0.2 μm dispersed in electrolyte containing more than $10^{-3}$ molar salt). For small particles in low dielectric constant media $f(ka)$ becomes 1 by *Huckel* approximation for non-aqueous measurements. κ is inverse Debye length, and $\kappa^{-1}$ is often taken as a measure of the "thickness" of the electrical double layer.

The instrument used in the present study (Malvern's Zetasizer-Nano) uses a combination of laser Doppler velocimetry and phase analysis light scattering (PALS) to measure particle electrophoretic mobility. Implementation of PALS enables even samples of very low mobility to be analyzed and their mobility distributions calculated. This allows the measurement of high conductivity samples, plus the ability to accurately measure samples that have low particle mobilities, such as samples dispersed in non-aqueous solvents. Further, the low applied voltages can be used to avoid Joule heating.

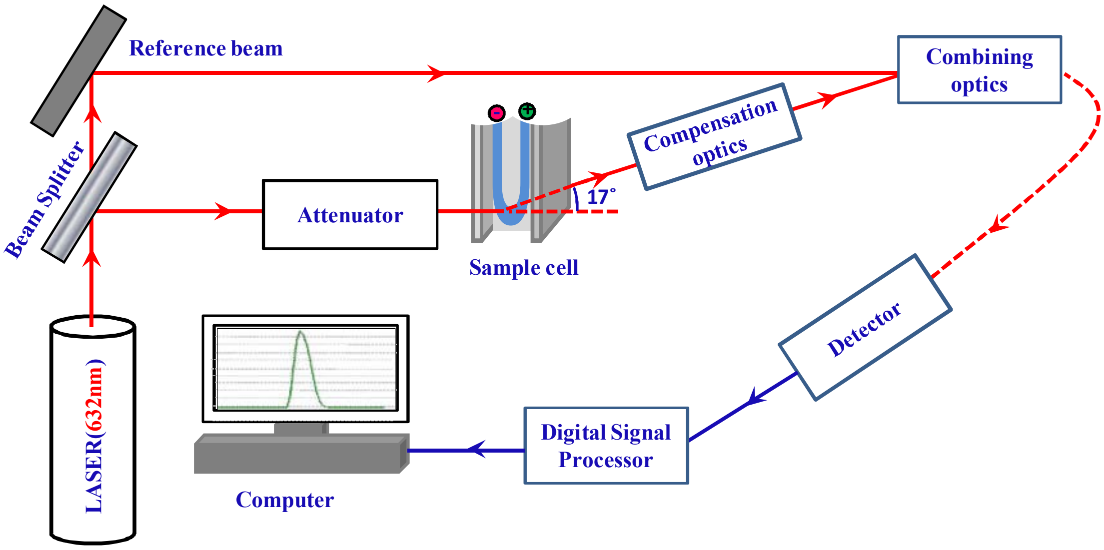

**Figure 2.9** Schematic representation of the experimental setup for electrophoretic mobility measurements.

For zeta potential measurement, the laser light source is split to provide an incident and reference beam as shown in **Fig. 2.9**. The incident laser beam passes through the centre of the sample cell, and the scattered light is detected at an angle of 17 °. When an electric field is applied to the cell, any particles moving through the measurement volume will cause the intensity of light detected to fluctuate with a frequency proportional to the particle speed and this information is passed to a digital signal processor and then to a computer. The Zetasizer-Nano software produces a frequency spectrum from which the electrophoretic mobility and hence zeta potential is calculated. The intensity of the detected scattered light must be within a specific range for the detector to successfully measure it, which is achieved by using an attenuator. To correct for any differences in the cell wall thickness and dispersant refraction, compensation optics are installed to maintain optimum alignment.[99]

### 2.4.3 Phase Contrast Optical Microscopy

Phase contrast microscope is widely used for examining unstained phase objects and is, developed in 1930s by Frits Zernike.[100-102] Phase contrast optical microscopy enhances contrast of transparent and colorless objects by influencing the optical path. When light passes through an object that is more optically dense than its environment, the wave fronts are retarded with respect to the unaffected, bypassing background light. The idea behind visualization of phase shift in the object is to change the phase of the background light in such a manner that background and object light weaken or even cancel each other out when interfering in the primary image plane. In phase contrast microcopy phase shifts of the light that are evoked by specimen passage are converted into amplitude shift. This results in highly improved contrast. **Fig. 2.10** shows schematic representation of a phase contrast microscope. Major components necessary for phase contrast are the condenser with annular ring and the objective with phase plate and the specimen. The light from a white light source passes through the condenser with an annular ring. After passing through the annular ring, the hollow cone of light is focused onto the specimen by the condenser. When light passes through an object that is more optically dense than its environment or background, a portion of light usually experience phase changes (yellow parts of the beams path) and is deflected to the inside and outside of the hollow cone of the light. Phase changes and deflection are induced by the specimen density components. The typical phase shift induced by specimen (90 °) is negative and about ¼th of the wavelength of the light $-\left(\frac{\lambda}{4}\right)$. However some portions of light are not affected by specimen, which remain in their original phase and they are not deflected. Inside the objective, phase changed and deflected light is still spatially separated from the light unaffected by the specimen. Now the light encounters the phase plate which is aligned with the annular ring in the condenser in terms of size and position.

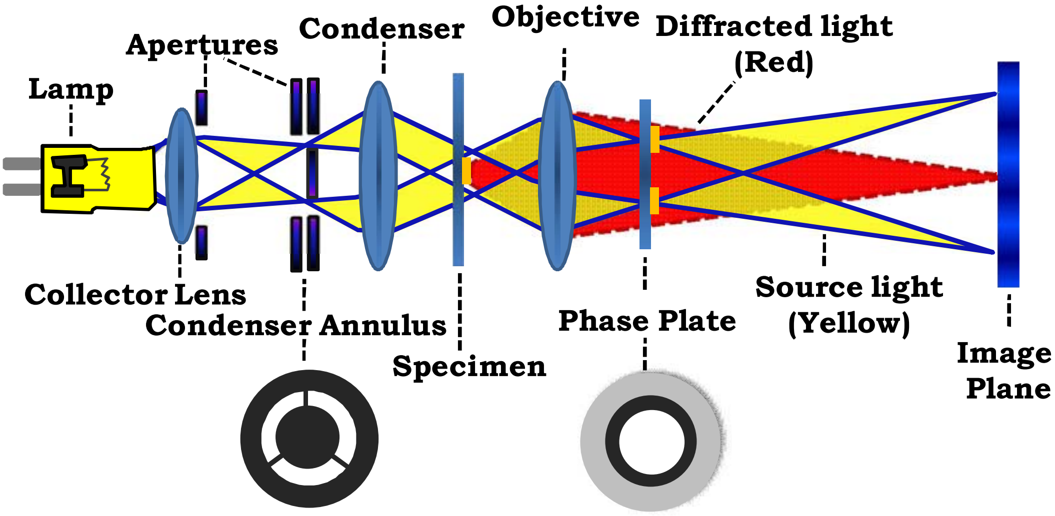

**Figure 2.10** Schematic representation of phase contrast optical microscope.

The phase plate is a semi-opaque coating on one of the lenses within the objective. Due to its optical properties and alignment with the annular ring, light that was not deflected while passing through the specimen hits the phase plate and the phase of the light is positively shifted by $+\left(\frac{\lambda}{4}\right)$ (red highlighted wave in **Fig. 2.11a**) resulting in a phase difference of $\frac{\lambda}{2}$ (180 °) between light that was phase-shifted by the specimen (highlighted yellow wave in

**Fig. 2.11c**) and light that was phase shifted by the phase plate. After passing through the objective, the total phase shift between the affected (yellow) and unaffected (red) light is half the wavelength. These two lights combine in the intermediate image plane and this leads to interference, which visualizes the phase shifts as brightness difference or contrast. This makes transparent objects shine out in contrast to its surroundings.

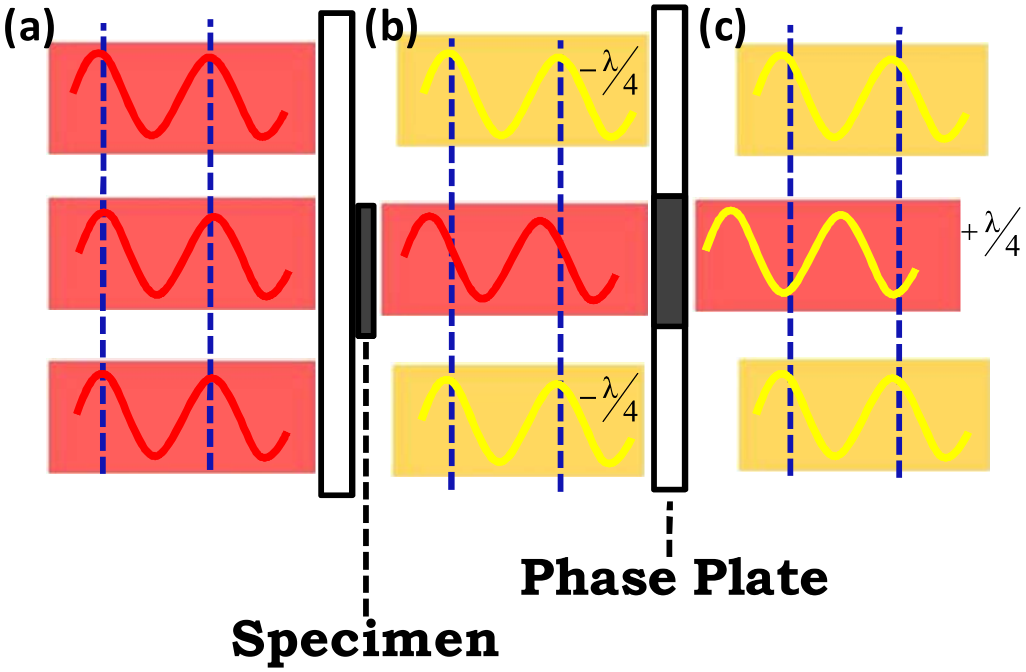

**Figure 2.11** Phase contrast due to specimen and the phase plate. (a) Incident wave (b) Specimen induces a phase shift of $-\frac{\lambda}{4}$ are shown as highlighted yellow wave. (c)The phase plate increases the phase of un-deflected light from specimen by $+\frac{\lambda}{4}$.

In the present study, the microstructure of the emulsion droplets is studied using a Leica inverted phase contrast optical microscope equipped with a digital camera (JVC) and a frame grabber card. The obtained images are processed using Leica Win software.

### 2.4.4 Viscometry

Viscometry is used to measure radius of gyration ($R_g$) of polymer solutions.[72] Ostwald viscometer is used to measure the viscosity. Exactly 20 ml (or the volume marked on the viscometer) of water at 25 °C was introduced into the bulb 'A' (**Fig. 2.12**) with a syringe or pipette and left for 5 min to equilibrate. Then either apply positive pressure to the wide limb (I) or gentle suction to the other limb (II) until the meniscus rises above the upper graduation mark 'B' (**Fig. 2.12**). Once the pressure is released, the time taken for the liquid to flow between the two graduation marks 'B' and 'C' is measured precisely.

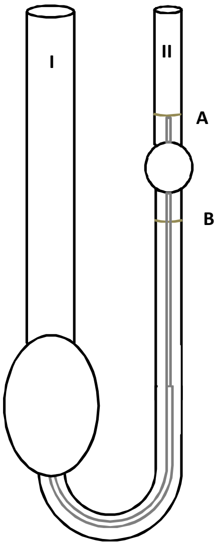

**Figure 2.12** Schematic of an Ostwald viscometer, A, B are the lower and upper graduation marks, respectively.

The average flow time of water ($t_0$) and the polymer solution ($t_1$) is related to the relative viscosity by,

$$\frac{\eta_1}{\eta_0} = \frac{t_1 \rho_1}{t_0 \rho_0} \tag{2.20}$$

where, '$\rho_0$' and '$\rho_1$' are density of water and polymer solution, respectively. In dilute concentrations ($\rho_0 \approx \rho_1$), viscosity follows Einstein's law,

$$\eta / \eta_0 = 1 + 2.5\phi \qquad (2.21)$$

where, $\eta$ is polymer solution viscosity, $\eta_0$ is pure solvent viscosity and $\phi$ is the coil volume fraction which is a function of hydrodynamic radius.[72, 79]

## 2.5 Nanomaterials Characterization Techniques

### 2.5.1 Thermo Gravimetric Analysis (TGA)

In thermogravimetric analysis the mass of a sample is measured as a function of temperature whilst the sample is subjected to a controlled linear temperature program. This measurement evaluates the thermal decomposition kinetics of materials such as, sintering, decomposition, oxidation or reduction. The typical sample masses are 5-25 mg and the mass change upon heating is detected within 0.1-10 μg resolution. TGA is performed in a controlled atmosphere such as oxygen, nitrogen, helium or argon with controlled flow rates. TGA of prepared oleic acid stabilized $Fe_3O_4$ nanoparticles were characterized using Mettler Toledo Large furnace which has temperature range of 30-1200 °C. From the weight loss curve, the amount of oleic acid attached to the $Fe_3O_4$ nanoparticles is derived quantitatively.

### 2.5.2 Vibrating Sample Magnetometer (VSM)

The working principle of VSM is Faraday's law of induction; an electromotive force is induced in a conductor by a time dependent magnetic flux. In a typical VSM experiment, sample is magnetized in a homogenous magnetic field and the sample is vibrated sinusoidally at constant amplitude with respect to stationary pickup coils. The sample is magnetized by the homogeneous magnetic field and the resultant field change B (t) at a point 'p' inside the coils induces voltage, V (t)

$$V(t) = \int_{A_{coil}} \frac{\partial B(t)}{\partial t} dA_{coil} \qquad (2.22)$$

where, '$A_{coil}$' is the area of the single turn of the coil and B(t) is given by dipolar approximation, assuming small dimensions of the magnetized sample in comparison to its distance from the detection coils,

$$B(p) = \frac{\mu_0}{4\pi}\left[\frac{m}{p^3} - \frac{3(m.p)}{p^3}\right] \text{ and} \tag{2.23}$$

$$\frac{\partial B}{\partial t} = \frac{\partial B}{\partial z(t)}\frac{\partial z(t)}{\partial t} \tag{2.24}$$

V (t) is measured through a high resolution lock-in amplifier and associated electronics. For stationary pickup-coils in a static magnetic field, the e.m.f induced in the coils is solely due to the vibration of sample. The measured voltage is then converted into magnetic moment of the sample by the voltage-moment calibration material.

Cryo-free mini VSM (Cryogenic, UK) is used for the magnetization measurements. The magnetization measurement is carried out at room temperature in the applied field range of -2.5 to + 2.5 Tesla.

### 2.5.3 Fourier Transformed Infrared (FTIR) Spectroscopy

Infrared region span the wavelength spectrum from ~750 nm to 300 µm, or~ 12800 to 10 $cm^{-1}$ wave numbers. Radiation is absorbed in this spectral region when its frequency matches a vibrational mode of the sample. Quantum mechanical selection rules dictate that only those modes of the molecule that undergo a change in dipole moment will absorb infrared radiation.[103] Molecules with heteroatomic substituent or having nonsymmetrical vibrational modes are IR active due to net charge density change upon molecular vibrations. In IR spectroscopy, the sample to be measured is illuminated with a broad band IR source. The resulting IR spectrum is measured with an IR Fourier transform spectrometer. Fourier transform spectrometry has advantage in terms of fast scanning process and dispersive absorption wave numbers. A typical FT-IR spectrometer uses a glowing black-body as IR source. IR beams pass through the aperture and is fed to interferometer resulting in an interferogram which is then transmitted through or reflected from the sample. Among the band of vibration frequencies, specific frequencies are absorbed by the sample. The signal from the sample is measured by detectors and fed to a computer, where the data is Fourier transformed. To normalize the absorption/ transmission intensity, background spectrum is recorded without the sample. ABB BOMEM MB 3000 FTIR spectrometer is used in the wave number range of 4000-400 $cm^{-1}$. The pellets were made by embedding $Fe_3O_4$ nanoparticles with the KBr powders (in 1:3 ratios).

### 2.5.4 X- Ray Diffraction (XRD)

X-ray diffraction technique reveals the structure of the crystal. It is also used for chemical analysis, stress measurements, to study the phase equlibira, crystal orientation and particle size.[104] The basic principle is Bragg's law of diffraction, $2d_{hkl} \sin\theta = n\lambda_{X-ray}$ where, $\theta$ is the Bragg angle, $d_{hkl}$ is the spacing between the crystal planes and $\lambda_{X-ray}$ is the wavelength. Since the wavelength of X-rays is in the order of crystal lattice spacing, diffraction of X-rays is observed when it interacts with crystals. Depending upon the phase of the diffracted X-rays, they interfere constructively in specific directions. During the diffraction measurements, X-ray source, sample and the detector lie on the circumference of a circle which is known as focusing circle. X-ray diffractometer Ultima IV from Rigaku Corporation was used for the study. X-ray source uses Copper target operating at 40 kV and 30 mA conditions and the detector is a scintillation detector. The X-ray source and sample are fixed and the detector moves through a range of angles from 20 ° to 80 ° in the step of 0.02 °, this geometry is called as $\theta - 2\theta$ geometry. The Cu $k_\alpha$ X-ray is obtained by filtering out the other wavelengths using a monochromator. The monochromatic X-rays are collimated by solar slits and falls on the sample. X-rays scattered from the sample passes through anti-scatter slit to reduce the background radiation in order to improve the peak to background ratio. Then the beam converges on the passing slit and reaches the detector. The intensity of the diffracted beam at each angle is detected and forms the diffraction pattern. Data provided by the joint committee on powder diffraction standards (JCPDS) are compared with diffraction data for the phase identification. From the peak broadening, the average crystallite size ($D_{Crystallite}$) can be calculated by using the Debye –Scherer equation,

$$D_{crystallite} = \frac{0.9\lambda_{X-ray}}{\beta \cos\theta} \tag{2.25}$$

where, $\beta$ is full width at the half maximum of the maximum intensity peak measured in radians and $\lambda_{X-ray}$ is wavelength of X-ray used. The peak position and full width at half maximum are determined by fitting the maximum intensity peak with a Voigt function.

### 2.5.5 Transmission Electron Microscopy (TEM)

Transmission electron microscopy (TEM) is one of the advanced techniques for the direct measurement of particle size distribution and morphology.[105] The working principle of TEM is same as that of optical microscopy, but in contrast to light source, a focused electron beam is used. Since resolution of a microscope depends on the wavelength of light used, shorter wavelength of electron enables a better resolution (~1000 times of optical microscope) than the optical microscope. When the highly focused electron beams interact with thin sample surface, some electrons may be scattered elastically or inelastically and the incident electron may also cause ejection of secondary electrons or X-rays by the sample. Different detectors are used to detect these interactions and each of them gives unique information about the sample. The elastic scattering involves no energy loss and gives rise to diffraction patterns. Inelastic scattering between electrons with grain boundaries, dislocations, defects, density variation and so on causes a complex absorption and scattering effects, which results in spatial variation in the intensity of the transmitted electrons. Electromagnetic lenses are used to focus the electron beams, which forms a diffraction pattern in the back focal plane and a magnified image of the diffraction pattern is obtained. The magnification of the TEM is due to the ratio of the distances between the specimen and the objective lens' image plane. The magnification in the electron microscope can be varied from hundred to several thousand times. JEOL TEM 2011 at an operating voltage of 200 KeV was used for obtaining the particle size distribution and morphology. As TEM needs sample in thin film form to visualize smaller particles and larger aggregates, a drop of nanoparticle dispersed in acetone is placed over a carbon grid and dried at room temperature overnight under a lamp to have a thin film of sample.

### 2.6 Characterization of Oleic Acid Functionalized $Fe_3O_4$ Nanoparticles

**Fig. 2.13a** shows the features of the XRD pattern of prepared nanoparticles, which shows diffraction peaks of (220), (311), (400), (422), (511), and (440) that are indexed to a cubic spinel structure of $Fe_3O_4$. The inverse spinel structure consists of oxide ions in the cubic close-packed arrangement in which 1/3 of tetrahedral interstices and 2/3 of octahedral interstices coordinate with oxygen. The average crystallite size obtained was ~10 nm.

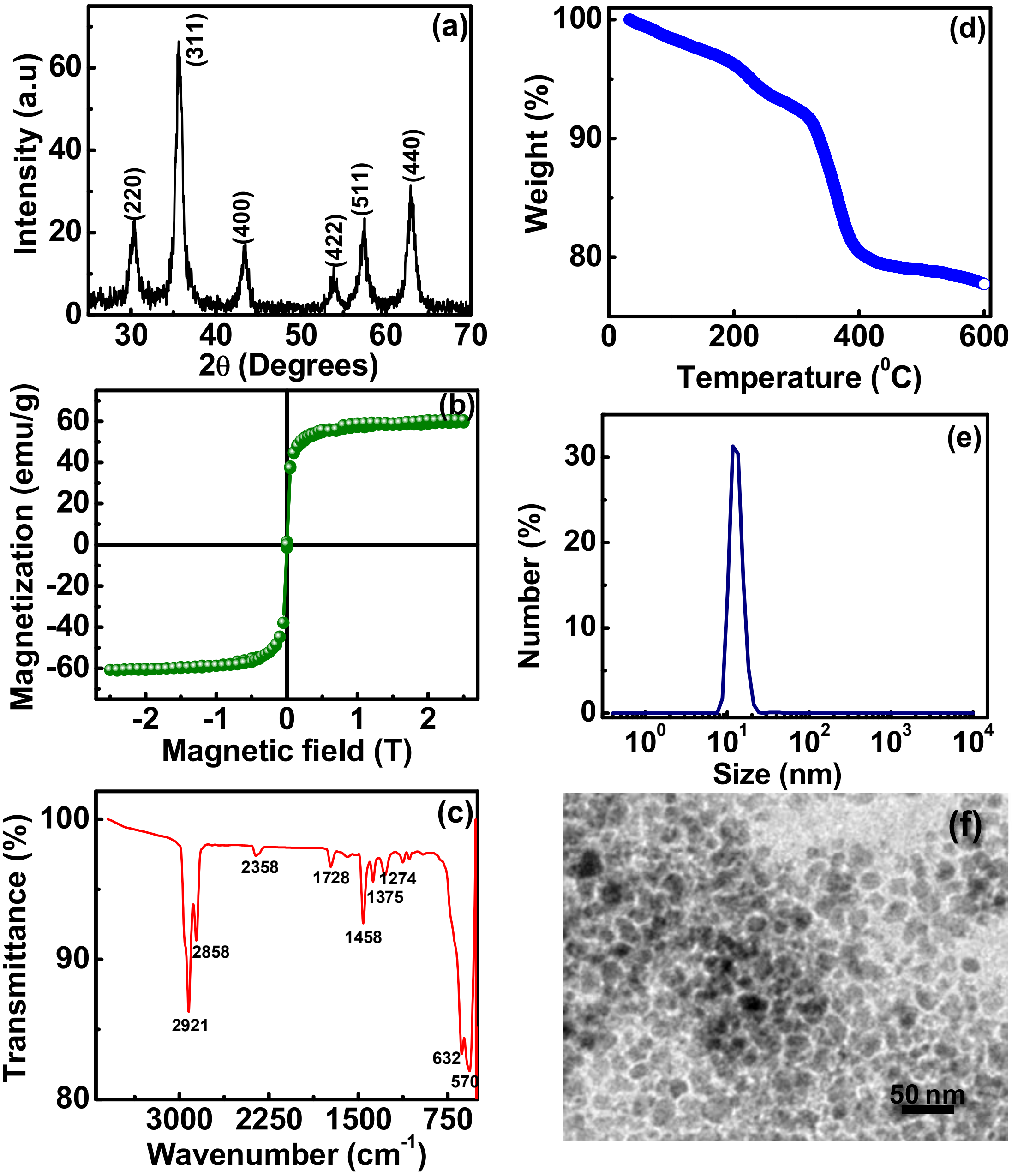

**Figure 2.13 (a-d**) XRD, VSM, FTIR and TGA results of the $Fe_3O_4$ nanoparticles prepared by chemical co-precipitation. **(e)** The hydrodynamic size distribution of the $Fe_3O_4$ nanoparticles in octane and **(f)** TEM of the iron oxide nanoparticles.

The room temperature magnetization curve for the iron oxide nanoparticles (**Fig. 2.13b**) shows superparamagnetic nature with zero remanence and coercivity. The saturation magnetization was found to be 59 emu/g. The parallel alignment of $Fe^{2+}$ and $Fe^{3+}$ ions spin in the adjacent octahedral sites leads to a net magnetization and thus a ferri-magnetic behavior. The capping of oleic acid on nanoparticles was confirmed from Fourier transform Infrared spectroscopy. **Fig. 2.13c** shows characteristic peaks at 2921, 2858, 2358, 1728, 1458, 1375, 1274, 632 and 570 $cm^{-1}$. The peaks at 2921 and 2858 $cm^{-1}$ are due to the asymmetric and symmetric stretching, respectively of the methylene group of the oleic acid. The peak at 1458 $cm^{-1}$ corresponds to the asymmetric stretching of the carboxylate ($COO^-$) group. The peak at 570 $cm^{-1}$ is attributed to the stretching of bonds between octahedral and tetrahedral metal ions to oxide ions while the one at 1728 $cm^{-1}$ is due to the presence of free oleic acid molecules. The rest of the peaks are attributed to vibrations in kerosene.[95-96] The thermogravimetric curve for the magnetite nanoparticles (**Fig. 2.13d**) shows a two-step weight loss at $\approx$ 199 and $\approx$ 320 °C. The first step should be due to the removal of loosely bound or free surfactant and the second step should be due to the removal of strongly bound surfactant molecules. The carboxylic acid group of oleic acid binds to the magnetite while the aliphatic chain extends out into the non-polar solvent thus providing steric hindrance between the particles. The charges at the carboxylate ion of oleic acid, de-localizes in between two oxygen atoms because of resonance effect. The surfactant coating thus prevents the agglomeration of particles against Van der Waals and magnetic attractive interactions and passivates the nanocrystals from oxidation. The average size of the nanoparticles obtained from dynamic light scattering measurements (**Fig. 2.13e**) was ~12.5 nm. The larger size obtained from DLS, compared to the XRD, is due to the fact that the former gives the hydrodynamic diameter that includes the dead surface layer and solvent molecules where as the latter gives the crystallite size. The TEM image of the sample is shown in **Fig. 2.13f.**

## 2.7 Characterization of Ferrofluid Emulsion by DLS and Zeta Potential Measurements

The hydrodynamic size and zeta potential of emulsions were measured using Zetasizer nano ZS (Malvern, UK). The measured hydrodynamic size and zeta potential values for magnetic nanoemulsion stabilized with SDS and PVA-Vac are listed in **Table 2.1**.

| Sample Code | Details | Hydrodynamic Size (nm) ± 2 % | Size polydispersity index (PdI) | Zeta Potential (mV) |
|---|---|---|---|---|
| ESD0.8 | Emulsion + 0.8 mM SDS | 200 | 0.017 | -49 |
| ESD0.08 | Emulsion + 0.08 mM SDS | 200 | 0.019 | -30 |
| EPVA40 | Emulsion + 0.6 wt% of PVA-Vac 40K | 220 | 0.012 | -12 |
| EPVA115 | Emulsion + 0.6 wt% of PVA-Vac 115K | 255 | 0.009 | -2 |
| EPVA155 | Emulsion + 0.6 wt% of PVA-Vac 155K | 550 | 0.01 | -1 |

**Table 2.1** Hydrodynamic size and zeta potential values for magnetic nanoemulsion stabilized with SDS and PVA-Vac.

The polydispersity index is used to describe the width of the particle size distribution, which is related to the standard deviation ($\sigma_{sd}$) and Z- average ($Z_d$) which is the intensity weighted mean hydrodynamic size as,[106]

$$PdI = \frac{\sigma_{sd}^2}{Z_D^2}. \qquad (2.26)$$

Owing to its amphiphilic nature, non-polar alkyl chains of SDS molecules protrude into the oil phase and the polar $DS^-$ extent into the water. In polymer stabilized emulsions, hydrophobic Vac part of the polymer prefers to remain inside the oil droplet, while the hydrophilic PVA part protrudes into the solvent to form a diffuse polymer layer. The negative zeta potential value indicates the presence of negatively charged head groups ($SO_4^-$) at the oil-water interface, in the case of SDS stabilized emulsion. For PVA-Vac stabilized system, the very small value of zeta potential indicates the presence of slight residual surface charges on the droplets, irrespective of repeated washing.

## 2.8 Conclusions

The preparation of magnetic nanoparticles and its characterization by X-ray diffraction, Vibrating sample magnetometer, Fourier transform infrared spectroscopy, Thermo gravimetric analysis, Dynamic light scattering and Transmission electron microscopy are discussed. The working principle of DLS, zeta potential, phase contrast optical microscopy and other analytical techniques used for the nanoparticles characterization are also briefly discussed. The preparation of ferrofluid oil, ferrofluid emulsion and its characterization using dynamic light scattering and zeta potential measurements and the details of the intermolecular force-distance and diffraction peak measurement techniques are presented.

# Chapter- III

## Interaction of mono, di and tri valent Cations with Surfactant and Polymer Stabilized Emulsions and its Influence on the Interaction Forces

# 3

# Interaction of mono, di and tri valent Cations with Surfactant and Polymer Stabilized Emulsions and its Influence on the Interaction Forces

## 3.1 Introduction

The strength and range of colloidal interaction can be varied by controlling charge and size of colloids. For instance, screening of charged colloids by counterions is central to the colloidal stability. Understanding coalescence and kinetic stability in emulsion systems are important for plethora of engineering applications.[107] Tunable interactions by different stimuli make colloids a wonderful model system to study the intermolecular interactions.[108] Interaction forces involving macromolecules, nanoparticles, surface active agent are strongly modified by ions, and such effects are essential in condensation of nucleic acids, cement hardening, water treatment.[109] Surface forces are essential in industrial processes, material engineering and biology. In industrial process, such as papermaking or food processing, the interaction forces control the stability and their rheology.[55] Surface forces are equally important in the context of new materials especially in self-assembly or surface pattering. In biological systems, such forces are further responsible for interactions involving proteins, nucleic acid or membranes.

Magnetically tunable property of emulsion is employed to study intermolecular interactions such as, electrostatic,[110] steric,[72, 78] electro-steric,[64] depletion,[88] irreversible polymer bridging,[111] bio-molecule growth kinetics.[32, 47, 83-85] Interaction of surfactants and polymers at an interface is well studied in the literature. Three different scenarios can exist at the interface depending upon the nature of surfactant, polymer and interface.[49, 80-82] Forces between a pair of charged colloids,[108] surfactant free emulsions droplets,[107] two dissimilar surfaces[55] in aqueous salt solutions were studied in the past. However the effect of interfering cation on the interaction forces between electrostatically and sterically stabilized emulsions are not attempted. The purpose of this study is to understand the effect of interfering cations on the intermolecular forces between anionic surfactant/di-block copolymer stabilized emulsion droplets and their role on the stability of the emulsion using magnetic chaining technique.

Cations plays major role in controlling the physiological activities such as maintaining levels of body fluids, control heart beat, transmission of nerve impulses and specific metal ions are crucial for the structure of cell membranes and DNA.[112] The deficiency of $Fe^{3+}$ can lead to permanent loss of motor skills and its excess can lead to diseases, such as Parkinson and Alzheimer diseases.[113] Essential cations in excess are lethal to all cells. In general, heavy metal ions are major source of pollutants in water bodies. Heavy metal ions such as sliver (Ag), mercury (Hg), tellurium (Te) and cadmium (Cd) are extremely hazardous to most bacteria and yeast at even exceptionally low concentrations.[114] Heavy metal ions are more specific to sulfhydryl groups that are found in proteins. Certain metal ions such as $Cu^{2+}$, $Fe^{2+}$ increase intracellular reactive oxygen species (ROS) that catalyze the production of superoxide and this leads to DNA damage and inhibition of particular enzyme activities that are vital for cell growth.[115] So understanding the ion interaction with changed and neutral interfaces in aqueous solution is key to understanding colloidal stability, water quality and disease diagnosis.

Towards these objectives, MCT is used to probe the interaction of various biologically important cations such as $Na^+$, $K^+$, $Ca^{2+}$ , $Cu^{2+}$, $Fe^{3+}$ and also toxic heavy metal ions $Ni^{2+}$, $Co^{2+}$, $Cd^{2+}$, $Pb^{2+}$ and $Ag^+$ at the electrostatically and sterically stabilized interfaces. Further, a simple approach suitable for recognition of large number of metal ions with ultra high sensitivity (ppb level) and selectivity using response-stimuli magnetic nanoemulsion is also explored.

## 3.2 Experimental Methods

### *3.2.1 Materials*

Magnetic nanoemulsions, *ESD0.8* and *EPVA115* are used in this study. Material preparation and experimental setup are detailed in *Chapter II*.

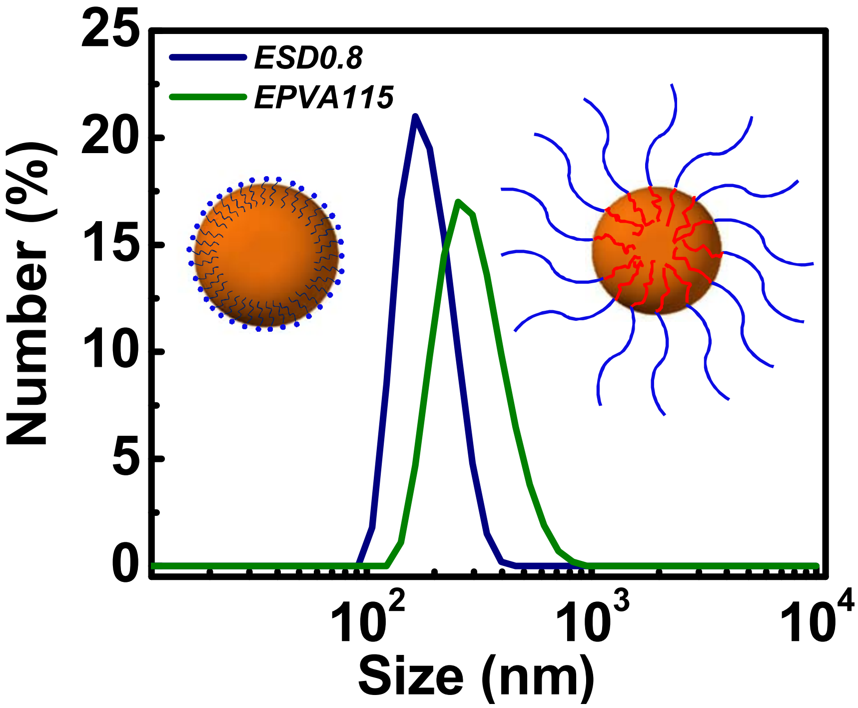

**Figure 3.1** Hydrodynamic size distribution of magnetic nanoemulsions *ESD0.8* and *EPVA115*. Inset of the figures shows the schematic of a droplet with adsorbed surfactant molecules and diblock co-polymers. The average hydrodynamic diameter of *ESDS0.8* and *EPVA115* nanoemulsions are ~164 and ~255 nm, respectively. The corresponding zeta potential values are  -41 and -1.8 mV, respectively.

**Fig. 3.1** shows the hydrodynamic size distribution of the magnetic nanoemulsions *EDS0.8* and *EPVA115*. The inset of the **Fig. 3.1** shows the schematic of the droplet with adsorbed surfactant and diblock co-polymer. The hydrophobic (vac) part of the polymer prefers to remain inside the oil droplet, while the hydrophilic PVA part protrudes into the solvent to form a diffuse polymer layer. The average hydrodynamic sizes of *EDS0.8* and *EPVA115* emulsions are found to be 190 and 255 nm, respectively and the corresponding zeta potential values are -41 and -2 mV, respectively. The negative zeta potential value in the case of *ESD0.8* emulsion indicates the presence of negatively charged head groups ($SO_4^-$) at the oil-water interface. For *EPVA115* emulsion, the very small value of zeta potential (-1.8 mV) indicates the presence of slight residual surface charges on the droplets, irrespective of repeated washing.

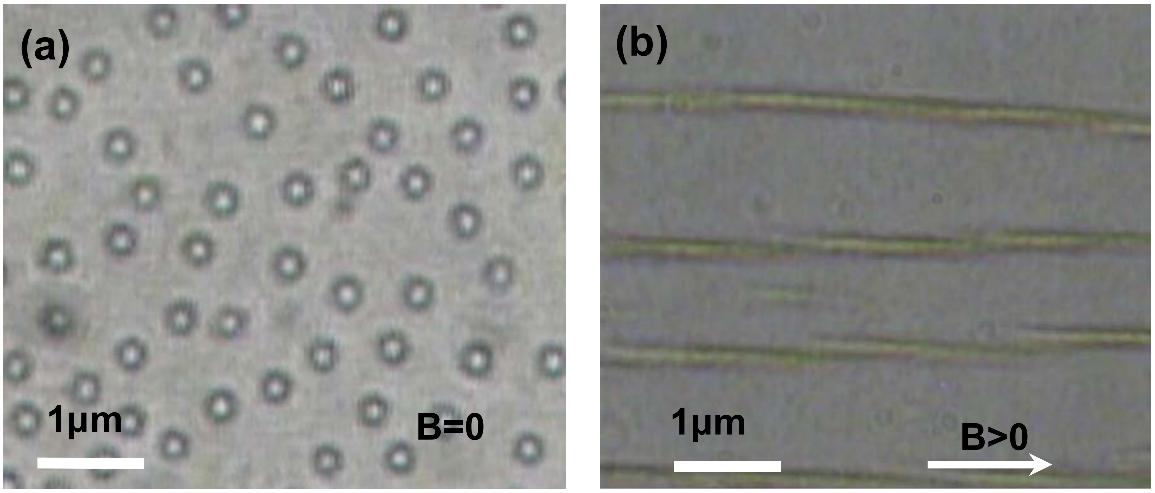

**Figure 3.2 (a &b)** Optical phase contrast microscopic images of emulsions without and with an applied magnetic field, respectively. The arrow indicates the applied magnetic field direction.

**Fig. 3.2 (a & b)** shows the microscopic images of emulsions without and with an applied magnetic field, respectively.

## 3.3 Results and Discussion

### 3.3.1 Effect of Cations on 1D Droplet Array Spacing

**Electrostatically Stabilized Emulsions**

To study the effect of interfering cations on the diffraction peak, 200 µl of the emulsion is taken in a cuvette or a cylindrical vial (1ml capacity) and is placed inside a small solenoid coil which is powered by a programmable direct current power supply. At a fixed magnetic field strength of ~90 Gauss, the sample is illuminated with a fiber optic based light source and the color of the sample is recorded at different concentrations of ions at the same magnetic field strength. For quantitative measurement, the reflected Bragg peak from the sample at 180 ° is measured using a fiber based reflection probe. At this external field, magnetic dipole moments are induced in the oil droplets due to the alignment of the nanoparticles inside the droplet. The strength of the dipolar interaction is given by the coupling constant, [25]

$$\Lambda = \pi\mu_0 a^3 \chi^2 H_a^2 / 6k_B T \tag{3.1}$$

where, '$a$' is the droplet radius, '$\chi$' is the magnetic susceptibility, '$H_a$' is the external magnetic field and '$k_B T$' is the thermal energy. When the repulsive forces (electrostatic + steric) balance the field induced dipolar attraction, the droplets form one dimensionally ordered structure along the field direction. As the particle size is of the order of the wavelength of visible light, each chain forms a lattice that diffracts light in the visible range and the scattered light from each particle in the chain thus interferes constructively. The interdroplet separation *'r'* for perfectly aligned droplets is related to the first order Bragg condition (for 180° diffraction geometry) is given by **Eqn. 2.5**.

For metal ions of different concentrations, the corresponding diffraction peak is recorded using a fiber optic spectrometer. The Bragg peak without metal ions is taken as the reference peak. The shift in the peak wavelength with respect to the reference peak is called Bragg peak shift ($\Delta\lambda_{peak}$). For qualitative measurements, in all the cases magnetic field is kept constant at 90 gauss and the diffraction peak is measured at 180° diffraction geometry. Under application of static magnetic field, cations of different concentrations were added, which results in the diffraction peak shift towards lower wavelength. The change in the diffraction peak wavelengths with different metal cations of $K^+$, $Co^{2+}$, $Mn^{2+}$, $Cu^{2+}$, $Ni^{2+}$, $Pb^{2+}$, $Cd^{2+}$, $Ag^+$ are recorded and the shift in the peak wavelength is calculated in each case is shown in **Table 3.1**.

**Fig. 3.3a** shows the Bragg reflection spectra of an *ESD0.8* nanoemulsion at various $Ag^+$ concentrations ranging from 0 to 525 ppb. In the absence of added cations, the diffraction peak occurs at 705 nm. The arrow indicates the direction of increasing concentration of $Ag^+$. It is observed that the Bragg reflection peak ($\lambda_{peak}$) monotonically blue shifts with increasing $Ag^+$ ion concentration and the diffraction peaks are symmetric and narrow, inferring that the 1-D ordering is stable. **Fig. 3.3b** shows the $\Delta\lambda_{peak}$ as a function of $Ag^+$ concentration for *ESD0.8* nanoemulsion. In the concentration range of 26- 195 ppb, the observed linear slope value is 0.19 and above 195 ppb, the slope is 0.065. The higher slope indicates a better sensitivity and the slope change at the higher concentrations indicates the change in the sensitivity.

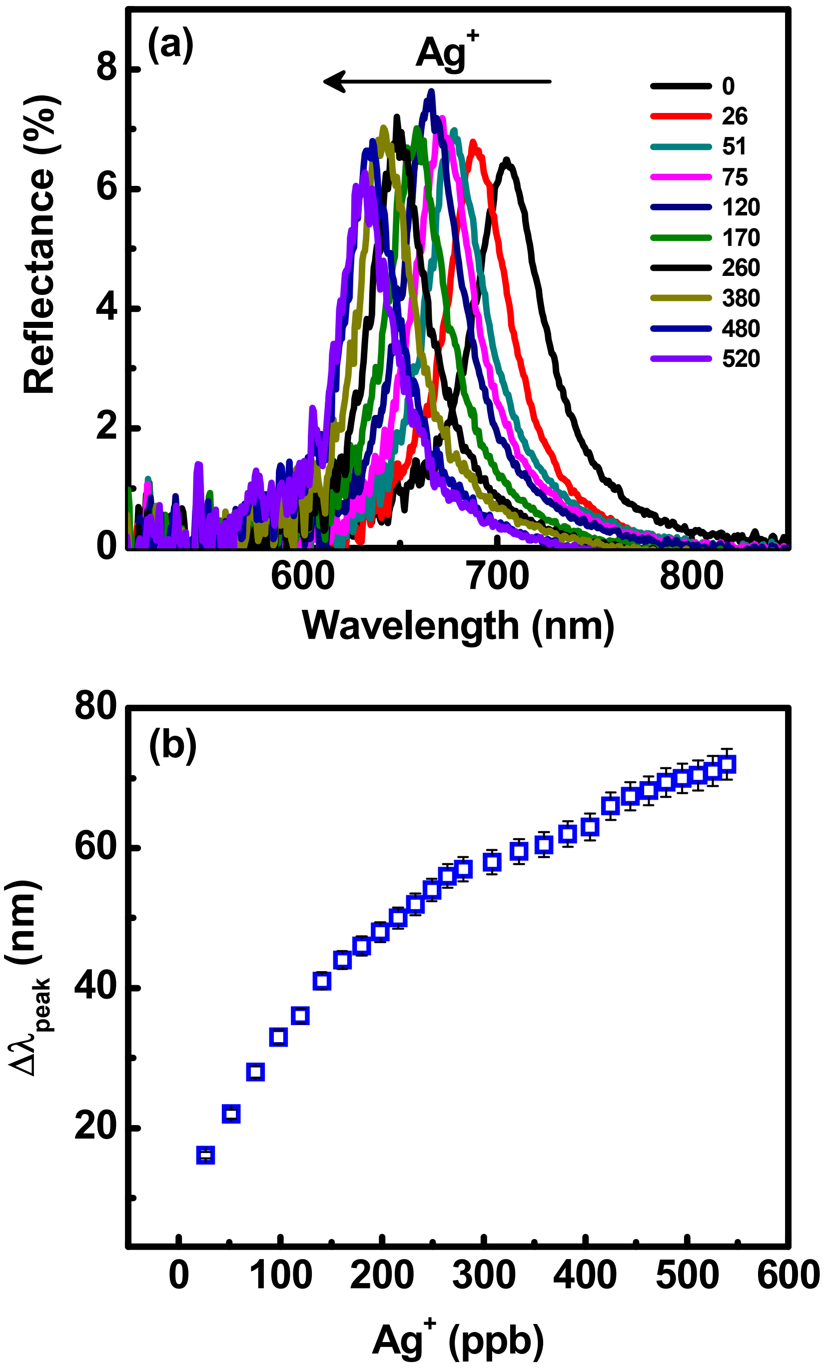

**Figure 3.3** (a) Reflection Bragg spectra of *ESD0.8* emulsion at different $Ag^+$ concentrations. The arrow indicates the direction of increasing $Ag^+$ concentration. (b) Bragg reflection peak wavelength shift ($\Delta\lambda_{peak}$) as a function of $Ag^+$ concentration for *ESD0.8* emulsion.

| Cations | Linear concentration range | Dynamic concentration range | Wavelength shift(nm) |
|---|---|---|---|
| $Na^+$ | 0-35 ppm | 0-400 ppm | 147 |
| $K^+$ | 0-40 ppm | 0-448 ppm | 146 |
| $NH_4^+$ | 0-520 ppm | 0-1500 ppm | 100 |
| $Ag^+$ | 26-195 ppb | 0-525 ppb | 73 |
| $Ca^{2+}$ | 5-35 ppm | 0-38 ppm | 85 |
| $Mn^{2+}$ | 5-30 ppm | 0-54 ppm | 101 |
| $Cu^{2+}$ | 1-14 ppm | 0-57 ppm | 83 |
| $Ni^{2+}$ | 2-16 ppm | 0-58 ppm | 98.6 |
| $Pb^{2+}$ | 8-49 ppm | 0-103 ppm | 97 |
| $Cd^{2+}$ | 0-1.6 ppm | 0-11 ppm | 31 |
| $Fe^{3+}$ | 4-14 ppm | 0-14 ppm | 54 |

**Table 3.1** Linear, dynamic concentration ranges and maximum shift in peak wavelength for different cations with *ESD0.8* emulsion.

**Table 3.1** presents the linear response range, where the peak shift changes linearly with cation concentration, and dynamic concentration (corresponds to the concentration range at which diffraction peak changes) for different cations along with the maximum peak shift measured.

### Sterically Stabilized Emulsions

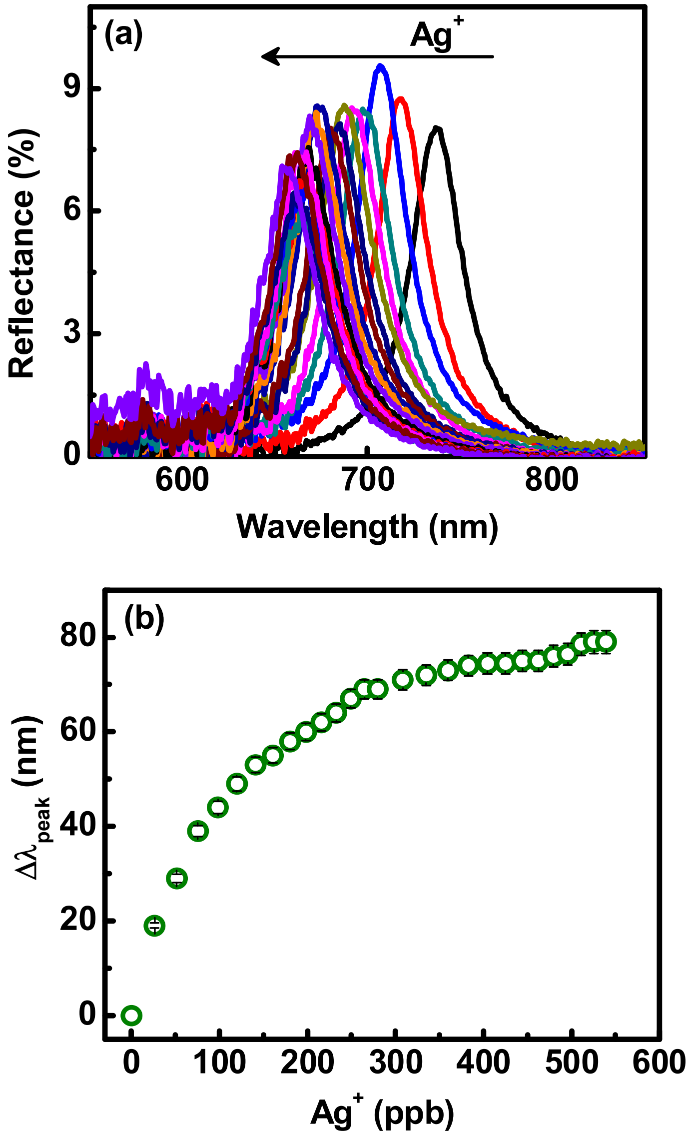

**Figure 3.4** (a) The Bragg reflection spectra of *EPVA115* emulsion at different $Ag^+$ concentrations. The arrow indicates the direction of increasing $Ag^+$ concentration. (b) $\Delta\lambda_{peak}$ as a function of $Ag^+$.

**Fig. 3.4a** shows the reflected Bragg peak observed for *EPVA115* emulsion at different $Ag^+$ concentrations. The arrow indicates the direction of increasing concentration of $Ag^+$. As observed in the case of SDS stabilized emulsion, the reflected Bragg peak monotonically blue shifts on increasing $Ag^+$ ion concentration. **Fig. 3.4b** shows the $\Delta\lambda_{peak}$ as a function of $Ag^+$. The inset shows the concentration range (20 - 124 ppb) where $\Delta\lambda_{peak}$ is linear. The slope of the linear fit and $R^2$ values are 0.32 and 0.97, respectively. Above 124 ppb, two different slopes are observed, one in the concentration range of 140 - 280 ppb, the second one for 300 - 490 ppb and the corresponding slopes are 0.123 and 0.031, respectively.

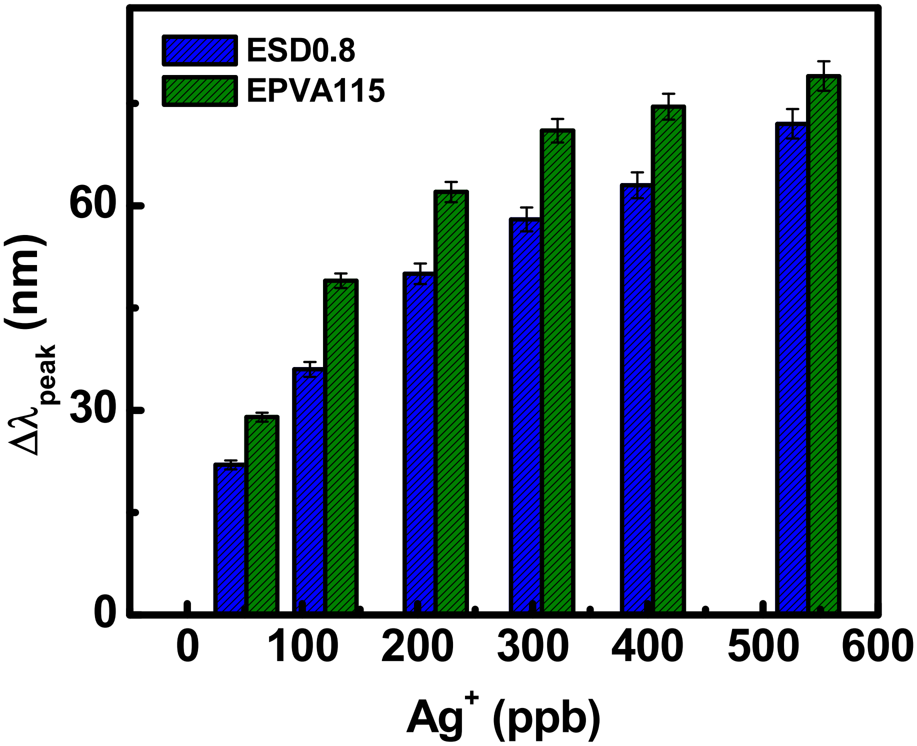

**Figure 3.5** Shift in diffraction peak ($\Delta\lambda_{peak}$) at different concentrations of $Ag^+$ for *ESD0.8* and *EPVA115* emulsions.

**Fig. 3.5** shows the $\Delta\lambda_{peak}$ at different concentrations of $Ag^+$ for *ESD0.8* and *EPVA115* nanoemulsions. The average $\Delta\lambda_{peak}$ value of *EPVA115* emulsion was ~ 12 nm greater than that of *ESD0.8*. This indicates that *EPVA115*emulsion has a higher sensitivity to $Ag^+$ as compared to *ESD0.8*. The possible reasons for the observed higher $\Delta\lambda_{peak}$ in *EPVA115* emulsion are discussed in intermolecular force measurement section.

### 3.3.2 Effect of Cations on the Interaction Forces

#### Interaction of Ag$^+$ with Electrostatically Stabilized Emulsions

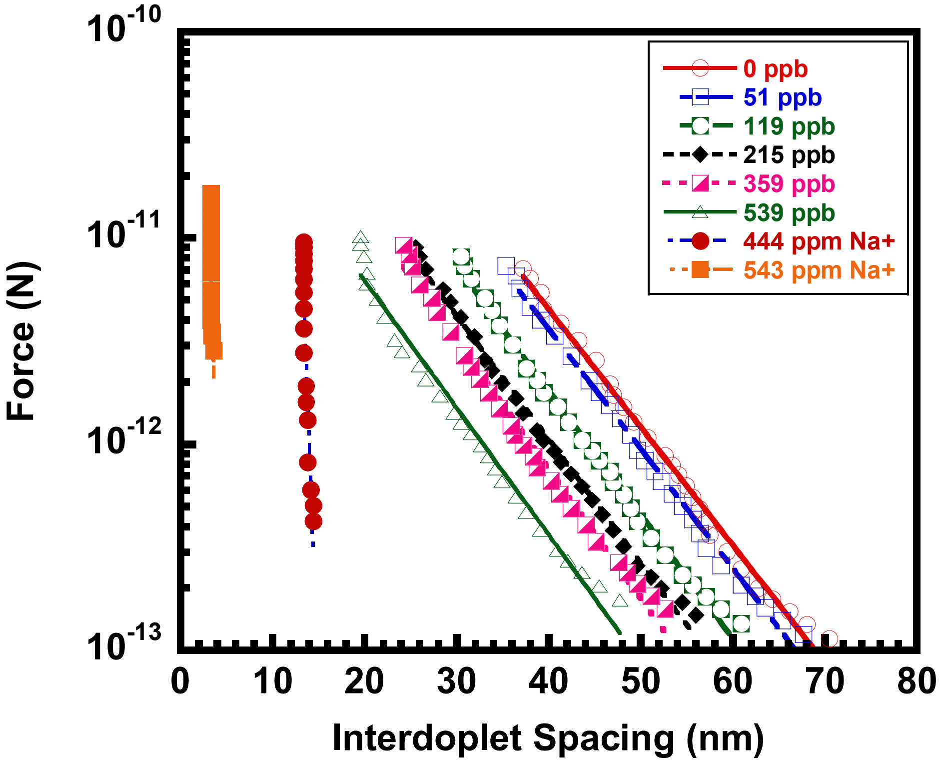

**Figure 3.6** Force–distance profiles at different Ag$^+$ concentrations for *ESD0.8* emulsion (scattered points). Solid lines correspond to fit using electrostatic double layer repulsion equation. For comparison, force distance profile measured at 444 and 543 ppm Na$^+$ also shown.

**Fig. 3.6** shows the force distance profile for SDS stabilized nanoemulsion at different Ag$^+$ concentrations. The contribution of Van der Waals attraction is also taken into consideration while calculating the net force between droplets.[116] The *ESD0.8* emulsions, without and with different $Ag^+$ concentrations show exponentially decaying repulsive force profiles. The decay length without $Ag^+$ ion was 7.6 nm. Owing to the amphiphilic nature, the SDS molecules adsorb at the droplet surface with the negatively charged head group exposed to water, thereby making the droplets negatively charged.

The co-ions with negative charge and the counter ions with positive charge form an electric double layer.[99] The chemical potential of counter ions in the solution is given by, $\mu = ze\psi + kT\log\rho$ where, '$\psi$' is the electrostatic potential, '*e*' is the electron charge, '*z*' is the valency of ions and '$\rho$' is the number density of ions at any point in the double layer. At lower surface charge densities the counter ion start to diffuse,[56] i.e., cations diffuse into a weak double layer which affect the strength of repulsion and the interdroplet spacing. According to electrical double layer theory, the repulsive force profile for $\kappa a < 5$ is given by **Eqn. 1.29**, and for thin electrical double layers with $\kappa a > 5$, the force profile is obtained via Derjaguin approximation where $\psi$ remains constant and independent of $h = r - 2a$, and is represented by **Eqn. 1.30**.[48] The best fit of the experimental data points using **Eqn. 1.30** is shown by the solid line in **Fig. 3.6**. From the force-distance profiles, we obtain three parameters: the first interaction length ($2L_0$) that corresponds to the interdroplet spacing at a force magnitude of $2.8 \times 10^{-13}$ N, the decay length ($\kappa^{-1}$) from the slope and the magnitude of force (K), which is dictated by the surface potential or the adsorbed polymer layer thickness. The variation of $K$, $\kappa^{-1}$ and $2L_0$ as a function cation concentrations are shown in **Table 3.2.** For $Ag^+$, the variation of $\kappa^{-1}$, $K$ and $2L_0$ as a function of $Ag^+$ concentration are shown in **Fig. 3.9.**

| Cations | Concentration (ppm) | K (nN) | $\kappa^{-1}$ (nm) | $2L_0$ (nm) |
|---|---|---|---|---|
| $Na^+$ | 11 | 12.6 | 6.49 | 67 |
| | 23 | 26.4 | 5.52 | 61 |
| | 46 | 37.1 | 4.95 | 54 |
| | 115 | 4.2 | 4.66 | 47 |
| | 230 | 0.195 | 5.37 | 43 |
| $K^+$ | 20 | 16.3 | 6.55 | 72 |
| | 39 | 22.4 | 5.9 | 67 |
| | 78 | 14.4 | 4.59 | 58 |
| | 195 | 1.07 | 5.14 | 51 |
| | 391 | 0.334 | 5.60 | 45 |
| $Ca^{2+}$ | 2 | 1.54 | 4.97 | 45 |
| | 3 | 2.62 | 4.59 | 41 |
| | 4 | 1.35 | 4.40 | 36 |
| $Mn^{2+}$ | 3 | 3.29 | 7.05 | 66 |
| | 6 | 4.56 | 6.2 | 60 |
| | 14 | 0.9119 | 6.25 | 50.5 |
| | 28 | 0.2869 | 6.49 | 45 |
| $Ni^{2+}$ | 1 | 4.60 | 6.99 | 70.5 |
| | 7 | 2.13 | 6.37 | 55 |
| | 17 | 1.83 | 5.73 | 48 |
| | 29 | 0.0811 | 7.27 | 44 |
| | 59 | 0.0252 | 5.90 | 37 |
| $Cu^{2+}$ | 3 | 7.63 | 7.20 | 73.5 |
| | 6 | 4.20 | 7.12 | 68.8 |
| | 16 | 3.8 | 6.63 | 62 |
| | 32 | 0.7533 | 6.65 | 55 |
| | 63 | 0.440 | 6.42 | 51 |
| $Fe^{3+}$ | 0.412 | 5.95 | 8.40 | 83.6 |
| | 0.82 | 7.43 | 7.95 | 80.8 |
| | 2 | 6.14 | 7.96 | 79.5 |
| | 4 | 7.73 | 7.66 | 78 |
| | 8 | 8.33 | 7.42 | 75.88 |

**Table 3.2** Debye lengths, force magnitude and onset repulsion for different cations measured as a function of cation concentration for *ESD0.8* emulsion.

The force-distance results suggest that the $Ag^+$ ions, even at very low concentration, screen the charges at the emulsion surface, probably through the formation of both Stern and diffuse electric double layers. The theoretical Debye length (**Eqn. 1.21**) for *ESD0.8* emulsion is 10 nm, which is in reasonable agreement with the value obtained from the best fit (~ 7.6 nm). The Debye length almost remains the same (~7.1 nm) for all the curves, irrespective of the concentration of $Ag^+$.

This is quite expected because the concentration of SDS was much higher compared to that of $Ag^+$ and hence the effective decay length is dictated by SDS ions. Calculation shows that the number of SDS and $Ag^+$ are 4.8 x $10^{20}$ and 3.0 x $10^{18}$ for 0.8 mM SDS, 539 ppb $Ag^+$, respectively. As the decay length remains almost constant, the bound stern layer contribution seems to play a prominent role in the charge screening process and hence the blue shift. The strong interaction between $Ag^+$ (a soft Lewis acid) and $RSO_4^-$ group of the surfactant is expected to cause abrupt changes in the magnitude of force. Such a strong association between soft acid and soft base is predicted by the Pearson's acid base theory.[117] The surface potential (calculated from the preexponential factor of the force distance profile) with different $Ag^+$ concentrations is varies from 14.11 to 4.9 mV. However, these values are much lower than the actual zeta potential measured. The reason for this discrepancy is yet to be understood. For comparison of decay length variation, the force profiles with 444 and 543 ppm of $Na^+$ ions are also included in **Fig. 3.6**. It can be seen that the force profiles show a hard sphere profile at high concentrations of $Na^+$ because of screening of surface potential. The three possible modes of interaction of SDS with $Ag^+$ ions are the direct binding of $Ag^+$ to SDS, hydrated $Ag^+$ sharing one water molecule with the SDS or $Ag^+$ interacting with the SDS via two water molecules (**Fig. 3.7a&b**).

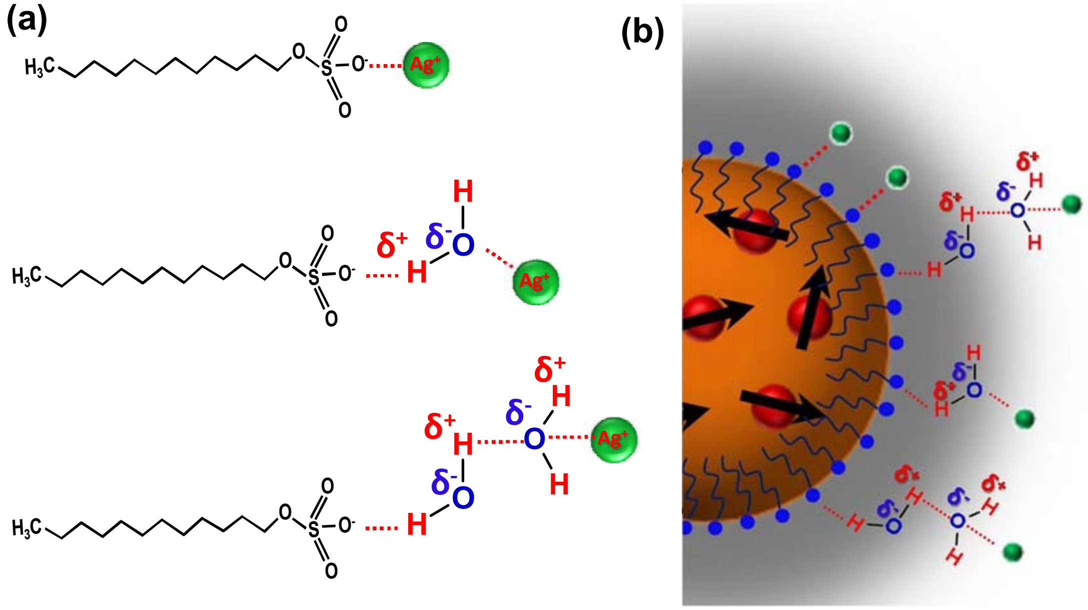

**Figure 3.7** (a) Three possible modes of interaction of $Ag^+$ and SDS: direct binding, binding through sharing of one water molecule and binding via sharing two water molecules (b) Schematic representation of SDS covered interface with $Ag^+$ and $H_2O$.

### Interaction of $Ag^+$ with Sterically Stabilized Emulsions

The force distance profiles (**Fig. 3.8)** of *EPVA115* nanoemulsion with different $Ag^+$ concentrations also show exponentially decaying nature. The zeta potential of *EPVA115* emulsion (-1.8 mV), indicates that, though not significant there are some residual charges at the oil interface even after the washing process. However, the observed decay length of 9.2 nm (comparable to the $R_g$ of polymer) clearly indicates that the droplet interface is covered by polymer where steric force is significant. Otherwise, the decay length would have been much higher. Without and with different $Ag^+$ concentrations, the repulsive force profiles are exponentially decaying. Here, the observed force profile arises from the repulsive osmotic force due to the unfavorable entropy associated with the compression of chains between the droplet surfaces.[56, 118]

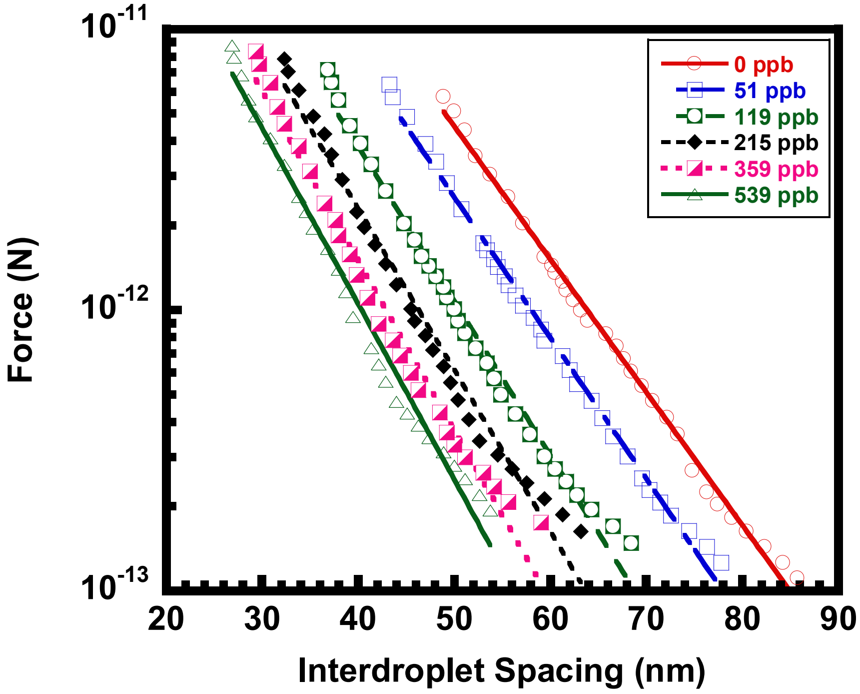

**Figure 3.8** Force – distance profiles at different $Ag^+$ concentrations for *EPVA115* emulsion. Solid lines correspond to the fit to the **Eqn. 1.37**.

According to Alexander-de Gennes equation[119-120] for polymeric brush bearing surfaces, the osmotic repulsion between the coils favors their expansion that can lead to an increase in $2L_0$ and the elastic stretch energy of the chains can favor a contraction or a decrease in $2L_0$. The steric forces are complex and depend on the surface coverage, nature of binding (physiadsorption or grafting with functional moieties) and the quality of solvent. In the present case, the physisorbed PVA coils bind reversibly at a number of points on the droplet interface where the adsorbed layers are highly dynamic and hence the measured forces can be time-dependent and history-dependent, approach or separation rate-dependent or hysteretic.[56] However, our studies shows that incubation over a period of more than 48 hrs is sufficient to achieve an equilibrium binding of the polymers where the force profiles are found to be time independent and non- hysteretic. Studies reveal various interesting scenario when polymer or surfactant or both interact with an interface.[121-122] The variations of $2L_{0,}$ characteristic decay length (*'$\lambda_d$'*) and K as a function $Ag^+$ concentrations for *EPVA115* (open symbols) are shown in **Fig. 3.9a-c.**

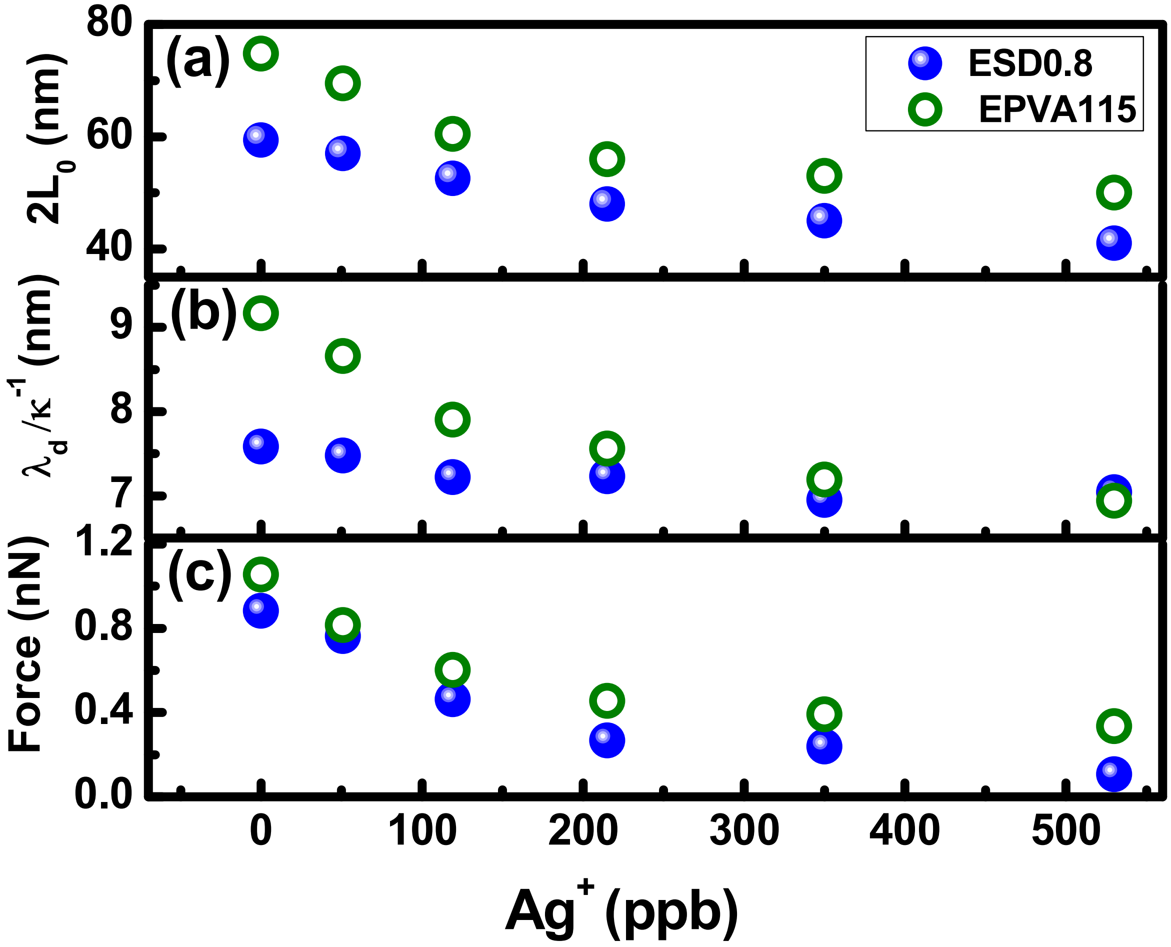

**Figure 3.9** (a) First interaction length ($2L_0$) (b) decay length ($\lambda_d$) or Debye length ($\kappa^{-1}$) and (c) magnitude of force (K) for *ESD0.8* and *EPVA115* emulsions as a function of $Ag^+$ concentration.

With the addition of 539 ppb of $Ag^+$, the $2L_0$ decreases from 72 to 52 nm and the magnitude of force falls by an order of magnitude from 5.9 to 0.59 nN. For polymer covered emulsion droplets, the force profiles are repulsive in nature and follow a simple exponential function as given by **Eqn. 1.37**. Without added cations, the observed '$\lambda_d$' value is comparable to the radius of gyration of a free polymer (~ 12 nm). At a distance larger than '$\lambda_d$', the concentration is dominated by the tails where the force is repulsive and decays exponentially with the distance. The increased osmotic pressure between the surfaces due to the overlap of adsorbed polymers leads to a repulsive interaction. It is known that the magnitude and range of steric forces can be many times of $R_g$ ( $>10R_g$ in aqueous solutions) due to high polymer surface coverage, higher Flory radius due to segment-segment repulsion (in good solvents), hydration layers or additional repulsive electrostatic interactions between charged segments.[123]

With increasing $Ag^+$ concentration, the decay length decreases marginally from 9.1 to 6.8 nm but the $2L_0$ decreases drastically from 74.8 to 50 nm. This shows a dramatic conformational change in the adsorbed polymer layer at the droplet interface. The decrease in the first interaction length indicates a collapse of stretched tail regions. Such a collapse is observed with the addition of salt in polyelectrolytes and under poor solvent conditions.[124] Further, the magnitude of the repulsive force decreases from 1.06 to 0.34 nN, as the concentration of $Ag^+$ is increased from 0 to 539 ppb. The mean field approach[42] distinguishes loops and tail sections in the adsorbed chains and involves the adsorbed layer thickness $\lambda$ and the adsorption length z* that separates the regions. The monomer concentration is dominated by loops, tails and a microscopic length '$b$' inversely proportional to the adsorption strength.

According to the mean field approach, in the strong adsorption limit ($\lambda/b>>1$), the adsorbed layer thickness is proportional to $R_g$ and weakly dependent on the adsorption strength and polymer concentration. At a distance larger than $\lambda$, the concentration is dominated by tails, and the force is expected to be repulsive and exponentially decaying.

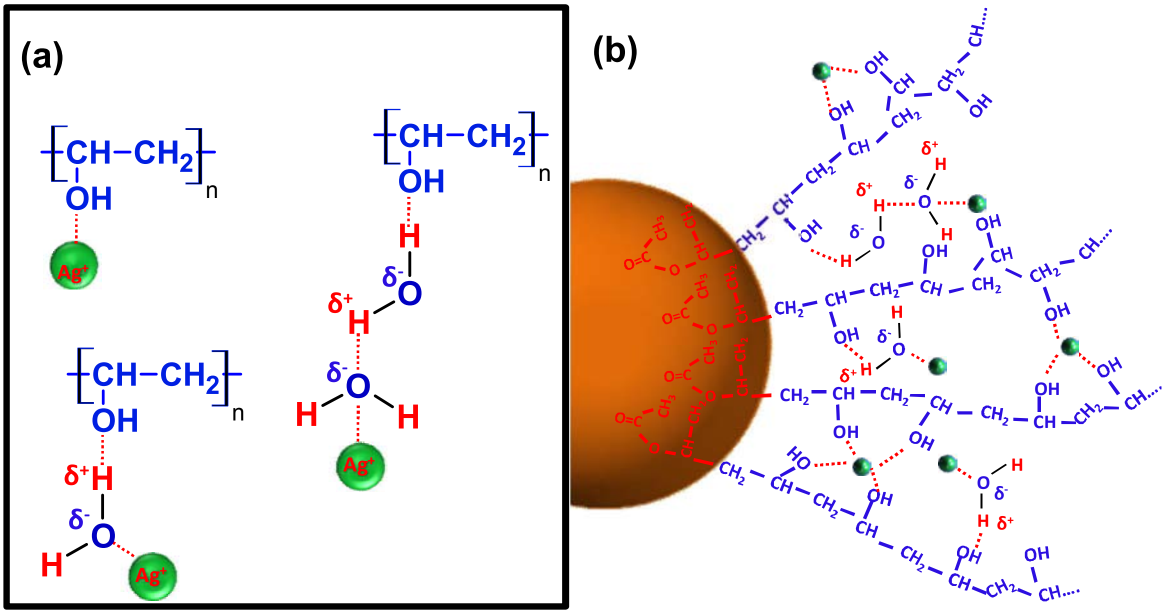

**Figure 3.10** (a) The possible interaction of OH of PVA and $Ag^+$ molecules and (b) Schematic of the conformation of PVA-$Ag^+$ at the droplet interface.

The interaction of cations with PVA-Vac can lead to three possible modes of interactions: the direct binding of cations to the oxygen in the PVA-Vac chains, hydrated cations sharing one water molecule with the polymer and cations interacting with the polymer via two water molecules.[125] The strongly hydrated $Ag^+$ is expected to bind with the hydrophilic part of PVA-Vac by changing the entropy of hydration of water around the polymer using one of the mechanisms discussed above. Three possible interactions of OH of PVA with $Ag^+$ are shown in **Fig. 3.10a**. **Fig. 3.10 b** shows the schematic of the conformation of PVA-$Ag^+$ at the droplet interface.

The variation of $2L_0$ in presence of $Ag^+$ in *ESD0.8* and *EPVA115* emulsion droplets are shown schematically in **Fig. 3.11a** and **b**, respectively. Molecular dynamics simulation study shows that the hydrated cations can be wrapped by seven oxygen atoms from three PVA-Vac chains due to the strong Coulombic attraction between cations and oxygen which tends to entangle or bridge segments of the chains together.[126-127] The observed dramatic reduction in the $2L_0$ value with increasing $Ag^+$ concentration is in line with the simulation predictions. The interaction of $Ag^+$ with the polymer by two water molecules in their first hydration shell, when compared to interaction via a single water molecule or direct interaction by $Ag^+$, is expected to cause maximum conformational changes in the adsorbed tail regions of the PVA, as shown schematically in **Fig. 3.11**.

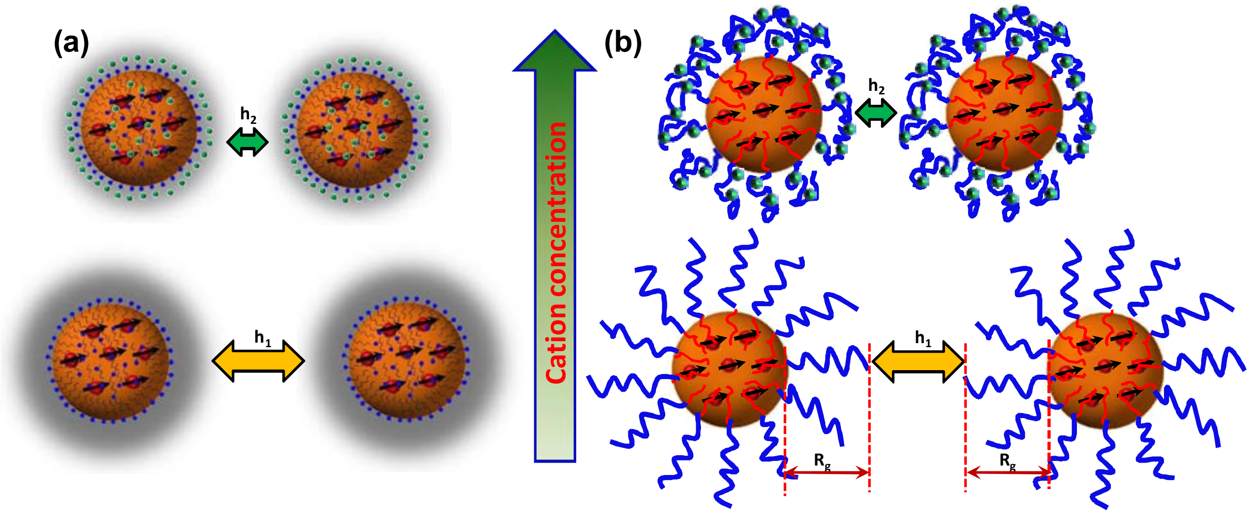

**Figure 3.11** Schematic representation of the interdroplet spacing variation in presence of $Ag^+$ (green spheres) for (a) *ESD0.8* (electric double layer is shown as shadow) and (b) *EPVA115* emulsion droplets and their conformations.

### 3.3.3 Potential Applications

The linear shift in the diffraction peak position measured at static magnetic field, with increasing concentration, in a certain concentration range which offers possibilities of magnetic nanoemulsion based cation detection in aqueous solutions. To check the sensitivity of the emulsion to other cations, $\Delta\lambda_{peak}$ measurements are carried out for *ESD0.8* emulsion with different cations. The $\Delta\lambda_{peak}$ variation is linear within certain concentration range for different cations. The linear $\Delta\lambda_{peak}$ concentration ranges for $K^+$, $Cu^{2+}$, $Ni^{2+}$, $Pb^{2+}$, $Cd^{2+}$ and $Ag^+$, are tabulated in **Table 3.1**. **Fig. 3.12a** shows the $\Delta\lambda_{peak}$ at 119.8 ppb of $Ag^+$ and 1ppm of other cations for SDS stabilized nanoemulsion. The larger $\Delta\lambda_{peak}$ for $Ag^+$ shows that the nanoemulsion has a better selectivity to $Ag^+$ when compared to other cations used. To further evaluate the effect of interfering cations on detectability of $Ag^+$, we have carried out experiments with a mixture containing $Ag^+$ and other cations (X) of higher concentrations. **Fig. 3.12 b** shows the $\Delta\lambda_{peak}$ for different $Ag^+$: X ratio of 539 ppb: 1 ppm. Without other interfering cations, for 539 ppb of $Ag^+$, the $\Delta\lambda_{peak}$ was ~ 70 nm. In the mixture with 1 ppm of $Pb^{2+}$, $Ni^{2+}$, $K^+$, $Cu^{2+}$, $Mn^{2+}$, $Na^+$, $Cd^{2+}$ and $Ca^{2+}$, the $\Delta\lambda_{peak}$ is 1.5, 1.6, 5.7, 7, 10, 12, 13 and 24 nm, respectively. Even with 1 ppm of the interfering cations, the $\Delta\lambda_{peak}$ remains nearly the same (~ 70 nm). This clearly demonstrates the ultrahigh sensitivity and selectivity of this approach for $Ag^+$ detection. Among various cations, the maximum sensitivity (Bragg peak shift) is observed for $Ag^+$ ions. All these cations come under the soft acid group, which are acceptor atoms with a low positive charge and large size with several easily excitable outer electrons. According to hard soft acid and base (HSAB) principle,[128] soft acids prefer to coordinate with soft bases because electrons can be transferred readily either in one or both directions to form a covalent bond. The increasing $\Delta\lambda_{peak}$ with the cations, followed the sequence $Pb^{2+} < Ni^{2+} < K^+ < Cu^{2+} < Mn^{2+} < Na^+ < Cd^{2+} < Ca^{2+} < Ag^+$. This trend can be partially understood on the basis of specific ion effects and the hydration of ions at interfaces.[129] $Ag^+$ is the softest acid among the studied cations and the next softer cation is $Cd^{2+}$. Therefore, the observed order is in accordance with HSAB theory.

The situation becomes more complex as the specific ion effects on physicochemical properties of aqueous processes follow an empirical trend.[130] Further, the extend of interaction in Hofmeister cations not only depend on their hydration ability but also on the difference in size, polarizability and effect on water structure. To the best of our knowledge, the range for $Ag^+$ in Hofmeister series is not reported in the literature. Hofmeister sequence for (as salting-out agents in colloidal suspensions) anions and cations follows $SO_4^{2-} > Cl^- > NO_3^-$ and $Na^+ > K^+ > Ca^{2+} > Ni^{2+} > Co^{2+}$, respectively.[131] However, the above cation sequence is not exactly followed in our case, probably because of the associated anions. Earlier molecular dynamics simulation and X-ray absorption spectroscopic studies reveal that the hydrated $Ca^{2+}$ cations can coordinate to oxygen atoms.[126] Further, it has also been shown that the solvated $Ca^{2+}$ ion can wrap several oxygen atoms from the adsorbing species due the strong Coulombic attraction between $Ca^{2+}$ ion and oxygen. $Ag^+$ being the softest acid, on the basis of this finding, a stronger interaction between the ions and oxygen from the PVA is anticipated, which would have resulted in a larger Bragg shift. Among the studied cations, $Ag^+$ and $Cd^{2+}$ are soft acids and $Pb^{2+}$, $Cu^{2+}$, $Ni^{2+}$ lies in the borderline and $K^+$, $Na^+$ are classified as hard acids. Therefore, the observed order is in accordance with HSAB theory.

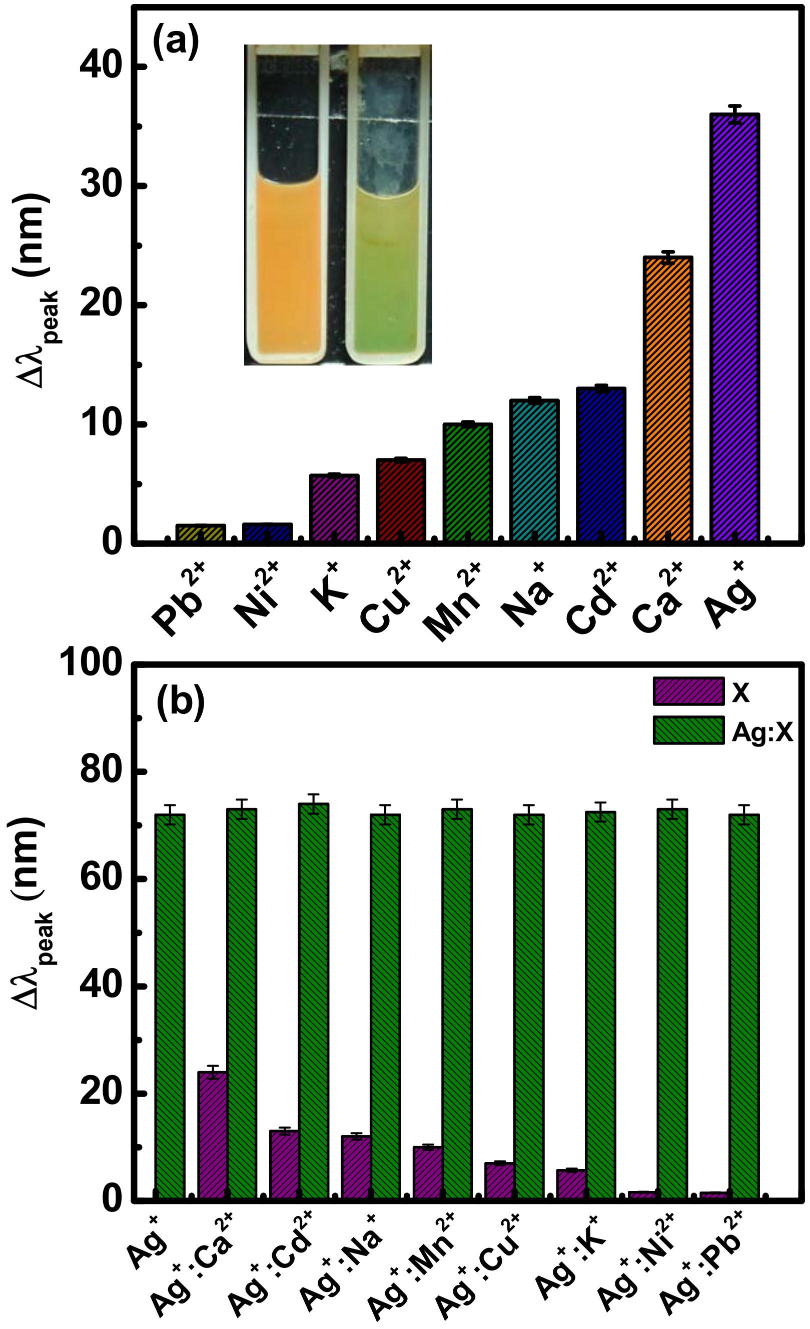

**Figure 3.12** (a) $\Delta\lambda_{peak}$ for *ESD0.8* emulsion at 119 ppb $Ag^+$ and for other cations at 1ppm. Inset shows photograph of the emulsion without (left) and with 119 ppb of $Ag^+$ (right). (b) $\Delta\lambda_{peak}$ for *ESD0.8* emulsion containing 539 ppb $Ag^+$ mixed with 1 ppm of different cations where X= $Ca^{2+}$, $Cd^{2+}$, $Na^+$, $Mn^{2+}$, $Cu^{2+}$, $K^+$, $Ni^{2+}$, $Pb^{2+}$.

**Response Time**

The emulsion exhibits another interesting property of time independent response, which is evident from the response at different time interval at an applied field strength of 90 G (**Fig. 3.13**). The black line shows the response without magnetic field. It is observed that the response time is ~ a second. The reduction in the intensity of the Bragg peak with time is probably due to increase in temperature of the sample, due to the heat generated by the solenoid on prolonged application of field, which enhances the Brownian motion of the droplets. The Bragg peak wavelength shift over the observation time is within 1 nm.

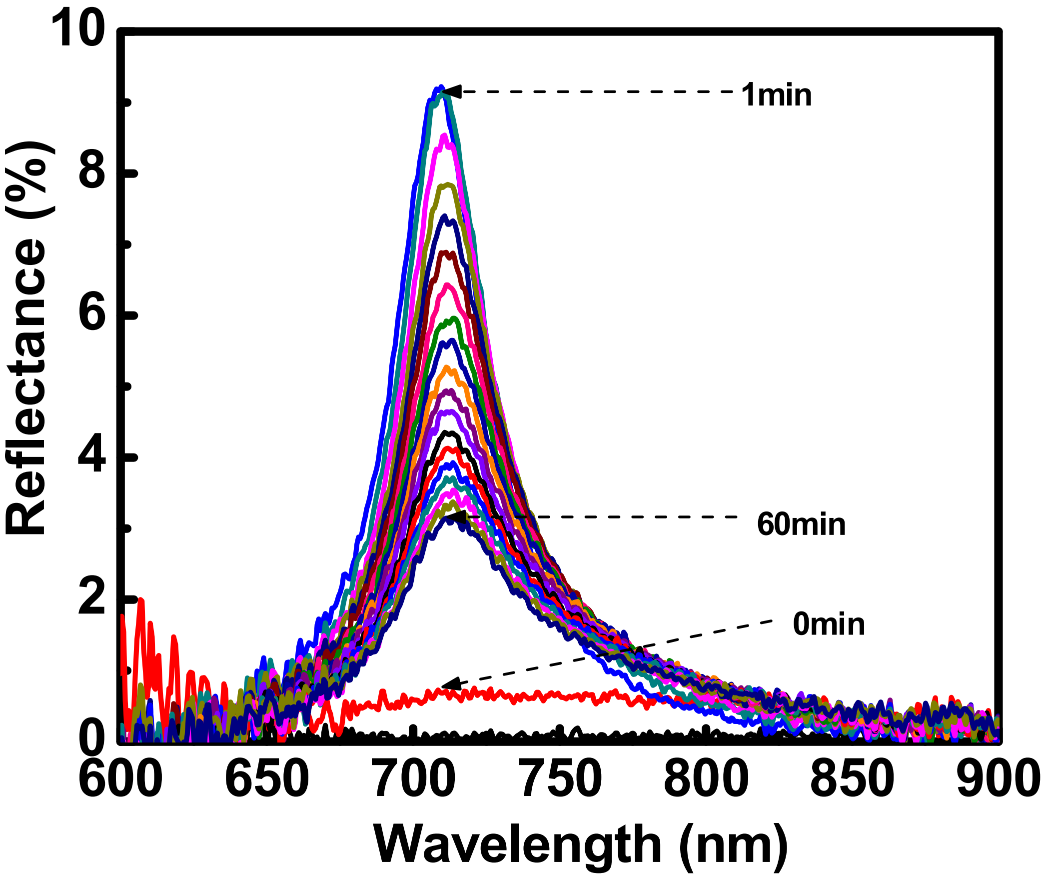

**Figure 3.13** Bragg peak at different time for *ESD0.8* at applied field strength of 90 G.

## 3.4 Conclusions

The effect of cation interaction on 1-Dimensional interdroplet array spacing and the electrostatic and steric forces between stimuli-responsive nanoemulsions are studied. A large blue shift in the diffracted light because of the reduction in the interdroplet spacing in the presence of interacting $Ag^+$ is observed. The order of increase in the Bragg peak shift for different cations followed a sequence $Pb^{2+} < Ni^{2+} < K^+ < Cu^{2+} < Mn^{2+} < Na^+ < Cd^{2+} < Ca^{2+} < Ag^+$. The in-situ equilibrium force-distance measurement results suggest that the $Ag^+$ ions screen the charges at emulsion surface through the formation of both Stern and diffuse electric double layer, and produce a dramatic blue shift. In the presence of interfering cations, emulsion shows excellent selectivity for $Ag^+$ due to strong interaction of hydrated $Ag^+$ with surfactant/polymer, which offers the possibility of selective detection of $Ag^+$. With *ESD0.8* and *EPVA115* emulsions, the linear dynamic detection ranges for $Ag^+$ detection are 50 -175 ppb and 24-124 ppb, respectively. The possible mechanisms of interaction of $Ag^+$ with surfactant and polymer are discussed.

# Chapter- IV

## Interaction of Alcohol with Surfactant Stabilized Emulsion and its Consequence on Interaction Forces

# 4

# Interaction of Alcohol with Surfactant Stabilized Emulsion and its Consequence on Interaction Forces

## 4.1 Introduction

Colloidal interactions are strongly influenced by the addition of alcohols. Ion-solvent complex interactions between the ions with increasing alcohol concentration can amplify the ion-specific effects.[132] Electrostatic interaction in the charged colloidal system determines the life time of the dispersion. The electrostatic interaction can be tuned by either addition of salt or the addition of organic solvents to the aqueous solutions. For instance, by the addition of ions extended double layer decreases because of the electrostatic screening effects of the added ions.[37] When organic solvents are added to aqueous solutions, the dielectric constant of solvent is reduced and therefore the extend of counterion condensation increases upon the addition of organic solvents to aqueous solutions.[133] It has been reported that the cation specific conformational behavior of polyelectrolyte brushes, specific ions effects or Hofmeister effects etc. can be amplified by alcohols.[132-135] Most of the studies were on the effect of methanol on the polymer or polyelectrolyte conformations and the counterion condensation, and the specific ion effects in the bulk solution.[132, 134-137] The role of methanol on the electrostatic interactions between surfactant stabilized emulsions is not attempted.

Here, a systematic study has been carried out on the interaction of methanol with anionic surfactant stabilized emulsion by magnetic chaining technique. Upon changing the alcohol molecular concentrations, visually perceptible color changes in the emulsions occurs due to red-shift of the diffraction peak wavelength in the presence of a static magnetic field. New insights into the mechanism of red shift from the measurement of intermolecular forces in presence of methanol molecules are obtained.

## 4. 2 Experimental Methods

Magnetic nanoemulsion, *ESD0.8* is used in this study. The average hydrodynamic diameter and the corresponding zeta potential values of SDS stabilized emulsions are 200 nm and -41 mV, respectively. The intermolecular interactions for different methanol concentrations were measured by magnetic chaining technique. Material preparation, experimental setup for force measurements are detailed in *Chapter II*.

## 4.3. Results and Discussion

### 4.3.1 Effect of Methanol on 1D Droplet Array Spacing

To study the effect of methanol on 1-D array spacing, diffraction peaks are measured as discussed in **3.3.1.** The Bragg peaks measured for *ESD0.8* emulsion at different methanol concentrations starting from 0 to 5000 ppm is shown in **Fig. 4.1**. The Bragg peak monotonically red shifts with increasing concentrations of methanol, as shown by the arrow. The diffraction peaks are fairly symmetric and narrow in all the cases, which indicate a stable 1-D ordering of the droplets in the presence of methanol molecules.[36, 39] As discussed in **3.3.1,** the origin of diffraction peak can be explained by Bragg's law.

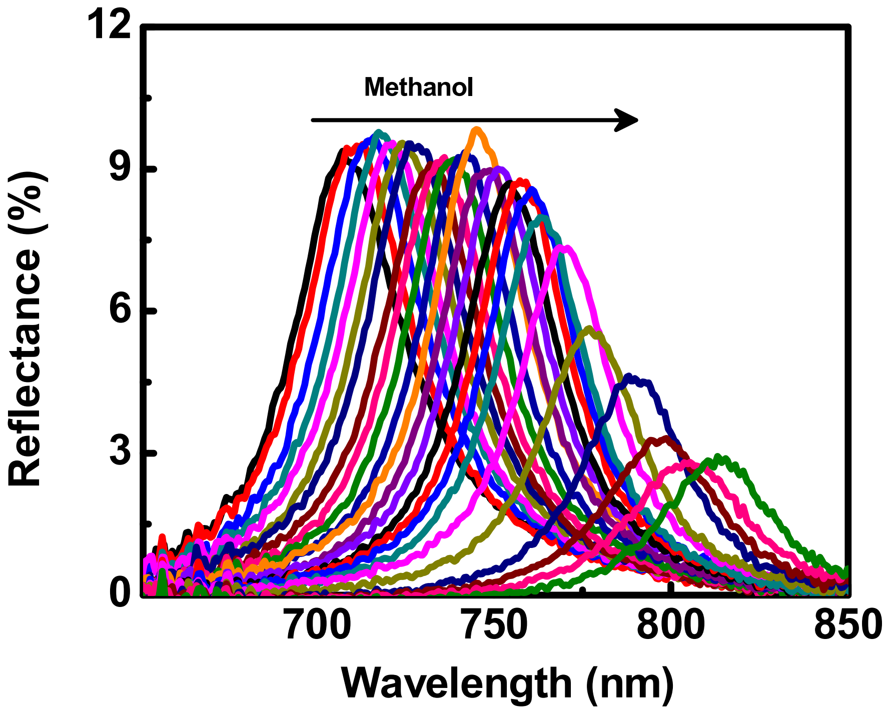

**Figure 4.1** Effect of methanol on the Bragg peak. The arrow indicates the increase in methanol concentration.

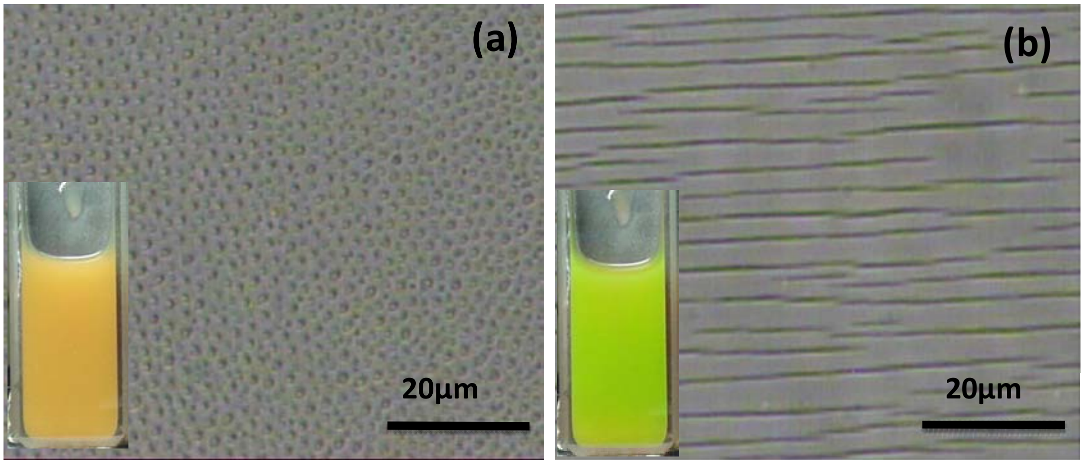

**Figure 4.2** Phase contrast optical microscopic images of droplets (a) without magnetic field show Brownian droplets and (b) with magnetic field show aligned droplets in 1-D respectively. (Inset) The photographs of emulsion under identical conditions show different colors in the emulsions.

In the presence of magnetic field, a 1-D droplet array forms along the field direction as shown in the **Fig. 4.2. Fig. 4.2 (a & b)** shows the phase contrast optical microscopic images of the droplets without and with magnetic field respectively. The former shows Brownian droplets, while the latter shows aligned droplet array in 1-Dimension.

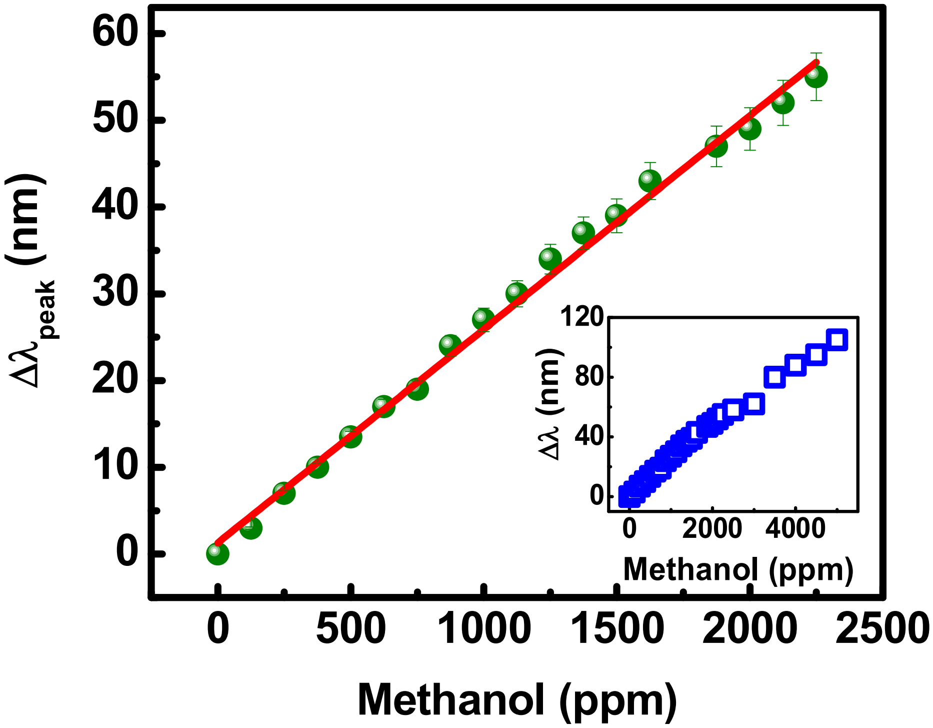

**Figure 4.3** Bragg peak wavelength shift as a function of methanol concentrations. Linear response concentration range (0-2250 ppm) is shown as scattered points and the solid line shows the linear fit with $R^2$ value of 0.99447. The inset shows the full concentration range. The quality ($R^2$) of the linear fit is found to be 0.99447.

**Fig. 4.3** shows the Bragg peak shift as a function of methanol concentrations. The Bragg peak shift was monotonic and linear in the concentration range of 0-2250 ppm, above which a slight change in the slope is observed. The Bragg peak shift for the entire concentrations range is shown in the inset of **Fig.4.3**. The shift in the diffraction peak was 3.5 nm as the concentration is increased from 0 to 125 ppm. The corresponding increase in the interdroplet spacing was 1.5 (± 0.2) nm. For 5000 ppm, the peak wavelength shift was 105 (± 0.2) nm.

### 4.3.2 Effect of Methanol on the Interaction Forces

To obtain insight into the observed red-shift, interdroplet force measurements are carried out in the presence of methanol of different concentrations. **Fig. 4.4** shows the inter-droplet force-distance profiles in the presence of methanol of 0, 125, 500, 2500 and 5000 ppm. The experimental data are fitted with **Eqn.1.30,** and $2L_0$, $\kappa^{-1}$ and K values are extracted.

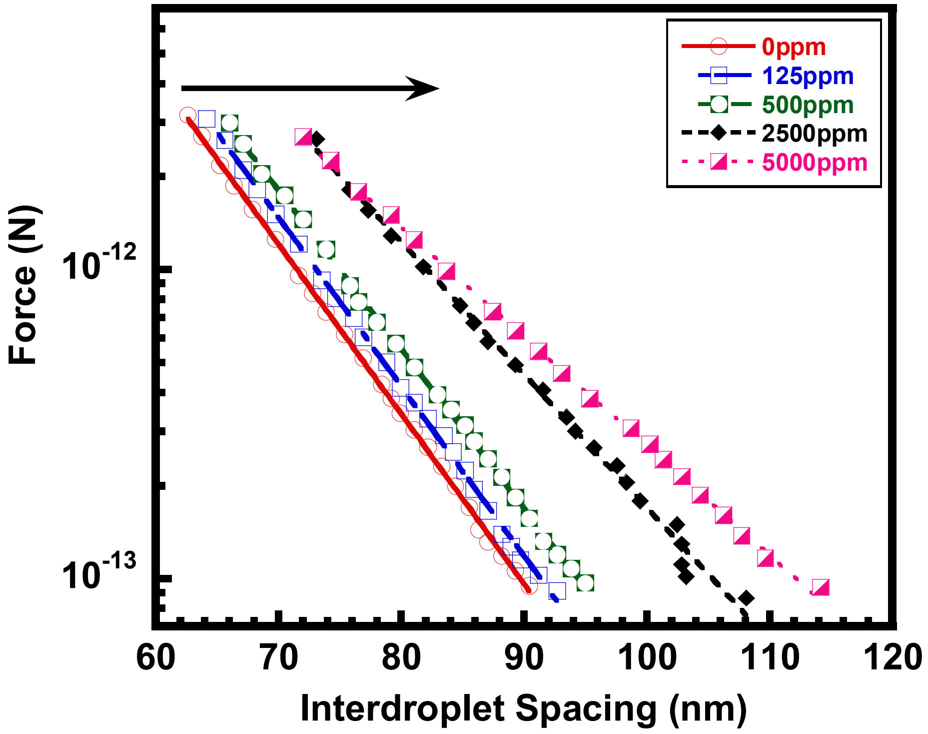

**Figure 4.4** Force-distance profiles in the presence of methanol of four different concentrations, 0, 125, 500, 2500 and 5000 ppm. The arrow indicates increase in methanol concentration.

In all the four concentrations, the force profiles were exponentially decaying with the inter-droplet spacing. The $2L_0$ for the concentrations 0, 125, 500, 2500 and 5000 ppm are 81, 83, 85, 94 and 98.7 nm, respectively. The decay length increases from 7.9 to 12.3 nm as the concentration of methanol increases and the force magnitude decreases by an order from 8.5 to 0.9 nN.

The exponential scaling obtained on the experimental force profiles reaffirm that the forces between the emulsion droplets is electrostatic in nature. The observed profile mimic the hydrophobic forces measured between two macroscopic curved mica surfaces in water using surface force microscope where the force profile was found to be exponentially decaying with distance in the range of 4-10 nm with a decay length about 1 nm.[138] The magnitude of the hydrophobic force needed to separate the two molecules (of diameter 0.57 nm) from contact is found to be ~15 pN. Of course, in our case, the magnitude was 3-4 orders high, owing to the larger size droplets. The short range repulsions between the surfaces in water can also occur due to alteration of its properties such as diffusivity and dielectric constant near the interface.[139] The variations in the diffusivity and dielectric constant in the presence of alcohol molecules might have caused the changes in the onset of repulsion. Such short range interactions leads to interesting phase behavior in dispersions.[140] For two approaching particles, the force profiles are indeed affected by the dynamics of association process between the counterions and the interacting species. Besides the structuring of water at a hydrophobic surface in the presence of alcohol molecules, directional binding of molecules could also affect the onset of repulsion.[141] A recent sum frequency study on oil-in-water emulsions, stabilized with sodium dodecyl sulfate, show that the oil molecules predominantly oriented parallel with respect to the plane of the interface and the SDS alkyl tail forms a disordered state partially in contact with water.[142] Systematic computer simulation studies may shed more light into this aspect. **Table 4.1** summarizes the force measurement results. The concentrations of methanol, K, $2L_0$, Debye length, Bragg peak wavelength and inter droplet spacing are tabulated.

| **Concentration (ppm)** | **K (N)** | **$2L_0$ (nm) (± 1)** | **$\kappa^{-1}$ (nm)** | **$\lambda_{peak}$ (nm)** | **h (nm) (± 1)** |
|---|---|---|---|---|---|
| 0 | $8.5532 \times 10^{-9}$ | 81 | 7.89 | 730 | 84.4 |
| 125 | $1.0121 \times 10^{-8}$ | 83.4 | 7.92 | 736 | 86.7 |
| 500 | $7.2566 \times 10^{-9}$ | 85 | 8.4 | 746 | 90.45 |
| 2500 | $3.3992 \times 10^{-9}$ | 94 | 10.1 | 786 | 105.5 |
| 5000 | $9.1949 \times 10^{-10}$ | 98.7 | 12.3 | 823 | 119.4 |

**Table 4.1** Effect of methanol on interdroplet interactions. Concentration of methanol, magnitude of repulsive force, the first interaction length ($2L_0$), Debye length, Bragg peak wavelength and inter droplet spacing.

Our results show that an increase in the concentration of methanol molecules increases the $2L_0$ values by several nanometers, which results in a red shift of the Bragg peak. Though large change in the double layer is evident from the $2L_0$, the change in the decay length was not significant in the concentration range studied. Probably this is due to the failure of Poisson-Boltzmann theory at a small inter-particle spacing due to ion-correlation effects, finite ion size effect, image forces, discreteness of surface charges and solvation forces.[143-144] The Poisson-Boltzmann (PB) method becomes asymptotically exact in the limit of weak surface charges, low counter-ion valency and high temperature. However, the PB approach fails for multi-valent ions and for highly charged surfaces due to correlated ion-density fluctuations and the additional non-electrostatic interactions between ions and the surfaces. Therefore, the force between charged surfaces in electrolyte solutions is highly ion specific. The liquid molecular structure and hydration effects can also play an important role in the effective forces.[145] The interaction of the hydroxyl group of alcohol molecules with the amphiphilic DS (-) ions of sodium dodecyl sulfate (SDS) at the droplet interface induce changes in the intermolecular forces. Here, the electrostatic interaction remains dominant at the larger interdroplet spacing compared to the forces due to hydrogen bonding, dipolar, and dispersion forces between molecules.[141, 146]

### 4.3.3 Proposed Interaction Mechanism

**Fig. 4.5** shows the schematic representation of the emulsion droplets with increasing concentrations of alcohol. The drops containing aligned nanograins of iron oxide nanoparticle are shown in the core. The droplets are adsorbed with a monolayer of surfactant where the polar head groups reside at the interface while the hydrophobic alkyl chains reside inside the oil droplets. The diffused double layer around the nanodrops is shown by the blue circle. The addition of alcohol leads to changes in the double layer conformation, resulting in an increase in inter-droplet spacing or red shift. The change in the double layer with different alcohol concentration is shown in a red shade. The arrow indicates the increasing methanol concentration. The diffraction peaks measured at respective conditions are shown along with the schematic representation of each condition.

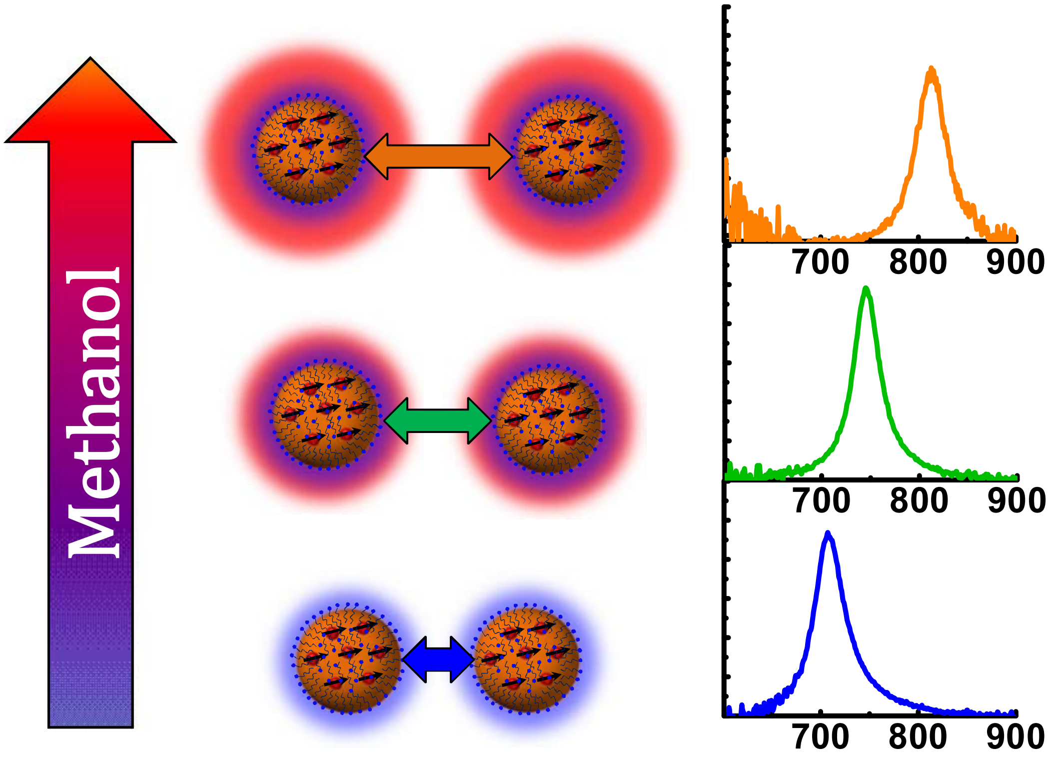

**Figure 4.5** schematic representation of emulsion droplets with increasing concentrations of alcohol. The arrow indicates increasing concentration of alcohols. The drops containing aligned nanograins of iron oxide nanoparticle are shown in the core. These droplets are stabilized with a monolayer of surfactant, where the polar head groups reside at the interface while the hydrophobic alkyl chains reside inside the oil droplets. The diffused double layer around the nanodrops is shown by the blue circle. The addition of alcohol leading to changes in the double layer conformation and this is shown in a red shade, resulting in an increase in inter-droplet spacing or red shift.

The large red shift in the diffraction peak wavelength with increasing methanol concentrations offers an optical sensing methodology for methanol detection in aqueous solutions. The typical time scale[84] for the typical Brownian and Neel relaxation times for 200 nm size droplets in water are ~ 3 ms and 1 ns respectively. Therefore, nano-emulsion based optical sensor offers rapid response compared to other sensors. The variation in the Bragg peak intensity as a function of time for the sensor with methanol at 90 G shows the peak formation within 1 second. The peak position remains stable for a long time (more than1 hr), which indicate the stability of the sensor. A small reduction in the Bragg peak intensity with time is observed, which is due to the increase in the sample temperature on prolonged application of field that enhances the Brownian motion of the droplets and their colliding frequency.

## 4.4. Conclusions

The effect of methanol on the 1-D droplet array spacing in a static applied magnetic field and the role of methanol on the electrostatic interactions are studied by magnetic chaining technique for the first time. Upon increasing methanol concentrations, the inter-droplet spacing of the 1-D droplet array produces a red shift in Bragg peak. The measurement of intermolecular forces in the presence of methanol molecules shows that the diffusion of organic molecules into the electric double layer and reduction of the net dielectric constant of water results in extended electrical double layers and a large red shift in the diffracted Bragg peak. Our results suggest that this approach is useful for measuring methanol concentration in aqueous solution in a dynamic range of 0- 2250 ppm within 1 second. Force measurement results show that the nature of interaction of the alcohol molecules with the hydrophobic interfaces in presence of charged surface active species has important implications in the self assembly of soft systems.

# Chapter- V

## Interaction of Glucose with Electrostatically Stabilized Magnetic Nanoemulsions and a Novel Application of Magnetic Nanoemulsions

# 5

# Interaction of Glucose with Electrostatically Stabilized Magnetic Nanoemulsions and a Novel Application of Magnetic Nanoemulsions

## 5.1 Introduction

There has been an increasing demand for the selective and sensitive detection methodologies for monitoring glucose levels in body fluids, food products and biochemistry.[147] The normal glucose level in human body is 4.2-6.4 mM and for diabetes mellitus it is above 7.0 mM. An elevated urine glucose concentration indicates a familial renal hyperglycemia[148] or diabetes mellitus. Over the years, several methodologies have been developed for glucose detection, of which most of them are based on glucose oxidase coupled to electrochemical system where the response depends on enzyme activity or glucose mass transport.[149-147] Some of the recent techniques are based on 3D Graphene-cobalt oxide electrodes,[150] platinum-cobalt (PtCo) bimetallic alloy nanoparticles decorated graphene,[151] dielectric properties of polymers,[152] surface plasmon resonance,[153] zinc oxide (ZnO) nanowires modified with gold (Au) nanoparticles,[154] three-dimensional porous sensing platform using nickel foam[10], copper sulphate (CuS) nanotubes[11] and opal closest-packing photonic crystals.[155] Most of the reported sensors are enzyme labeled.[149, 156-159] Two other issues with existing approaches that limit their practical applications are long response time and instrumentation. The notable optical sensing approaches are based on optical diffraction.[147, 160-161] Some of the drawbacks of optical methodologies are non-glucose specificity, long response time and pH dependence.[147] Towards exploring the use of nanoemulsion for glucose detection, the interactions of nanoemulsion with glucose of different concentrations are studied here.

Glucose is used in many food and pharmaceutical industries. The concentration of glucose in aqueous solutions largely influences the quality and shelf-life of final products.[162] Sugar plays important role in stabilization of biological structures and functions.[163-164] Some living organisms are able to survive in hostile environments such as extreme cold or drought conditions due to the secretion of carbohydrates.[165] Also, glucose is shown to be a promising candidate for structural modification of free-standing surfactant films owing to its capability to form hydrogen bonds.[166] There are also reports on the role of glucose in enhancing the stability of aqueous silica gels against dehydration.[165] Therefore, the interactions of glucose with colloidal dispersions are of fundamental interest too.

The present work is aimed to investigate the possible interaction of D-glucose with surfactant stabilized emulsions by equilibrium force measurements for better understanding the role of carbohydrates in colloidal stability. The influence of glucose on the electrostatic interactions as a function of glucose concentration is probed by force measurements. The effect of glucose on the 1D droplet array spacing is also studied at different D-glucose concentrations. Towards development of some practical applications, effort is also made to develop a label free (without boronic acid derivative and enzyme) glucose detection approach and a non-destructive optical sensor for detecting buried defects in ferromagnetic structures using magnetic nanoemulsions.

## 5.2. Materials and Methods

D-Glucose anhydrous with 99.9 % purity was purchased from E-Merck and used without further purification. The magnetically polarizable nanoemulsion used in the present study is *ESD0.8* and *ESD0.08*. Magnetic nanoemulsion preparation methods are discussed in *Chapter II.*

## 5.3 Results and Discussion

### 5.3.1 Effect of Glucose on 1D Droplet Array Spacing

To study the effect of glucose on the 1D array spacing, diffraction peaks are measured with different glucose concentrations by the same experimental procedure followed in **3.3.1.**

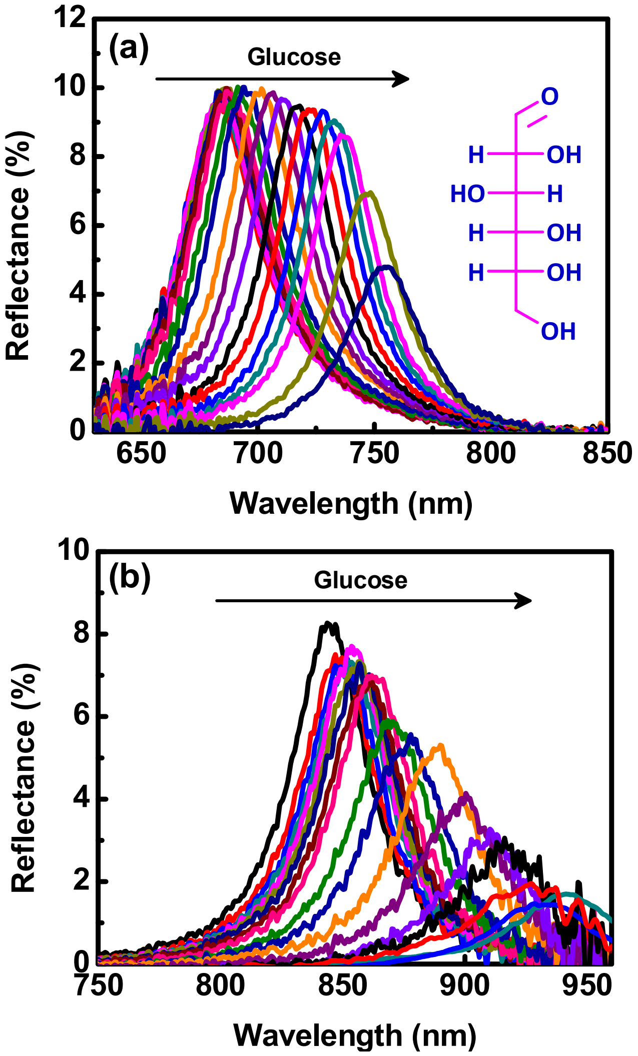

**Figure 5.1** The Bragg peaks at different D-glucose concentrations in (a) *ESD0.8* emulsion at an applied magnetic field strength of 81 G and (b) *ESD0.08* emulsion at 117 G. Arrow indicates increasing concentration of D-glucose form 243 μM – 25 mM. The inset of **Fig. 5.1(a)** shows molecular structure of D-glucose.

**Fig. 5.1a** shows Bragg peaks measured for different D-glucose concentrations starting from 1.2 to 30 mM at an applied magnetic field of 81 G for *ESD0.8* emulsion. The molecular structure of D-Glucose is shown in the insert of **Fig. 5.1a**. Without D-glucose, nanoemulsion shows a fairly symmetric diffraction peak ($\lambda_{peak}$), which shifts towards higher wavelength with increasing concentration of D-glucose. **Fig. 5.1b** shows spectral response of magnetic nanoemulsion stabilized with SDS at a lower concentration of 0.08 mM (*ESD0.08*) where the diffraction peaks are recorded at an applied magnetic field of 117 G (**Fig. 5.1b**). Without D-glucose, the diffraction peak appears at ~ 840 nm and it shifted towards higher wavelength with increasing D-glucose concentration.

**Fig. 5.2** shows the $\Delta\lambda_{peak}$ for *ESD0.8* stabilized nanoemulsion at applied magnetic field strengths of 81, 108 and for *ESDS0.08* at 117 G applied magnetic field as a function of different D-glucose concentrations. In the concentration range of 0.243 to 1 mM, $\Delta\lambda_{peak}$ was not significant but above 1 mM, $\Delta\lambda_{peak}$ changes linearly. The $\Delta\lambda_{peak}$ value at 30 mM D-glucose concentration was 69 nm. At higher applied magnetic field strengths, the diffraction peak appears at a lower wavelength of 640 nm (compared to 685 nm for 81 G) due to stronger dipolar coupling. Again, the diffraction peak position moves towards higher wavelengths with increasing D-glucose concentrations. At lower concentrations, up to 4.5 mM, $\Delta\lambda_{peak}$ was almost the same for both applied magnetic field strengths of 81 and 108 G, but above 4.5 mM, the $\Delta\lambda_{peak}$ was higher at 81 G. The maximum $\Delta\lambda_{peak}$ observed at 30 mM (at 108G) D-glucose was 54 nm.

The *ESD0.08* emulsion showed a better linearity in the concentration range 0.24 – 25 mM at an applied field of 117 G. As the maximum $\Delta\lambda_{peak}$ is ~100 nm, even naked eye D-glucose visualization of color change in the emulsion is possible. The colors seen in the emulsion without (left) and with 25 mM D-glucose (right) at a magnetic field strength of 117 G are shown in the inset of **Fig. 5.2**. $\Delta\lambda_{peak}$ changes linearly with D-glucose concentrations at applied magnetic field strengths of 81, 108 and 117 G. Solid lines in **Fig. 5.2** correspond to the linear fits, y=2148.6x-3.8, $R^2$=0.968; y=1703.2x-16, $R^2$=0.974; y=3696x+3; $R^2$=0.996. Though the emulsion showed a linear response in the concentration range of 0-30 mM, at all three magnetic field strengths, the best linearity is observed for applied field of 117 G.

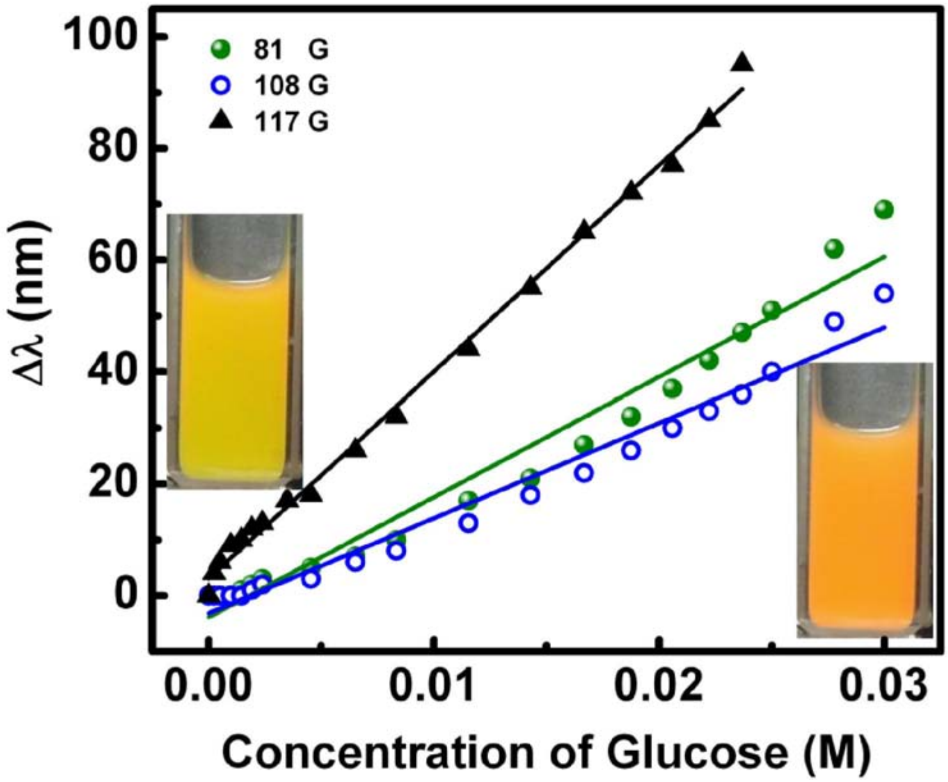

**Figure 5.2** The shift in the diffraction peak wavelength with increasing D-glucose concentration at different magnetic field strengths for *ESD0.8* and *ESD0.08* emulsions. Photographic image of cell containing emulsion without (left) and with 25 mM D-glucose (right) at a magnetic field strength of 117 G are shown in the inset.

### 5.3.2 Effect of Glucose on Interaction Forces

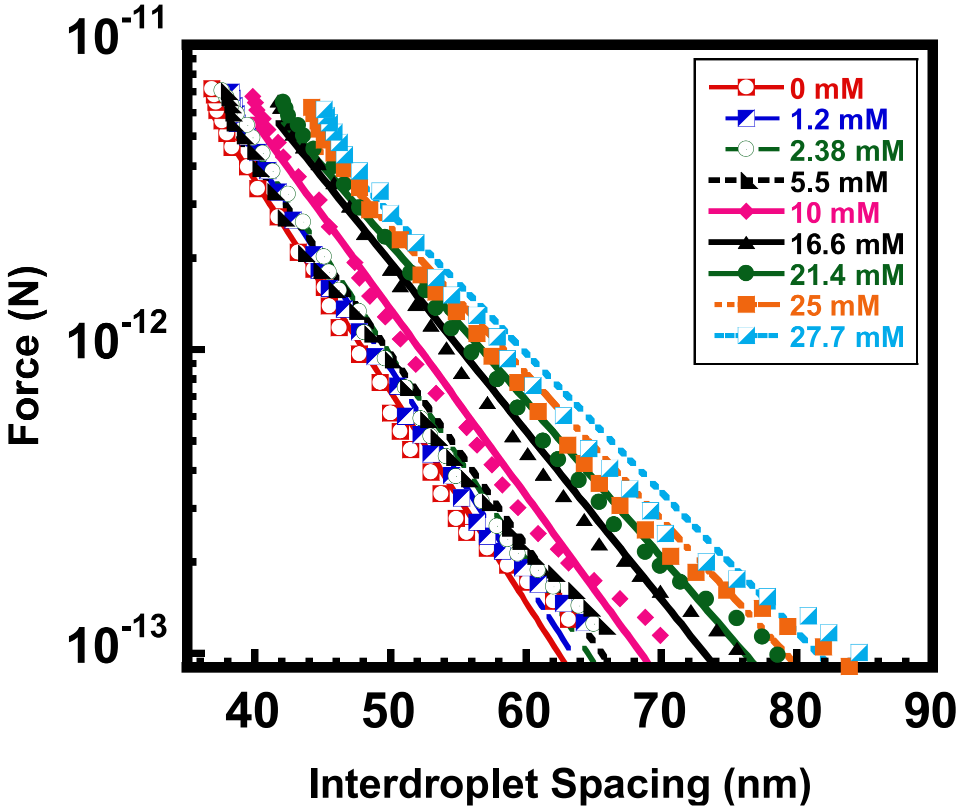

**Figure 5.3** Force-distance profiles measured at different D-glucose concentrations for *ESD0.8* emulsion. Solid lines correspond to fit using **Eqn. 1.30**.

To decipher the observed red shift in the Bragg peak upon D-glucose addition, the interdroplet force profiles were measured. **Fig. 5.3** shows the force-distance profiles measured at different concentrations of D-glucose in *ESD0.8* emulsion. Here, the force-distance profiles were exponentially decaying with the inter-droplet spacing. The force-distance profiles are fitted (solid lines) with the overlapping diffuse electric double layers force profile (**Eqn. 1.30**).[48] From the force distance profile we have extracted the $2L_0$, $\kappa^{-1}$ and K. Before the addition of D-glucose, the force profile decays with a $\kappa^{-1}$ of 6.2 nm and a $2L_0$ of 55.6 nm. The $\kappa^{-1}$ values extracted for D-glucose concentrations of 2.38, 5.5, 16.7, 25 and 30 mM were 6.4, 6.8, 7.8, 9.3 and 10 nm, respectively and the corresponding $2L_0$ values were 58.7, 58.6, 64, 68.7 and 70 nm, respectively. In the D-glucose concentration range of 0-30 mM, the force magnitude decreases from $2.1\times10^{-9}$ to $4.5\times10^{-10}$ N.

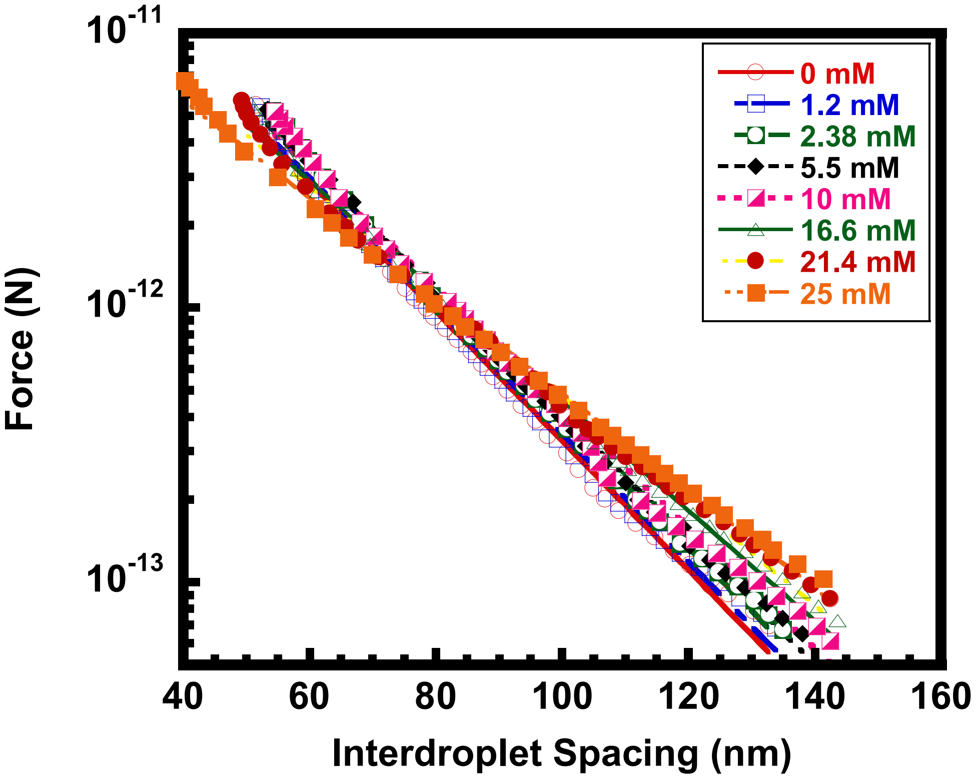

**Figure 5.4** Force-distance profiles measured at different D-glucose concentrations for *ESD0.08* emulsion. Solid lines correspond to the best fit using **Eqn. 1.29**.

**Fig. 5.4** shows exponentially decaying force-distance profiles for *ESD0.08* emulsion measured at different D-glucose concentrations. The interaction force between two spherical particles with small charge densities (extended electric double layer, $\kappa a < 5$) is represented by **Eqn. 1.29** (solid lines in **Fig. 5.4**).[58] From the best fit using **Eqn. 1.29**, the $\kappa^{-1}$ values were 18.4, 18.7, 21.6 and 24.4 nm for D-glucose concentrations of 0, 2.3, 16.6 and 25 mM, respectively. The corresponding $2L_0$ values were 102.6, 106, 110.5 and 116 nm, respectively. These results show that the force-distance profiles are dictated by the electrical double layer forces due to the adsorbed SDS molecules at the oil-water interface and the D-glucose molecules do not affect the decay length significantly. Surprisingly, in the presence of D-glucose, the onset of interaction ($2L_0$) increases significantly when the D-glucose molecules are introduced. Therefore, the interdroplet spacing is increased significantly upon the addition of D-glucose.

### 5.3.3 Proposed Interaction Mechanism

Glucose is known to form hydrogen-bonding with an organic functional group, a property that has been successfully exploited for the synthesis of mesoporous silica materials with D-glucose as a nonsurfactant pore-forming agent in the sol gel reactions,[167] to produce self-assembled polymer nanotubes in water,[168] self-assembled chiral organogels from achiral hydrogen bonded hydrazide foldamers by induction of chiral[169] produce self-assembled free-standing air–water interfacial $ZrO_2$ films.[166] The preparation of superior quality inorganic/organic nanostructures using surfactant-templated self assembly became popular since the emergence of nanotechnology. The crystalline metallic oxide/surfactant hybrid films prepared by surfactant-templated self assembly exhibit periodic nanostructures with different curvatures.[166] Earlier studies revealed that the glucose molecules are associated with SDS through hydrogen-bonding interactions.[166] Depending on the ratio of glucose to SDS, different architectural packings are possible. The X-ray diffraction and high resolution transmission electron microscopy studies showed that Glucose-SDS template can form lamellae structures.[166] The recent simulation and vibrational sum frequency studies show that at the oil/water interface, SDS head group is surrounded by water molecules while the hydrophobic tail part is in a disordered state and partially in contact with water.[141-142]

Before the introduction of glucose, the SDS molecules adsorb at the droplet surface with the negatively charged head group exposed to water. The co-ions with negative charge and the counter ions with positive charge form an electric double layer.[99] For *ESD0.8* with 1.3mM (30 mM) of glucose, the numbers of SDS and D-glucose molecules are 4.818 x $10^{20}$ and 7.34 x $10^{20}$ (1.8 x $10^{22}$), respectively. This means that even at the lowest D-glucose concentration, more than one SDS molecules/glucose is present in the system. At 5 mM D-glucose, the ratio of D-glucose to SDS molecule is 7, which increases to 37 at 30 mM. The force-distance curves show that the $\kappa^{-1}$ increases from 6 to ~10 nm as the concentration of D-glucose is increased from 1 to 30 mM, where the magnitude of force decreases from 2 x $10^{-9}$ to 4.5 x $10^{-10}$ N. This means that the association of SDS with D-glucose gives rise to a more diffused overlapping double layer (i.e. less screening effect). As the minimum interdroplet spacing is much larger, the short-range forces such as Van der Waals forces and structuring forces do not have any dominant contributions to the force profiles.

Based on the observed Bragg peak shift, force-distance profile data, and the HRTEM/XRD studies on glucose-SDS complexes, the possible architecture of glucose-water-SDS at the emulsion interface is schematically shown in **Fig. 5.5**. The glucose molecules interact with SDS via hydrogen-bonding and the association of glucose-water- SDS leads to a stretched lamellae like structure,[166] that eventually increases the inter-droplet spacing leading to a red-shift in the Bragg peak. Of course, more systematic simulation and experimental studies are necessary to fully unravel the exact architecture of the self assembled structures. As emulsion shows a linear change in the peak wavelength in the concentration range of 0.243 to 25 mM, it offers an ideal condition for diabetic glucose detection. Owing to the smaller droplet size, the typical response time of the emulsion is ~1.5 sec, which is quite rapid compared to many solid state sensors which is another advantage of the present approach.

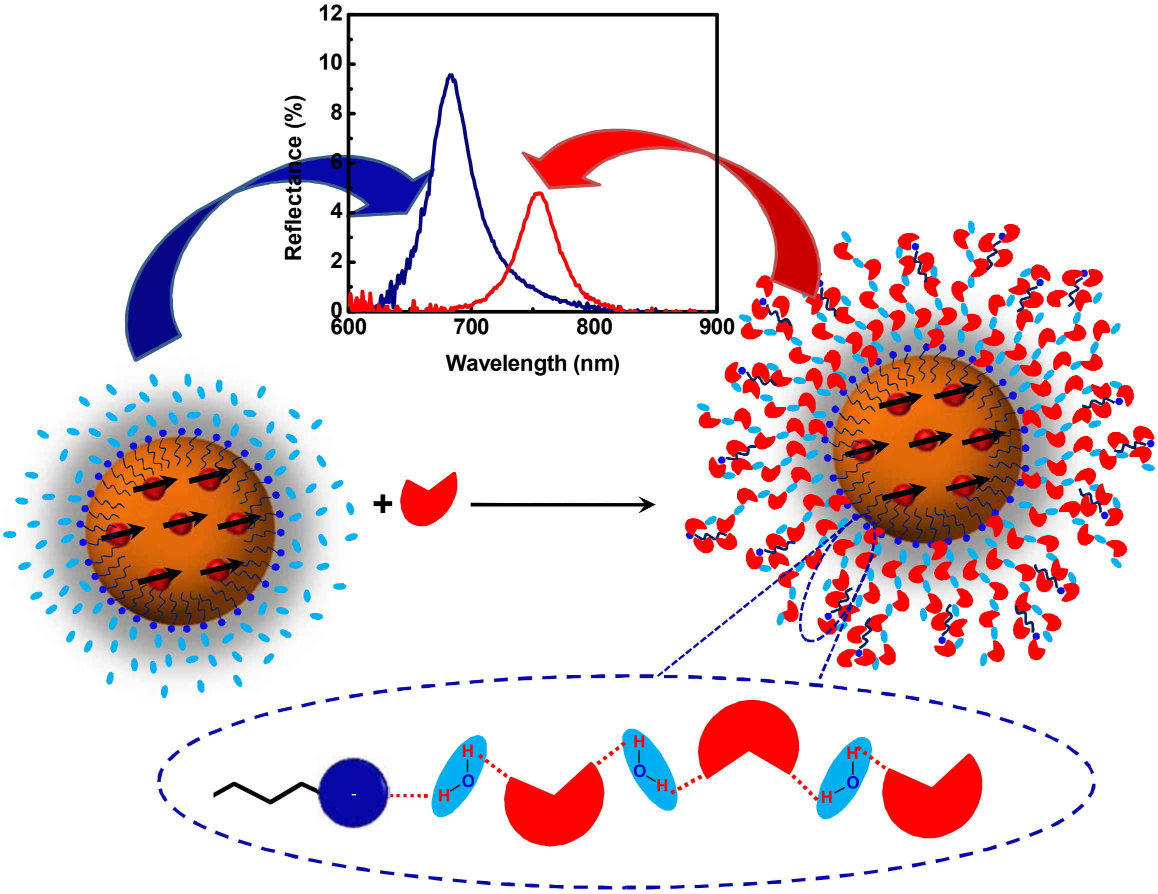

**Figure 5.5** Schematic representation of droplet without (left) and with D-glucose bound on droplet via SDS and water molecules (right) along with the Bragg peaks and the enlarged view of glucose –water-SDS complex at interface (bottom).

## 5.4 Application of Magnetic Nanoemulsions in Defect Detection

Inspired from the magnetic field tunable diffraction of visible wavelengths by magnetic nanoemulsion, a novel naked eye magnetic field sensor for visualizing buried defects of different morphologies and dimensions in ferromagnetic structures is developed. Detection of defects in materials or components in a non-destructive manner is popularly known as Nondestructive testing (NDT). It is very important for many industries in ensuring safety of machines and components, productivity and unexpected shutdowns. Several traditional NDT techniques have been established, yet new ones that are user friendly, rapid, compact, non-contact, highly sensitive and cost effective are being developed. Among magnetic testing of components, magnetic flux leakage (MFL) has been one of the popular techniques for defect detection in ferromagnetic materials, due to their simplicity and ease in usage.[170-174]

The presence of a defect or crack or inclusion causes a sudden local change in the magnetic permeability that results in a flux leakage around the defective region. To detect such defects and to quantify their features such as morphology, dimension and location within the material, the leakage field near the defect is detected by a magnetic field sensor such as Hall probe, flux gate sensor, magneto-diode, search coil, magnetic particle, Forester micro probe.[175-178] Recently, new magnetic sensors such as SQUID,[179] Giant magneto resistance (GMR),[180-181] giant magneto impedance (GMI)[182-183] and anisotropic magneto resistance (AMR)[184] have been used to detect the defects with high sensitivity. Magneto optic (MO) sensors which work on the Faraday's rotation change with the MFL also appear as attentive and sensitive for visualization of defects.[185-186] In MFL techniques, the raw data needs to be processed along with computationally intensive numerical modeling to obtain accurate information on the defect shapes, dimension and the location within the test components. Analytical models are fast and simple but less accurate because of many approximations used in the calculations. Whereas numerical models are accurate but they are computationally expensive.[187] These problems associated with conventional MFL techniques warrant the need for more reliable, simple, cost effective and sensitive techniques for detection of leakage of magnetic flux in ferromagnetic components and structures. Towards realizing this goal, here a new methodology to detect defects of different morphologies to quantify the defect shape, location and dimensions is developed. The new approach is tested and validated in specimens with artificial defects of different geometries.

### 5.4.1 Theoretical Background

Prior knowledge about the MFL profile of a defective region is useful for interpreting the defect features. There are several analytical [171, 174, 188-196] and numerical models [187, 197-206] to predict the magnetic flux leakage from a defective region. Although Zatsepin and Shcherbinin model, [207] based on magnetic line and surface dipoles, yields reasonably good results with respect to experiments, it cannot be readily adapted for overlapping defects and defects of different morphologies. In such cases, finite element approaches are ideal for the analysis of defects of different morphologies.[195, 208] We use the simple analytical approach of Uetake-Saito[192] to obtain the MFL profiles for testing our experimental results. The magnetic flux leakage originates from magnetic reluctance of the defective region where the magnetic permeability is much lower than that of the sound region. According to a simple dipole model, normal components of the leakage flux from rectangular defect with depth $Y_0$ and width $l$ is given by, [209]

$$H_y = \frac{H_g}{2\pi}\ln\left(\frac{(x+l/2)^2+(y+Y_0)^2}{(x-l/2)^2+(y+Y_0)^2}\right)\left(\frac{(x-l/2)^2+y^2}{(x+l/2)^2+y^2}\right) \tag{5.1}$$

where, '$H_g$' is the field inside the defect for an applied field '$H_a$' and is given by,

$$H_g = \frac{2Y_0/l+1}{(1/\mu)\,2Y_0/l+1}H_a \tag{5.2}$$

Here, the tangential and normal components of the leakage fluxes are calculated with an assumption that the surface charge density on the faces of the defect is a constant. The origin of the x-y coordinate axes is at the center of the top surface of the defect. It should be noted that the tangential component of leakage flux peaks at the center of the crack and falls to zero at the defect edges. Zhang et al.,[191] has developed analytical expressions for magnetic leakage field of two types of internal defects by taking into consideration the magnetic image effects from the spatial boundary and the defect boundary using the modified dipole model and image theory. We use the modified dipole model for adjacent parallel surface slots to obtain the leakage field profile. The schematic representation of the two adjacent defects geometry is shown in **Fig. 5.6**. The depths and widths of slot1, slot2 and the separation between the two adjacent slots are $y_1$, $y_2$, $l_1$, $l_2$, and $2l_g$, respectively. According to the modified dipole model, the normal component of the two leakage fields from two parallel surface slots are given by,[192]

$$B_y = \frac{H_g}{2\pi}\left\{\begin{array}{l}\ln\dfrac{(x+l_g)^2+(y+y_1)^2}{(x+l_g)^2+y^2} - \ln\dfrac{(x+l_1+l_g)^2+(y+y_1)^2}{(x+l_1+l_g)^2+y^2} \\ +\ln\dfrac{(x-l_2-l_g)^2+(y+y_2)^2}{(x-l_{12}-l_g)^2+y^2} - \ln\dfrac{(x-l_g)^2+(y+y_2)^2}{(x-l_g)^2+y^2}\end{array}\right\} \tag{5.3}$$

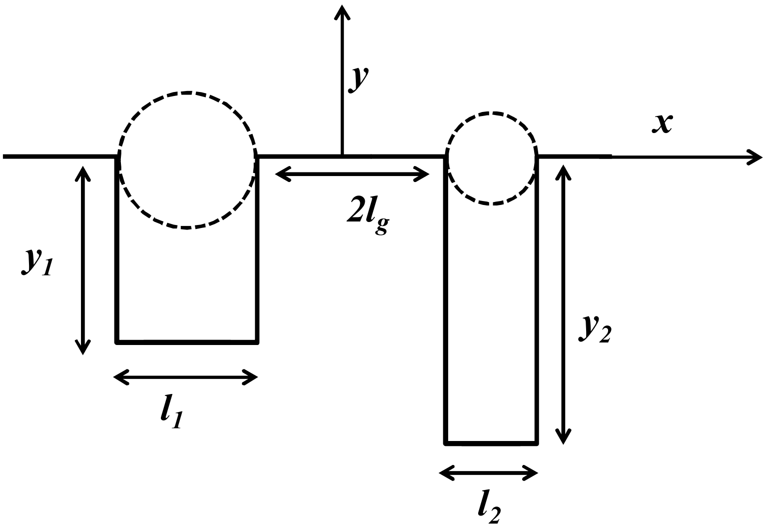

**Figure 5.6.** Schematic representation of adjacent cylindrical slots (defects).

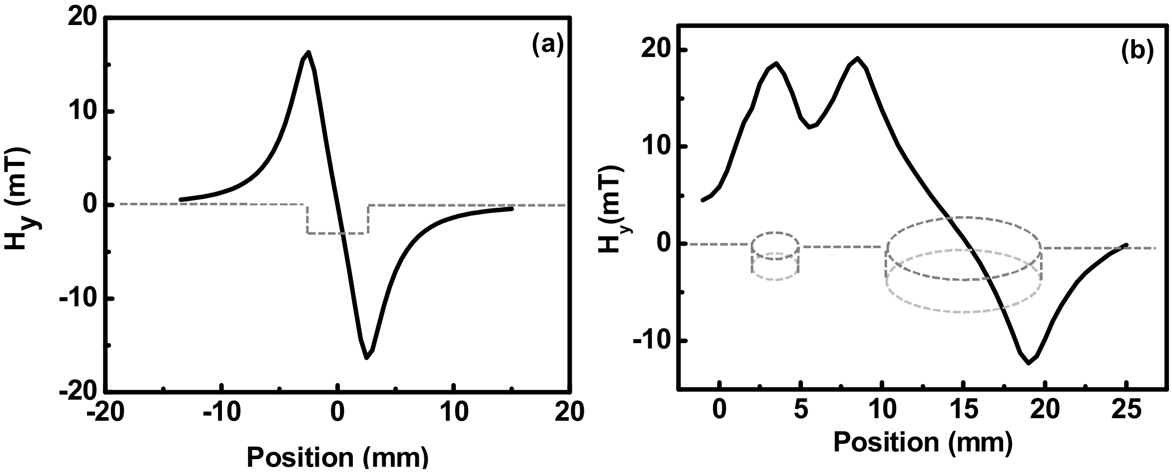

**Figure 5.7** Calculated normal component of leakage field profile (a) rectangular slot and (b) for two adjacent cylindrical slots.

The normal component of leakage field profile for a rectangular slot defect and two adjacent cylindrical slots, calculated using **Eqn. 5.1** and **Eqn. 5.3** respectively, is shown in **Fig. 5.7**.

### 5.4.2 Experimetal Setup

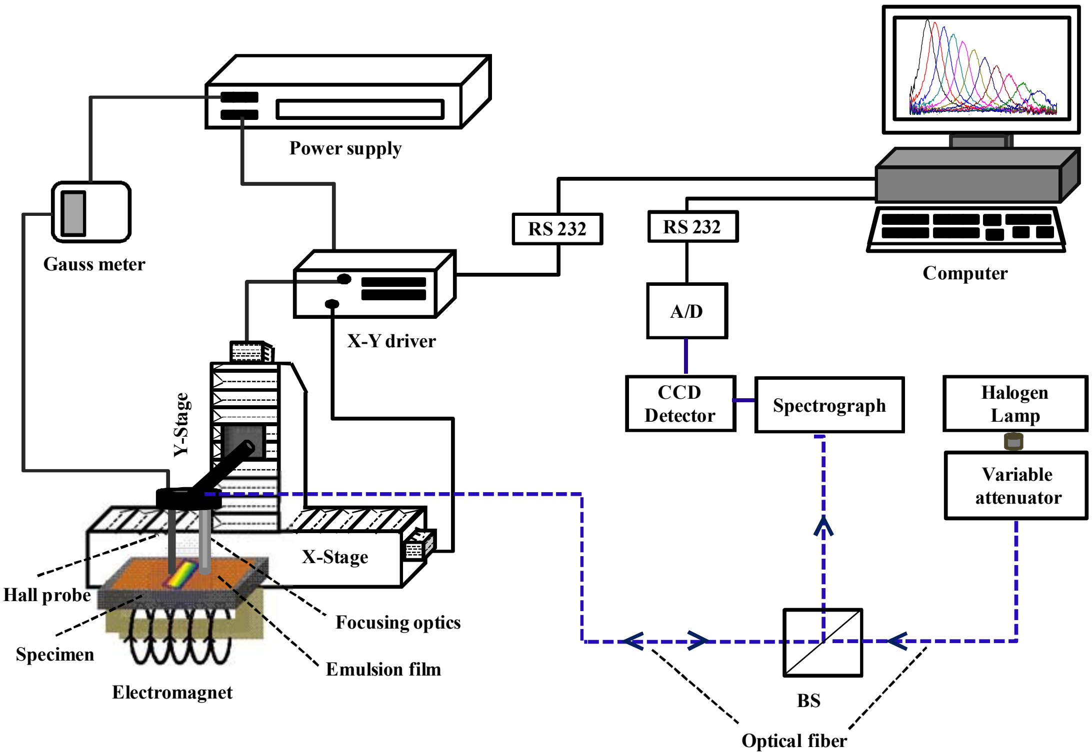

**Figure 5.8** Schematic representation of typical experimental setup used for magnetic leakage field measurement and defect imaging with nanoemulsion.

**Figure 5.8** shows schematic representation of a typical experimental setup for leakage field measurement and defect imaging. The specimens were magnetized using a DC magnetic yoke. The normal component of leakage flux around the defect were measured at a constant lift-off distance of 1 mm, using a hall probe. The specimen was first magnetized with an electromagnetic yoke and then the thin film sensor head was placed on the rear surface, at a constant lift of distance of 1mm. The color pattern on the sensor was recorded using a digital camera or observed with the naked eye. The color patterns in the sensor were analyzed more carefully to assess the severity of the defects. The sensor is scanned across the specimen surface to map the MFL profile across the entire specimen. To understand the correlation between the colour pattern and the leakage field from different specimens, the MFL values are measured with a Hall probe.

### 5.4.3 Sensor Head Fabrication and Specimen Details

Nanoemulsion is sandwiched between two optically transparent (microscopic) glass slides. A spacer of 300 µm thickness is used to achieve desired uniform gap. The sides of the cells are sealed to avoid seepages, moisture trapping and contamination of emulsion with foreign particles from outside.

| Specimen | Width/Diameter (mm) | | Depth (mm) | | Gap between slots $2l_g$ (mm) |
|---|---|---|---|---|---|
| | Slot1 | Slot2 | Slot1 | Slot2 | |
| S1(two cylindrical) | 5 | 10.5 | 8 | 7.5 | 5 |
| S2(rectangular, cylindrical) | 3 | 6.5 | 4 | 8 | 8 |
| S3a (rectangular) | 0.5 | - | 2 | - | - |
| S3b (rectangular) | 0.5 | - | 3 | - | - |
| S3c (rectangular) | 0.5 | - | 4 | - | - |
| S3d (rectangular) | 0.5 | - | 5 | - | - |
| S4(rectangular) | 3 | - | 4 | - | - |
| S5 (cylindrical) | 10.5 | - | 5 | - | - |

**Table 5.1** Details of the specimens used in the studies. The specimen dimension in all cases (L × B × T) are 21 × 4.5 × 1 (cm).

Mild steel plates 50 mm length, 25 mm width and thickness of 10 mm with several well defined defect dimensions and shapes were fabricated for the test. The different defect geometries used for the study and their dimensions are listed in **Table 5.1**.

### 5.4.4 Nanoemulsion Sensor Response

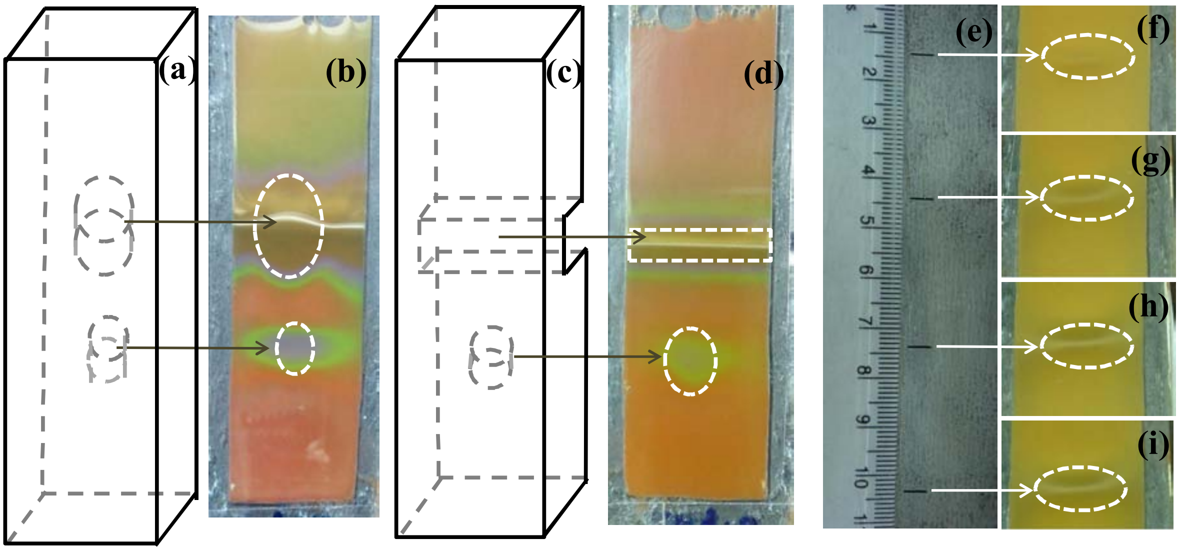

**Figure 5.9** Schematics of the specimens S1–S3a–d (a, c and e) and the corresponding photographic images of nanofluid sensor (b, d and f–i), respectively. (f–i) are S3a, S3b, S3c, S3d, respectively. The defective regions of each sample are encircled in the photographic images.

**Fig. 5.9 a-i** show the schematics of the specimen S1, S2, S3 (a-d) and the corresponding photographic images of the nanofluid sensor response. The sensor exhibits a natural color of brown (without MFL) due to the presence of iron oxide nanoparticles in the oil droplets. The defective region of each sample is encircled for clarity. On both sides of the defect, a color spectrum is observed due to the leakage of the magnetic flux around the defects. The centre line on the colour pattern was straight for the rectangular slot and semicircular pattern for the cylindrical slot. **Fig. 5.9e** shows the photograph of the specimen S3 (a-d) and the corresponding sensor images are shown in **Fig. 5.9f-i**. The defects are clearly discernible from the images, though color contrasts were not very clear. This is mainly due to the lower leakage flux, owing to the smaller defects present and the larger remnant thickness of the specimens. However, the defect centre was very clearly discernible from the image.

In brief, a new approach to image and visualize defects buried inside ferromagnetic components is established. Colour pattern from MFL induced self-assembly of nanoemulsion is unique for different defect morphology which enables a user friendly and a naked eye defect detection approach. As the color pattern in the sensor is totally reversible, the sensor is reusable. This new approach will have potential applications in simultaneous inspection of large area ferromagnetic components and structures.

## 5.5 Conclusions

The optical properties and intermolecular interactions in magnetically responsive oil-in water nanoemulsions in the presence of an anionic surfactant and D-glucose is studied. The Bragg reflected light intensity from the emulsions at a fixed magnetic field strength shows that the equilibrium interdroplet distance between the emulsion droplets in the 1D array is increased by several nanometers in the presence of glucose because of intermolecular hydrogen bonding of glucose with sodium dodecyl sulphate molecules at oil-water interface. The intermolecular hydrogen bonding of glucose with sodium dodecyl sulphate molecules at oil-water interface gives rise to stretched lamellae like structures that un-screen the overlapping double layer, thereby increasing the onset of repulsion and the decay length significantly**.** The observed large red shift in the diffracted Bragg peak (~80 and100 nm) and the linear response in the glucose concentration range of 0.25-25 mM offer a simple, fast and cost effective non-enzymatic approach for glucose detection.

A new approach to image and visualize defects buried inside ferromagnetic components by using magnetically polarizable nanoemulsion has been demonstrated. Leakage magnetic flux induced self-assembly of nanoemulsion, causes visible colour patterns in the sample. Defect dimensions can be quantitatively extracted from the RGB profile analysis. The extracted defect widths are in good agreement with the magnetic flux leakage measurement. As the color pattern in the sensor is reversible, the sensor is reusable and allows inspection of large area specimens.

# Chapter-VI

## Probing of Competitive Displacement Adsorption of Casein at Oil-in-Water Interface using Equilibrium Force Distance Measurements

# 6

# Probing of Competitive Displacement Adsorption of Casein at Oil-in-Water Interface using Equilibrium Force Distance Measurements

## 6.1 Introduction

Understanding the nature and reversibility of competitive displacement adsorption of smaller molecules at interfaces covered with macromolecules is important from practical applications point of view.[210] Such competitive displacement adsorption provides a unique possibility to reuse adsorbents.[211] As the competitive interactions between different adsorbing species determine the stability and product life time, several studies have been carried out on the interaction of protein-with other molecules at air-water and oil-water interface.[92, 212-225] The recent neutron reflectivity studies show that a synergistic interaction between certain nonionic surfactants and proteins can lead to spontaneous self-assembly at the air–water interface to form layered surface structures.[222] Such protein-anionic surfactant interactions can also effectively be used to tune electrostatic interactions.[223]

The protein adsorption at oil/water interface is important in manufacturing industries such as, pharmaceutical, food emulsions.[86, 222, 226-227] Milk proteins are used as a stabilizer in food hydrocolloids because of their exceptional amphiphilic nature and stabilizing properties.[226, 228-229] In bovine milk, casein consists of four major proteins, $\alpha_{s1}$-casein, $\alpha_{s2}$-casein, β-casein and κ-casein, which are known to adsorb rapidly at the oil-water interface and provides stability via electro-steric stabilization.[228, 230-231] $\alpha_{s1}$-casein and β-casein are the major content (~75 %) of milk casein.[230] The average molecular weight of β casein is ~ 24 kDa with a net charge of -15e at neutral pH.[232] β-Casein is an unstructured protein and has no internal covalent crosslinks and has 209 amino acid residues and the non-uniform distribution of hydrophobic and hydrophilic residues gives rise to a distinctly amphiphilic molecular structure.[232-233] β-Casein possess a strong negative charge with four of the five phosphate groups being located at the N terminal end between amino acid residues 13 and 21.[232] The average molecular weight of $\alpha_{s1}$ is ~23.5 kDa with a net charge of -22e at neutral pH.[232, 234] $\alpha_{s1}$ casein is also amphiphilic with non-uniform and more randomly distributed 199 hydrophobic and hydrophilic residues than that of β-casein.[233] β-casein is more hydrophobic and surface active than $\alpha_{s1}$ casein.[230] The casein resembles a block copolymer with alternating charge and hydrophobicity i.e., a charged phosphopeptide loop and a hydrophobic train.[235] $\alpha_{s1}$-casein has N-terminal hydrophobic train, followed by a charged loop and a final C-terminal hydrophobic train.[236] The k-casein micelle diameter is ~ 23 nm and consists of approximately 30 monomers and the CMC value varies from 0.02-0.05 wt% .[237]

The stability aspects of protein stabilized emulsions, under various conditions like temperature,[238] pH,[233] cations[225] and biochemical environment,[218, 239-240] have been studied in food hydrocolloids. In general, the polymer adsorption at solid interfaces is strongly influenced by solution properties such as pH and ionic strength.[241] The experiments suggest that the ionizable character of silica plays a key role in the adsorption of neutral polymer chains.[242] Though nonionic polymer adsorption (e.g., poly (ethylene oxide) and poly (N vinylpyrollidone)) onto charged solid surfaces in water have been widely studied, measurements at oil-water interface are limited.[243-246]

An understanding of competitive displacement adsorption is important for extending the shelf life and reuse of many products such as pharmaceutical formulations, drug delivery globules, cosmetics, paints, detergents and pesticides. Despite intense research on protein adsorption behavior at interfaces, the understanding is still vague because of the complex interaction between the protein molecules and surfaces through Van der Waals, electrostatic, hydrophobic, and hydrogen bonding interactions. Measurement of interaction forces in presence of adsorbing species at a solid interface is carried out using atomic force microscopy[247] and surface force apparatus.[248] Here an attempt is made to obtain better insight into these complex interactions between proteins and oil-water (O/W) interface in presence of diblock polymer mediation using in situ colloidal force measurements. Towards this goal, the competitive displacement adsorption efficiency of casein at an oil-water interface stabilized with either negatively charged surfactant or neutral polymer is probed by employing intermolecular force, zeta and hydrodynamic diameter measurements. The questions tackled from this study are the following. (a) Can casein proteins be effective in displacing adsorbed diblock copolymers from O/W interface? (b) How casein-diblock polymer interaction affects the force parameters and stability of O/W emulsions? (c) What is the effect of polymeric size on nature of forces during and after competitive displacement adsorption?

## 6.2 Materials and Methods

To study the effect of surface charge and casein interaction, *ESD0.8* emulsion is used. To study the effect of adsorbed polymer and casein interaction, *EPVA40* and *EPVA115* emulsions are used. The sample preparation and material details are provided in *Chapter II. ESD0.8*, *EPVA40* and *EPVA115* emulsions were characterized for the hydrodynamic size and zeta potential using dynamic light scattering and electrophoretic mobility measurements, respectively. The average hydrodynamic sizes of *ESD0.8*, *EPVA40* and *EPVA115* emulsions are found to be 190, 293, 500 nm, respectively and the corresponding zeta potential values were -46, -14 and -2 mV, respectively. The force profiles measurements were done at 25 ˚C.

### 6.2.1 Casein Preparation

Pasteurized cow milk (fat ~4.5 g/100 g, protein ~2.9 g/100 g, carbohydrate ~4.9 g/100 g and calcium ~114 mg/100 g) is used to prepare casein. In cow milk, casein comprised of 80 % of the total protein and the remaining protein components are α-Lactalbumin, β-lactolobulin, serum albumin, immunoglobulin and other proteins. Casein is extracted from skimmed milk.[249] Whole milk is centrifuged at 6000 rpm for 20 minutes to remove fat (due to its lower density it forms a cream layer). Then the pH of the skimmed milk was brought down to pH 4.6, the isoelectric point of casein where the casein starts precipitating and the filtrate (α-lactalbumin and β-lactoglobulin, Bovine serum albumin) is called as whey protein. Casein was separated from whey proteins by filter paper. The other possible residuals α-lactalbumin and β-lactoglobulin do have tendency to adsorb at the interface, however β-casein $\alpha_{s1}$ have more preferential adsorption than other proteins.[250-251] The concentration of the isolated casein as obtained by thermo gravimetric analysis is 4.2 wt%. From the concentrated casein, the desired wt% is prepared by diluting it in milliQ water. The isolated casein is characterized by hydrodynamic diameter and electrophoretic mobility measurements.

### 6.2.2 Force Distance Measurements

Typical experimental setup and working principle of magnetic chaining technique used for probing the intermolecular interactions between the magnetic emulsions at nano scales in the presence of casein is discussed in detail in *Chapter II.*

## 6.3 Results and Discussion

### 6.3.1 SDS Stabilized Emulsion-Casein Interactions

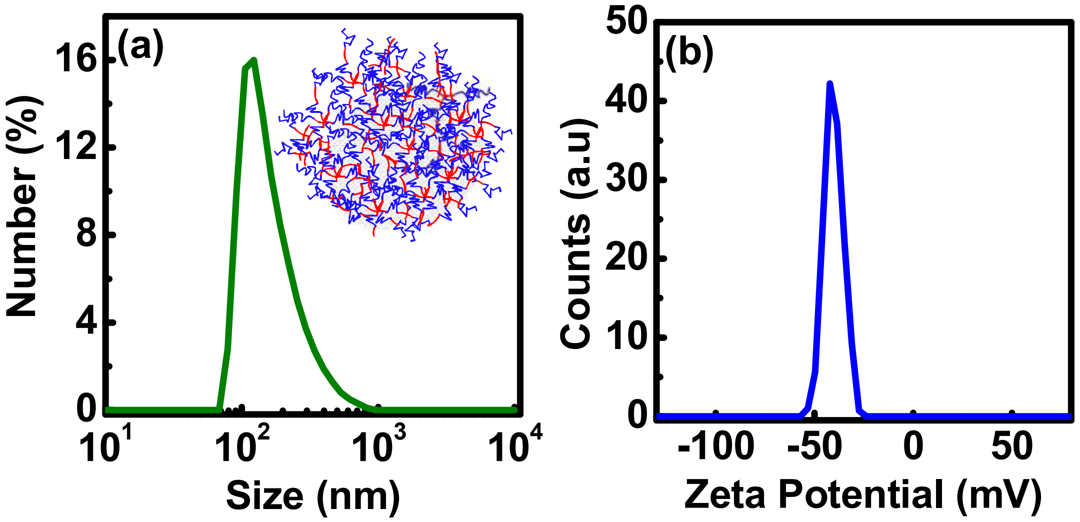

**Figure 6.1** The distribution of (a) hydrodynamic diameter and (b) zeta potential values of 0.42 wt% casein. The average values of hydrodynamic diameter and the zeta potential values are found to be ~120 nm and -40 mV, respectively at pH 6.69. The schematic representation of casein micelle is shown in the inset of **Fig. 6.1a**.

**Fig. 6.1** shows the hydrodynamic diameter and zeta potential of pure casein. The average hydrodynamic diameter and the zeta potential values are found to be ~120 nm and -40 mV at a pH value of 6.69, respectively, which is in agreement with the reported values.[249]

To study the casein interaction at a negatively charged interface, the initial emulsion is washed and stabilized with 0.8 mM of SDS (*ESD0.8*). Because of the adsorbed $DS^-$ head group at the oil-water interface, droplet surface is negatively charged and this was evident from the negative zeta potential (-35 mV) observed in *ESD0.8* emulsions. The molecular dynamic simulation and sum frequency studies shows that SDS head group is fully surrounded by water molecules and the SDS alkyl tail is in contact with oil, where at least two chain defects are needed to bend the alkyl tail towards the surface.[142] **Fig. 6.2** shows the force distance profile *ESD0.8* emulsion at different casein concentrations ranging from 0 to 0.0033 wt%. The reported value of casein CMC is 0.05 mg/mL. The force profile at zero casein concentration decays exponentially with the interdroplet distance, where the decay length is found to be 8 nm, which is comparable to the theoretical Debye length (~10 nm) for 0.08 mM SDS. With increase in casein concentrations, the force profiles are akin to that of the one stabilized with SDS but with slightly different slopes, onset of interaction and magnitude of force. From the best fit obtained from the electrostatic repulsion equation **Eqn. 1.30** (solid lines in **Fig. 6.2**), we extracted three parameters: magnitude of force decay or the pre-exponential factor (K) dictated by the surface potential, Debye length ($\kappa^{-1}$) from the slope of the curve and the first interaction length or onset repulsion ($2L_0$), corresponding to the distance at which magnitude of force is $2x10^{-13}$ N. The $\kappa^{-1}$ decreases from 8 to 7 nm as the casein concentration is increased from 0 to 0.0033 wt% and the $2L_0$ is found to decrease from 67 to 57 nm in the above concentration range. For all the casein concentrations, the force profiles are repulsive in nature and decay exponentially with interdroplet distance. Without casein, the observed decay length of 8 nm was close to the theoretical decay length value for SDS (0.8 mM). The radius of gyration $R_g$, of β-casein micelles is about 12 nm.[237] As the concentration of casein used here is much lower than the CMC value of casein, free micelles are not present in the emulsion. The decay length comparable to the decay length at 0.8 mM SDS shows that the O/W interface is still intact with SDS molecules. However, from the force measurement data, we cannot completely rule out the possibility of the absence of some casein molecules at O/W interface.

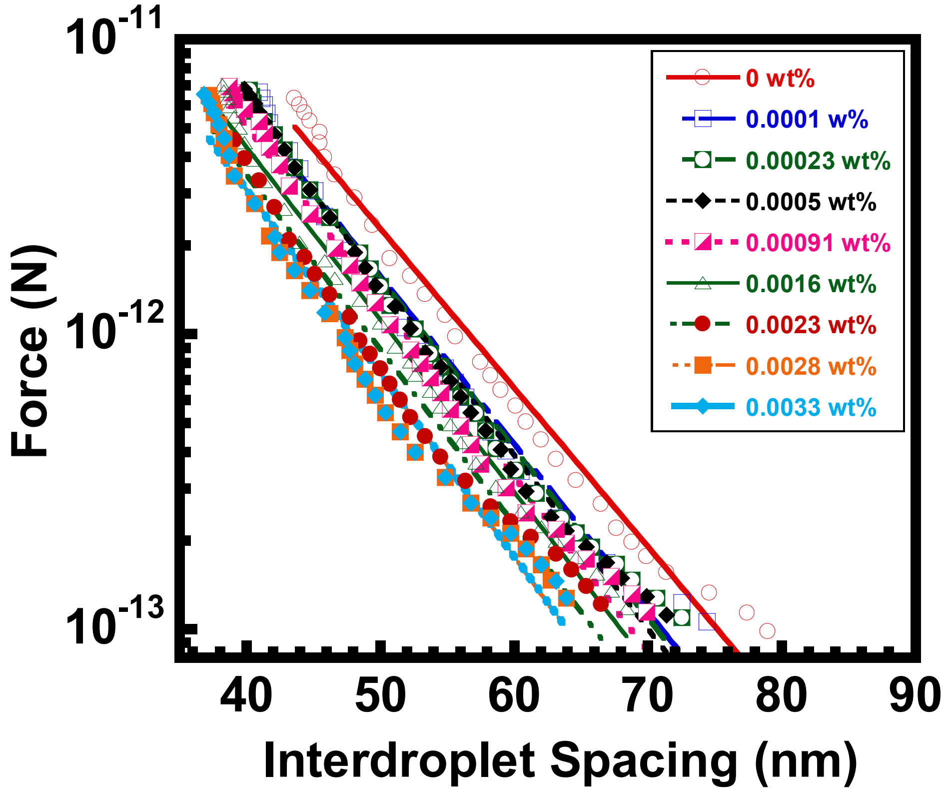

**Figure 6.2** Force distance profiles at different casein concentrations for *ESD0.8* emulsion. The solid lines correspond to fit on the experimental data using electrical double layer repulsion equation (**Eqn. 1.30**).

The amphiphilic behavior with high proportion of non-polar and polar residues of casein seems to enable them to adsorb at the oil-water interface.[230] Recent Monte Carlo simulation study show that the unstructured β-casein adsorb on to both positively and negatively charged surfaces through several interactions such as direct electrostatic, hydrophobic interactions, structural rearrangement and charge regulation due to proton uptake and release.[252] With increasing casein concentration up to 0.0023 wt%, the droplet starts interacting at shorter interdroplet spacing than the SDS stabilized interfaces.

For a thin electrical double layer, κa > 5, (for 0.8 mM SDS, κa = 9.34), the electrostatic repulsion as a function of distance is given by **Eqn. 1.30**.[59-60] By increasing casein concentration from 0 to 0.0033 wt%, the range of repulsion is found to be decreasing while the magnitude of force decreases slightly from 1.15 to 0.95 nN. The observed repulsive nature with increasing casein concentration indicates that some casein molecules may form a patchy coverage at the interface and increases the surface charge of oil-water interface through hydrophobic interactions as reported by Evers et al.,.[252] Similar force profile was observed with increasing SDS concentration, where the added SDS monomers co-adsorbs at the interface and screen the surface charges, resulting in a reduction in the onset of repulsion.[80] With increasing casein concentration beyond 0.0023 wt%, the force-distance profiles did not show much change.

The measured autocorrelation function, hydrodynamic diameter and zeta potential for *ESD0.8* emulsion (pH 6.24) at different casein concentrations are shown in **Fig. 6.3**. The hydrodynamic diameter of emulsion droplets varies slightly from 190 to 192 nm as the casein concentration is increased from 0 to 0.005 wt%. However, a drastic reduction in the zeta potential from -45 to -30 mV is observed when 0.005 wt% of casein is incorporated in the emulsion. Here, the variation in the zeta potential and hydrodynamic diameter of the mixed dispersion roughly follow the superposition of size/zeta distribution.

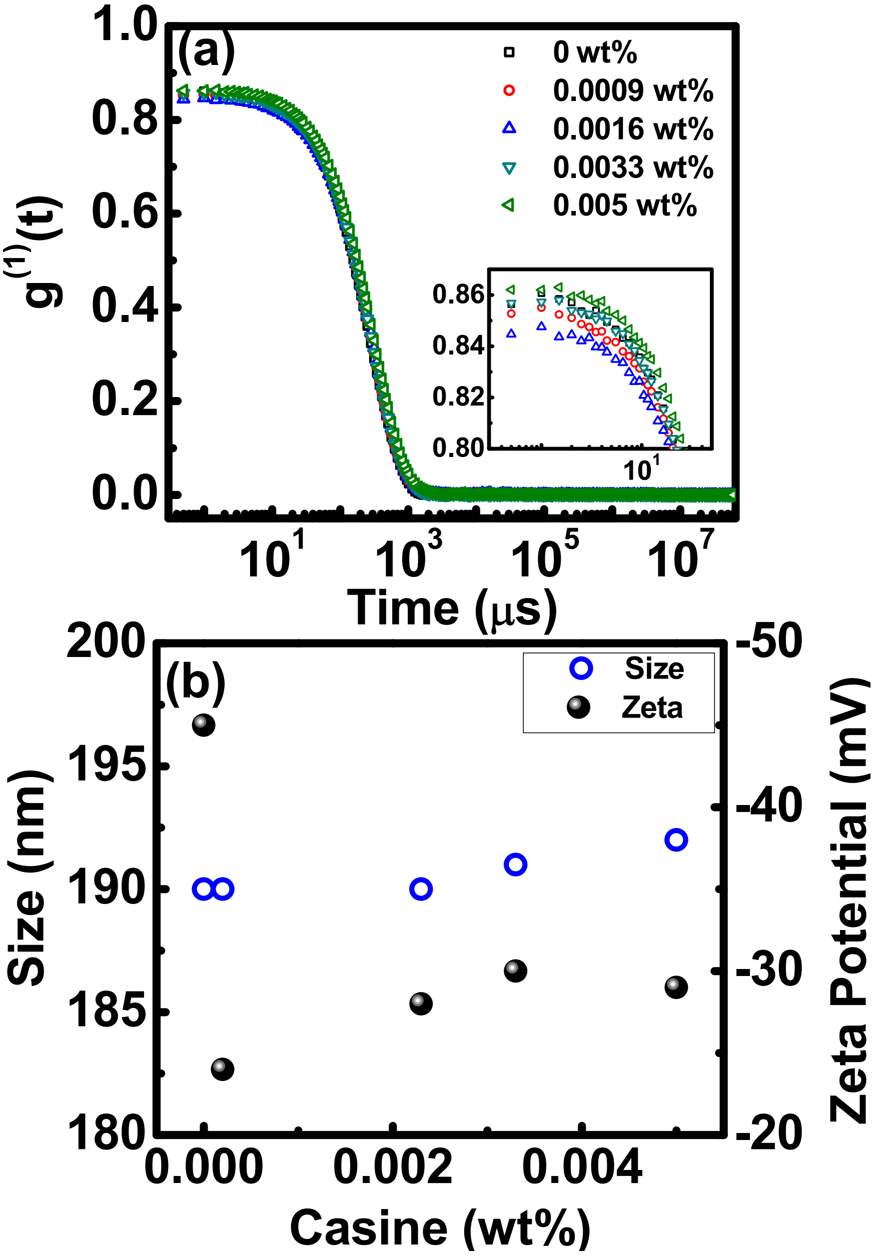

**Figure 6.3** (a) Autocorrelation function of scattered light (inset shows an enlarged view at shorter time interval) for *ESD0.8* emulsion at different casein concentrations (pH6.24). (b) Hydrodynamic diameter (open symbols) and zeta potential (solid symbols) for *ESD0.8* emulsion at different casein concentrations.

### 6.3.2 PVA-Vac Stabilized Emulsions–Casein Interactions

To study the effect of casein adsorption on the intermolecular forces between the polymer stabilized droplets, the emulsion is stabilized with 0.6 wt% of PVA-vac of two different molecular weights. The hydrophobic Vac goes into the oil phase and the hydrophilic PVA extends into water. Due to finite size of confined segments (excluded volume effect) and hydration layers, the steric force magnitude and range can be much greater than $10R_g$, in aqueous solutions.[253] **Fig. 6.4a** shows the force distance profile for *EPVA40* stabilized emulsion at different casein concentrations. At all the studied casein concentrations, force profiles decay exponentially with interdroplet distance. The force profile without added casein is taken as a reference curve, which decays exponentially. It has been shown that the force profile between polymer covered particles is repulsive and can be represented by **Eqn. 1.37**.[72] From the best fit to the equation, we have extracted three parameters, decay length ($\lambda_d$) from the slope and the $2L_0$ or the first interaction length and magnitude of force (K) which is dictated by the adsorbed polymer layer. Without casein, the characteristic decay length $\lambda_d$= 7.5 nm, which was close to the unperturbed $R_g$ value of free polymer, was measured using viscometry (~ 8 nm). With the addition of 0.004 wt% of casein, the $\lambda_d$ decreases from 7.5 to 7 nm. The $\lambda_d$ values were 6, 5 and 4.5 nm for 0.016, 0.054 and 0.14 wt% casein, respectively. Interestingly the $2L_0$ decreases drastically from 77.5 (~10 $R_g$) to 57 nm (~7 $R_g$) when 0.14 wt% casein was present in the emulsion, where the force magnitude also increases from 10 to 30 nN with casein.

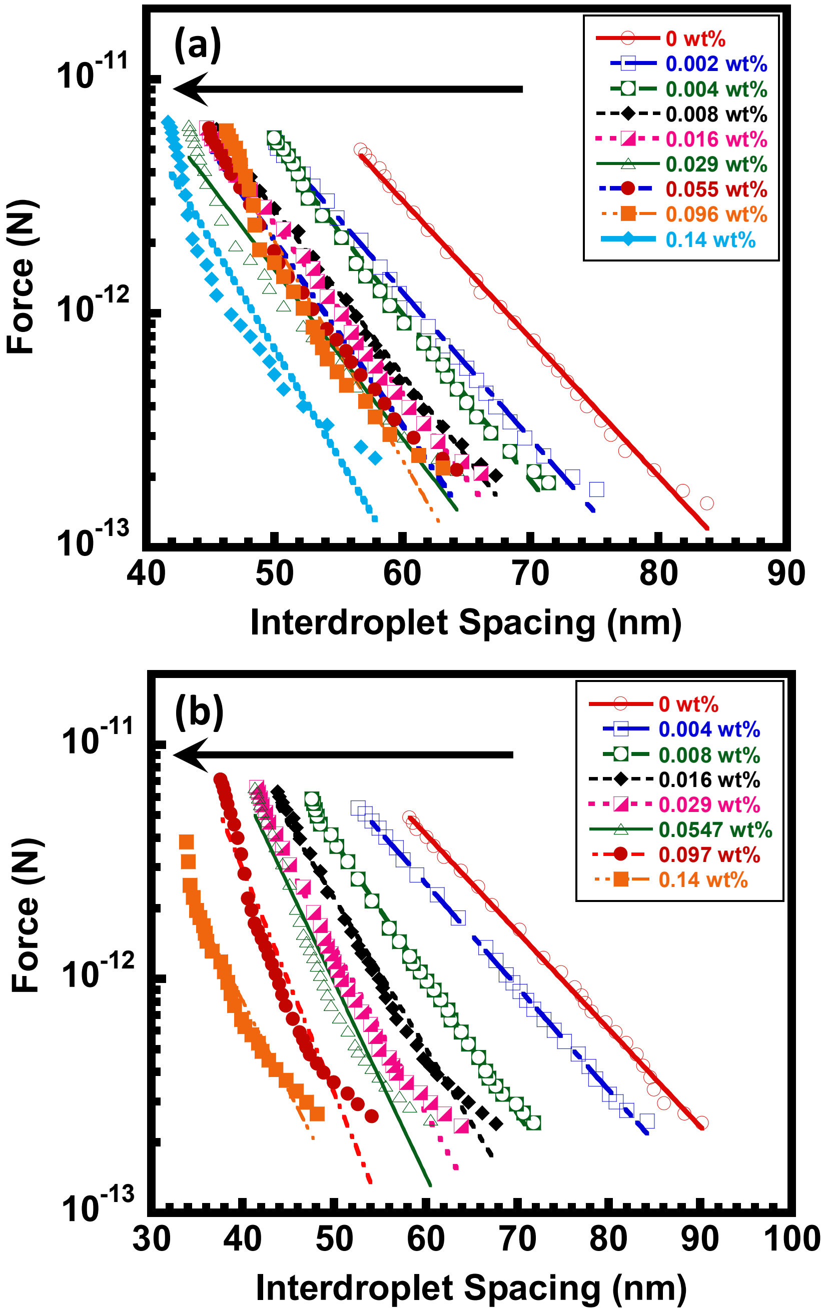

**Figure 6.4** Force distance profiles at different casein concentrations for (a) *EPVA40* and (b) *EPVA115* emulsions. The arrow indicates the increase in casein concentration. Solid lines correspond to the theoretical fit to the **Eqn. 1.37**.

**Fig. 6.4b** shows the force distance profile measured at varying casein concentration for *EPVA115* nanoemulsion. The force distance curves were exponentially decaying with interdroplet distance, though slight deviations are observed at higher casein concentrations. Without casein, $\lambda_d$ = 10.5 nm, which is close to the unperturbed Rg value of PVA-Vac 115K and this was measured from viscometry (~12 nm). The decay lengths were 9.8, 7.4, 6.7, 6 and 4.5 nm for 0.004, 0.008, 0.016, 0.029, 0.096 and 0.14 wt% of casein, respectively. In this concentration range, the onset repulsion decreases from 88 (~7.3 $R_g$) to 48 nm (~4 $R_g$), where as the magnitude of force increases from 1 to 19 nN.

**Figure 6.5** shows the change in $2L_0$, $\lambda_d$ and K as a function of casein concentration. Both *EPVA40* and *EPVA115* emulsion $\lambda_d$ and $2L_0$ values decrease with casein whereas an increase in the force magnitude is observed. The significant diminution in the $\lambda_d$ and $2L_0$ value suggests that the adsorbed polymer is replaced by casein through competitive interaction. If the polymer remains at the interface along with the casein molecules, the decay length would not have reduced to 4.5 nm. The increase in force magnitude with casein concentration suggests that the casein volume fraction at the droplet interface also increases. As expected, such adsorption of casein molecules at an interface leads to an electrostatic repulsive force due to the negative charges of $\alpha_{s1}$ and β casein ( -22 e and -15 e, respectively).[254] To understand the competitive displacement adsorption phenomena, we have carried out zeta potential measurements in *EPVA40* emulsion at different casein concentration.

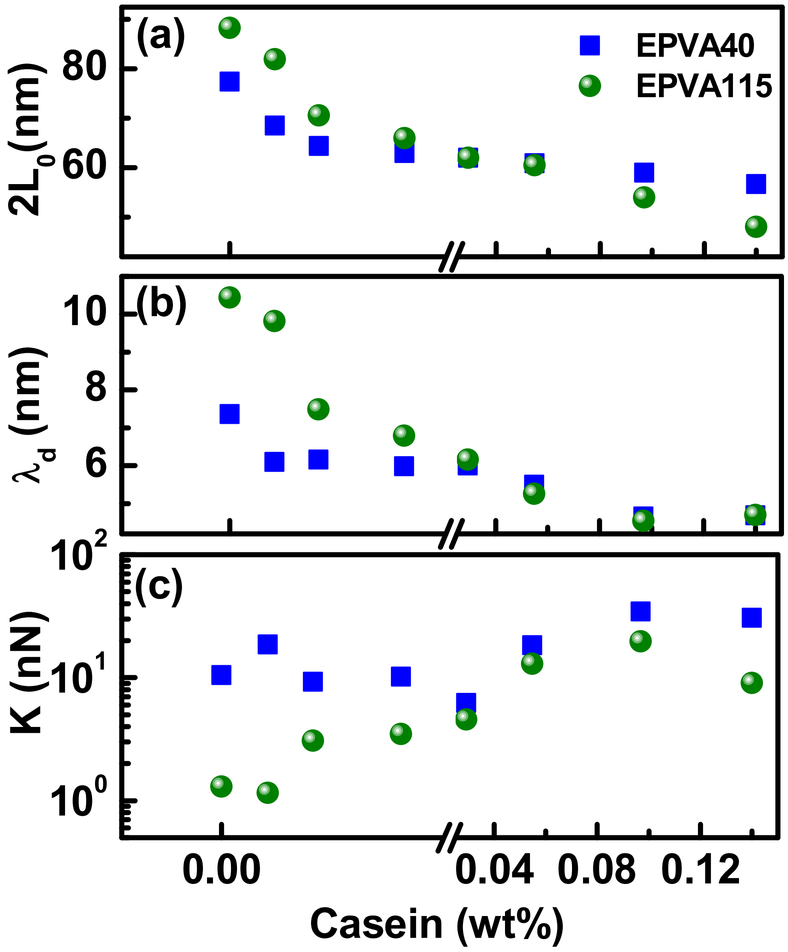

**Figure 6.5** (a) First interaction length ($2L_0$), (b) decay length ($\lambda_d$) and (c) force magnitude (K) for *EPVA40* (square) and *EPVA115K* (sphere) as a function of casein concentration.

**Fig. 6.6** shows the autocorrelation function, hydrodynamic diameter and zeta potential for different casein concentration for *EPVA40* emulsion. All the measurements were carried out at 25 °C and the result plotted is the average of 45 measurements. The average hydrodynamic diameter of the emulsion droplets with 0, 0.01, 0.02, 0.04, 0.07, 0.14 and 0.21 wt% casein are 295, 284, 280, 270, 264, 244 and 189 nm, respectively.

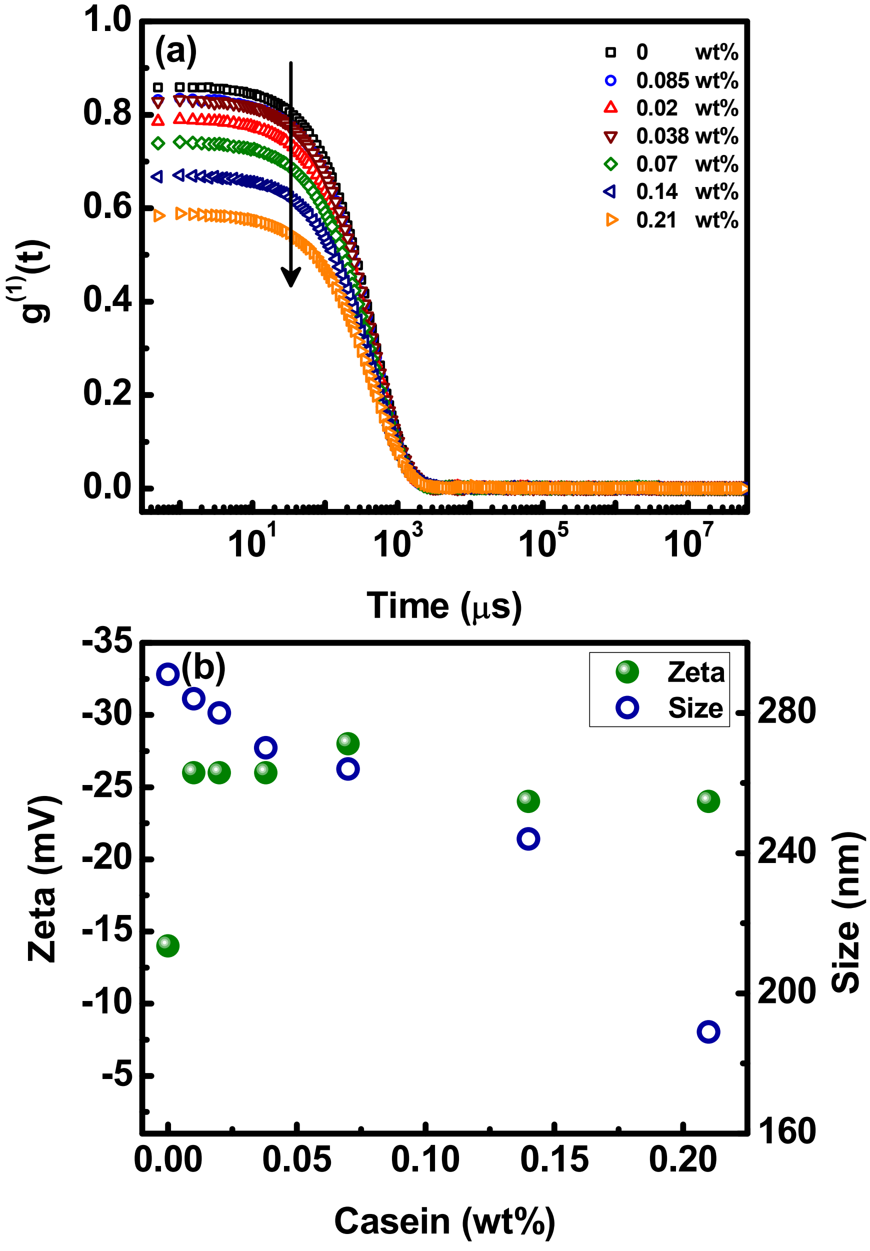

**Figure 6.6** (a) Auto correlation function as a function of time at different casein concentrations (b) hydrodynamic diameter (open symbols) and zeta potential (solid symbols) for *EPVA40* emulsion (pH 6.53) as a function of casein concentration. The arrow (in **Fig. 6.6a**) indicates the increase in casein concentrations.

Up to 0.04 wt% of casein, the hydrodynamic diameter distribution was narrow and monomodal but on further increase in casein concentration, the distribution became broad (100-300 nm), though the peak remains monomodal. The significant reduction in the hydrodynamic diameter (~ 120 nm less) with 0.21 wt% of casein, unambiguously confirms the competitive adsorption of casein by displacing the adsorbed polymer molecules at the oil-water interface. Obviously, such displacement of adsorbed polymers should lead to a reduction in the $2L_0$ values due to absence of extended polymer trains, loops and tails from the O/W interface, which is in excellent agreement with our results. To confirm this further, we have carried out the zeta potential measurements with different casein concentration and the results are shown in the **Fig. 6.6b**. Though the oil-in-water emulsion droplets are washed and incubated with polymers, some residual negative charges are present at interfaces due to the usage of anionic surfactant during the emulsification process, which gives rise to the observed negative zeta potential value of ~ -15 mV (pH 6.53). When casein concentration is increased to 0.01 wt%, the zeta potential value increases to - 26 mV and remains constant thereafter. Among the four major protein components $\alpha_{s1}$-casein, $\alpha_{s2}$ -casein, $\kappa$-casein and $\beta$-casein, $\alpha_{s1}$ – casein and $\beta$- casein are the main individual components coexisting at oil-water interfaces.[230] Our results are in good agreement with the earlier findings that both $\alpha_{s1}$-casein and $\beta$ -casein molecules can absorb strongly and coexist at oil-water interfaces.[214, 235]

Therefore, the adsorption of casein molecules at the O/W interface by replacing the pre-adsorbed PVA-vac molecules is evident from the increase in the zeta potential and the decrease in hydrodynamic diameter with increasing concentrations of casein. From earlier studies, it was concluded that the adsorbed $\beta$ -casein has an extended long tail in aqueous medium, whereas the $\alpha_{s1}$-casein forms a short loop at the interface and the interaction between β -casein adsorbed interfaces is strongly repulsive at all ionic strengths due to contributions from steric and electrostatic forces.[230, 255-256] The net repulsive interaction observed in the present study shows that the β -casein adsorbed at the oil water interface contributes to the repulsion, as the interaction between $\alpha_{s1}$-casein covered interfaces is attractive.

**Fig. 6.7** shows the hydrodynamic diameters of pure casein, *ESD0.8* without and with casein, *EPVA40* emulsion without and with 0.21 wt% casein. The average hydrodynamic diameter of pure casein, *ESD0.8* and *EPVA40* emulsion are 115, 190 and 294 nm, respectively. On addition of 0.21 wt% casein, the average hydrodynamic diameter of *EPVA40* emulsion is reduced and the distribution becomes broader. Here, the average diameter was 190 nm, with a distribution ranging from 100 to 300 nm. No change in the hydrodynamic diameter is observed on adsorption of casein at *ESD0.8* emulsion. The larger hydrodynamic diameter distribution for *EPVA40* with casein shows the conformational changes of adsorbed PVA-vac, which originally forms a loop-train-tail conformation where the vac part of the polymer chains remain inside the oil core and the PVA segments form a thick adsorbed layer and extend into the solution as loops and tails. Here, some loosely bound polymers may bind to other free polymer coils through casein linkers. The observed variation in the hydrodynamic diameters with different additives and adsorbing moieties can also be explained in terms of the mixing of two different sizes.

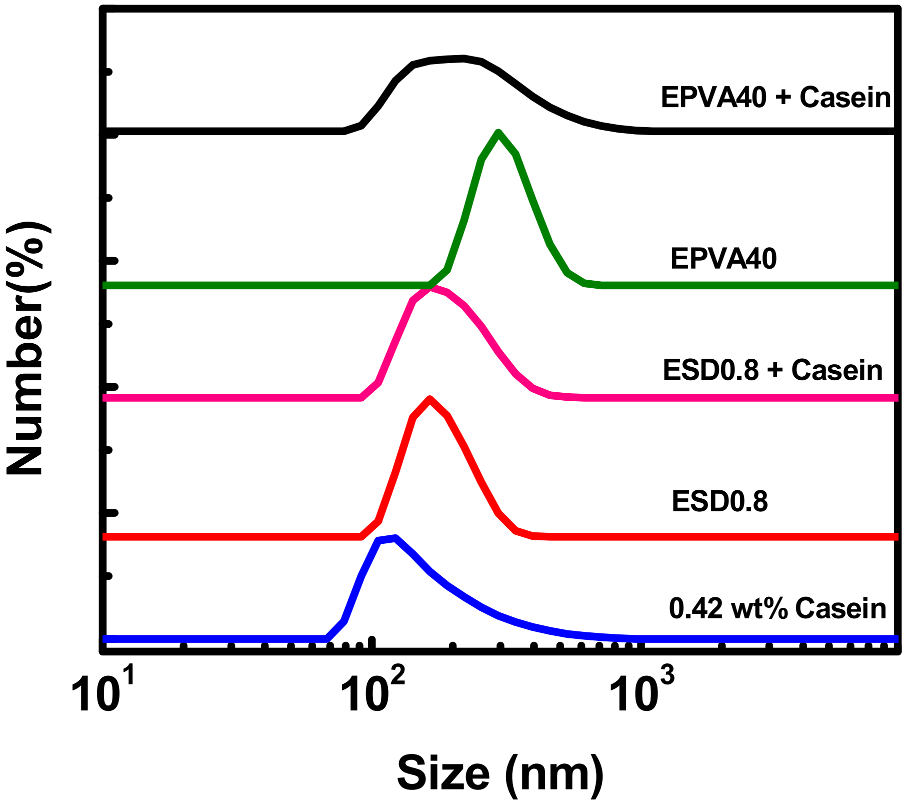

**Figure 6.7** Hydrodynamic diameter distribution of casein, *ESD0.8* emulsion without and with 0.004 wt% casein, *EPVA40* emulsion without and with 0.21 wt% casein.

Why do the low molecular weight casein molecules displace the pre-adsorbed PVA-vac and adsorb at the oil-water interface? It is known that the competitive displacement adsorption at an interface pre-adsorbed with polymer chains can be initiated by smaller or chemically different displacer molecules where the conformation and the nature of interactions between surfaces and polymer chains, surfaces and solvents, and solvents and polymer chains are the important parameters influencing such competitive displacement adsorption.[257] Casein has a disordered structure, which resembles a random coil polymer.[235]

Cohen Stuart et al.[258] showed that the complete displacement of adsorbed polymer by the displacer molecule is favorable, if the desorption energy of the displacer molecule is greater than or equal to the adsorption energy of the polymer segment, which was derived from the critical displacer concentration, $\phi_{cr}$, at which the polymer surface excess just vanishes. According to theory, the displacer adsorption energy is given by, [243, 258]

$$\chi_s^{pd} = \ln\phi_{cr} + \chi_{sc} - \lambda_1 \chi^{pd} - (1-\phi_{cr})(1-\lambda_1)\Delta\chi^{do} \tag{6.1}$$

where, $\lambda_1$ represents the fraction of contacts that a lattice site makes with sites in one of the adjoining layers and $\Delta\chi^{do}$ is the combined solvency parameter defined as,

$$\Delta\chi^{do} = (\chi^{po} - \chi^{pd} - \chi^{do}) \tag{6.2}$$

The superscripts of the $\chi$-parameters '*po*', '*pd*' and '*do*' correspond to the contact free energies between polymer and solvent, polymer and displacer, and displacer and solvent, respectively. The adsorption of flexible polymers at interfaces is governed by the free energy of mixing of polymer and solvent, represented by Flory-Huggins parameter, and the free energy associated with the formation of polymer-surface contacts and the concomitant breaking of solvent-surface contacts.

The hydrodynamic diameter and zeta potential data suggest that a very low concentration of casein (0.01 - 0.2 wt%) is sufficient for the complete displacement of adsorbed polymers (~ 0.6 wt%) from the O/W interface. The force measurement, hydrodynamic diameter and zeta results suggest that casein form a patchy coverage on SDS covered O/W interface whereas they vividly adsorb at O/W by displacing the larger PVA-vac polymer molecules.

### 6.3.3 Proposed Interaction Mechanism

Based on our results, the conformation of polymer, surfactant and casein at O/W interface along with the experimentally obtained Bragg peak positions at various concentrations of casein are schematically represented in **Fig. 6.8**.

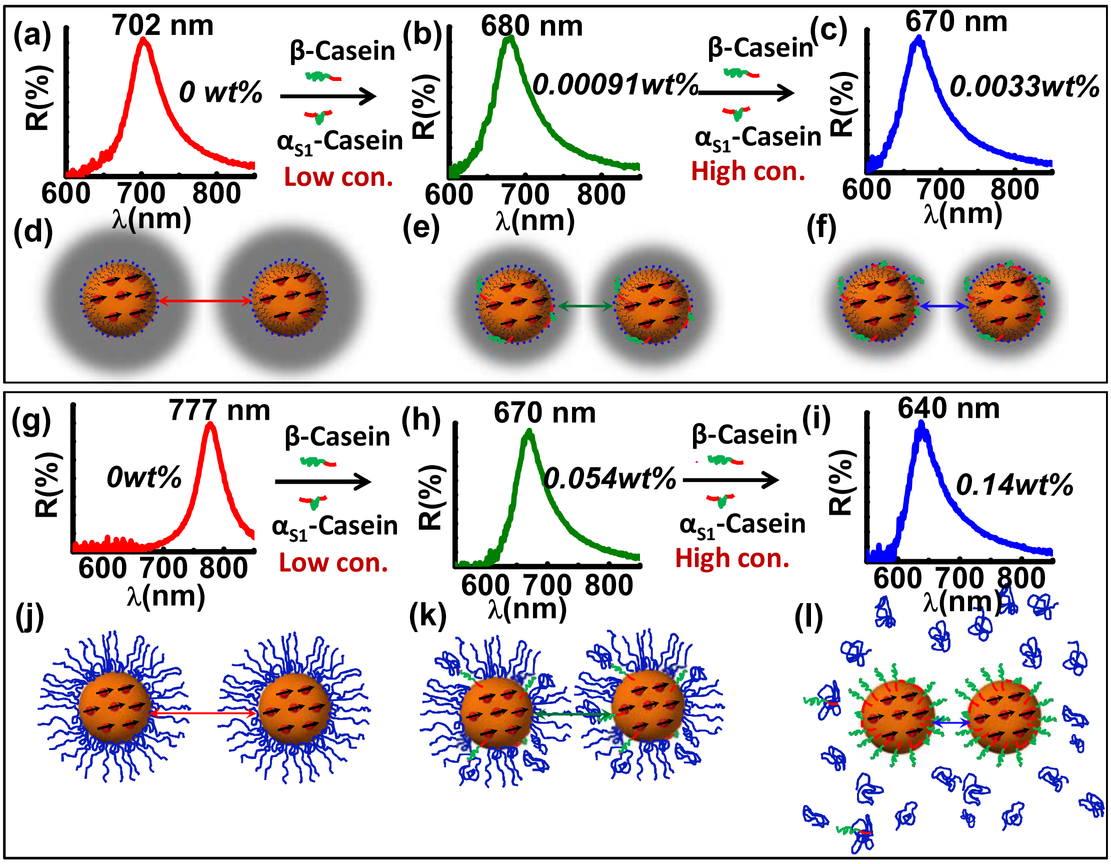

**Figure 6.8** Bragg peak at different casein concentrations at a fixed magnetic field of 126 gauss and the schematic representation of β-casein and $\alpha_{s1}$ casein conformation at the oil-water interface. (a-c) Diffraction peak at 0, 0.00091 and 0.0033 wt% casein (d-f) and the corresponding schematic representation of the interdroplet spacing. (g-i) & (j-l) shows diffraction peaks at 0, 0.054, 0.14 wt% casein and the schematic representation of casein conformation at PVA-vac interface.

**Fig. 6.8 a-c** show the diffraction peak without and with different casein concentrations in SDS stabilized emulsion and **(d-f)** shows the corresponding changes in the interdroplet spacing. With increasing concentrations of casein in the dispersion, casein molecules form a patchy coverage at O/W interface due to the hydrophobic interactions.[252] **Fig. 6.8 (g-i)** show the diffraction peak without and with different casein concentrations in PVA-vac stabilized emulsion and **(j-l)** shows the corresponding changes in the interdroplet spacing. With increasing concentrations of casein in the dispersion, casein displaces PVA-vac and adsorb at the O/W interface. Our equilibrium force, hydrodynamic diameter and zeta potential results suggest that casein molecules are excellent displacers for replacement of adsorbed macromolecules at O/W interface.

## 6.4 Conclusions

The competitive displacement adsorption of casein at polymer stabilized O/W emulsion droplet interface has been studied using in situ equilibrium intermolecular force measurements. A significant change in the force distance profiles under competitive displacement adsorption of casein at an O/W interface is observed. With addition of casein in PVA-vac diblock polymer stabilized emulsion, the onset repulsion decreases from 88 to 48 nm whereas the force decay length (~10.5 nm) is reduced to 4.5 nm upon the addition of casein, which provides unambiguous evidence for the replacement of extended polymer coils by smaller sized casein molecules. The hydrodynamic diameter and zeta potential results, corroborate the observed casein mediated polymer displacement and adsorption of casein at O/W interface. In the case of anionic surfactant covered interfaces, a feeble change in the onset of repulsion and force profiles are observed, which suggest that some casein molecules coexist with the surfactant covered O/W interface. Our results suggest that the casein molecules are effective displacers for replacement of adsorbed macromolecules from emulsion interface, which may find several important practical applications for reuse of formulations.

# Chapter- VII

## Role of Ionic Structure on the Adsorbed Macromolecular Conformation at Oil-Water Interface

# 7 Role of Ionic Structure on the Adsorbed Macromolecular Conformation at Oil-Water Interface

## 7.1 Introduction

Adsorption and conformation of polymers at different interfaces in the presence of ions that are common in natural environments are very important from practical application point of view (e.g. colloidal assembly, protein folding, enzyme activity, bacterial growth and transport across membranes, etc.) and have been an area of intense research both experimentally and theoretically over the last four decades.[210, 259-262] The tremendous interest in such studies stems from the biological implications of specific ion effect in living systems, which is abundant with macromolecular assemblies containing amphiphilic molecules and water.[262-266] The specific ion effects and hydrophobic effects greatly influence the membrane formation, interfacial contact thickness, and stability of structures.[267-268] Also, hydrated highly charged metal ions play critical roles in mineral formation and extraction, biochemical reactions and in the transport of toxic materials.[269] The understanding of specific ion effects is still elusive because of complicated solvation structure near interfaces.[268] The recent advances in high-resolution atomic force microscopy with atomic level precision made it possible to directly visualize the adsorption of various ions to solid surfaces in contact with aqueous electrolytes.[270] The indirect techniques such as attenuated total reflection Fourier transform infrared (ATR-FTIR) spectroscopy and vibrational sum frequency spectroscopy (VSFS) have been extensively used to study the association between different molecules, and the chloride salts of different valencies in bulk solution.[268] In addition, X-ray photoelectron spectroscopy,[271] second harmonic (SH) generation,[268] resonant SH reflection[272] and sum frequency generation[264, 273] measurements have been used to probe the interfacial structures in the presence of various ions. Recently, the effect of anions on the phase behaviors of a triblock copolymer was investigated with an automated melting point system.[274]

As polymers along with other additives (e.g., surfactant, nanoparticles and cations of different valencies) are used as stabilizers and rheological modifiers of industrial formulations (e.g., food, pharmaceuticals, personal care products, cosmetics ), it is important to understand the intermolecular and surface forces between interfaces, adsorbing polymers, solvent molecules and other additives. Irrespective of intense research efforts, the experimental data on macromolecular conformational changes at interfaces in the presence of specific ions is limited mainly because of the lack of experimental tools and the very complex intermolecular and surface forces between macromolecule covered interfaces.[275] The phase behavior and the stability of colloidal dispersions are strongly influenced by adsorbing moieties such as cations, anions and neutral materials.[125, 274] Measurement of interaction forces such Van der Waals, electrostatic, steric, hydrophobic, and hydrogen bonding provide better insight into the complex interaction between various components in aqueous dispersions. Although the effect of surfactant and free polymers on inter surface forces between polymer adsorbed droplets are studied,[49, 80-82] the effect of cation valency on forces between polymer covered O/W interfaces is not studied.

Here we report the effect of cation valency on the intermolecular force between neutral polymer stabilized emulsion droplets using magnetic chaining technique. The questions we try to address from this study are the following: (1) How do cations in solutions interact with adsorbed polymers at an O/W interface? (2) Can cation interaction lead to desorption of adsorbed polymers from the interface? (3) How the polymer conformation at O/W an interface is altered by cations? (4) What is the effect of cation valencies on such interaction forces and the stability of emulsions? As hydration of ions is crucial in colloidal formulations,[276] lubrications,[277] protein folding,[260] adhesion and growth of bio-films,[278] phase transition in polymer solutions[125] and biological activities,[279] this study provides better insight into the role of hydrated ions on interaction forces and the stability of emulsions.

## 7.2 Materials and Methods

*EPVA40* and *EPVA155* emulsions are used in this study. The experiments were carried out by varying the $Na^+$, $Ca^{2+}$, $Ni^{2+}$, $Mn^{2+}$ and $Fe^{3+}$ concentrations from 0 to 5 mM. Emulsion preparations, materials description and MCT apparatus and the working principle and schematic experimental setup of MCT are described in *Chapter II*.

## 7.3 Results and Discussion

### 7.3.1 Effect of Cations on Interaction Forces

#### ***EPVA40***- Cation Interaction

The measured force-distance profiles with $Na^+$, $Ca^{2+}$ and $Fe^{3+}$ at different concentrations for *EPVA40* emulsion is shown in **Fig. 7.1(a-c)**. At all concentrations, the force profile decays exponentially with interdroplet spacing and the onset of repulsion shifts to a shorter distance with increasing cation concentration. When two polymer covered surfaces approach each other, they experience a force when the inter-surface separation is below the radius of gyration of the adsorbed polymer ($R_g$). This interaction usually leads to a repulsive osmotic force due to the unfavorable entropy of adsorbed polymers.

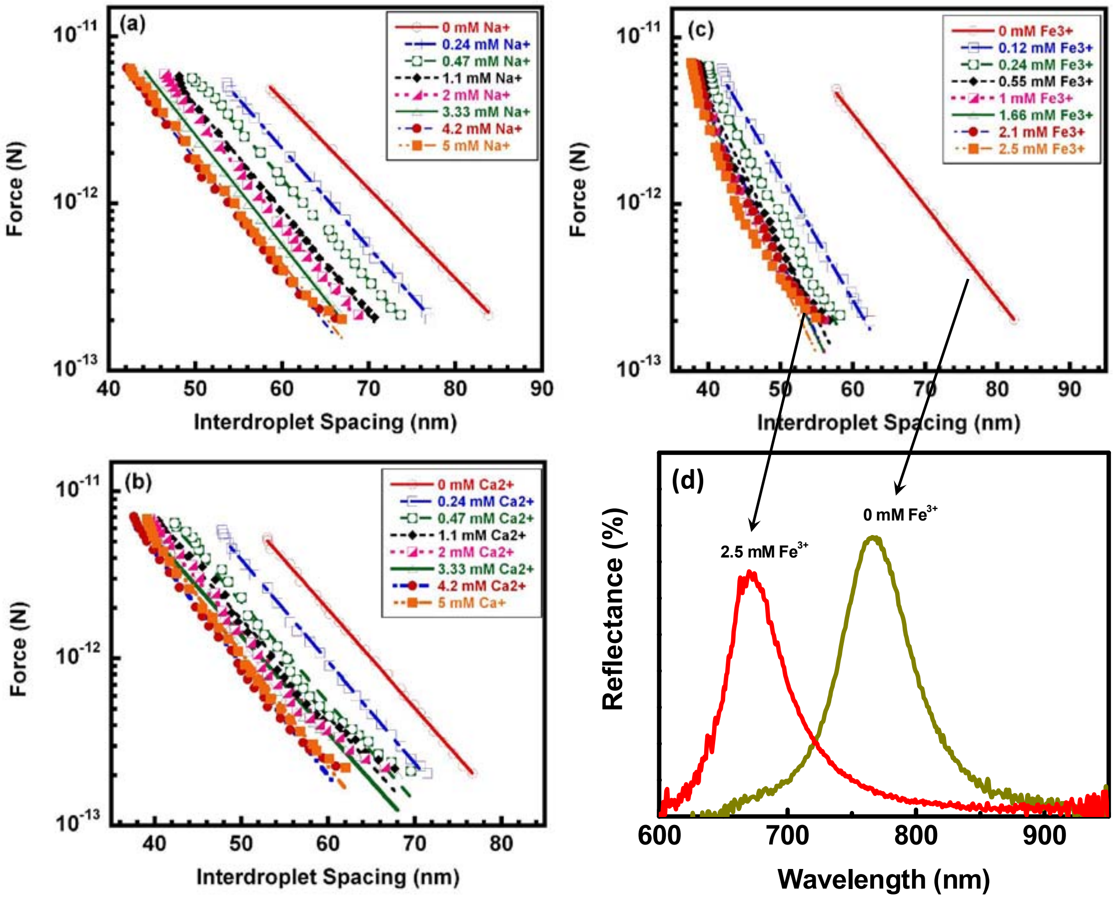

**Figure 7.1** Measured force distance profiles for *EPVA40* emulsion at different cation concentrations of (a) Na$^{+}$ (b) Ca$^{2+}$ and (c) Fe$^{3+}$. The best fit of **Eqn. 1.37** is shown by the solid lines (d) The Bragg peak at 90 gauss for the lowest and the highest ion concentration.

Below the overlapping concentration, each polymer chain interacts with the opposite surface independent of the other chain. Over the distance regime of h = 8 $R_g$ to 2 $R_g$ the repulsive force is roughly exponential.[67] The force profile for sterically stabilized system can be represented by **Eqn. 1.37**.

For sterically stabilized systems, the mean field and scaling approach distinguishes the loops and tail sections of the adsorbed chains that involves three length scales, namely the adsorbed layer thickness '$\lambda$', adsorption length z* that separates the regions where the monomer concentration is dominated by loops and by tails and a microscopic length 'b' that is inversely proportional to the adsorption strength,[70] proportional to $R_g$ and weakly dependent on the adsorption strength and the polymer concentration. At distances larger than '$\lambda$', the concentration is dominated by the tails and the force is always repulsive and exponentially decaying with distance. The di-block copolymers are often found to have mushroom or brush conformations, as one of the blocks binds to the interface and the other protrudes into the water to form a diffuse polymer layer.[280] The range of steric effects is many times of $R_g$, due to finite size of confined segments (excluded volume effect) and from hydration layers. Such steric forces having a range greater than 10 $R_g$ in aqueous solutions was reported.[281]

With increasing cation concentration and valency, the interdroplet distance decreases significantly. The experimental data points are fitted with Eqn**. 1.37** (solid line in **Fig. 7.1**) and from the best fit, $2L_0$, $\lambda_d$ from the slope and force magnitude $K$ values are extracted. To show the dramatic change in the onset of repulsion upon addition of 2.5 mM $Fe^{3+}$, the Bragg peak at 90 gauss is shown in **Fig.7.1 d**. The variation of $\lambda_d$, $2L_0$ and the $K$ for *EPVA40* emulsions as function of $Na^+$, $Ca^{2+}$ and $Fe^{3+}$ concentration is shown in **Fig. 7.1**. Without added cation, the characteristic decay length is ~ 8.5 nm, which is very close to the $R_g$ (8nm) value of the free polymer. At 5 mM concentration of $Na^+$ and $Ca^{2+}$, the decay length values are 8.5 to 7.5 nm, respectively. With the addition of 0.12 mM $Fe^{3+}$, we observed a drastic decrease in the decay length from 8.2 to 6 nm, which is further reduced to 5 nm at 5 mM $Fe^{3+}$ (**Fig. 7.2a)**. Though the $\lambda_d$ shows less variation with cation concentrations, the $2L_0$ is highly sensitive to the cation concentration and valency. Without cations, the $2L_0$ is ~80 nm, which is ≈ 10 $R_g$ and it is in excellent agreement with the SFA measurements.[282]

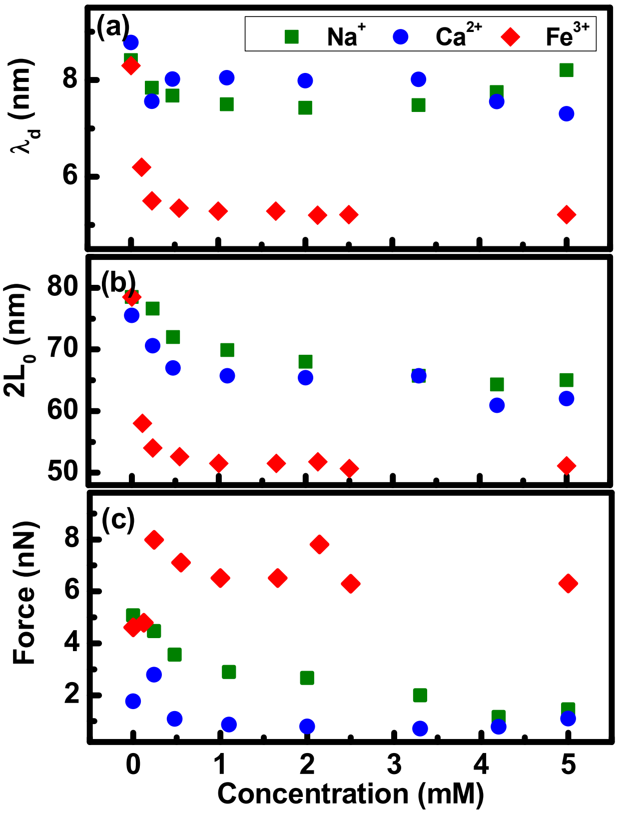

**Figure 7.2** Variation of (a) decay length (b) onset of repulsion and (c) force magnitude for *EPVA40* as function of $Na^+$, $Ca^{2+}$ and $Fe^{3+}$ concentration.

In good solvent conditions, the onset repulsion is observed at 10-15 $R_g$ for polymer bearing mica surfaces.[282] For grafted polymers at high surface coverage, where one end is attached to the surface and the other end extends into the medium, the equilibrium surface interaction remains monotonically repulsive at all surface coverage.[56] The measured $2L_0$ and force magnitudes at different cation concentrations for all the three ions are shown in **Fig. 7.2(b-c)**. At a low concentration of 0.24 mM $Na^+$, the onset repulsion decreases from 83 to 76.6 nm and this is further reduced to 65 nm as the concentration is increased to 5 mM. For $Ca^{2+}$, the $2L_0$ values are 70.6, 67, 65.7, 65.4, 65.7, 60.9 and 62 nm for 0, 0.24, 0.476, 1.1, 2, 3.3, 4.2 and 5 mM, respectively. For 0.14 mM $Fe^{3+}$, the onset repulsion decreases from 80 to 58 nm and this is further reduced by another 4 nm as the concentration is increased to 0.24 mM. The $2L_0$ value was 51 nm at 1 mM $Fe^{3+}$, which remains unchanged up to 5 mM. The force magnitude increases slightly with increasing cation concentration and cation valency.

### ***EPVA155*- Cation Interactions**

The measured force distance profiles for *EPVA155* emulsion at different concentrations of $Na^+$, $Ca^{2+}$ and $Fe^{3+}$ is shown in **Fig. 7.3 (a-c)**. The force profiles decay exponentially with interdroplet distance similar to the *EPVA40* emulsion.

Without cations, the $\lambda_d$ value obtained from the best fit is 14.5 nm which is close to $R_g$ (16 nm) value of the free polymer (PVA155K). At 5 mM $Na^+$ concentration, the $\lambda_d$ value is reduced to 12.5 nm. As observed in the case of *EPVA40*, the presence of $Na^+$ showed a less influence on $R_g$ compared to $Ca^{2+}$ and $Fe^{3+}$. For $Ca^{2+}$, $\lambda_d$ changes from 14 to 9.8 nm at 5 mM. At 0.24 mM $Fe^{3+}$, the measured $\lambda_d$ value is 11.5 nm, which is reduced to 8.5 nm at 4.7 mM and beyond which no significant change is observed. The $\lambda_d$ values corresponding to 0.24, 0.476, 1.1, 2, 3.3, 4.2 and 5 mM $Fe^{3+}$ are 11, 8.5, 8.5, 8.6, 8.5, 8.8 and 8.7 nm, respectively. The dramatic change in $2L_0$ is evident from the large shift in the Bragg peak after the addition of 5 mM $Fe^{3+}$ (**Fig. 7.3d**). The observed trend in the onset repulsion is similar to that of *EPVA40* and the effect was stronger for cation with higher valency.

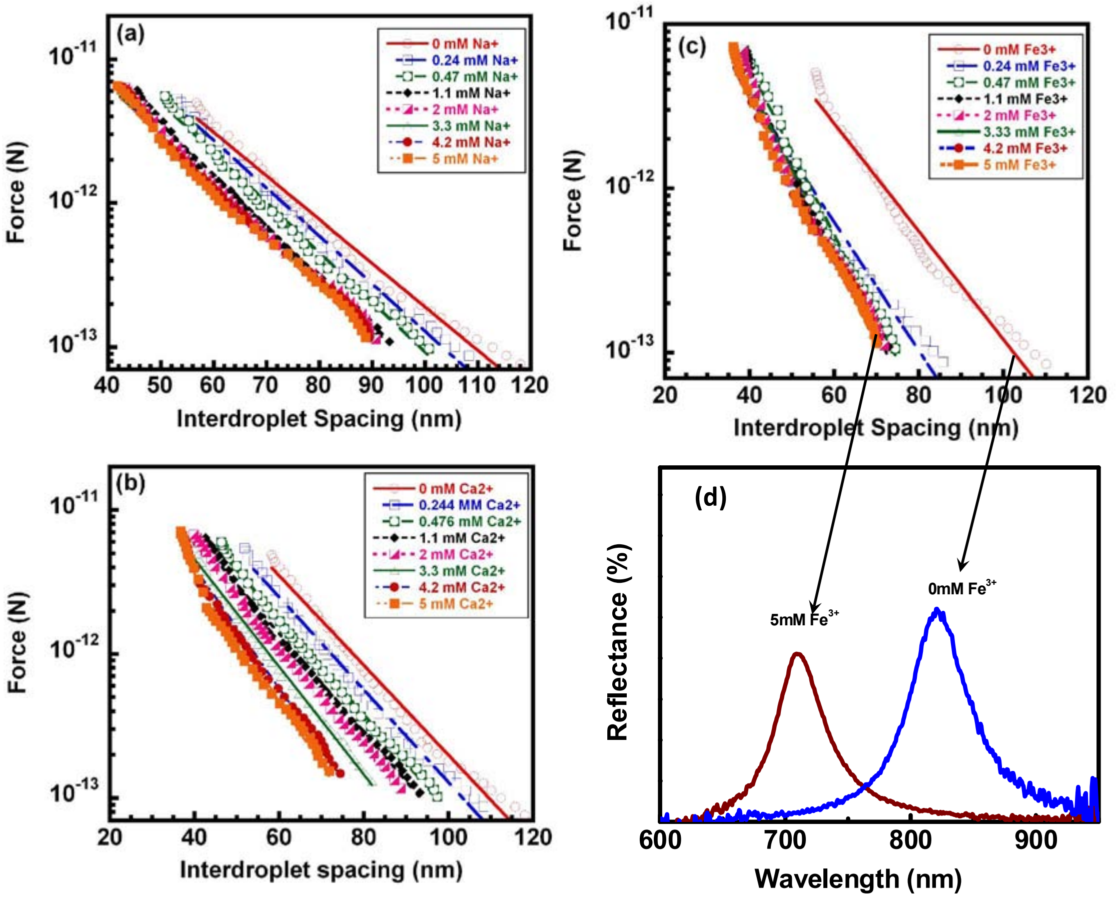

**Figure 7.3** Measured force distance profile for *EPVA155* emulsion at different concentrations of (a) $Na^+$ (b) $Ca^{2+}$ and (c) $Fe^{3+}$. The best fits are shown by the solid lines. (d) The Bragg peak positions at a field value 90 Gauss for the lowest and highest ion concentration.

**Fig. 7.4(a-c)** shows the variation of decay length, first interaction length and force magnitude, respectively for *EPVA155* as a function of different cation concentrations. In the absence of cations, the $2L_0$ value was 75.5 nm ($\approx 6R_g$). With 5 mM $Na^+$ and $Ca^{2+}$, it decreases to 77.4 nm (5.5 $R_g$) and 65 nm (4.6 $R_g$), respectively. The decrease in $2L_0$ with $Fe^{3+}$ concentration was much steeper compared to $Na^+$ and $Ca^{2+}$. For 0.24 mM $Fe^{3+}$ concentration, the $2L_0$ is reduced to 66 nm (4.7 $R_g$), which became 61 nm (4 $R_g$) at 5 mM. The force magnitude change was also akin to that of *EPVA40*. The change in the force parameters follow the order $Fe^{3+}$ > $Ca^{2+}$ > $Na^+$ for both *EPVA40* and *EPVA155*. The force measurements are also carried out with $Mn^{2+}$ and $Ni^{2+}$ where a similar variation in the force parameters with cation valency is observed.

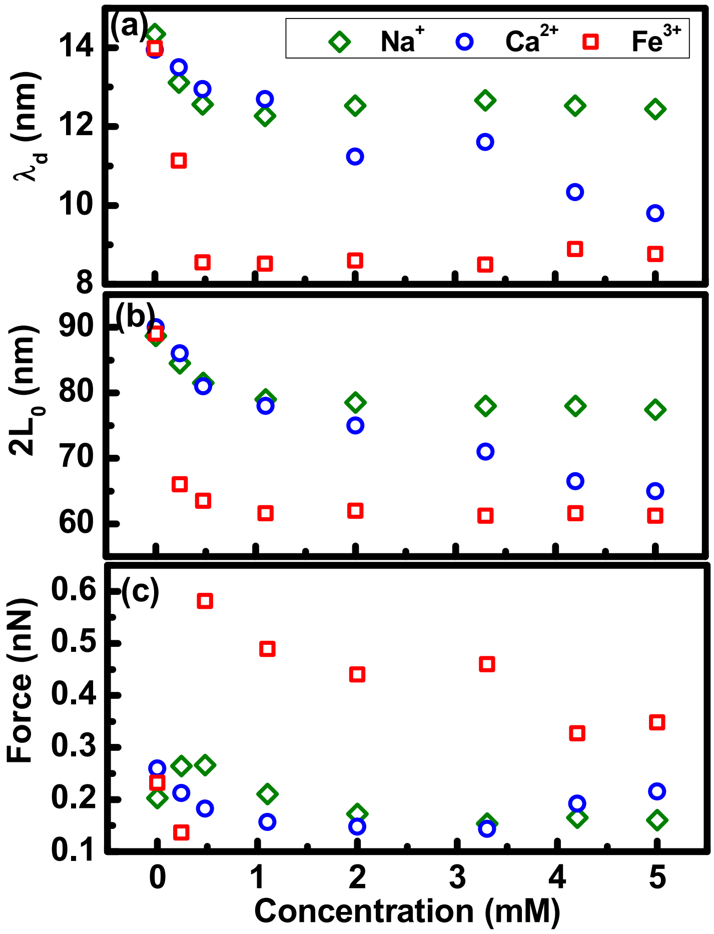

**Figure 7.4** Variation of (a) decay length ($\lambda_d$) (b) onset of repulsion ($2L_0$) and (c) force magnitude (K) for *EPVA155* as a function of different cation concentrations.

The interaction of ions with water molecules affects the equilibrium properties of solutions and kinetic properties like viscosity, electrical conductivity, diffusion, etc. The hydration process involves the binding of a certain number of water molecules of the solution (hydration numbers) and the translational motion of the water molecules close to the ions and the exchange of water molecules in close proximity of the ions and the associated change in activation energy.[283] The hydration enthalpy ($\Delta H_{hydr}$) of an ion (i.e. the enthalpy change which accompanies the dissolution of one mole of the ideal gaseous ion in an infinite volume of water at a temperature and a pressure of 298 °K and 1 atm, respectively) depend on the polarizing power of the ion. But the polarizing power of a cation does not depend on its charge and crystal radius alone.[284] The thermodynamic hydration parameters used to describe the properties of ions are enthalpy ($\Delta H_{hydr}$) and Gibbs free energy ($\Delta G_{hydr}$).[283] It also involves heat capacity at constant pressure, entropy and volume (aq, ion). Empirical equations for hydration energies are given by Born equations ,[285]

$$\Delta G_{hyd} = -\frac{N_A e^2 z^2}{2r_{ion}}\left(1-\frac{1}{\varepsilon}\right) = -677.808\frac{z^2}{r_{ion}{}^2} \text{ kJ mole}^{-1} \tag{7.1}$$

$$\Delta S_{hyd} = \frac{N_A e^2 z^2}{2\varepsilon r_{ion}}\left(\frac{\partial \ln \varepsilon}{\partial T}\right)_p = -39.421\frac{z^2}{r_{ion}} \text{ JK}^{-1}\text{mole}^{-1} \tag{7.2}$$

where, '$z$' is charge of the ion, '$r_{ion}$' is the radius of the central ion plus the diameter of the water molecule, '$\varepsilon$' is the dielectric constant of water, '$N_A$' is the Avogadro number. One of the empirical equations for hydration enthalpy of $M^{Z+}$ ion is given by,[286]

$$\Delta H^0_{hyd} = \frac{930(z-0.2)^2}{r+1(1/2z)} \text{ kJ mole}^{-1} \tag{7.3}$$

Both $\Delta G_{hydr}$ and $\Delta H_{hydr}$ are inversely proportional to ionic radius.[125, 286]

In the present study, we have used chloride salts in water environment to probe the effect of cations valency on inter colloidal interactions. It is known that the $Cl^-$ binds to the oil-water interface and increase the interfacial tension.[274] Cations interact with polymers in three different ways: direct binding of cations to the oxygen in the polymer chain, cation sharing one water molecule with the polymer in their first hydration shell and cation interacting with the polymer via two water molecules in the first hydration shell.[125, 287] The hydration of cations and anions are different because of different orientations of the water molecules in their first hydration shells. During hydration, water molecules turn their oxygen atoms, with one of the two lone pairs of electrons. The water molecules and cations act as donors and acceptors, respectively and coordinate bonds of transition metal cations dictate the geometry of the first hydration shell. The hydration of large ions is different from mono atomic ones due to hydrophobic hydration. Beyond the hydration layer, the ion interacts electrostatically with the water.

**Table 7.1** presents ionic radii, hydration number and other thermodynamic parameters for different ions under study. The hydration number and the ionic radius follow the order $Fe^{3+} > Ni^{2+} > Mn^{2+} > Ca^{2+} > Na^{+}$. Hydration number gives the information about the number of water molecules in the vicinity of the ion.[283] For small or multivalent ions in highly polar solvents such as water, the strong orientational dependence of their ion-dipole interaction leads to the orientation of solvent molecules around them.

**Table 7.1** Different thermodynamic properties of hydration, hydration number and ionic radius values of different cations used in the present study.[283]

| **Ionic Properties** | **$Na^+$** | **$Ca^{2+}$** | **$Mn^{2+}$** | **$Ni^{2+}$** | **$Fe^{3+}$** |
|---|---|---|---|---|---|
| Ionic radius (pm) | 102 | 100 | 83 | 69 | 65 |
| $\Delta S_{hydr}(JK^{-1}mol^{-1})$ | -111 | -252 | -292 | -351 | -557 |
| $\Delta H_{hydr}(kJ\ mol^{-1})$ | -416 | -1602 | -1874 | -2119 | -4462 |
| $\Delta G_{hydr}(kJ\ mol^{-1})$ | -375 | -1515 | -1770 | -1992 | -4271 |
| Hydration number | 3.5 | 7.2 | 8.7 | 10.4 | 16.6 |
| Water structure ($\Delta G_{HB}$) | -0.03 | 0.34 | 0.57 | 0.9 | 0.65 |

Thus, cations will have a number of water molecules orientationally bound to the hydrated cations and the number of water molecules bound is known as hydration number. Smaller ions are more hydrated due to their more intense electric field.[56] Since cations are strongly hydrated than the anions of the same valency, the residence time of water molecules in the primary hydration shells is typically $\sim 10^{-9}$ s, while divalent cations are more strongly solvated than monovalent cations and has a life time of $\sim 10^{-8}$ s; for trivalent it is in seconds or hours. In such cases the binding is so strong that ion-water complex is actually formed in stoichiometry. Water molecules in the first hydration shell interact directly with the charged ion (a solute solvent interaction), while secondary hydration shell interacts only with water molecules (solvent-solvent interaction) and only indirectly with the ion.[56] Among the mono, di and tri valent cations, $Na^+$ is weakly hydrated and has 3.5 water molecules to interact with polymer and probably this is the reason for the little influence of $Na^+$ on polymer collapse than other cations. Divalent cations and cations with high charge density have a tendency to bind electrostatically with polymer.[125, 284] The binding of divalent cations with polymer can create a local bridging between polymer chains, due to the interaction of two positive charges with two oxygen atoms belonging to different chains.[287]

With increasing cation concentration, we observe a significant reduction in the $2L_0$ and hard sphere distances (distance at which the force is maximum i.e. $10^{-11}$ N), which unambiguously confirms that the polymer chain undergoes a collapsed conformation. The order of conformation increases with the cation valency, which can be attributed to the stronger hydration and interaction that result in bridging of different polymer chains. Molecular dynamic simulations and X-ray absorption spectroscopic studies reveals that $Ca^{2+}$ ion can make conformational changes in the back bone of PVA by binding with seven oxygen from three PVA chains. The PVA – $Ca^{2+}$ complexation is due to the strong coulombic attraction between $Ca^{2+}$ and oxygen, which tends to pull the segment of chains together.[126] The substantial changes in the force parameters with the $Fe^{3+}$ ions can be attributed to the smaller size effect and higher hydration number. The strong binding of $Fe^{3+}$ ion to the PVA backbone may have resulted in the collapsed conformation of PVA chain than $Na^{+}$ and $Ca^{2+}$.

To check the effect of hydration of cations and their sizes on the adsorbed polymer conformation, we have plotted the change in $L_0$ ($\Delta 2L_0$) at four different concentrations as a function of different hydration parameters (**Fig. 7.5**). $\Delta 2L_0$ is the difference in $2L_0$ at the respective ionic concentrations to the $2L_0$ without added cation. Here, the $\Delta 2L_0$ value for *EPVA40* at 0.24, 1, 2 and 5 mM concentrations are plotted against the hydration entropy ($\Delta S_{hydr}$), hydration enthalpy ($\Delta H_{hydr}$), hydration Gibbs free energy ($\Delta G_{hydr}$) and ionic radius.

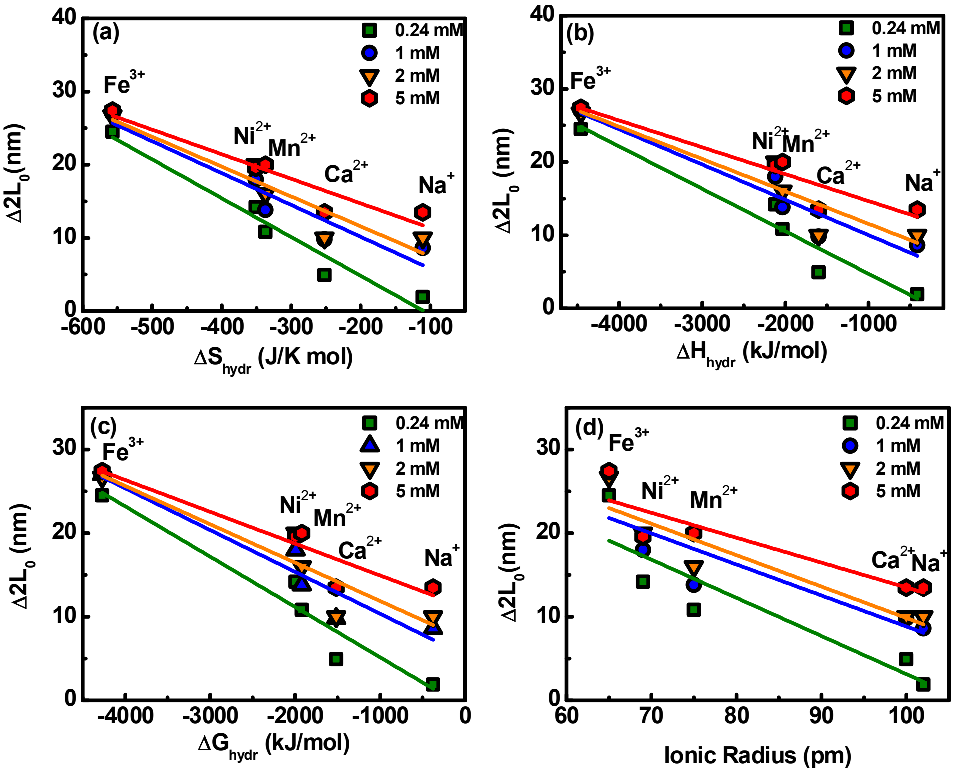

**Figure 7.5** Change in the onset of repulsion ($\Delta 2L_0$) at 0.24, 1, 2 and 5 mM cation concentrations as a function of different hydration parameters for *EPVA40* (solid line corresponds to linear fit to the data points). $\Delta 2L_0$ as a function of (a) hydration entropy (b) hydration enthalpy (c) hydration free energy and (d) ionic radius.

**Fig. 7.5** shows the $\Delta 2L_0$ as a function of hydration parameters and ionic radius for *EPVA40*. The $\Delta 2L_0$ varies linearly with the hydration enthalpy, with a slope of 0.029 for $Na^+$ and $Ca^{2+}$ whereas the slope was 0.02 for $Fe^{3+}$. This again confirms the weak interaction of PVA with poorly hydrated $Na^+$ as compared to well hydrated $Fe^{3+}$. The $\Delta 2L_0$ for *EPVA40* emulsion, changes linearly with hydration entropy and the slope values are -0.053, -0.0462, -0.0433 and -0.048 for 0.24, 1, 2 and 5 mM cations, respectively. For hydration enthalpy the slope values are -0.0058, -0.0052, -0.00482 and -0.0044 for 0.24, 1, 2 and 5 mM cations, respectively. For the hydration free energy, the slope values are -0.006, -0.0052, -0.005 and -0.00459 for 0.24, 1, 2 and 5 mM cations, respectively. For $\Delta 2L_0$ vs. ionic radius, the slopes are -0.456, -0.409, -0.37 and -0.375 for 0.24, 1, 2 and 5 mM cations, respectively.

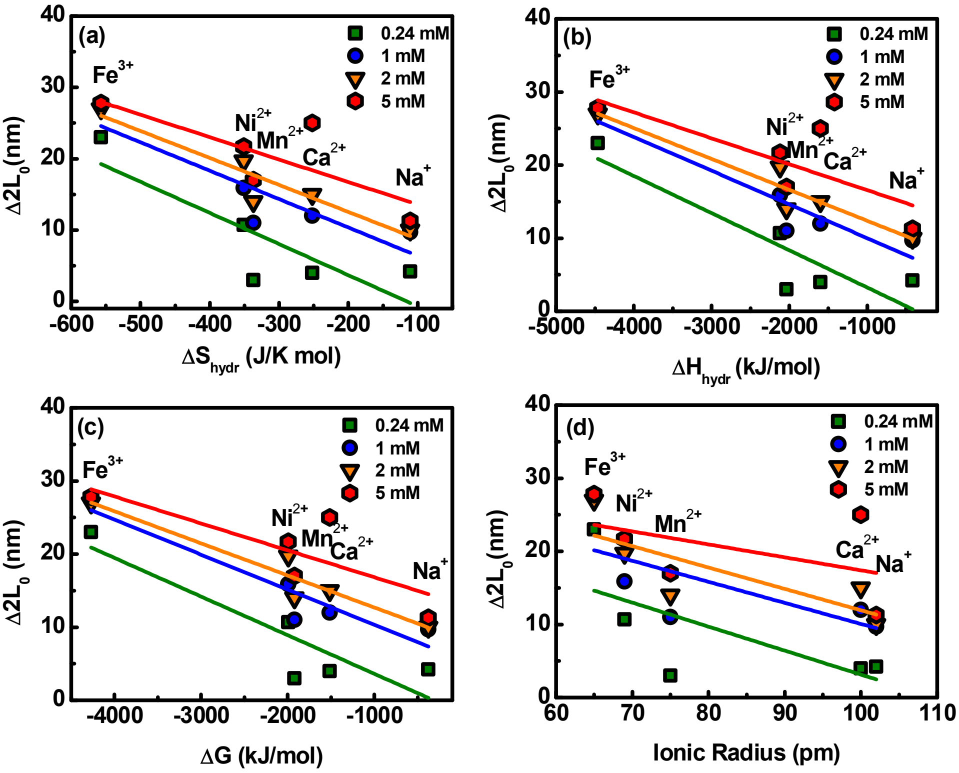

**Figure 7.6** Change in the onset repulsion ($\Delta 2L_0$) at 0.24, 1, 2 and 5 mM cation concentrations as a function of different hydration parameters for *EPVA155* (solid line corresponds to linear fit to the data points). $\Delta 2L_0$ as a function of (a) hydration entropy (b) hydration enthalpy (c) hydration free energy and (d) ionic radius.

A similar trend is observed for *EPVA155* (**Fig. 7.6**). The $\Delta 2L_0$ changes linearly with hydration entropy and the slope values are -0.045, -0.0418, -0.038 and -0.032 for 0.24, 1, 2 and 5 mM cations, respectively. For hydration enthalpy the slope values are -0.005, -0.0048, -0.0042 and -0.0035 for 0.24, 1, 2 and 5 mM cations, respectively. For the hydration free energy, the slope values are -0.0052, -0.00499, -0.0043 and -0.0036 for 0.24, 1, 2 and 5 mM cations, respectively. For $\Delta 2L_0$ vs. ionic radius the slopes values are -0.328, -0.316, -0.28, -0.292 and - 0.1773 for 0.24, 1, 2 and 5 mM cations, respectively.

It is established that the metal ion (for 2+ or higher ions), water bond is stronger than the hydrogen bonds in solution where the motion of the first shell hydrating waters is restricted and this strong interaction prevents the water in the first hydration shell to form acceptor bonds with the second hydration shell.[269] On the contrary, larger monovalent cations with smaller charge density have a weaker interaction with water molecules through electrostatic attraction.[125] Gel sieving chromatography experiment shows that $Na^+$ has 0.25 tightly bound water molecules [288] whereas for $Ca^{2+}$ and $Fe^{3+}$ have 2.15 and 6 tightly bound water molecules , respectively.[269, 289] The observed change in the $2L_0$ with the thermodynamic hydration parameters is in conformity with the interaction of strongly hydrated $Ca^{2+}$, $Fe^{3+}$ with OH group of polymer via two water molecules leading to larger conformational changes and the larger cations showing a salting-out effect.[125]

### 7.3.2 Proposed Interaction Mechanism

Based on our experimental findings, PVA conformation at the oil-water interface is schematically presented in **Fig. 7.7 (a-b)**. **Fig. 7.7b** shows a magnified view of the O/W interface where the hydrophobic Vac part goes into the oil phase and hydrophilic PVA part extends into water. Cations can interact with OH segment of polymer backbone via three ways; (c) direct binding (d) binding by sharing one water molecule and (e) binding by sharing two water molecules from the hydration shell.

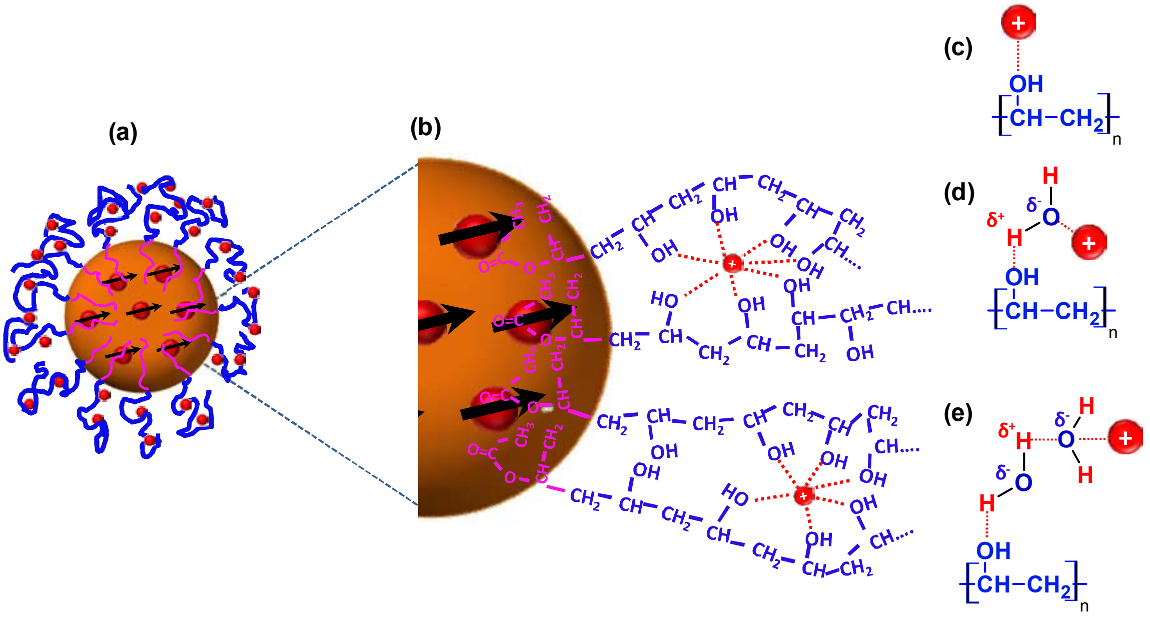

**Figure 7.7** (a) Schematic representation of polymer conformation on interaction with cations. (b) Enlarged view of cation – PVA interaction, cations bind with seven OH group from two polymer chains. Emulsion stabilized with PVA (blue)-Vac (pink), where hydrophobic Vac adsorb at the oil water interface and hydrophilic PVA chain extend into the water. (c-e) Three possible interaction mechanism of cation and the oxygen form PVA chain (c) direct binding (d) binding by sharing one water molecule and (e) binding by sharing two water molecules from the hydration shell.

## 7.4 Conclusions

The interaction forces between diblock copolymer covered oil-in-water nanoemulsion droplets in water in the presence of monovalent, divalent and trivalent chloride salts are studied using equilibrium force-distance measurements. With increasing cation concentration, decay length of exponentially decaying interdroplet force is reduced from the initial polymer radius of gyration ($R_g$) to 0.6 $R_g$ for $Fe^{3+}$ cations, where as the reduction was

~0.9 $R_g$, 0.8 $R_g$ for $Na^+$ and $Ca^{2+}$, respectively. The interdroplet distances at the minimum measurable repulsive force in the presence of $Na^+$, $Ca^{2+}$ and $Fe^{3+}$ cations at 0.24 mM for *EPVA40* stabilized emulsion were 76.6, 70.5 and 54 nm, respectively. A dramatic decrease in the magnitude force and the onset repulsion were observed on increasing the cation concentration and valency. Force measurement data suggested a collapsed conformation of polymers at O/W interface in the presence of hydrated ionic surface structures without total displacement of adsorbed polymers. A linear correlation between the first interaction length and the hydration thermodynamic properties of cations are compared. The possible conformation of polymers at O/W interface on cation interaction is proposed. The results of our studies may find useful applications in optimizing properties of industrial formulations and their long term stability.

# Chapter- VIII

## Conclusions and Recommendations for Future Work

# 8 Conclusions and Recommendations for Future Work

## 8.1 Conclusions

The repulsive interaction between emulsion drops is probed by measuring the in-situ equilibrium force-distance in the presence of analytes using magnetic chaining technique.

A large blue shift in the diffracted light is observed in the presence of interacting cations. The in-situ equilibrium force-distance measurement results show that the onset of repulsions and the magnitude of repulsive forces are strongly influenced by the presence of cations in parts per billion (ppb) to parts per million (ppm) levels. This suggests that cations screen the surface charges through the formation of both stern and diffuse electric double layer, and produces a dramatic blue shift in surfactant stabilized emulsion, whereas a dramatic conformational change  in the adsorbed polymer layer causes a reduction in the 1D array spacing in the diblock polymer stabilized emulsion.  The force-distance results are compared with the predictions of electrical double-layer and repulsive steric forces. The emulsion droplets show an excellent selectivity to $Ag^+$ due to its strong interaction of $Ag^+$ with the stabilizing moieties at the oil-water interface. The possible mechanisms of interaction of $Ag^+$ with surfactant and polymer are, (a) direct binding to the PVA backbone, (b) binding via sharing single water molecule and (c) bind via sharing two water molecules. . The dramatic decrease in the 1D array spacing in the presence of cations show promising practical applications in the development of optical sensors for selective detection of $Ag^+$ with ultrahigh sensitivity.

Methanol in ppm level gives rise to a red shift in the incident white light and a visually perceptible color change of the nanoemulsion. The origin of the red shift is studied by measuring the subtle changes in the intermolecular forces between emulsion droplets in the presence of methanol molecules. The diffusion of methanol molecules significantly reduces the dielectric constant of water, which extends the electric double layer and increases the droplet array spacing. The shift in the Bragg peak wavelength in the presence of methanol offers potential use of nanoemulsion for the detection of methanol in aqueous solution.

The equilibrium interdroplet distance between the emulsion droplets in a 1-dimensional array increases by several nanometers in the presence of glucose because of intermolecular hydrogen bonding of glucose with sodium dodecyl sulphate molecules at the oil-water interface that gives rise to a stretched lamellae-like structure. The observed large red shift in the diffracted Bragg peak (~50-100 nm) and the linear response in the glucose concentration range of 0.25-25 mM offer a simple, fast and cost effective non-enzymatic approach for glucose detection. From the insight into the 1D array spacing variation with different analytes, an interesting application of magnetic nanoemulsion for magnetic flux leakage (MFL) detection is also developed using nanoemulsions stabilized with different surface active molecules. The response of the nanoemulsions to the leaked magnetic flux from the defective region is exploited to locate the region where defect is present. In the presence of leaked magnetic flux, the nanoemulsion shows a visually perceivable color change due to changes in the interparticle spacing within the self-assembled nano-arrays. The detection methodologies to quantify the defect shape, location and dimensions are validated using specimens with simulated defects of different geometries in ferromagnetic materials.

The nature of forces involved in the surfactant-casein and polymer-casein interactions is probed by the equilibrium force distance measurement, dynamic light scattering and zeta potential measurements. A significant change in the force distance profiles was observed under the competitive displacement adsorption of casein, which is further confirmed from the hydrodynamic size and zeta potential measurements. On increasing the concentration of casein above 0.04 wt%, a saturation in the onset of repulsion and force parameters are observed because of the complete replacement of adsorbed diblock polymers by casein molecules. The hydrodynamic radii and zeta potential results corroborate the casein mediated polymer displacement and the competitive adsorption of casein at O/W interface. In the case of anionic surfactant covered interfaces, casein molecules weakly associate at the O/W interface without displacing the smaller size SDS molecules where no significant change in the onset of repulsion and force profiles are observed.

The interaction forces between diblock copolymer covered oil-in-water nanoemulsion droplets in water in the presence of monovalent, divalent and trivalent chloride salts are measured to understand the effect of hydrated ionic environment on the adsorbed macromolecular conformation. Without added cations, the interdroplet forces decay exponentially with a characteristic decay length comparable to the polymer radius of gyration ($R_g$). With 5 mM concentration of $Na^+$, $Ca^{2+}$ and $Fe^{3+}$ cations, the decay lengths were found to be ~0.9 $R_g$, 0.8 $R_g$ and 0.6 $R_g$ respectively. The interdroplet distances at the minimum repulsive interaction observed in presence of $Na^+$, $Ca^{2+}$ and $Fe^{3+}$ cations of the same concentration (0.24 mM) were 276.6, 270.5 and 254 nm, (284.5, 273, and 266 nm) respectively for *EPVA40* (*EPVA155*). On increasing the cation concentration and valency, a dramatic decrease in the magnitude force and the onset repulsion were observed. The observed change in the force parameters with increasing cation concentrations and valency suggested a collapsed conformation of polymers at O/W interface in the presence of hydrated ionic surface structures that interact with the OH group of polymer. However the hydrated ion environment has not resulted in the displacement of adsorbed polymers.

Key Findings are summarized below,

- Cation interactions with emulsions lead to a large blue shift in the diffracted wavelength, due to change in the interdroplet spacing. The order of increase of Bragg peak shift for different cations followed a sequence $Pb^{2+} < Ni^{2+} < K^{+} < Cu^{2+} < Mn^{2+} < Na^{+} < Cd^{2+} < Ca^{2+} < Ag^{+}$. Among various interfering cations, excellent selectivity is observed for $Ag^{+}$ due to strong interaction of hydrated $Ag^{+}$ with surfactant/polymer.
- The measurement of intermolecular forces in the presence of alcohol molecules shows that the diffusion of organic molecules into the electric double layer reduces the dielectric constant that results in an extended electric double layer and a red shift in the diffracted Bragg peak.
- The Bragg reflected light intensity from emulsion droplets show that the equilibrium interdroplet distance between the emulsion droplets is increased by several nanometers in the presence of glucose because of intermolecular hydrogen bonding of glucose with SDS molecules at the oil-water interface, which gives rise to stretched lamellae like structure.
- A new methodology to detect MFL signals to image morphologies of defects in ferromagnetic components is developed by using magnetically polarizable nanoemulsions, where the leaked magnetic flux from the defective region is found to alter the optical properties of nanoemulsions.

- Upon competitive displacement adsorption of casein, a decrease in the onset of repulsion and decay length are observed, indicating the replacement of extended polymer coils by the smaller size casein molecules. The greater adsorption energy of protein molecules than the PVA-Vac favors the competitive displacement adsorption of casein at O/W interface.
- The observed change in the force parameters with increasing cation concentrations and valency suggested a collapsed conformation of polymers at O/W interface in the presence of hydrated ionic surface structures that interact with the OH group of polymer.

## 8.2 Recommendations for Future Work

- To probe the effect of mono and multivalent anions on the electrostatic and steric interaction forces.
- To probe the competitive adsorption of cations and anions at O/W interface.
- To probe the role of linear and branched alcohols on the electrostatic interaction, and steric interactions.
- Studies on the interaction of globular proteins on the electrostatic and steric interaction forces.
- Competitive adsorption of stimuli responsive molecules at colloidal interfaces towards tunable colloidal interaction forces.
- Fabrication of flexible large area ferrofluid emulsion film for diverse applications.
- Developing color pattern fixing methods.

## List of Reference

1. Hunter, R. J. *Foundations of colloidal science*; Oxford Universiy Press: Great Britain, 2001. p 640.
2. Leal-Calderon, F.; Schmitt, V.; Bibette, J. *Emulsion science : Basic principles*; Second ed.; Springer: New Yok, US, 2007. p 236.
3. Paquin, P. Technological properties of high-pressure homogenizers: The effect of fat globules, milk proteins, and polysachharides. *Int. Dairy J* **1999,** *9*, 329.
4. Soon, S. Y.; Harbidge, J.; Titchener-Hooker, N. J.; Shamlou, P. A. Prediction of drop breakage in an ultra velocity jet homogenizer. *J. Chem. Eng. Jpn.* **2001,** *34*, 640.
5. Mohan, S.; Narsimham, G. Coalescence of protein-stabilized emulsions in a high-pressure homogenizer. *J. Colloid Interface Sci.* **1997,** *192*, 1.
6. Narsimham, G.; Goel, P. Drop coalescence during emulsion formation in a high-pressure homogenizer for tetradecane-in-water emulsion stabilized by sodium dodecyl sulfate. *J. Colloid Interface Sci.* **2001,** *238*, 420.
7. Taisne, L.; Walstra, P.; Cabane, B. Transfer of oil between emulsion droplets. *J. Colloid Interface Sci.* **1996,** *184*, 378.
8. Lobo, L.; Svereika, A. Coalescence during emulsification. 2. Role of small molecule surfactants. *J. Colloid Interface Sci.* **2003,** *261*, 498.
9. Walstra, P. *Formation of Emulsions*. Marcel Dekker: New York 1983.
10. Walstra, P.; Smulders, P. E. A. *Emulsion Formation*. The Royal Society of Chemistry: Cambridge, UK, 1998.
11. Kandori, K. *Application of microporous glass membranes: Membrane emulsification*. Elsevier: Amsterdam, 1995.
12. Peng, S. J.; Williams, R. A. Controlled production of emulsions using a cross-flow membrane. *Part. Part. Syst. Charact.* **1998,** *15*, 21.
13. Kawakatsu, T.; Kikuchi, Y.; Nakajima, M. Regular-sized cell creation in micro-channel emulsification by visual microprocessing method. *JAOCS* **1997,** *74*, 317.
14. Sugiura, S.; Nakajima, M.; Iwamoto, S.; Seki, M. Interfacial tension driven monodisperseddroplet formation from micro fabricated channel array. *Langmuir* **2001,** *17*, 5562.
15. Sugiura, S.; Nakajima, M.; Itou, H.; Seki, M. Synthesis of polymeric microspheres with narrow size distributions employing microchannel emulsification. *Macromol. Rapid Commun.* **2001,** *22*, 773.
16. Groves, M. J. Spontaneous emulsification. *Chem. Indust.* **1978,** *12*, 417.
17. Quincke, G. Ueber Emulsionbildung Und Den Einfluss Der Galle Bei Der Verdauung. *Pluger Arch. Physiol.* **1879,** *19*, 129.
18. Gopal, R. E. S. *Principles of Emulsion Formation*. Academic press: London, 1968.
19. Mason, T. G.; Bibette, J. Emulsification in viscoelastic media. *Phys. Rev. Lett.* **1996,** *77*, 3481.
20. Tadros, T. F. *Emulsion science and technology*; WILEY-VCH Verlag GmbH&co.: Weinheim, 2009. p 335.
21. Bibette, J. Monodisperse ferrofluid emulsions. *J. Magn. Magn. Mater.* **1993,** *122*, 37-41.

22. Philip, J.; Jayakumar, T.; Kalyanasundaram, P.; Raj, B. Stabilized magnetic emulsion and a process of making it. India Patent No. 205114 2002.

23. Bibette, J. Depletion interactions and fractionated crystallization for polydisperse emulsion purification. *J. Colloid Interface Sci.* **1991,** *147*, 474-478.

24. Myers, D. *Surfaces, interfaces and colloids principles and applications*; Wiley-VCH: New York, 1999.

25. Liu, J.; Lawrence, E. M.; Wu, A.; Ivey, M. L.; Flores, G. A.; Javier, K.; Bibette, J.; Richard, J. Field-induced structures in ferrofluid emulsions. *Phys. Rev. Lett.* **1995,** *74* (14), 2828-2831.

26. Xu, X.; Majetich, S. A.; Asher, S. A. Mesoscopic monodisperse ferromagnetic colloids enable magnetically controlled photonic crystals *J. Am. Chem. Soc.* **2002,** *124* (46), 13864 -13868.

27. Nair, S. S.; Thomas, J.; Sandeep, C. S. S.; Anantharaman, M. R.; Philip, R. An optical limiter based on ferrofluids. *Appl. Phys. Lett.* **2008,** *92*, 171908.

28. Philip, J.; Laskar, J. M.; Raj, B. Magnetic field induced extinction of light in a suspension of $Fe_3O_4$ nanoparticles. *Appl. Phys. Lett.* **2008,** *92*, 221911.

29. Philip, J.; Jaykumar, T.; Kalyanasundaram, P.; Raj, B. A tunable optical filter. *Meas. Sci. Technol.* **2003,** *14*, 1289–1294.

30. Dreyfus, R.; Baudry, J.; Roper, M. L.; Fermigier, M.; Stone, H. A.; Bibette, J. Microscopic artificial swimmers. *Nature* **2005,** *437* (6), 862 -865.

31. Bibette, J.; Mason, T. G.; Gang, H.; Weitz, D. A. Kinetically induced odering in gelation of emulsions. *Phys. Rev. Lett.* **1992,** *69*, 981-984.

32. Koenig, A.; Hebraud, P.; Gosse, C.; Dreyfus, R.; Baudry, J.; Bertrand, E.; Bibette, J. Magnetic force probe for nanoscale biomolecules. *Phys. Rev. Lett.* **2005,** *95*, 128301.

33. Boitard, L.; Cottinet, D.; Kleinschmitt, C.; Bremonda, N.; Baudry, J.; Yvert, G.; Bibette, J. Monitoring single-cell bioenergetics via the coarsening of emulsion droplets. *Proc. Natl. Acad. Sci.* **2012,** *109* (19), 7181–7186.

34. Mahendran, V.; Philip, J. Nanofluid based optical sensor for rapid visual inspection of defects in ferromagnetic materials. *Appl. Phys. Lett.* **2012,** *100*, 073104.

35. Mahendran, V.; Beautlin, R. A.; Philip, J. Magnetic nanofluid based approach for imaging defects. *J. Nanofluids* **2013,** *2*, 112-119.

36. Mahendran, V.; Philip, J. An optical technique for fast and ultrasensitive detection of ammonia using magnetic nanofluids. *Appl. Phys. Lett.* **2013,** *102*, 063107.

37. Mahendran, V.; Philip, J. Spectral response of magnetic nanofluid to toxic cations. *Appl. Phys. Lett.* **2013,** *102*, 163109.

38. Mahendran, V.; Philip, J. Sensing of biologically important cations such as Na+ , K+ , Ca2+ , Cu2+ , and Fe3+ using magnetic nanoemulsions. *Langmuir* **2013,** *29*, 4252-4258.

39. Laskar, J. M.; Philip, J.; Raj, B. Light scattering in a magnetically polarizable nanoparticle suspension. *Phys. Rev. E* **2008,** *78*, 031404.

40. Laskar, J. M.; Philip, J.; Raj, B. Experimental investigation of magnetic-field-induced aggregation kinetics in nonaqueous ferrofluids. *Phys. Rev. E* **2010,** *82*, 021402.

41. Brojabasi, S.; Philip, J. Magnetic field dependant backscattering of light in water based ferrofluid containing polymer covered $Fe_3O_4$ nanoparticles. *J. Appl. Phys.* **2013,** *113*, 054902.

42. Cohen-Tannoudji, L.; Bertrand, E.; Bressy, L.; Goubault, C.; Baudry, J.; Klein, J.; Joanny, J.-F.; Bibette, J. Polymer bridging probed by magnetic colloids. *Phys. Rev. Lett.* **2005,** *94*, 038301.

43. Zerrouki, D.; Rotenberg, B.; Abramson, S.; Baudry, J.; Goubault, C.; Leal-Calderon, F.; Pine, D. J.; Bibette, J. Preparation of doublet, triangular, and tetrahedral colloidal clusters by controlled emulsification. *Langmuir* **2006,** *22* (1), 57 - 62.

44. Thiam, A. R.; Bremond, N.; Bibette, J. From stability to permeability of adhesive emulsion bilayers. *Langmuir* **2012,** *28*, 6291-6298.

45. Philip, J.; Bonakdar, L.; Poulin, P.; Bibette, J.; Leal-Calderon, F. Viscous sintering phenomena in liquid-liquid dispersions. *Phys. Rev. Lett.* **2000** *84*, 2018-2021.

46. Philip, J.; Poirier, J. E.; Bibette, J.; Leal-Calderon, F. Gelation and coarsening in dispersions of highly viscous droplets. *Langmuir* **2001** *17*, 3545-3552.

47. Brangbour, C.; Roure, O. d.; Helfer, E.; Demoulin, D.; Mazurier, A.; Fermigier, M.; Carlier, M.-F.; Bibette, J.; Baudry, J. Force-velocity measurements of a few growing actin filaments. *PLoS Biol.* **2011,** *9* (4), e1000613.

48. Leal-Calderon, F.; Stora, T.; Mondain Monval, O.; Bibette, J. Direct measurement of colloidal forces. *Phys. Rev. Lett.* **1994,** *72*, 2959.

49. Philip, J.; Gnanaprakash, G.; Jaykumar, T.; Kalyanasundaram, P.; Raj, B. Stretching and collapse of neutral polymer layers under association with ionic surfactants. *Phys. Rev. Lett.* **2002,** *89*, 268301.

50. Bremond, N.; Thiam, A. R.; Bibette, J. Decompressing emulsion droplets favors coalescence. *Phys. Rev. Lett.* **2008,** *100*, 024501.

51. Thiam, A. R.; Bremond, N.; Bibette, J. Breaking of an emulsion under an ac electric field. *Phys. Rev. Lett.* **2009,** *102*, 188304.

52. London, F. Zur theorie und systematik der molekularkrafte. *Z. Phys.* **1930,** *63*, 245-279.

53. Lyklema, J. *Fundamentals in colloidal and interface science*; Elsevier: Amsterdam, 1991; Vol. 1.

54. Lekkerkerker, H. N. W.; Tuinier, R. *Colloids and the depletion interaction*; Springer Heidelberg: Heidelberg, 2011; Vol. 883. p 248.

55. Popa, I.; Sinha, P.; Finessi, M.; Maroni, P.; Papastavrou, G.; Borkovec, M. Importance of charge regulation in attractive double-layer forces between dissimilar surfaces. *Phys. Rev. Lett.* **2010,** *104*, 228301.

56. Israelachvili, J. N. *Intermolecular and surface forces*; Academic Press: San Diego, 1985.

57. Ebeling, D.; Ende, D. v. d.; Mugele, F. Electrostatic interaction forces in aqueous salt solutions of variable concentration and valency. *Nanotechnology* **2011,** *22*, 305706.

58. Verwey, E. J. W.; Overbeek, J. T. G. *Theory of stability of lyophobic colloids. The interaction of sol particles having an electric double layer*; Elsevier: Amsterdam, 1948.

59. Derjaguin, B. On the repulsive forces between charged colloidal particles and on the theory of slow coagulation and stability of lyophobe sols. *Trans. Faraday. Soc.* **1940,** *35*, 203-215.

60. Verwey, E. J. W. Electrical double layer and stability of emulsions. *Trans. Faraday. Soc.* **1940,** *35*, 192-203.

61. Tadros, T. F. *Colloidal stability : The role of surface forces, Part 1*. Wiley-VCH Verlag GmbH & Co.: Weinheim, 2007; Vol. 1.

62. Tan, Q.; Zhao, G.; Qiu, Y.; Kan, Y.; Ni, Z.; Chen, Y. Experimental observation of the ion-ion correlation effects on charge inversion and strong adhesion between mica surface in aqueous electrolye solutions. *Langmuir* **2014,** *30*, 10845-10854.

63. Omarjee, P.; Espert, A.; Mondain-Monval, O.; Klein, J. Polymer-induced repulsive forces at solid-liquid and at liquid-liquid interfaces. *Langmuir* **2001,** *17*, 5693-5695.

64. Philip, J.; Mondain-Monval, O.; Leal-Calderon, F.; Bibette, J. Colloidal force measurements in the presence of a polyelectrolyte. *J. Phys. D: Appl. Phys.* **1997,** *30* 2798.

65. Kaggwa, G. B.; Nalam, P. C.; Kilpatrick, J. I.; Spencer, N. D.; Jarvis, S. P. Impact of hydrophilic/hydrophobic surface chemistry on hydration forces in the absence of confinement. *Langmuir* **2012,** *28*, 6589−6594.

66. Valtiner, M.; Donaldson, S. H.; Gebbie, M. A.; Israelachvili, J. N. Hydrophobic forces, electrostatic steering, and acid−base bridging between atomically smooth self-assembled monolayers and end-functionalized pegolated lipid bilayers. *J. Am. Chem. Soc.* **2014,** *134*, 1746−1753.

67. Dolan, A. K.; Edwards, S. F. Theory of the stabilization of colloids by adsorbed polymer. *Proc. R. Soc. Lond. A* **1974,** *337*, 509-516.

68. Johner, A.; Bonet-Avalos, J.; Linden, C. C. v. d.; Semenov, A. N.; Joanny, J. F. Adsorption of neutral polymers : Interpretation of the numerical self-consistent field results. *Macromolecules* **1996,** *29*, 3629-3638.

69. Semenov, A. N. Theory of long-range interactions in polymer systems *J. Phys. II* **1996,** *6*, 1759-1780

70. Semenov, A. N.; Bonet Avalos, J.; Johner, A.; Joanny, J. F. Adsorption of polymer solutions onto a flat surface. *Macromolecules* **1996,** *29*, 2179-2196.

71. Semenov, A. N.; Joanny, J. F.; Johner, A.; Avalos, J. B. Interaction between two adsorbing plates: The effect of polymer chain ends. *Macromolecules* **1997,** *30*, 1479-1489.

72. Mondain-Monval, O.; Espert, A.; Omarjee, P.; Bibette, J.; Leal-Calderon, F.; Philip, J.; Joanny, J. F. Polymer-induced repulsive forces: Exponential scaling. *Phys. Rev. Lett.* **1998,** *80*, 1778-1781.

73. Israelachvili, J. N.; Tandor, R. K.; White, L. R. Measurement of forces between two mica surfaces in aqueous poly(ethylene oxide) solutions. *Nature* **1979,** *277*, 120-121.

74. Ducker, W. A.; Senden, T. J.; Pashley, R. M. Direct measurement of collodal forces using Atomic force microscope. *Nature* **1991,** *353*, 239-241.

75. Temple, P. A. Total internal reflection microscopy: A surface inspection technique. *Appl. Opt.* **1981,** *20*, 2656-2664.

76. Ashkin, A. Acceleration and trapping of particles by radiation pressure. *Phys. Rev. Lett.* **1970,** *24*, 156-159.

77. Dreyfus, R.; Lacoste, D.; Bibette, J.; Baudry, J. Measuring colloidal forces with the magnetic chaining technique. *Eur. Phys. J. E* **2009,** *28*, 113-123.

78. Espert, A.; Omarjee, P.; Bibette, J.; Calderon, F. L.; Mondain-Monval, O. Forces between liquid interfaces in the presence of polymer: Concentration, solvent and mass effects. *Macromolecules* **1998,** *31*, 7023-7029.

79. Omarjee, P.; Hoerner, P.; Riess, G.; Cabuil, V.; Mondain-Monval, O. Diblock copolymers adsosrbed at the water-oil interface. *Eur. Phys. J. E* **2001,** *4*, 45-50.

80. Philip, J.; Gnanaprakash, G.; Jaykumar, T.; Kalyanasundaram, P.; Mondain-Monval, O.; Raj, B. Interaction between emulsion droplets in the presence of polymer−surfactant complexes. *Langmuir* **2002,** *18*, 4625.
81. Philip, J.; Jaykumar, T.; Kalyanasundaram, P.; Raj, B.; Mondain-Monval, O. Effect of polymer-surfactant association on colloidal force. *Phys. Rev. E* **2002,** *66*, 011406.
82. Philip, J.; Gnanaprakash, G.; Jayakumar, T.; Kalyanasundaram, P.; Raj, B. Three distinct scenarios under polymer, surfactant, and colloidal interaction. *Macromolecules* **2003,** *36*, 9230-9236.
83. Baudry, J.; Bertrand, E.; Lequeux, N.; Bibette, J. Bio-specific recognition and applications: from molecular to colloidal scales. *J. Phys.: Condens. Matter* **2004,** *16*, R469–R480.
84. Baudry, J.; Rouzeau, C.; Goubault, C.; Robic, C.; Cohen-Tannoudji, L.; Koenig, A.; Bertrand, E.; Bibette, J. Acceleration of the recognition rate between grafted ligands and receptors with magnetic forces. *Proc. Natl. Acad. Sci.* **2006,** *103* (44), 16076–16078.
85. Cohen-Tannoudji, L.; Bertrand, E.; Baudry, J.; Robic, C.; Goubault, C.; Pellissier, M.; Johner, A.; Thalmann, F.; Lee, N. K.; Marques, C. M.; Bibette, J. Measuring the kinetics of biomolecular recognition with magnetic colloids. *Phys. Rev. Lett.* **2008,** *100*, 108301.
86. Dimitrova, T. D.; Leal-Calderon, F. Forces between emulsion droplets stabilized with tween 20 and proteins. *Langmuir* **1999,** *15*, 8813-8821.
87. Roper, M.; Dreyfus, R.; Baudry, J.; Fermigier, M.; Bibette, J.; Stone, H. A. Do magnetic micro-swimmers move like eukaryotic cells? *Proc. R. Soc. A* **2008,** *464*, 877–904.
88. Mondain-Monval, O.; Leal-Calderon, F.; Philip, J.; Bibette, J. Depletion forces in the presence of electrostatic double layer repulsion. *Phys. Rev. Lett.* **1995,** *75*, 3364-3367.
89. Beaman, D. K.; Robertson, E. J.; Richmond, G. L. Metal ions: Driving the orderly assembly of polyelectrolytes at a hydrophobic surface. *Langmuir* **2012,** *28*, 14245−14253.
90. Nylander, T.; Wahlgren, N. M. Forces between adsorbed layers of β-casein. *Langmuir* **1997,** *13*, 6219-6225.
91. Liu, Y.; Guo, R. Interaction between casein and the oppositely charged surfactant. *Biomacromolecules* **2007,** *8*, 2902-2908.
92. Liu, Y.; Yang, L.; Guo, R. Interaction between β-casein micelles and imidazolium-based ionic liquid surfactant. *Soft Matter* **2013,** *9*, 3671-3680.
93. Kragel, J.; Wustneck, R.; Husband, F.; Wilde, P. J.; Makievski, A. V.; Grigoriev, D. O.; Li, J. B. Properties of mixed protein/surfactant adsorption layers. *Colloids Surf. B* **1999,** *12*, 399–407.
94. Dan, A.; Kotsmar, C.; Ferri, J. K.; Javadi, A.; Karbaschi, M.; Kragel, J.; Wustneck, R.; Miller, R. Mixed protein–surfactant adsorption layers formed in a sequential and simultaneous way at water–air and water–oil interfaces. *Soft Matter* **2012,** *8*, 6057-6065.
95. Shima, P. D.; Philip, J. Tuning of thermal conductivity and rheology of nanofluids using an external stimulus. *J. Phys. Chem. C* **2011,** *115*, 20097–20104.
96. Shima, P. D.; Philip, J.; Raj, B. Synthesis of aqueous and nonaqueous iron oxide nanofluids and study of temperature dependence on thermal conductivity and viscosity. *J. Phys. Chem. C* **2010,** *114*, 18825−18833.
97. Zhang, H.; Widom, M. Field-induced forces in colloidal particle chains. *Phys. Rev. E* **1995,** *51*, 2099-2103.

98. Berne, B. J.; Pecora, R. *Dynamic light scattering: with applications to biology, chemistry and physics*; John Wiley: New York, 1976.

99. Hunter, R. J. *Zeta potential in colloid science: Principles and applications*; Academic Press: London, 1981.

100. Zernike, F. Phase contrast, a new method for the microscopic observation of transparent objects- Part I. *Physica* **1942,** *9*, 686-698.

101. Zernike, F. Phase contrast, a new method for the microscopic observation of transparent objects - Part II. *Physica* **1942,** *9*, 974-988.

102. Zernike, F. How I discoveres phase contrast. *Science* **1955,** *121*, 345-349.

103. Hollas, J. M. *Modern spectroscopy*; John Wiley & sons, Ltd: West Sussex, England, 2004.

104. Cullity, B. D. *Elements of X-ray diffraction*; Addison- Wesley publishing company Inc.: Massachusetts, USA, 1956.

105. Williams, D. B.; Carter, C. B. *Transmission electron microscopy : A textbook for materials science*; Springer: New York, 1996.

106. What does polydispersity mean? on http://www.malvern.com.

107. Lockie, H.; Manica, R.; Tabor, R. F.; Stevens, G. W.; Grieser, F.; Chan, D. Y. C.; Dagastine, R. R. Anomalous pull-off forces between surfactant-free emulsion drops in different aqueous electrolytes. *Langmuir* **2012,** *28*, 4259−4266.

108. Gutsche, C.; Keyser, U. F.; Kegler, K.; Kremer, F.; Linse, P. Forces between single pairs of charged colloids in aqueous salt solutions. *Phys. Rev. E* **2007,** *76*, 031403.

109. Sinha, P.; Szilagyi, I.; Ruiz-Cabello, F. J. M.; Maroni, P.; Borkovec, M. Attractive forces between charged colloidal particles induced by multivalent ions revealed by confronting aggregation and direct force measurements. *Phys. Chem. Lett.* **2013,** *4*, 648−652.

110. Mondain-Monval, O.; Leal-Calderon, F.; Bibette, J. Forces between emulsion droplets: Role of surface charges and excess surfactant. *J. Phys. II France* **1996,** *6* 1313-1329.

111. Goubault, C.; Leal-Calderon, F.; Viovy, J.-L.; Bibette, J. Self-assembled magnetic nanowires made irreversible by polymer bridging. *Langmuir* **2005,** *21* (9), 3725 - 3729.

112. Waldron, K. J.; Robinson, J. N. How do bacterial cells ensures that metalloproteins get the correct metal? *Nat. Rev. Microbiol.* **2009,** *7*, 25-35.

113. Bhalla, V.; Sharma, N.; Kumar, N.; Kumar, M. Rhodamine based fluorescence turn-on chemosensor for nanomolar detection of Fe 3+ ions. *Sens. Actuators B* **2013,** *178*, 228-232.

114. A Lemire, J.; J Harrison, J.; J Turner, R. Antimicrobial activity of metals: mechanisms, molecular targets and applications. *Nat. Rev. Microbiol.* **2013,** *11*, 371–384.

115. Imlay, J. A. Pathways of oxidative damage. *Annu.Rev. Microbiol.* **2003,** *57*, 395-418.

116. Hamaker, H. C. The London-van der Waalsattraction between spherical particles. *Physica* **1937,** *4*, 1058-1071.

117. Pearson, R. G. Acids and bases. *Science* **1966,** *151*, 172-177.

118. Manor, O.; Chau, T. T.; Stevens, G. W.; Chan, D. Y. C.; Grieser, F.; Dagastine, R. R. Polymeric stabilized emulsions: Steric effects and deformation in soft systems. *Langmuir* **2012,** *28*, 4599−4604.

119. Gennes, P. G. D. Polymers at an interface. 2. Interaction between two plates carrying adsorbed polymer layers. *Macromolecules* **1982**, 492–500.

120. Gennes, P. G. d. Dynamics of entangledpolymer solutions. 1. The Rouse model. *Macromolecules* **1976,** *9*, 587-593.

121. Zhang, H.; Zeeb, B.; Salminen, H.; Feng, F.; Weiss, J. Solubilization of octane in electrostatically-formed surfactant–polymer complexes. *J. Colloid Interface Sci.* **2014,** *417*, 9-17.

122. Kim, J.; Gao, Y.; Hebebrand, C.; Peirtsegaele, E.; Helgeson, M. E. Polymer-surfactant complexation as a generic route to responsive viscoelastic nanoemulsions. *Soft Matter* **2013,** *9*, 6897-6910.

123. Klein, J.; Rossi, G. Analysis of the experimental implications of the scaling theory of polymer adsorption. *Macromolecules* **1998,** *31*, 1979-1988.

124. Skerjanc, J.; Kogej, K.; Vesnaver, G. Polyelectrolyte-surfactant interactions: enthalpy of binding of dodecyl- and cetylpyridinium cations to poly(styrenesulfonate) anion. *J. Phys. Chem.* **1988,** *92*, 6382–6385.

125. Lutter, J. C.; Wu, T.-y.; Zhang, Y. Hydration of cations: A key to understanding of specific cation effects on aggregation behaviors of PEO-PPO-PEO triblock copolymers. *J. Phys. Chem. B* **2013,** *117*, 10132−10141.

126. Merat, K.; Chaodamrongsakul, J.; Tanthanuch, W.; Vao-soongnern, V. Atomistic solvation structure of calcium ion in poly(vinyl alcohol) as studied by molecular dynamics simulation and X-ray absorption spectroscopy. *J. Non-Crystal. Solids* **2013,** *371-372*, 47-52.

127. Yang, L.; Fan, Y.; Gao, Y. Q. Differences of cations and anions: Their hydration, surface adsorption, and impact on water dynamics. *J. Phys. Chem. B* **2011,** *115*, 12456–12465.

128. Pearson, R. G. Hard and soft acids and bases. *J. Am. Chem. Soc.* **1963,** *85*, 3533-3539.

129. Tobias, D. J.; Hemminger, J. C. Getting specific about specific ion effects. *Science* **2008,** *319*, 1197-1199.

130. Hofmeister, F. Zur Lehre von der Wirkung der Salze. *Arch. Exp. Pathol. Pharmakol.* **1888,** *24*, 247-260.

131. Nostro, P. L.; Ninham, B. W. Hofmeister phenomena: An update on ion specificity in biology. *Chem. Rev.* **2012,** *112*, 2286–2322.

132. Xu, Y.; Liu, G. Amplification of Hofmeister effect by alcohols. *J. Phys. Chem. B* **2014,** *118*, 7450−7456.

133. Wang, T.; Long, Y.; Liu, L.; Wang, X.; Craig, V. S. J.; Zhang, G.; Liu, G. Cation-specific conformational behavior of polyelectrolyte brushes: From aqueous to nonaqueous solvent. *Langmuir* **2014,** *30*, 12850−12859.

134. Long, Y.; Wang, T.; Liu, L.; Liu, G.; Zhang, G. Ion specificity at a low salt concentration in water−methanol mixtures exemplified by a growth of polyelectrolyte multilayer. *Langmuir* **2013,** *29*, 3645−3653.

135. Liu, L.; Wang, T.; Liu, C.; Lin, K.; Ding, Y.; Liu, G.; Zhang, G. Mechanistic insights into amplification of specific ion effect in water−nonaqueous solvent mixtures. *J. Phys. Chem. B* **2013,** *117*, 2535−2544.

136. Liu, L.; Wang, T.; Liu, C.; Lin, K.; Liu, G.; Zhang, G. Specific anion effect in water−nonaqueous solvent mixtures: Interplay of the interactions between anion, solvent, and polymer. *J. Phys. Chem. B* **2013,** *117*, 10936−10943.

137. Wang, T.; Liu, G.; Zhang, G.; Craig, V. S. J. Insights into ion specificity in water−methanol mixtures via the reentrant behavior of polymer. *Langmuir* **2012,** *28*, 1893−1899.

138. Israelachvili, J. N.; Pashley, R. The hydrophobic interaction is long range, decaying exponentially. *Nature* **1982,** *300*, 341-342.

139. Israelachvili, J.; Wennerstrom, H. Role of hydration and water structure in biological and colloidal interactions. *Nature* **1996,** *379*, 219-225.

140. Aaron P.R. Eberle; Norman J. Wagner; Castaneda-Priego, R. Dynamical arrest transition in nanoparticle dispersions with short range interactions. . *Phys. Rev. Lett.* **2011,** *106*, 105704

141. Vacha, R.; Roke, S. Sodium dodecyl sulfate at water-hydrophobic interfaces: A simulation study. *J. Phys. Chem. B* **2012,** *115*, 11936-11942.

142. Aguiar, H. B. d.; Strader, M. L.; Beer, A. G. F. d.; Roke, S. Surface structure of sodium dodecyl sulfate surfactant and oil at the oil-in-water droplet liquid/liquid interface: a manifestation of a nonequilibrium surface state. *J. Phys. Chem. B* **2011,** *115*, 2970–2978.

143. Pashely, R. M.; Ninham, B. W. Double-layer forces in ionic micellar solutions. *J. Phys. Chem.* **1987,** *91*, 2902-2904.

144. Kohonen, M. M.; Karaman, M. E.; Pashely, R. M. Debye length in multivalent electrolyte solutions. *Langmuir* **2000,** *16*, 5749-5753.

145. Netz, R. R. Electrostatistics of counter-ions at and between planar charged walls: From Poisson-Boltzmann to the strong-coupling theory. *Eur. Phys. J. E* **2001,** *5*, 557-574.

146. Harris, A. L.; Chidsey, C. E. D.; Levinos, N. J.; Loiacono, D. N. Monlayer vibratiuonal spectroscopy by infrared visible sum generation at metal and semiconductor surfaces. *Chem. Phys. Lett.* **1978,** *141*, 350-356.

147. Steiner, M.-S.; Duerkop, A.; Wolfbeis, O. S. Optical methods for sensing glucose. *Chem. Soc. Rev.* **2011,** *40* (4805-4839), 4805-4839.

148. Dokken, B. The kidney as a treatment target for type 2 diabetes. *Diabetes Spect.* **2012,** *25*, 29-36.

149. Wu, Q.; Wang, L.; Yu, H.; Wang, J.; Chen, Z. Organization of glucose-responsive systems and their properties. *Chem. Rev.* **2011,** *111*, 7855–7875.

150. Dong, X.-C.; Xu, H.; Wang, X.-W.; Huang, Y.-X.; Chan-Park, M. B.; Zhang, H.; Wang, L.-H.; Huang, W.; Chen, P. 3D Graphene-cobalt oxide electrode for high-performance supercapacitor and enzymeless glucose detection. *ACS Nano* **2012,** *6* (4), 3206-3231.

151. Yang, P.; Jin, S.-Y.; Xu, Q.-Z.; Yu, S.-H. Decorating PtCo bimetallic alloy nanoparticles on graphene as sensors for glucose detection by catalyzing luminol chemiluminescence. *Small* **2013,** *9*, 199–204.

152. Huang, X.; Li, S.; Schultz, J. S.; Wang, Q.; Lin, Q. A dielectric affinity microbiosensor. *Appl. Phys. Lett.* **2010,** *96*, 033701.

153. Zhang, Y.; Liu, K.; Guan, Y.; Zhang, Y. Assembling of gold nanorods on P(NIPAM–AAPBA) microgels: a large shift in the plasmon band and colorimetric glucose sensing. *RSC Adv.* **2012,** *2*, 4768-4776.

154. Lin, S.-Y.; Chang, S.-J.; Hsueh, T.-J. ZnO nanowires modified with Au nanoparticles for nonenzymatic amperometric sensing of glucose. *Appl. Phys. Lett.* **2014,** *104*, 193704.

155. Hong, X.; Peng, Y.; Bai, J.; Ning, B.; Liu, Y.; Zhou, Z.; Gao, Z. A novel opal closest-packing photonic crystal for naked-eye glucose detection. *Small* **2014,** *10*, 1308-1313.

156. Wei, A.; Sun, X. W.; Wang, J. X.; Lei, Y.; Cai, X. P.; Li, C. M.; Dong, Z. L.; Huang, W. Enzymatic glucose biosensor based on ZnO nanorod array grown by hydrothermal decomposition. *Appl. Phys. Lett.* **2006,** *89*, 123902.
157. Dhobale, S.; Joshee, P.; Deore, G.; Laware, S. L.; Kale, S. N. Nanostructured glucose-oxidase immobilized SnO2 thin films for glucose sensing. *Appl. Phys. Lett.* **2011,** *98*, 073704.
158. You, X.; Pikul, J. H.; King, W. P.; Pak, J. J. Zinc oxide inverse opal enzymatic biosensor. *Appl. Phys. Lett.* **2013,** *102*, 253103.
159. Ibupoto, Z. H.; Khun, K.; Lu, J.; Willander, M. The synthesis of CuO nanoleaves, structural characterization, and their glucose sensing application. *Appl. Phys. Lett.* **2013,** *102*, 103701.
160. James, T. D.; Sandanayake, K. R. A. S.; Shinkai, S. Saccharide sensing with molecular receptors based on boronic acid. *Angew. Chem. Int. Ed.* **1996,** *35*, 1910-1921.
161. Zhang, X.; Guan, Y.; Zhang, Y. Ultrathin hydrogel films for rapid optical biosensing. *Biomacrolecules* **2012,** *13*, 92-97.
162. Benitez, E. I.; Genovese, D. B.; Lozano, J. E. Effect of typical sugars on the viscosity and colloidal stability of apple juice. *Food Hydrocolloids* **2009,** *23*, 519– 525.
163. Holmstrom, K.-O.; Welin, E. M. B.; Palva, A. M. E. T.; Tunnela, O. E.; Londesborough, J. Drought tolerance in tobacco. *Nature* **1996,** *379*, 683-684.
164. Cesaro, A. Carbohydrates all dried up. *Nat. Mater.* **2006,** *5*, 593−594.
165. Lelong, G.; Heyd, R.; Charalambopoulou, G.; Steriotis, T.; Brandt, A.; Beck, K.; Vayer, M.; Price, D. L.; Brady, J. W.; Saboungi, M.-L. Role of glucose in enhancing stability of aqueous silica gels against dehydration. *J. Phys. Chem. C* **2012,** *116*, 9481−9486.
166. Ji, H.; Liu, X.; Jin, L.; Zhou, B.; Yao, X.; Wang, X. Effect of glucose on self-assembly of free-standing air–water interfacial lamellar ZrO2 films. *Colloids Surf. A: Physicochem. Eng. Aspects* **2011,** *380*, 182-190.
167. Wei, Y.; Xu, J.; Dong, H.; Dong, J. H.; Qiu, K.; Jansen-Varnum, S. A. Preparation and physisorption characterization of D-glucose-templated mesoporous silica sol gel materials. *Chem. Mater.* **1999,** *11*, 2023-2029.
168. Gress, A.; Heilig, A.; Smarsly, B. M.; Heydenreich, M.; Schlaad, H. Hydrogen-bonded polymer nanotubes in water. *Macromolecules* **2009,** *42*, 4244-4248.
169. Cai, W.; Wang, G.-T.; Du, P.; Wang, R.-X.; Jiang, X.-K.; Li, Z.-T. Foldamer organogels : A circular dichrosm study of glucose-mediated dynamic helicityinduction and amplification. *J. Am. Chem. Soc.* **2008,** *130*, 13450-13459.
170. Blitz, J. *Electrical and magnetic methodes of nodestructive testing*; Adam Hilger: New York, 1991.
171. Forster, F. New findings in the field of non-destructive magnetic leakage field inspection *NDTE Int.* **1986,** *19*, 3-14.
172. Wang, Z. D.; Gu, Y.; Wang, Y. S. A review of three magnetic NDT technologies. *J. Magn. Magn. Mater.* **2012,** *324*, 382–388.
173. Gloria, N. B. S.; Areiza, M. C. L.; Miranda, I. V. J.; Rebello, J. M. A. Development of a magnetic sensor for detection and sizing of internal pipeline corrosion defects. *NDTE Int.* **2009,** *42*, 669–677.
174. Kopp, G.; Willems, H. Sizing limits of metal loss anomalies using tri-axial MFL measurements: A model study. *NDTE Int.* **2013,** *55*, 75-81.

175. Kosmas, K.; Sargentis, C.; Tsamakis, D.; Hristoforou, E. Non-destructive evaluation of magnetic metallic materials using Hall sensors. *J. Mater. Process. Technol.* **2005,** *161*, 359-362.

176. Bowler, J. R.; Bowler, N. Evaluation of the magnetic field near a crack with application to magnetic particle inspection. *J. Phys. D: Appl. Phys.* **2002,** *35*, 2238-2245.

177. Sun, Y.; Kang, Y.; Qiu, C. A new NDT method based on permanent magnetic field perturbation. *NDTE Int.* **2011** *44*, 1-7.

178. Tsukada, K.; Yoshioka, M.; Kiwa, T.; Hirano, Y. A magnetic flux leakage method using a magnetoresistive sensor for nondestructive evaluation of spot welds. *NDTE Int.* **2011,** *44*, 101-105.

179. Krause, H. J.; Kreutzbruck, M. v. Recent development in SQUID NDE. *Physica C* **2002,** *368*, 70-79.

180. Chen, L.; Que, P. W.; Jin, T. A giant-magneto resistive sensor for magnetic flux leakage nondestructive testing of pipeline. *Russ. J. Nondestr. Test* **2005,** *41*, 462-465.

181. Singh, W. S.; Rao, B. P. C.; Vaidyanathan, S.; Raj, T. J. a. B. Detection of leakage magnetic flux from near-side and far-side defects in carbon steel plates using a giant magneto-resistive sensor. *Meas. Sci. Technol.* **2008,** *19*, 015702-015710.

182. Tehranchi, M. M.; Ranjbarana, M.; Eftekhari, H. Double core giant magneto-impedance sensors for the inspection of magnetic flux leakage from metal surface cracks. *Sens. Actuators A* **2011,** *170*, 55-61.

183. Goktepe, M.; Ege, Y.; Bayri, N.; Atalay, S. Non-destructive crack detection using GMI sensor. *Phys. Status Solidi (C)* **2004,** *1*, 3436-3439.

184. Allweins, K.; Kreutzbruck, M. V.; Gierelt, G. Defect detection in aluminium laser welds using an AMR sensor array. *J. Appl. Phys.* **2005,** *97*, 10Q102.

185. Tehranchi, M. M.; Hamidi, S. M.; Eftekhari, H.; Karbaschi, M.; Ranjbaran, M. The inspection of magnetic flux leakage from metal surface cracks by magneto-optical sensors. *Sens. Actuators A* **2011,** *172*, 365-368.

186. Klank, M.; Hagedorn, O.; Holthaus, C.; Shamonin, M.; Dotsch, H. Characterization and optimization of magnetic garnet films for magneto-optical visualization of magnetic field distributions. *NDTE Int.* **2003,** *36*, 375–381.

187. Ravan, M.; Amineh, R. K.; Koziel, S.; Nikolova, N. K.; Reilly, J. P. Sizing of multiple cracks using magnetic flux leakage measurements. *IET Sci. Meas. Technol.* **2010,** *4*, 1-11.

188. Edwards, C.; Palmer, S. B. The magnetic leakage field fo surface-breaking cracks. *J. Phys. D: Appl. Phys.* **1986,** *19*, 657-674.

189. Pashagin, A. I.; Bogdanovich, B. N.; Shcherbinin, V. E. On Correlation between the field and the flaw dimensions in magnetic nondestructive testing of hot-rolled pipes. *Defektoskopiya* **1988,** *3*, 91-93.

190. Mandal, K.; Atherton, D. L. A study of magnetic flux-leakage signals. *J. Phys. D: Appl. Phys.* **1998,** *31*, 3211-3218.

191. Zhang, Y.; Sekine, K.; Watanabe, S. Magnetic leakage field due to sub-surface defects in ferromagnetic specimens *NDTE Int.* **1995,** *28* (2), 67-71.

192. Uetake, I.; Saito, T. Magnetic flux leakage by adjacent parallel surface slots *NDTE Int.* **1997,** *30* (6), 371-376.

193. Minkov, D.; Shoji, T. Method for sizing of 3-D surface breaking flaws by leakage flux. *NDTE Int.* **1998,** *31* (5), 317-323.

194. Mandache, C.; Clapham, L. A model for magnetic flux leakage signal predictions. *J. Phys. D: Appl. Phys.* **2003,** *36*, 2427-2432.

195. Lukyanets, S.; Snarskii, A.; Shamoninc, M.; Bakaevc, V. Calculation of magnetic leakage field from a surface defect in a linear ferromagnetic material: an analytical approach. *NDTE Int.* **2003,** *36*, 51-55.

196. Gobov, Y. L.; Loskutov, V. R.; Reutov, Y. Y. A dipole model for magnetic leakage fields created by a circular butt-wellded joint. *Defektoskopiya* **2005,** *41*, 85-90.

197. Hwang, J. H.; Lord, W. Finite Element modeling of magnetic field / defect interactions. *J. Test. Eval.* **1975**, 21-25.

198. Lord, W.; Hwang, J. H. Defect characterization from magnetic leakage fields. *Brit. J. NDT* **1977,** *19* (1), 14-18.

199. Schifini, R.; Bruno, A. C. Experimental verification of a finite element model used in a magnetic flux leakage inverse problem. *J. Phys. D: Appl. Phys.* **2005,** *38*, 1875-1881.

200. Al-Naemi, F. I.; Hall, J. P.; Moses, A. J. FEM modeling techniques of magnetic flux leakage type NDT for ferromagnetic plate inspection. *J. Magn. Magn. Mater.* **2006,** *304*, 790-793.

201. Li, Y.; Tian, G. Y.; Ward, S. Numerical simulation on magnetic flux leakage evaluation at high speed. *NDTE Int.* **2006,** *39*, 367-373.

202. Zuoying, H.; Peiwen, Q.; Liang, C. 3D FEM analysis in magnetic flux leakage method. *NDTE Int.* **2006,** *39*, 61-66.

203. Amineh, R. K.; Koziel, S.; Nikolova, N. K.; Bandler, J. W.; Reilly, J. P. A space mapping methodology for defect characterization from magnetic flux leakage measurements. *IEEE Trans. Magn.* **2008,** *44*, 2058-2064.

204. Zhang, Y.; Ye, Z.; Wang, C. A fast method for rectangular crack sizes reconstruction in magnetic flux leakage testing. *NDTE Int.* **2009,** *42*, 369-375.

205. Chen, Z.; Yusa, N.; Miya, K. Some advances in numerical analysis techniques for quantitative electromagnetic nondestructive evaluation. *Nondestr. Test. Eval.* **2009,** *24* (1-2), 35.

206. Yuan, X.; Wang, C.; Zuo, X.; Hou, S. A method of 2D defect profile reconstruction from magnetic flux leakage signals based on improved particle filter. *Insight* **2011,** *53* 152-155.

207. Zatsepin, N. N.; Shcherbinin, V. E. Calculation of the magnetostatic field of surface defects, I. Field topography of surface defect models. *Defektoskopia* **1966,** *5*, 500.

208. Katoh, M.; Masumoto, N.; Nishio, K.; Yamaguchi, T. Modeling of the yoke-magnetization in MFL-testing by finite elements. *NDTE Int.* **2003,** *36*, 479-486.

209. Philip, J.; Rao, C. B.; Jayakumar, T.; Raj, B. A new optical technique for detection of defects in ferromagnetic materials and components. *NDTE Int.* **2000,** *33*, 289-295.

210. Napper, D. H. *Polymeric stabilization of colloidal dispersions*; Academic press: New York, 1983. p 441.

211. Fleer, G.; Cohen Stuart, M.; Scheutjens, J.; Cosgrove, T.; Vincent, B. *Polymer at interfaces* Chapman and Hal: London, 1993.

212. Feijter, J. A. D.; Benjamins, J.; Tamboer, M. Adsorption displacement of proteins by surfactants in oil-in-water emulsions. *Colloids Surf.* **1987,** *27*, 243-266.

213. Dickinson, E.; Rolfe, S. E.; Dalgleish, D. G. Competetive adsorption of $\alpha_{s1}$-casein and β-casein in oil-in-water emulsion. *Food Hydrocolloids* **1988,** *2*, 397-405.

214. Dickinsion, E.; Rolfe, S. E.; Dalgleish, D. G. Competetive adsorption in oil-in-water emulsions containing α–lactalbumin and β–lactaglobulin *Food Hydrocolloids* **1989,** *3*, 193-203.

215. Dickinson, E.; Hunt, J. A.; Dalgleish, D. G. Competetive adsorption of phosvitin with milk proteins in oil-in-water emulsions. *Food Hydrocolloids* **1991,** *4*, 403-414.

216. Courthaudon, J.-L.; Dickinson, E.; Matsumura, Y.; Clark, D. C. Competitive adsoprtion of β lactoglobulin + tween 20 at the oil-water interface. *Colloids Surf.* **1991,** *56*, 293-300.

217. Chen, J.; Dickinson, E. Protein/surfactant interfacial interactions Part 3. Competitive adsorption of protein + surfactant in emulsions. *Colloids Surf. A* **1995,** *101*, 77-85.

218. Maldonado-Valderrama, J.; Woodward, N. C.; Gunning, A. P.; Ridout, M. J.; Husband, F. A.; Mackie, A. R.; Morris, V. J.; Wilde, P. J. Interfacial characterization of β-lactoglobulin networks: Displacement by bile salts. *Langmuir* **2008,** *24*, 6759-6767.

219. Woodward, N. C.; Gunning, A. P.; Maldonado-Valderrama, J.; Wilde, P. J.; Morris, V. J. Probing the in situ competitive displacement of protein by nonionic surfactant using atomic force microscopy. *Langmuir* **2010,** *26*, 12560–12566.

220. Delahaije, R. J. B. M.; Gruppen, H.; Nieuwenhuijzen, N. H. v.; Giuseppin, M. L. F.; Wierenga, P. A. Effect of glycation on the flocculation behavior of protein-stabilized oil-in-water emulsions. *Langmuir* **2013,** *29*, 15201−15208.

221. Zhai, J. L.; Day, L.; Aguilar, M.-I.; Wooster, T. J. Protein folding at emulsion oil/water interfaces. *Curr. Op. Colloids Interface Sci.* **2013,** *18*, 257-271.

222. Tucker, I. M.; Petkov, J. T.; Penfold, J.; Thomas, R. K.; Li, P.; Cox, A. R.; Hedges, N.; Webster, J. R. P. Spontaneous surface self-assembly in protein−surfactant mixtures: Interactions between hydrophobin and ethoxylated polysorbate surfactants. *J. Phys. Chem. B* **2014,** *118*, 4867−4875.

223. Engelhardt, K.; Weichsel, U.; Kraft, E.; Segets, D.; Peukert, W.; Braunschweig, B. Mixed layers of β-lactoglobulin and SDS at air−water interfaces with tunable intermolecular interactions. *J. Phys. Chem. B* **2014,** *118*, 4098−4105.

224. Setter, O.; Livney, Y. The effect of sugar stereochemistry on protein self-assembly: the case of β -casein micellization in different aldohexose solutions. *Phys. Chem. Chem. Phys.* **2015,** *1*, 3599-3607.

225. Tercinier, L.; Ye, A.; Anema, S. G.; Singh, A.; Singh, H. Interactions of casein micelles with calcium phosphate particles. *J. Agri. Food Chem.* **2014,** *DOI: 10.1021/jf501814*.

226. Thompson, A.; Boland, M.; Singh, H. *Milk proteins: From expression to food*. Academic press: San Diego,USA, 2008; p 561.

227. Murakami, R.; Binks, B. P.; Moriyama, H.; Yamamoto, M.; Rocher, A. Particle stabilization of oil-in-water-in-air materials *Adv. Mater.* **2012,** *24* (6), 767-71.

228. Dickinson, E. Properties of emulsions stabilized with milk proteins: Overview of some recent developments. *J. Dairy Sci.* **1997,** *80*, 2607–2619.

229. Cao, C.; Lei, J.; Zhang, L.; Du, F.-P. Equilibrium and dynamic interfacial properties of protein/ionic-liquid-type surfactant solutions at the decane/water interface. *Langmuir* **2014,** *30*, 13744−13753.

230. Dickinson, E. Caseins in emulsions: interfacial properties and interactions. *Int. Dairy J.* **1999,** *9*, 305-312.

231. Dalgleish, D. G. The sizes and conformations of the proteins in adsorbed layers of individual caseins on latices and in oil-in-water emulsions *Colloids Surf. B: Biointerfaces* **1993,** *1*, 1-8.

232. Modler, H. W. Functional properties of nonfat dairy ingredients- A review. Modification of products containing casein. *J. Dairy Sci.* **1985,** *68*, 2195-2205.

233. Dickinson, E. Structure formation in casein-based gels, foams and emulsions. *Colloids Surf. A: Physicochem. Eng. Aspects* **2006,** *288*, 3-11.

234. Eigel, W. N.; Butler, J. E.; Ernstrom, C. A.; Farrell, H. M.; Harwalkar, V. R.; Jenness, R.; Whitney, R. M. Nomenclature of proteins of cow's milk: Fith revision. *J. Dairy Sci.* **1984,** *67*, 1599-1631.

235. Dickinson, E. Mixed proteinaceous emulsifiers: review of competitive protein adsorption and the relationship to food colloid stabilization. *Food Hydrocolloids* **1986,** *1*, 3-23.

236. Qi, P. X. Studies of casein micelle structure: the past and the present. *Lait* **2007,** *87*, 363-383.

237. Kruif, C. G. d.; Grinberg, V. Y. Micellisation of β-casein. *Colloids Surf. A: Physicochem. Eng. Aspects* **2002,** *210*, 183-190.

238. Liang, Y.; Patel, H.; Matia-Merino, L.; Ye, A.; Golding, M. Structure and stability of heat-treated concentrated dairy-protein-stabilised oil-in-water emulsions: A stability map characterisation approach. *Food Hydrocolloids* **2013,** *33*, 297-308.

239. Singh, H.; Ye, A. Structural and biochemical factors affecting the digestion of protein-stabilized emulsions. *Curr. Op. Colloids Interface Sci.* **2013,** *18*, 360–370.

240. Shapira, A.; Markman, G.; Assaraf, Y. G.; Livney, Y. D. β-casein–based nanovehicles for oral delivery of chemotherapeutic drugs: drug-protein interactions and mitoxantrone loading capacity. *Nanomedicine* **2010,** *6*, 547-555.

241. Vos, W. M. d.; Cattoz, B.; Avery, M. P.; Cosgrove, T.; Prescott, S. W. Adsorption and surfactant-mediated desorption of poly(vinylpyrrolidone) on plasma- and piranha-cleaned silica surfaces. *Langmuir* **2014,** *30*, 8425−843.

242. Spruijt, E.; Biesheuvel, P. M.; Vos, W. M. d. Adsorption of charged and neutral polymer chains on silica surfaces: The role of electrostatics, volume exclusion, and hydrogen bonding. *Phys. Rev. E* **2015,** *91*, 012601.

243. Stuart, M. A. C.; Fleer, G. T.; Scheutjens, J. M. H. M. Displacement of polymers.II Experiment. Determination of segmrntal adsorption enery of poly(vinylpyrrolidone) on silica. *J. Colloid Interface Sci.* **1984,** *97*, 526-535.

244. Mubarekyan, E.; Santore, M. M. The energy barrier to self exchange between PEO adsorbed on silica and in solution. *Macromolecules* **2001,** *34*, 7504-7513.

245. Beek, G. P. v. d.; Stuart, M. A. C.; Cosgrove, T. Polymer adsorption and desorption studies via $^1$H NMR relaxation of solvent. *Langmuir* **1991,** *7*, 327-334.

246. Cooper, C. L.; Cosgrove, T.; Duijneveldt, J. S. v.; Murray, M.; Prescott, S. W. Competition between polymers for adsorption on silica: A solvent relaxation NMR and small-angle neutron scattering study. *Langmuir* **2013,** *29*, 12670−12678.

247. Sakata, S.; Inoue, Y.; Ishihara, K. Quantitative evaluation of interaction force between functional groups in protein and polymer brush surfaces. *Langmuir* **2014,** *30*, 2745−2751.

248. Das, S.; Jr., S. H. D.; Kaufman, Y.; Israelachvili, J. N. Interaction of adsorbed polymers with supported cationic bilayers. *RSC Adv.* **2013,** *3*, 20405-20411.

249. Sangeetha, J.; Philip, J. The interaction, stability and response to an external stimulus of iron oxide nanoparticle-casein nanocomplexes. *Colloids Surf.A:Physiochem. Eng. Aspects* **2012,** *406*, 52-60.

250. Bijl, E.; Vries, R. d.; Valenberg, H. v.; Huppertz, T.; Hooijdonk, T. v. Factors influencing casein micelle size in milk of individual cows: Genetic variants and glycosylation of k-casein. *Int. J. Diary* **2014,** *34*, 135-141.

251. Wojciechowski, K.; Kezwon, A.; Lewandowska, J.; Marcinkowski, K. Effect of β-casein on surface activity of Quillaja bark saponin at fluid/fluid interfaces. *Food Hydrocolloids* **2014,** *34*, 208-216.

252. Evers, C. H. J.; Andersson, T.; Lund, M.; Skepo, M. Adsorption of unstructured protein β-casein to hydrophobic and charged surfaces. *Langmuir* **2012,** *28*, 11843−11849.

253. Klein, J.; Pincus, P. Interaction between surfaces with adsorbed polymers: poor solvents. *Macromolecules* **1982,** *15*, 1129–1135.

254. Swaisgood, H. E. Chemistry of milk protein. In *Developments in dairy chemistry*, Fox, P. F., Ed.; Elsevier Applied Science: London, 1982; Vol. 1, pp 1-59.

255. Dalgleish, D. G. Conformations and structures of milk proteins adsorbed to oil-water interfaces. *Food Res. Int.* **1996,** *29*, 541-547.

256. Horne, D. S. Casein interactions: Casting light on the *Black Boxes,* the structure in dairy products. *Int. Dairy J.* **1998,** *8*, 171-177.

257. Kawaguchi, M. Sequential polymer adsorption : Competition and displacement process. *Adv. Colloid Interface Sci.* **1990,** *32*, 1-41.

258. Stuart, M. A. C.; Fleer, G. J.; Scheutjens, J. M. H. M. Displacement of polymers. I. Theory. Segmental adsorption energy form polymer desorption binary solvent. *J. Colloid Interface Sci.* **1984,** *97*, 515-525.

259. Evans, F. D.; Wennerstrom, H. *The colloidal domain : Where physics, chemistry, biology and technology meet*; 2nd ed.; VCH Publishers: New Yark, 1999.

260. Pegram, L. M.; Wendorff, T.; Erdmann, R.; Shkel, I.; Bellissimo, D.; Felitsky, D. J.; Jr, M. T. R. Why Hofmeister effects of many salts favor protein folding but not DNA helix formation. *Proc. Natl. Acad. Sci. USA* **2010,** *107*, 7716–7721.

261. Mao, Y.; Du, Y.; Cang, X.; Wang, J.; Chen, Z.; Yang, H.; Jiang, H. Binding competition to the POPG lipid bilayer of Ca2+,Mg2+,Na+,and K+ in different ion mixtures and biological implication. *J. Phys. Chem. B* **2013,** *117*, 850−858.

262. Scheu, R.; Chen, Y.; Aguiar, H. B. d.; Rankin, B. M.; Ben-Amotz, D.; Roke, S. Specific ion effects in amphiphile hydration and interface stabilization. *J. Am. Chem. Soc* **2014,** *136*, 2040−2047.

263. Zhang, Y.; Furyk, S.; Bergbreiter, D. E.; Cremer, P. S. Specific ion effects on the water solubility of macromolecules: PNIPAM and the Hofmeister series. *J. Am. Chem. Soc.* **2005,** *127*, 4505-14510.

264. Chen, X.; Yang, T.; Kataoka, S.; Cremer, P. S. Specific ion effects on interfacial water structure near macromolecules. *J. Am. Chem. Soc.* **2007,** *129*, 12272-12279.

265. Lund, M.; Vrbka, L.; Jungwirth, P. Specific ion binding to nonpolar surface patches of preoteins. *J. Am. Chem. Soc.* **2008,** *130*, 11582-11583.
266. Okur, H. I.; Kherb, J.; Cremer, P. S. Cations bind only weakly to amides in aqueous solutions. *J. Am. Chem. Soc.* **2013,** *135*, 5062−5067.
267. Tanford, C. *The hydrophobic eeffect: Formation of micelles and biological membranes*; 2nd Edition ed.; Wiley-Interscience: New York, 1980.
268. Scheu, R.; Chen, Y.; Subinya, M.; Roke, S. Stern layer formation induced by hydrophobic interactions: A molecular level study. *J. Am. Chem. Soc.* **2013,** *135*, 19330-19335.
269. Bogatko, S. A.; Bylaska, E. J.; Weare, J. H. First principles simulation of bonding, vibrational, and electronic properties of the hydration shells of the high-spin Fe3+ ion in aqueous solutions. *J. Phys. Chem. A* **2010,** *114*, 2189-2200.
270. Siretanu, I.; Ebeling, D.; Andersson, M. P.; Stipp, S. L. S.; Philipse, A.; Stuart, M. C.; Ende, D. v. d.; Mugele, F. Direct observation of ionic structure at solid-liquid interfaces: A deep look into the stern layer. *Sci. Rep.* **2014,** *4*, 4956.
271. Winter, B.; Weber, R.; Schmidt, P. M.; Hertel, I. V.; Faubel, M.; Vrbka, L.; Jungwirth, P. Molecular structure of surface-active salt solutions: Photoelectron spectroscopy and molecular dynamics simulations of aqueous tetrabutylammonium iodide. *J. Phys. Chem. B* **2004,** *108*, 14558-14564.
272. Hayes, P. L.; Malin, J. N.; Konek, C. T.; Geiger, F. M. Interaction of nitrate, barium, strontium and cadmium ions with fused quartz/water interfaces studied by second harmonic generation. *J. Phys. Chem. A* **2008,** *112*, 660-668.
273. Robertson, E. J.; Beaman, D. K.; Richmond, G. L. Designated drivers: The differing roles of divalent metal ions in surfactant adsorption at the oil-water interface. *Langmuir* **2013,** *29*, 15511−15520.
274. Deyerle, B. A.; Zhang, Y. Effects of hofmeister anions on the aggregation behavior of PEO-PPO-PEO triblock copolymers. *Langmuir* **2011,** *27*, 9203–9210.
275. Philip, J.; Prakash, G. G.; Jaykumar, T.; Kalynasundaram, P.; Mondain Monval, O.; Raj, B. Interaction between emulsion droplets in the presence of polymer−surfactant complexes. *Langmuir* **2002,** *18*, 4625-4631.
276. Santos, A. P. d.; Levin, Y. Ion specificity and the theory of stability of colloidal suspensions. *Phys. Rev. Lett.* **2011,** *106*, 167801.
277. Ma, L.; Gaisinskaya-Kipnis, A.; Kampf, N.; Klein, J. Orgins of hydration lubrication. *Nat. Commun.* **2015,** *6*, 6060.
278. Bos, R.; Mei, H. C. v. d.; Busscher, H. J. Physico-chemistry of initial microbial adhesive interactions- its mechanism and methods for study. *FEMS Microbiol. Rev.* **1999,** *23*, 179-230.
279. Marcus, Y. Effect of ions on the structure of water: Structure making and breaking. *Chem. Rev.* **2009,** *109*, 1346-1370.
280. Zhao, B.; Brittain, W. J. Polymer brushes:surface-immobilized macromolecules. *Prog. Polym. Sci.* **2000,** *25*, 677-710.
281. Klein, J.; Luckham, P. Force betwee two adsaorbed polyethylene oxide layers immeresed in a good aqueous solvent. *Nature* **1982,** *300*, 429-431.
282. Klein, J. Long-ranged surface forces: The structure and dynamics of polymers at interfaces. *Pure Appl. Chem.* **1992,** *64*, 1577-1584.

283. Marcus, Y. *Ion properties*; Marcel Dekker Inc.: New York, 1997. p 259.

284. Marcus, Y. Thermodynamics of ion hydration and its interpretation in terms of a common model. *Pure Appl. Chem.* **1987,** *59*, 1093-1101.

285. Phillips, C. S. G.; Williams, R. J. P. *Inorganic chemistry I. Principles and non-metals*; Oxford university press: USA, 1965.

286. Smith, D. W. Ionic hydration enthalphies. *J. Chem. Educ.* **1977,** *54*, 540-542.

287. Beaudoin, E.; Gourier, C.; Hiorns, R. C.; Francois, J. Structure and properties of hydrophobically end-capped poly(ethylene oxide) solutions in the presence of monovalent and divalent cations. *J. Colloid Interface Sci.* **2002,** *251*, 398-408.

288. Collins, K. D.; Neilson, G. W.; Enderby, J. E. Ions in water : Characterizing the forces that control chemical processes and biological structure. *Biophys. Chem.* **2007,** *128*, 95-104.

289. Kiriukhin, M. Y.; Collins, K. D. Dyanmic hydration numbers for biologically important ions. *Biophys. Chem.* **2002,** *99*, 155-168.